SCUOLA
NORMALE
SUPERIORE

Classe di Scienze

Corso di perfezionamento in
Nanoscienze

XXXIII ciclo

Defect-engineered graphene functionalization via cycloaddition reaction − towards a versatile platform for nanoscale devices and 3D heterostructures

Settore Scientifico Disciplinare **FIS/03**

Candidato
dr. Luca Basta

Relatori   Supervisore interno

Dr. Stefano Veronesi   Prof. Luigi Rolandi

Dr. Stefan Heun

Defect–engineered graphene functionalization via cycloaddition reaction — towards a versatile platform for nanoscale devices and 3D heterostructures

PhD in Nanosciences

Luca Basta

Scuola Normale Superiore

2022

Abstract

In recent years it has been shown that the outstanding properties of graphene, a direct consequence of its unique 2D structure, could be further tailored by surface functionalization with suitable materials, towards a fine tuning of the system's physical and chemical properties. In particular, the covalent functionalization of graphene using organic functional groups has been explored as a pivotal step towards the formation of graphene composites at the nanoscale. Alongside the commonly diffused approach with diazonium salts (abundant and quick but hard to control), a more selective and controlled method has been shown as very promising: 1,3–dipolar cycloaddition (1,3–DC) of azomethine ylide has been investigated for the chemical modification of graphene–like systems. However, while graphene's high specific surface area of 2630 m^2/g provides numerous possible binding sites, its chemical inertness makes it difficult to modify graphene's structure without disrupting it or introducing excessive disorder. Thus, to finely control or intentionally design the binding sites of functionalizing molecules on the surface of graphene while preserving the high quality of its unique structure remains an open challenge. A promising route in order to locally improve the reactivity of graphene is to introduce beneficial structural defects. For example, due to the defect–induced electron charge redistribution, defective graphene shows increased chemical reactivity towards addition reactions. At the same time, the precise control in defect formation would allow a fine tailoring of the surface chemistry of graphene, fundamental for the engineering of its electronic properties or for sensing applications. The most versatile approach that satisfies the requirements for a controlled introduction of structural defects in graphene is based on particle irradiation techniques. Indeed, effective defect modulations can be patterned over a large area via electron beam irradiation (EBI), utilizing scanning electron microscopy (SEM), in a very flexible way.

The PhD research presented here builds upon this idea. Covalent functionalization of different graphene–based systems has been achieved, allowing to explore various parameters of the functionalization process, including EBI defect–engineering.

Firstly, the functionalization procedure is optimized utilizing graphene nanosheets (GNS) and reduced graphene oxide (rGO) dispersed in the liquid phase, and, for the first time, a comparison of the efficiency of 1,3–DC of azomethine ylide in different dispersant solvents (NMP and DMF) is reported. The functionalization is confirmed with electron energy loss spectroscopy (EELS) and energy–dispersive X–ray spectroscopy (EDX) measurements, and new Raman features arising from the functionalization with azomethine ylide are detected. Density functional theory (DFT) models for pristine and functionalized rGO are built and characterized by evaluating the restrained elec-

trostatic potential (RESP)–derived partial atomic charges, which highlighted the localization of the charges in the pristine rGO induced by the presence of defects (epoxy groups) in the initial structure. Furthermore, the computation of the power spectrum (PS) helps with the assignment of characteristic Raman peaks to the functionalization with the azomethine ylide. Finally, the elemental composition of pristine and functionalized graphene is investigated via x–ray photoelectron spectroscopy (XPS) measurements, allowing to confirm the stability of the functionalization (up to 180 °C) and to estimate the efficiency of the 1,3–DC on graphene. Thanks to the local inhomogeneity of the partial charges, due to the presence of oxygen functional groups in the initial structure, a higher functionalization is achieved on rGO ($\sim$ 2 times higher than on GNS).

The enhancement of the chemical reactivity measured in our defected graphene validates the interest in further exploring the possibility to control the position of defects on higher quality graphene systems. Defect patterns are designed on micromechanically exfoliated graphene flakes on silica substrates by EBI. Their distribution is analyzed with Raman spectroscopy, revealing that surface treatments of the graphene–supporting substrate have strong impact on the lateral resolution that can be achieved on the final defective pattern. Unintentional defects–rich zones are revealed in the adjacent parts of the irradiated areas, and Monte Carlo simulations of primary electrons scattering events demonstrate that these transition zones originate within the area where back–scattered electrons (BSEs) and secondary electrons (SEs) generated near the substrate surface by BSEs (by interaction with organic impurities adsorbed on the Si/SiO_2 substrate) escape from the substrate surface. These results can be exploited in order to design high spatially–resolved defect patterns on monolayer graphene flakes, introducing a selectively enhanced chemical reactivity towards the organic functionalization.

To explore this route, defect patterns are designed on exfoliated graphene flakes via low–energy (30 keV) EBI. Raman spectroscopy maps show the appearance of the characteristic D peak only in the patterned area, while AFM images confirm the spatial resolution of the pattern ($\sim$ 100 nm). The 1,3–DC of azomethine ylide in–situ involves the localization of a C=C bond of the graphene structure, which is favorable in presence of the defects, hence introducing a selective control of the chemical modification of graphene. The Raman analysis on functionalized graphene flakes exhibits new features only in the patterned area, while the unexposed area still presents the spectrum of pristine graphene, confirming the selectivity introduced via defect patterning. Moreover, AFM images of patterned graphene show an improved adhesion on the silica substrate, allowing to avoid detachment issues during the functionalization procedure in the organic solvent. DFT allows to identify the vibrational contributions of the functional groups of the azomethine ylide grafted on the graphene surface and of the modified vibrational modes of the graphene lattice in the experimental Raman spectrum. Furthermore, under laser irradiation (up to 1.6 mW) the Raman spectrum recovers towards the spectrum of non–functionalized patterned graphene, indicating the desorption of the ylide and the reversibility of the functionalization.

Then, the functionalization of epitaxial graphene (EG) on SiC is investigated, benefiting from the valuable addition of scanning tunneling microscopy (STM) and spectroscopy (STS). STM images of functionalized EG reveal the appearance of new structures, randomly arranged over the flat terraces (with lower density) and along the edges (with higher density), with an average height in the range 2 – 15 Å, and a graphene sur-

face coverage of $\sim 14\%$. The graphene structure is preserved after the functionalization procedure, as confirmed by atomically resolved STM images of its hexagonal lattice. STS spectra acquired on functionalization EG indicate the opening of a bandgap (of $0.13 - 0.20$ eV) in the local density of states (LDOS) of these structures, in contrast with the zero–gap linear behavior measured on graphene. The Raman analysis of functionalized EG exhibit new features, together with a downshift of the G and 2D peaks. These results indicate the grafting of azomethine ylides on graphene. Finally, to increase the efficiency of the covalent functionalization of EG and, in particular, to be able to spatially design the functionalization of EG, defect patterning via EBI is explored. After patterning, Peak Force – Quantitative NanoMechanical (PF–QNM) measurements allow to identify the designed defect pattern, confirming the spatial resolution of the technique (with different electron doses and e–beam scan step sizes). Moreover, the analysis of the adhesion forces reveals that the patterning results in an enhancement of the adhesion of the graphene with the substrate, as already seen in previous experiments. Although incomplete, these are valuable results in the outlook of a deterministic and controlled chemical functionalization of EG on SiC, which would be extremely beneficial for the fabrication of high quality devices at the nanoscale. In fact, EG on SiC eliminates the need for transfer procedures and presents favorable characteristics for large–scale graphene electronics.

The results discussed here open the route for a controlled functionalization of different graphene–based systems with designed molecules, which could act both as active functional groups or passive spacers towards multi–functional sensing devices or multilayered spaced graphene systems optimized for hydrogen storage or gas sensing.

List of Publications

- 2022 — *Deterministic Organic Functionalization of Monolayer Graphene Via High Resolution Surface Engineering*
  L. Basta, F. Bianco, A. Moscardini, F. Fabbri, L. Bellucci, V. Tozzini, S. Heun and S. Veronesi
  arXiv Materials Science, 2022, **preprint**, arXiv:2202.06609
  DOI: 10.48550/arXiv.2202.06609 – Currently submitted to Journal of Materials Chemistry C

- 2022 — *Morphology and electronic properties of incipient soot by scanning tunneling microscopy and spectroscopy*
  S. Veronesi, M. Commodo, L. Basta, G. De Falco, P. Minutolo, N. Kateris, H. Wang, A. D'Anna and S. Heun
  Combustion and Flame, 2022, **243**, 111980
  DOI: 10.1016/j.combustflame.2021.111980

- 2022 — *Substrate surface effects on electron-irradiated graphene*
  L. Basta, A. Moscardini, S. Veronesi and F. Bianco
  Surfaces and Interfaces, 2022, **28**, 101694 – DOI: 10.1016/j.surfin.2021.101694

- 2021 — *Covalent Organic Functionalization of Graphene Nanosheets and Reduced Graphene Oxide via 1,3-Dipolar Cycloaddition of Azomethine Ylide*
  L. Basta, A. Moscardini, F. Fabbri, L. Bellucci, V. Tozzini, S. Rubini, A. Griesi, M. Gemmi, S. Heun and S. Veronesi
  Nanoscale Advances, 2021, **3**, 5841 – DOI: 10.1039/D1NA00335F

- 2018 — *A sensitive calorimetric technique to study energy (heat) exchange at the nano–scale*
  L. Basta, S. Veronesi, Y. Murata, Z. Dubois, N. Mishra, F. Fabbri, C. Coletti and S. Heun
  Nanoscale, 2018, **10**, 10079 – DOI: 10.1039/C8NR00747K

Contents

Introduction

Nanoscience is a flourishing area of science with a remarkable potential to reshape the world around us. It consists in the study of matter at the *nanometre*–scale, where materials demonstrate novel and unexpected properties. The concepts at the root of nanoscience date back to December 29, 1959, when at the California Institute of Technology (CalTech), the physicist Richard Feynman gave a lecture entitled *There's Plenty of Room at the Bottom.*[1] In his talk, Feynman suggested a novel possibility for the manipulation of individual atoms and molecules. Actually, his dream became real only in 1981, when the development of the scanning tunneling microscope unlocked the ability to *see* and interact with single atoms.

Nowadays, after decades of research and development in nanoscience and nanotechnology, remarkable benefits in various areas, including electronics, energy, medicine, and communications, have been achieved for our society. However, the unparalleled ability to investigate and tailor the core structure of nanomaterials, which remains the essence of nanoscience, continues to drive scientists and inspire fascination in everyone of us.

Among the recent breakthroughs in nanomaterials, graphene arises as one of the milestones of the new millennium. Made only of carbon, the fourth most common element in the universe and the very building block of life, this material was thought not to exist[2,3] until its experimental discovery in 2004,[4] perfectly embodying both the spirit and the challenges of nanoscience.

This PhD project focuses on the covalent functionalization of graphene–based systems. The cycloaddition of organic molecules as functional groups is investigated for different graphene structures, towards increasing graphene quality, while the deterministic functionalization of defect–engineered graphene opens the route for devices and applications at the nanoscale.

A summary description of the thesis chapters is briefly listed below:

- in Chapter 1 we present the state of the art of the current research. The unique properties of graphene, along with the potentialities unlocked by its chemical functionalization, are presented. In addition, a brief report on the motivation for the introduction of structural defects in graphene is given;

- in Chapter 2 we describe the sample production methods, the experimental setups, and the measuring techniques utilized for the experiments;

- in Chapter 3 the cycloaddition with azomethine ylide on dispersed graphene is reported, along with a wide characterization of the functionalized systems with several techniques. The enhancement of the reactivity due to the presence of structural defects is revealed;

- in Chapter 4 the introduction of defect patterns on graphene flakes via electron beam irradiation is described. The importance of a clean substrate is revealed, along with the precise correspondence of the experimental patterns on graphene;

- in Chapter 5 we present the functionalization of patterned graphene flakes. The novel selectivity in the ylide grafting on graphene, arising from the locally enhanced reactivity of the patterned areas, is described;

- in Chapter 6 the preliminary investigation of the functionalization of epitaxial graphene is reported. The partial functionalization of pristine graphene, along with the effectiveness of patterning with electron beam irradiation are presented;

- in Chapter 7 we recollect and summarize the results of the present investigation. An outlook of future improvements and applications is given.

State Of The Art

<div style="text-align: right; font-size: 3em;">1</div>

1.1 Graphene

Since Novoselov and Geim isolated graphene for the first time in 2004,[4] graphene–based materials have had an enormous impact on a variety of disciplines, including physics, chemistry, and materials science, resulting in numerous breathtaking advances in nanoscience and nanotechnology.

Graphene's attractive properties are a direct consequence of its unique atomic structure: a two–dimensional lattice of carbon atoms arranged in a honeycomb geometry with a lattice parameter of 2.46 Å and a carbon–carbon spacing of 1.42 Å (see Figure 1.1). For each carbon, three of the four valence electrons form three in–plane σ bonds with sp^2 hybridization along 120° angled directions, while the remaining electron resides in an out–of–plane p_z orbital. This particular atomic configuration creates in graphene a continuous layer of both strong covalent bonds and delocalized π electrons. The former are responsible for the planar nature of graphene and its extraordinary thermal and mechanical properties, such as the highest thermal conductivity (5000 W m^{-1} K^{-1}) and tensile strength (130 GPa) ever measured,[5,6] a Seebeck coefficient ($\sim$ 80 μV K^{-1}) which outperforms those of semiconductors,[7] and an excellent flexibility.[8]

At the same time, the combination of the 2D structure of graphene, its hexagonal lattice with identical C atoms on all sites, and its delocalized π electrons generates a peculiar electronic structure. Applying the tight binding method with Bloch wavefunctions as basis, built using the p_z orbitals centered in the C atoms residing in two non–identical sublattices (due to symmetry considerations), the nearest neighbor Schrödinger equation can be solved,[11] and the electronic band structure is obtained (see Figure 1.1).[12] The π^* (valence) and π (conduction) bands display a linear behavior around the K and K' points (also called K$_+$ and K$_-$) of the reciprocal space, allowing the electrons in graphene to behave as zero–mass Dirac fermions (near these points) with a Fermi velocity of 10^6 m s^{-1} (only 300 times slower than light).[13] From these exclusive characteristics a plethora of remarkable electronic and optical properties arise in graphene, such as the ambipolar electric field effect,[14] a great carrier mobility (higher than 10^4 cm^2 V^{-1} s^{-1} under ambient conditions),[15] a low level of 1/f noise,[16] a wide–band optical response,[17] and high visual transparency (see Figure 1.2 for some examples).[18]

Notwithstanding graphene's great application potential,[21] its outstanding properties are also a limitation. Due to the absence of a band–gap, graphene's use as
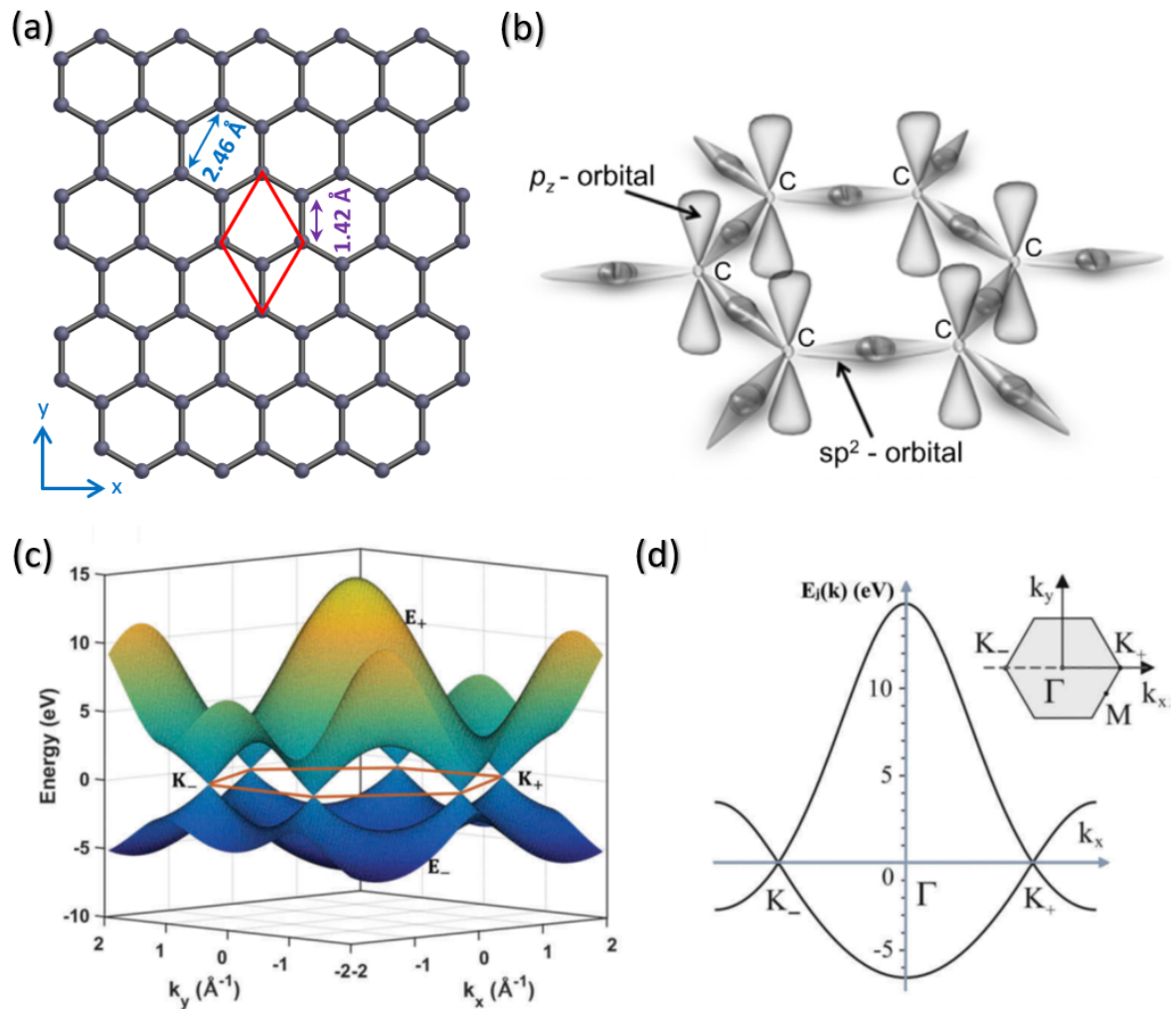
Figure 1.1: (a) Lattice structure of graphene: the lattice parameter of 2.46 Å (blue arrow), the carbon–carbon spacing of 1.42 Å (purple arrow), and the unit cell (red diamond) are indicated. (b) Schematic illustration of sp^2 hybridization of C atoms that form the 2D crystal structure of graphene together with the delocalized p_z orbitals. (c) Band structure of graphene calculated with the tight binding method. (d) Cross–section through the band structure shown in panel (c), where the energy bands are plotted as a function of wave vector component k_x along the line $k_y = 0$. The inset shows the Brillouin zone in reciprocal space corresponding to the unit cell in the space shown in panel (a). Figures adapted from Refs. 9,10.
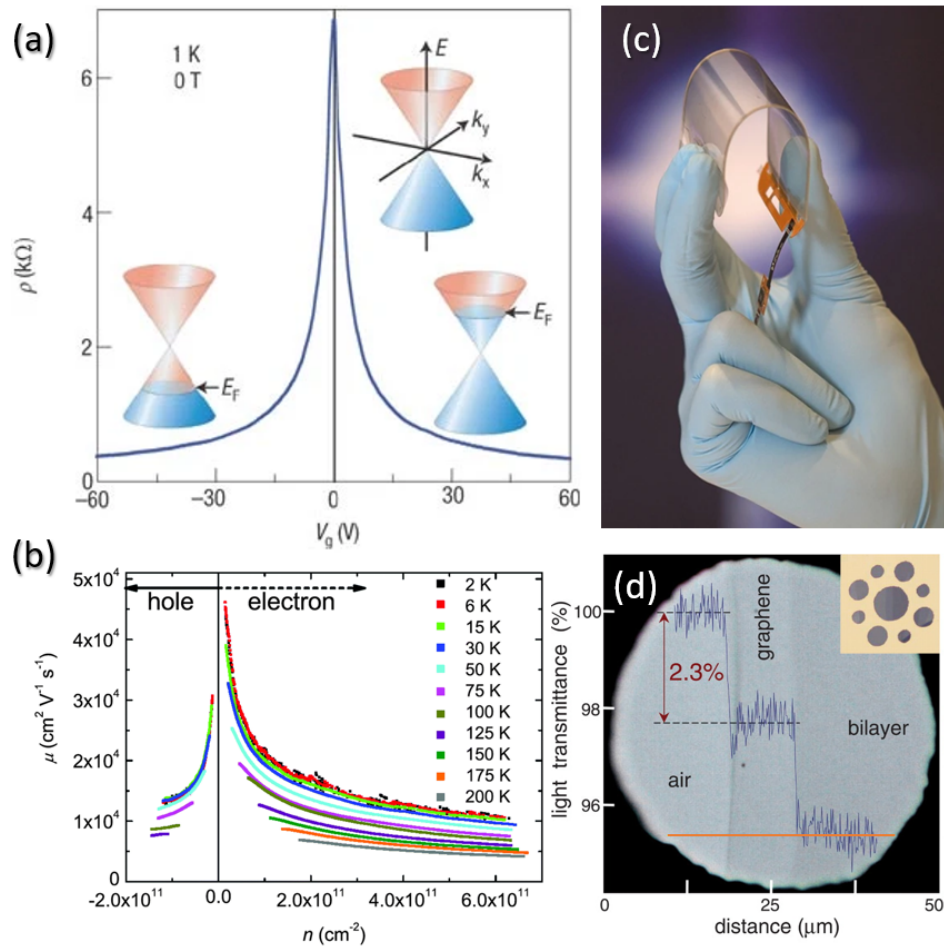
Figure 1.2: Properties of graphene–based devices. (a) Ambipolar electric field effect in single–layer graphene; the insets show its conical low–energy spectrum $E(k)$, indicating changes in the position of the Fermi energy E_F with gate voltage V_g. (b) Hole and electron mobility as a function of carrier density and temperature of epitaxial graphene on SiC. (c) Graphene–based multi–touch screen showing excellent flexibility. (d) Photograph of a 50–μm aperture partially covered by mono– and bi– layer graphene. The line scan profile shows the intensity of transmitted white light along the orange line. Figures adapted from Refs. [14,19,20,18].

an active element in electronic devices and sensors encounters many limitations and, therefore, some sort of engineering of the structure of graphene is required.[22] It has been suggested that a powerful method to overcome these impediments is provided by an efficient surface functionalization with suitable materials.

1.2   Functionalization of Graphene

Functionalization of graphene offers the possibility to finely tune the system's physical and chemical properties, resulting in a synergistic combination of the individual features of each component. However, while graphene's high specific surface area of 2630 m^2/g[23] provides numerous possible binding sites, its chemical inertness makes it difficult to modify the structure of graphene without disrupting it or introducing excessive disorder,[24] and graphene functionalization reveals to be a complex process.
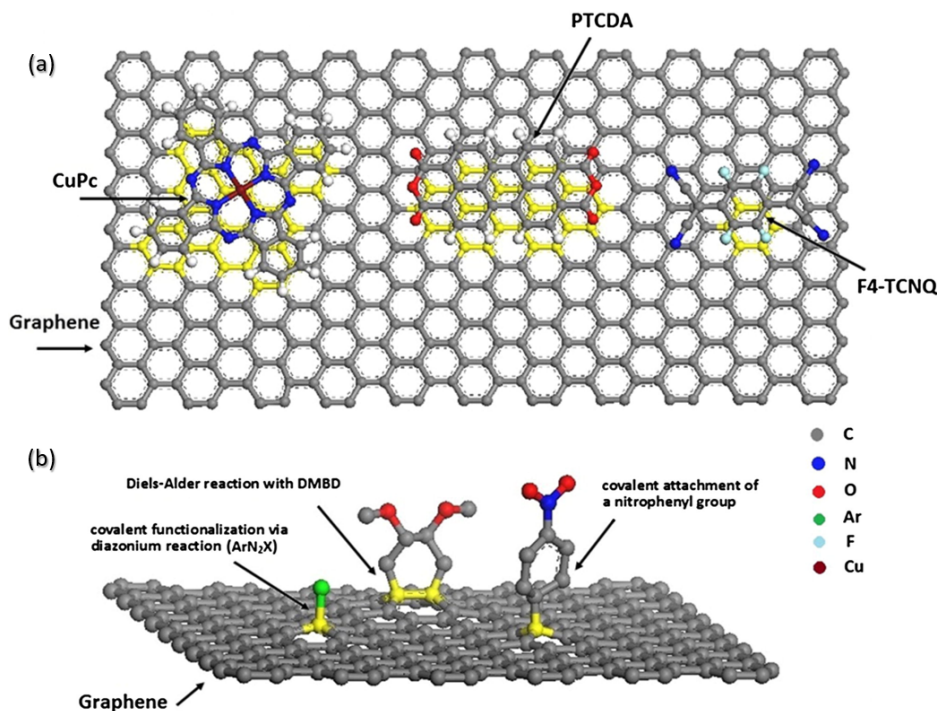
Figure 1.3: Exemplary schematic illustrations of (a) non–covalent and (b) covalent functionalization of graphene. Figures adapted from Ref. 25.

Generally, graphene functionalization can be achieved through either non–covalent interactions or covalent bonds (see Figure 1.3 for a schematic illustration of some exemplary functionalizations).[26,27] The non–covalent chemical modifications are usually realized by intermolecular interactions, such as van der Waals forces,[28] electrostatic interactions,[29] or π–π stacking interaction.[30–32] For example, bandgap opening,[33,32] surface transfer doping,[34] and improved dispersibility and stability[35] can be achieved via functionalization with molecular adsorbates. Typically, non–covalent chemistry presents the advantage of a minimal perturbation of the conjugated π network, and, therefore, of the physical properties of graphene. On the downside, systems with limited stability and higher disorder are often obtained. In contrast, the covalent functionalization is usually realized via rehybridization of graphene's unsaturated sp^2 carbon atoms into an sp^3 configuration, for example with substitution of carbon atoms in the basal plane of graphene by heteroatoms (atom doping)[36,37] or reaction with molecular functional groups.[38–41] Even though this modification is accompanied by a local loss of the electronic conjugation, the chemical alterations result to be deeper and more stable, allowing for more controlled systems. Figure 1.4 shows some examples of non–covalent and covalent functionalized graphene–based systems for different applications.
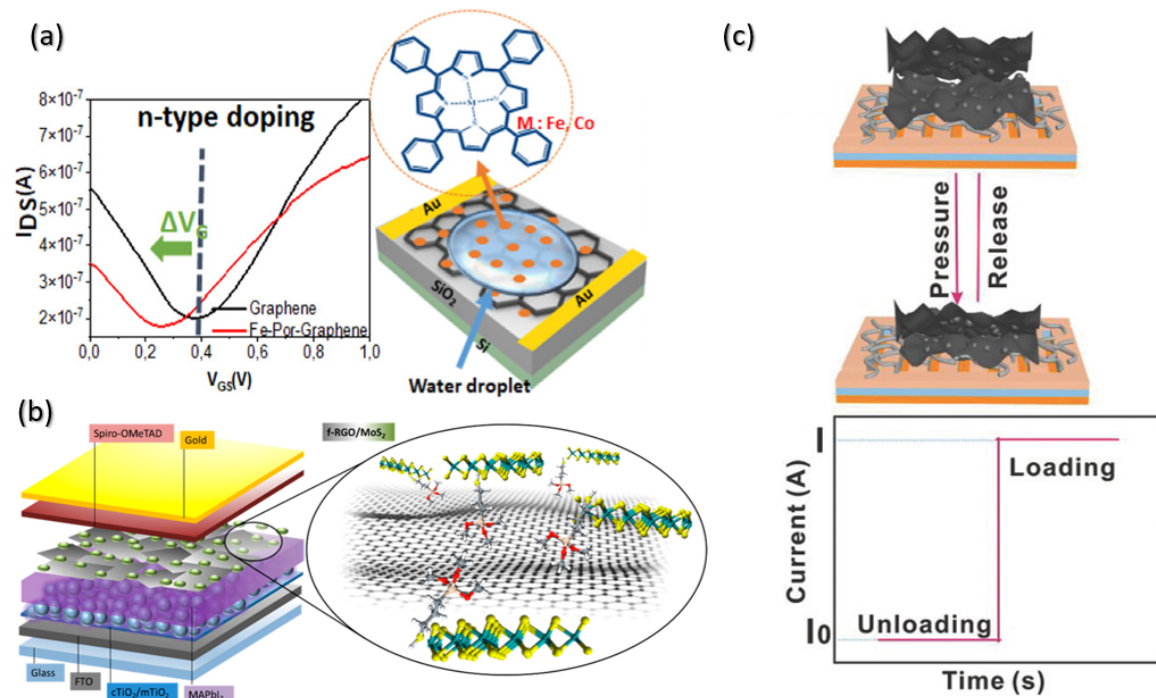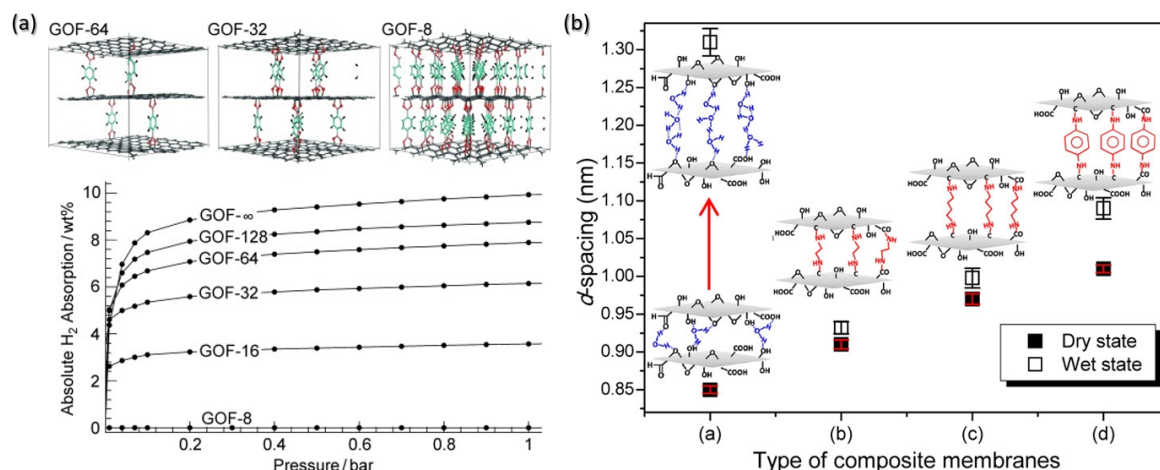
Figure 1.4: Applications of functionalized graphene–based devices. (a) Transfer characteristics of non–covalent functionalized GFET showing molecular n–type doping. (b) Organic photovoltaic device incorporating covalent functionalized graphene–based (MoS_2 QDs:f-RGO hybrid) layers for high efficiency solar cells. (c) Schematic of the sensing mechanism of a flexible piezoresistive sensor based on innerconnected polyvinyl alcohol nanowires and ultrathin wrinkled graphene film, and current variation in response to loading and unloading. Figures adapted from Refs. 42–44.

Moreover, the covalent functionalization of graphene's surface with heteroatoms or functional groups allows enhanced performance where the three–dimensionality of graphene–based materials becomes fundamental. For example, in fuel–gas storage (like H_2) or electrochemical energy storage (like batteries or supercapacitors) applications a large exposed functionalized surface is required.[45,46] It has been shown that multilayer functionalized graphene can be obtained using organic molecules as spacing pillars between multiple graphene sheets, achieving variable spacing with different molecules together with enhanced adsorption capabilities (as shown in Figure 1.5).[47–50]

In particular, the covalent functionalization of graphene sheets using organic functional groups has been explored as a pivotal step towards the formation of graphene composites at the nanoscale. A common approach is the use of diazonium salts, often done through electrochemical or heating processes. Upon surface reduction of the diazonium compound, a highly reactive free radical is produced, which attacks the sp^2 carbon atoms of the graphene lattice, forming a covalent bond (see Figure 1.6).[53–55]

While this mechanism leads to an abundant and quick functionalization, thanks to its high tolerance for different experimental conditions, the potential oligomerization and the required heating and radical conditions make it hard to control, and introduce abundant defects. Instead, cycloaddition reactions have been shown to be a very promising alternative, resulting in a more selective, controlled, and even reversible method. Cycloadditions cause the closing of C–atom rings and are guided by HOMO–LUMO interactions between a diene or a dipolar compound (electron–donating group)

Figure 1.5: Applications of functionalized graphene–based 3D devices. (a) Simulation of functionalized graphene oxide framework (GOF) as a promising H$_2$ storage medium. (b) Structural diagram of composite GOF membranes produced by cross–linking different diamine monomers, showing increasing d–spacing. Figures adapted from Refs. 51,52.
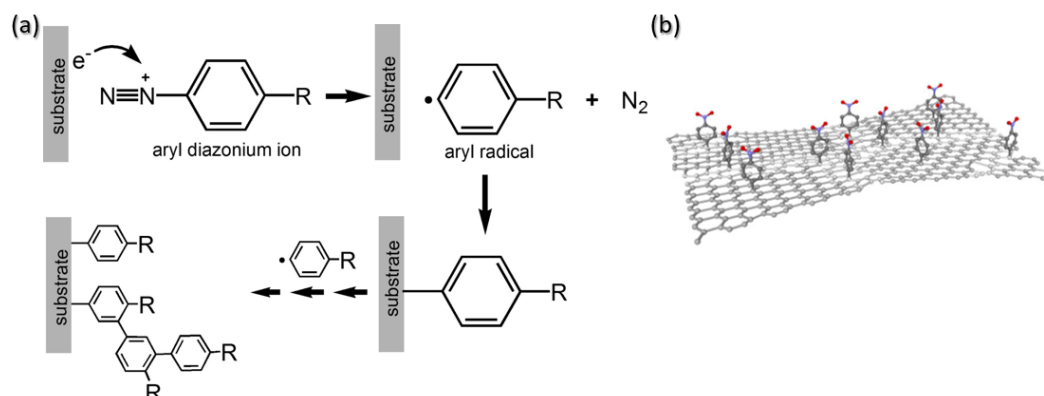
Figure 1.6: (a) Reduction of aryl diazonium salts. The aryl diazonium cation accepts one electron from the substrate and forms an aryl radical through the release of a nitrogen molecule. The aryl radical can then covalently react with the surface or with other surface–mounted aryls leading to aryl oligomers. (b) Schematic of functionalized graphene with aryl diazonium molecules. Figures adapted from Refs. 56,57.

and a dienophile (electron–withdrawing group). Noteworthy, due to the its zero–gap Dirac point, graphene can act both as a diene and a dienophile,[58] enabling chemical reactivity towards different organic molecules. In literature, 1,3–dipolar cycloaddition (1,3–DC) of azomethine ylide (which behaves as the dipolar compound) has been reported for the chemical modification of carbon nanotubes, fullerenes, and other carbon nanostructures.[59–64] Its versatility arises from the availability of a plethora of organic derivatives, obtained by selecting the appropriate precursors, with interesting applications in a variety of fields, such as biotechnology, sensors at the nanoscale, and solar energy conversion.[65–67]

Recently, the graft of azomethine ylide on graphene via 1,3–DC has been reported after the successful production of graphene sheets directly from graphite dispersed in organic solvents (see Figure 1.7(a)).[68] In a similar way, the selective binding between the amino groups involved in the 1,3–DC on dispersed graphene and gold nanorods has

been obtained (see Figure 1.7(b)).[69] However, these were pioneering works, lacking a systematic and wide investigation on solvent effects, computational investigation, XPS analysis, or specific Raman signature of the functionalization. Therefore, a detailed description of graphene functionalized with azomethine ylide is still missing, as well as a deeper investigation on functionalization efficiency and signature.
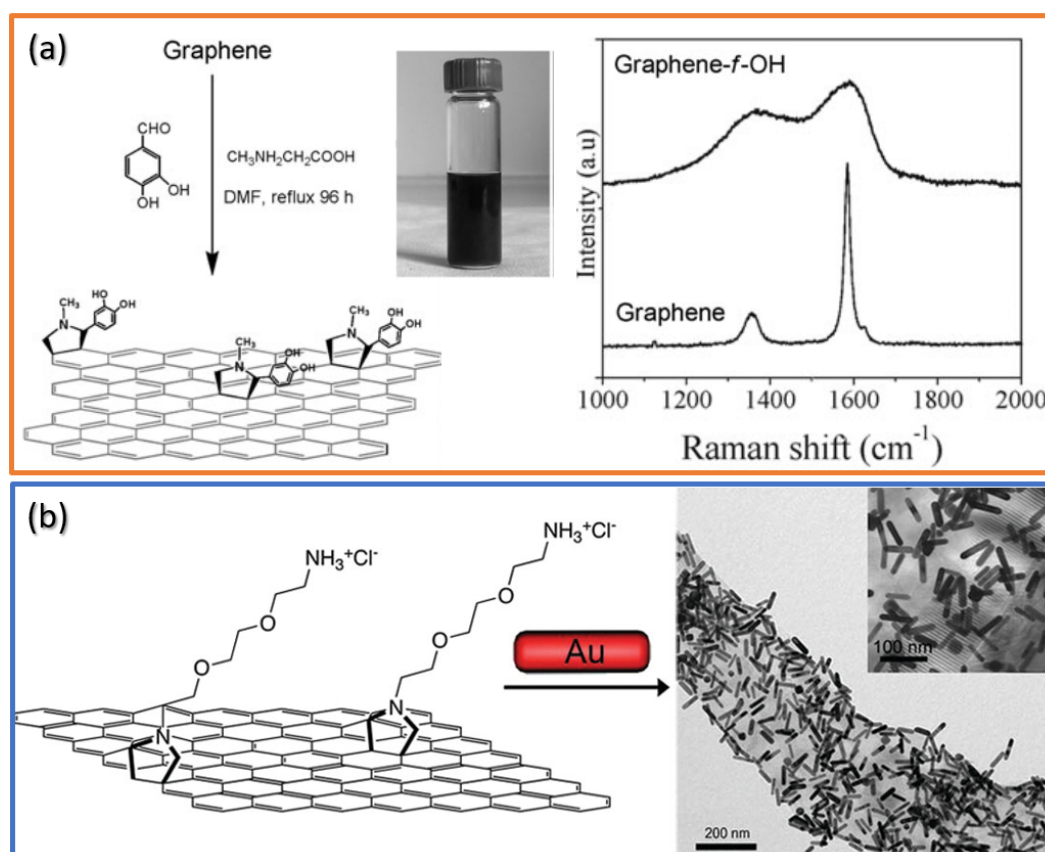
Figure 1.7: 1,3–DC on graphene. (a) Scheme of the 1,3–DC of azomethine ylide on graphene (the inset shows a photo of the dispersion of functionalized graphene in ethanol), and the Raman spectra of pristine graphene and functionalized graphene (labeled as graphene–f–OH). (b) Scheme of functionalized graphene derivatives and TEM images showing further functionalization with nanorods of amine–functionalized graphene sheets. Figures adapted from Refs. 68,69.

Moreover, in spite of these remarkable results, to finely control or intentionally design the binding sites of functionalizing molecules on graphene's surface while preserving the high quality of its unique structure remains an open challenge.

1.3   Structural Defects in Graphene

A promising route in order to locally improve the reactivity of graphene is to introduce beneficial structural defects, i.e. engineered inhomogeneities and irregularities of the ideal structure.[70] Defects in graphene, and more generally in any crystal structure, are commonly classified as topological defects, adatoms, vacancies, and sp^3–defects.

Topological defects alter the lattice orientation and introduce disclinations (addition or removal of one wedge to the hexagonal graphene cell without changing the coordination of carbon atoms) and dislocations (pairs of complementary disclinations). These can combine in aligned one–dimensional chains and produce boundary–like defects (see Figure 1.8).
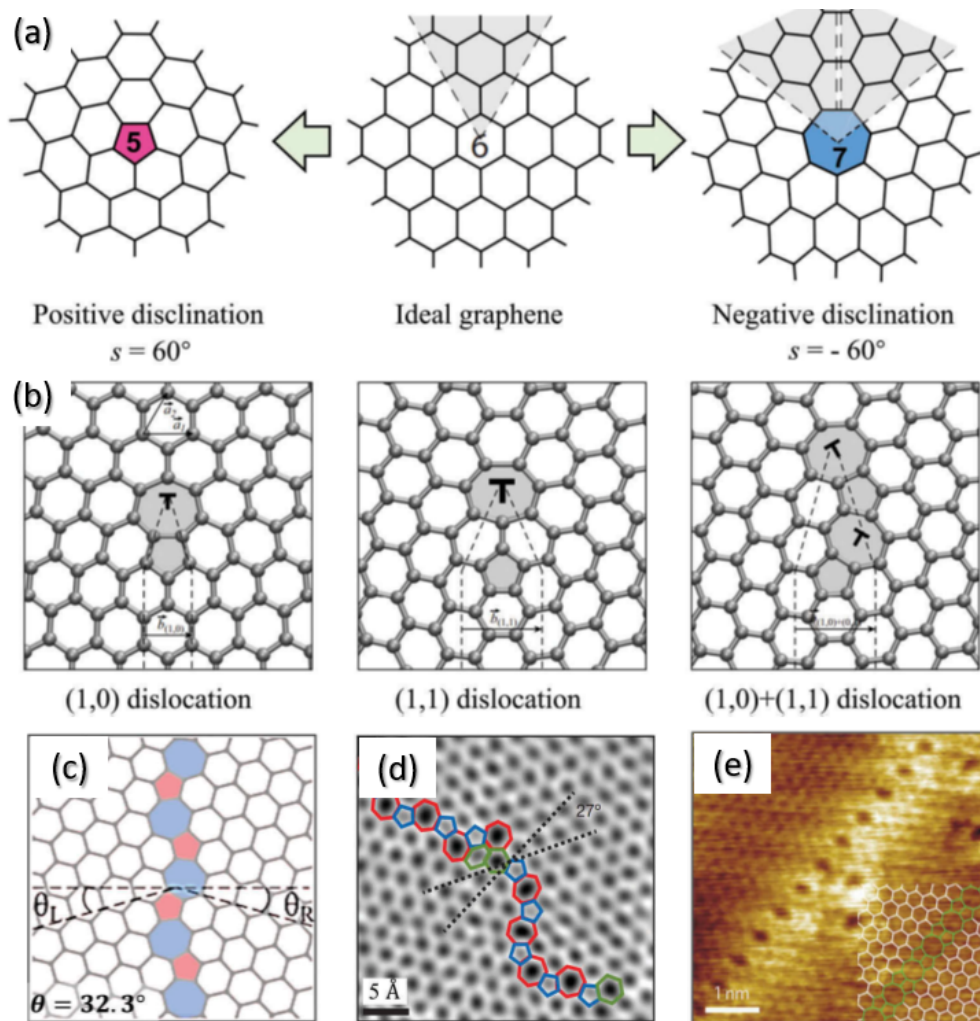
Figure 1.8: Topological defects in graphene. Configurations of (a) disclinations, (b) dislocations, and (c) boundary–like defects in the graphene lattice. (d) ADF–STEM image of two grains which intersect with a relative rotation of 27°, and are stitched together by an aperiodic line of dislocations. (e) STM image of a regular line defect in graphene on Ni(111). Non–six–membered rings are colored. Figures adapted from Refs. 71–73.

Adatoms, vacancies, and sp^3–defects are more perturbative inhomogeneities (see Figure 1.9). External atoms can adsorb on unperturbed graphene in different positions above the lattice, favoring the one with minimal configuration energy. Moreover, in presence of vacancies, i.e. missing atoms, external atoms can be introduced into the

graphene lattice, introducing structural perturbation due to the different length of their chemical bonds. Both adatoms and substitutional atoms are often utilized to achieve doping, by shifting the Fermi energy in the valence or conduction bands,[74] and can, for example, enhance the hydrogen adsorption capabilities, by multi–step charge exchanges[75] or catalyzing hydrogen spillover.[76] Finally, sp^3–defects involve the evolution of unsaturated sp^2 carbon atoms into sp^3 configuration, and consist in the fundamental step for covalent graphene functionalization.
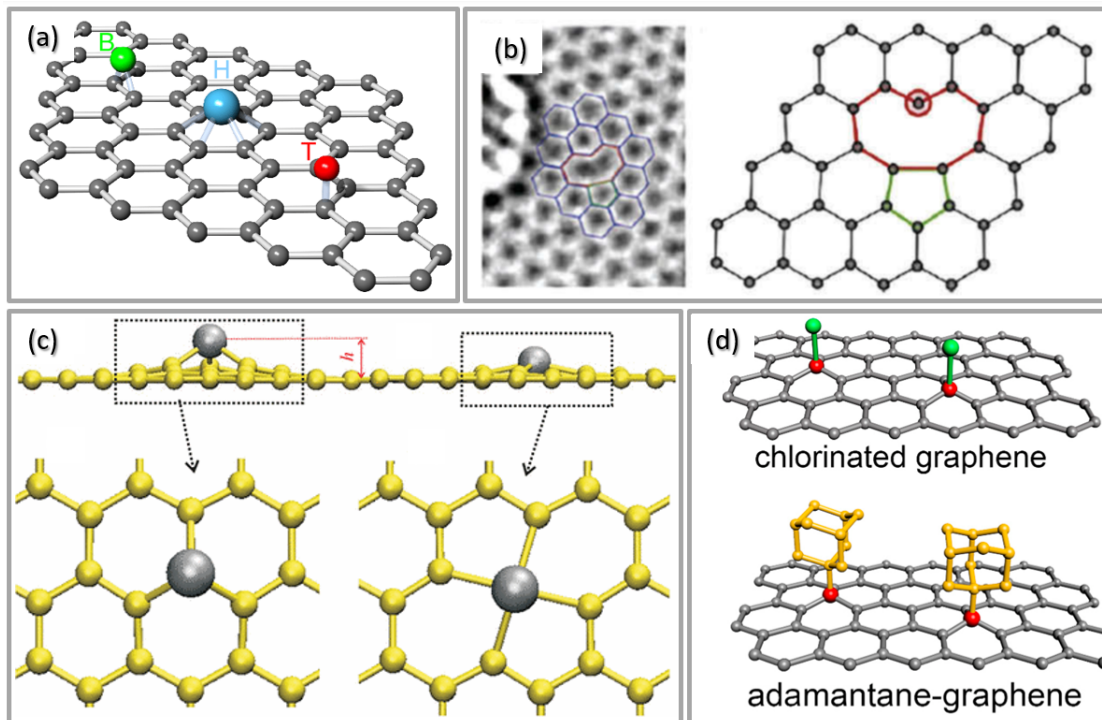
Figure 1.9: (a) Depending on the element, adatoms favor either the high symmetry bridge (B), hollow (H), or top (T) position in the graphene sheet. (b) HRTEM image and configuration of a single vacancy. Configurations of (c) adatoms adsorbed on single and double vacancies and (d) sp^3–defects. Figures adapted from Refs. 77–80.

Defects can profoundly influence the chemical properties of graphene,[81] as well as its mechanical, thermal, and electronic properties (see Figure 1.10).[10] For example, they modify the thermal properties of graphene via defect–phonon scattering, resulting in the tailoring of its thermal conductivity by defects population[82] and in the enhancement of thermoelectric performance.[83] Theoretical and experimental studies have also demonstrated the relevance of structural defects in enhancing the surface chemical reactivity of graphene sheets both in the presence (vacancy–type defects) or the absence (topological–type defects or reconstructed vacancies) of dangling bonds.[84–86] For example, due to the induced electron charge redistribution,[87–89] defective graphene has shown increased chemical reactivity towards addition reactions,[86] which are commonly used approaches for the covalent organic functionalization of graphene–based materials, as mentioned above.

While these approaches exploited already existing defects in graphene, like intrinsic boundaries and edges, a precise control on the spatial distribution of the defects would be more valuable in order to obtain a position–controlled surface functionalization. Nonetheless, defect engineering of graphene requires an accurate control of the amount
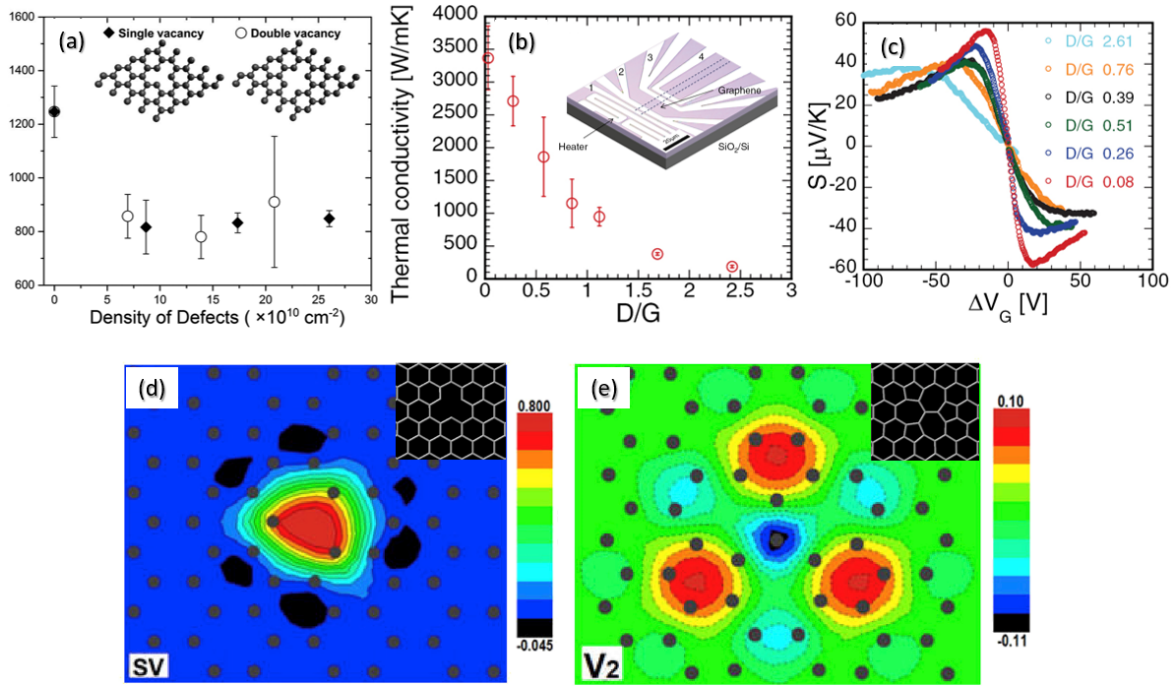
Figure 1.10: (a) Simulation results for the thermal conductivity of graphene with single and double vacancies. Measured defect density dependence of (b) the thermal conductivity and (c) the Seebeck coefficient (tuned by the gate voltage, ΔV_G) in defected graphene. The inset to panel (b) shows the device setup. Calculated charge density difference in defected graphene relative to perfect graphene, for (d) single and (e) double vacancies (shown in the insets). Figures adapted from Refs. 82,83,88.

of defects, and the minimization of contamination from external sources remains critical.[90] Moreover, a precise control, with high lateral resolution, of the surface chemistry of graphene is fundamental for specific applications in band gap engineering, device fabrication, and sensors.[91–94]

The most versatile approach that satisfies the requirements for a controlled introduction of structural defects in graphene is based on particle irradiation techniques, i.e. the exposure of a graphene sheet to the focused beam of energetic particles, such as ions or electrons.[10] While ion or high energy (> 50 keV) electron exposure involves elaborated and expensive equipment (such as ion implanters or electron accelerators) and is limited to small chip areas, effective defect modulation can be patterned over a large area via electrons generated by widely diffuse scanning electron microscopes (SEMs).[96–99] Indeed, depending on the electron energy, via electron beam irradiation (EBI) a large variety of structural defects can be created in graphene, such as topological defects, vacancies, or sp^3–defects.[10] In order to ensure high chemical reactivity, dangling bonds or electron cloud deformations via bond rotation are necessary, and to fulfill this requirement, long exposure to low–energy electrons can be employed. Although the threshold beam energy for C–atom knockout in perfect graphene is 86 keV,[100] continuous irradiation with low–energy electrons results in the creation of point-like (single or double vacancies) and boundary–like defects (see Figure 1.11).[82,95,101] Consequently, by utilizing standard electron beam lithography systems, structural defects can be patterned across the graphene surface in a very flexible way.
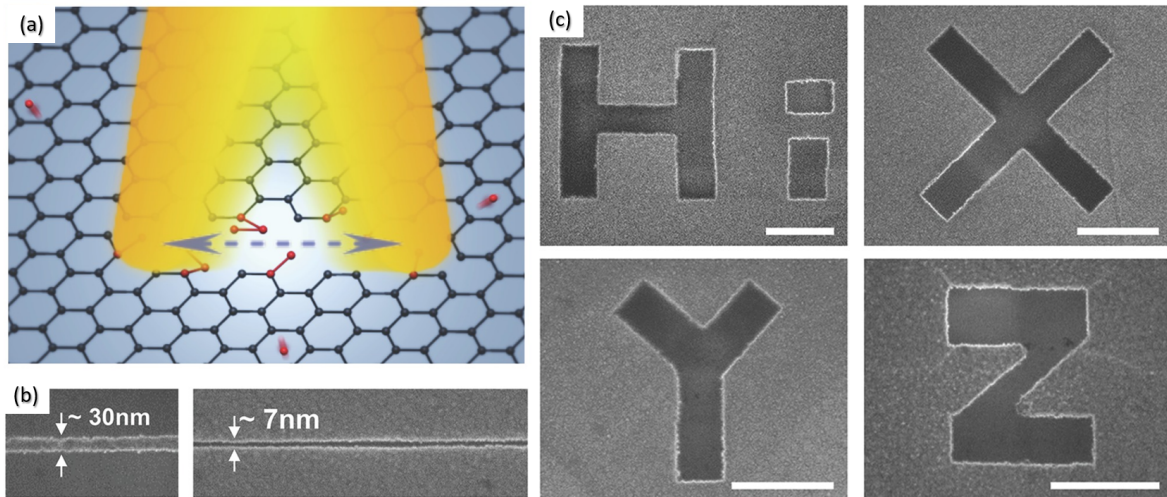
Figure 1.11: Electron–beam patterning of graphene. (a) Schematic illustration of graphene patterning mechanism. (b) Smallest feature sizes achieved (ribbon width ~ 30 nm and slit width ~ 7 nm). (c) Letters composed of rectangular exposure windows (the acceleration voltage is 25 kV for all patterns, the scale bars in all images represent 500 nm). Figures adapted from Ref. 95.

The PhD research presented in the following Chapters is part of this framework. Covalent functionalization of different graphene–based systems has been achieved, allowing to explore various parameters of the functionalization process. Enhancement of the chemical reactivity in defected graphene has been experimentally observed, and EBI has been employed to engineer beneficial defect patterns in high quality graphene systems. In this way, a selective, spatially–resolved, chemical functionalization of graphene monolayer has been achieved, opening the route for designing multi–functional graphene–based devices.

Experimental Methods

2

In this chapter the experimental apparatus are described, to allow a complete understanding of the measurement setups utilized for the experiments.

2.1 Graphene

Graphene can be produced by several techniques, either by *top–down* or *bottom–up* procedures.[102] The former approach generally involves the exfoliation of graphite through chemical (liquid phase exfoliation, graphite oxide exfoliation and reduction), electrochemical (oxidation/reduction or exfoliation) or simply mechanical (scotch tape) processes, which weaken the van der Waals forces between the graphene layers in order to separate them. On the other hand, the bottom–up approach generates graphene by assembling small molecular building blocks into single or few layer graphene structures by catalytic (chemical vapor deposition, CVD), thermal (SiC decomposition), or chemical (organic synthesis) processes. In the work presented in this thesis, we explored different graphene or graphene–like systems: dispersed graphene nanosheets (GNS), dispersed reduced graphene oxide (rGO), micromechanically exfoliated graphene flakes, and epitaxially grown graphene (buffer and monolayer).

2.1.1 Exfoliation of graphene nanosheets

Wet–jet milling (WJM) exfoliated graphene powder was provided by BeDimensional Srl, Italy. By using high pressure (180 – 250 MPa), the WJM process drives the mixture of solvent and layered–crystal through perforated disks with variable hole widths (0.3 – 0.1 mm, termed *nozzle*). The 2D crystal planes of graphite, in our case, slide as a result of the shear stress,[103,104] starting the exfoliation process (see Figure 2.1 for a scheme of the setup).[105] This technique allows to obtain exfoliated few–layer graphene nanosheets having an average thickness of $\sim$ 1.6 nm and an average lateral size of $\sim$ 500 nm.
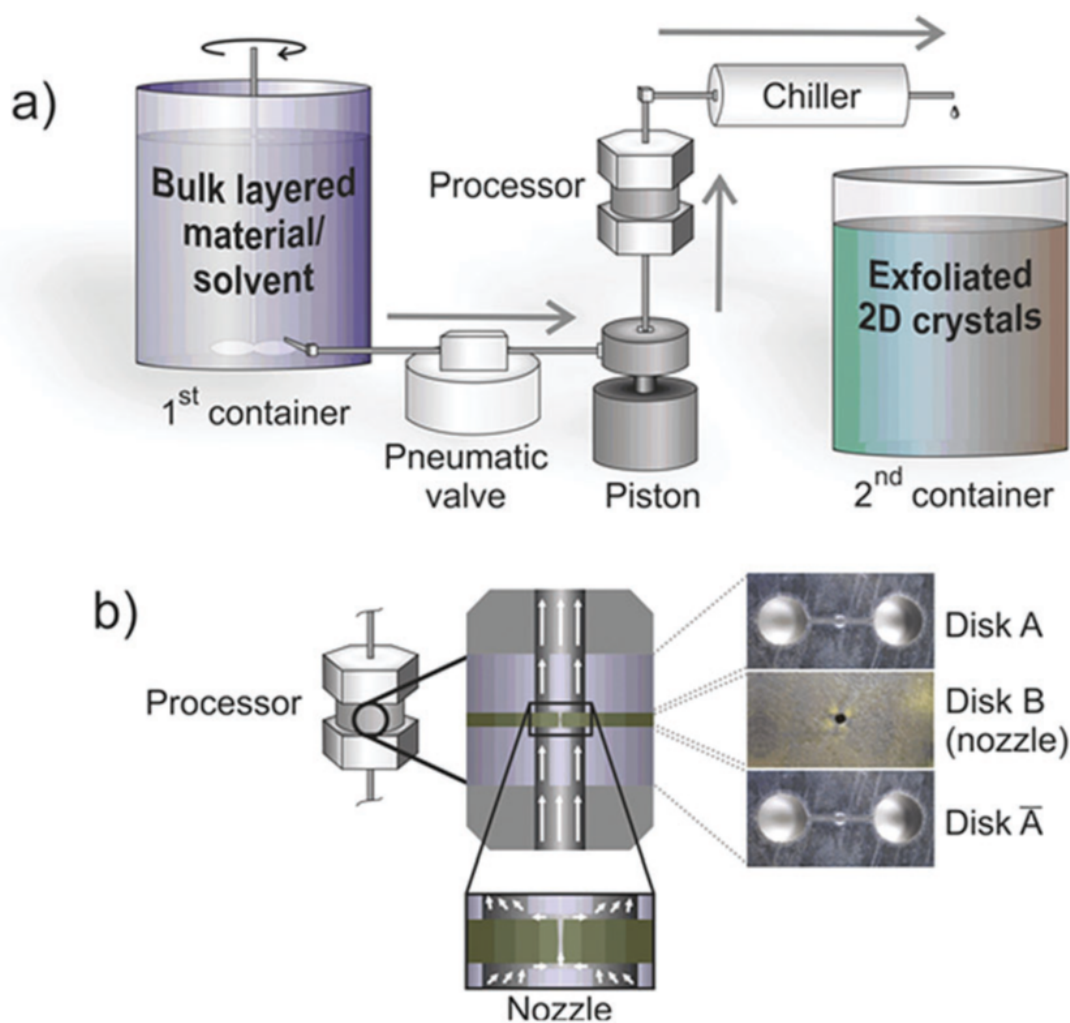
Figure 2.1: (a) Scheme of the wet–jet mill (WJM) system. The arrows indicate the flow of the solvent through WJM, and (b) close–up view of the processor. The zoomed–in image in (b) shows the channel configuration and the disk arrangement. The solvent flow is indicated by the white arrows. On the right is a top view of the holes and channels on each disk. The disks A and Ā have two holes of 1 mm in diameter, separated by a distance of 2.3 mm from centre to centre and joined by a half–cylinder channel of 0.3 mm in diameter. The thickness of the A and Ā disks is 4 mm. Disk B is the core of the system; the image ((b), disk B) shows the 0.10 mm nozzle. It can be changed to 0.10, 0.20, and 0.30 mm nozzle diameter disks according to the size of the bulk layered crystals. The thickness of the B disk is 0.95 mm. Figure and caption adapted from Ref. 105.

2.1.2 Reduced graphene oxide

Reduced graphene oxide (rGO) in nanoflake form was purchased from Graphenea, Spain. The reduction of GO, i.e. the partial removal of the oxygen functionalities from its original structure, was achieved via chemical methods.[106] The resulting rGO sheets contain an oxygen percentage of $\sim 13\%$ (see Figure 2.2), as obtained from the elemental analysis performed by the producer.
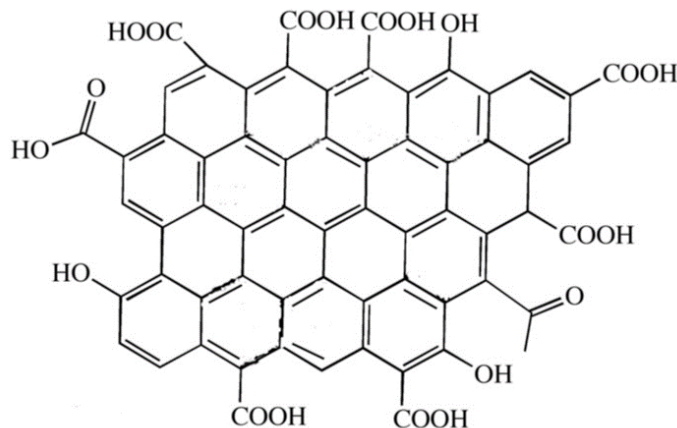
Figure 2.2: Schematic structure of reduced graphene oxide (rGO). Figure adapted from the datasheet of the producer.

2.1.3 Mechanical exfoliation of graphene flakes

Micromechanical exfoliation of graphite consists in the repeated peeling of layers of graphite by using scotch tape (see Figure 2.3). This simple process is possible thanks to the weak wan der Waals interplanar interactions between adjacent graphite layers and allows to isolate few–layers and single–layer graphene flakes. By pressing the tape onto a substrate, usually silica, the so obtain flakes can be transferred and further modified or studied. Thanks to its perfect crystalline structure and the extremely low presence of undesired defects, micromechanically exfoliated graphene is of the highest quality, even if this method is extremely labor–intensive and time–consuming.

For our experiments, graphene flakes were micromechanically exfoliated from highly oriented pyrolytic graphite (HOPG) and transferred on boron–doped Si substrates (about 7×7 mm^2 in size) having 300–nm–thick thermally–grown SiO$_2$. Metallic markers were lithographed by electron–beam (e–beam) and metal (Au) evaporation for defining flake positions. Before the exfoliation process, the substrate surface was cleaned either only by e–beam resist residue removal solution or also by oxygen plasma at 100 W for 5 minutes. In Chapter 4 the former will be referred to as *no–plasma–treated substrate*, while the latter will be referred to as *plasma–treated substrate*. All substrates used in the experiments reported in Chapter 5 were cleaned using both steps. The exfoliation, marker lithography, and cleaning procedure were performed by Dr. Federica Bianco at NEST Laboratory.
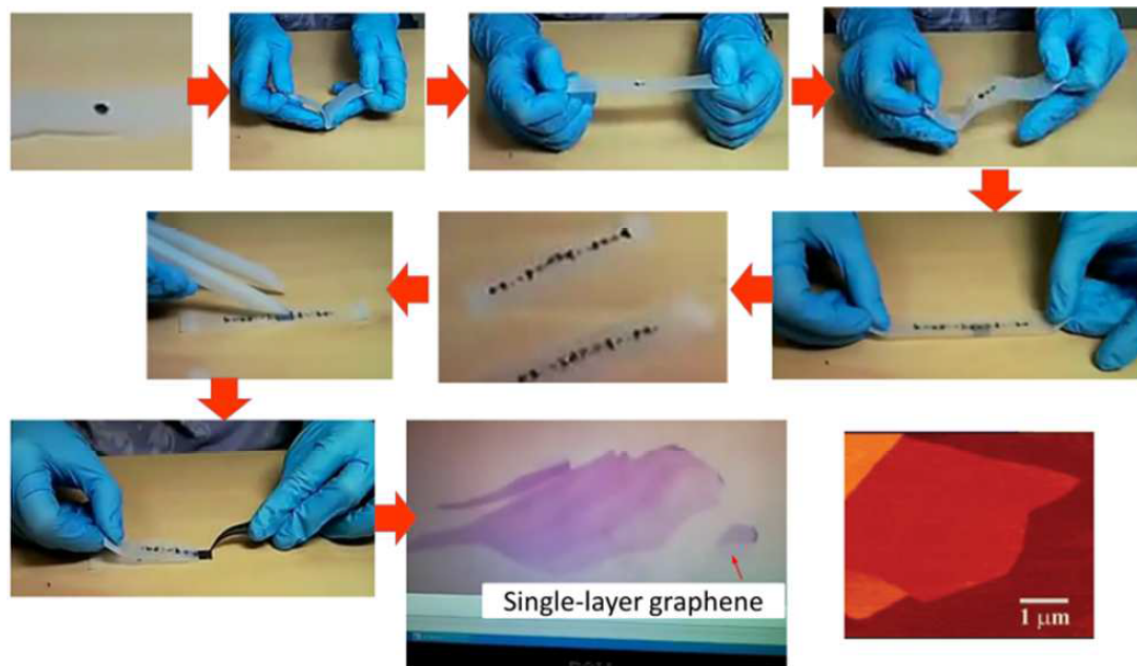
Figure 2.3: Illustrative procedure of Scotch–tape based micromechanical cleavage of graphite. Figure and caption adapted from Ref. 107.

2.1.4 Epitaxial growth of graphene on SiC

By thermal decomposition of silicon carbide (SiC), the epitaxial growth of graphene directly on the substrate is possible. Because of the different vapor pressures of silicon and carbon, only the Si atoms are removed from the surface via sublimation and the remaining C atoms rearrange on the surface.[108] By controlling the temperature (usually in the range of 1200 – 1800 °C), the atmosphere (vacuum or inert gases), and the heating time it is possible to grow both single–layer and multi–layer graphene samples.[109] In particular, increasing the annealing temperature, C and Si atoms are provided with higher kinetic energy and their mobility increases, leading to an easier surface reconstruction. On the other hand, with higher temperature, a faster desorption of the Si atoms occurs, leading to a more difficult control on the number of layers. This issue can be solved by placing the samples in an atmosphere of Si or inert gases, such as Ar. This leads to an improved control on the sublimation speed of Si atoms, allowing to slow down their emission from the surface and leading to a more uniform surface reconstruction. The first carbon layer that forms on the SiC surface is called *buffer* layer (or *zeroth* layer). Its structure is already the atomic structure of graphene, but around 1/3 of its C atoms are bound to the Si dangling bonds of the SiC substrate (see Figure 2.4). This strong interaction results in a high corrugation of the layer and causes the electronic dispersion of the buffer layer to deviate from that of perfect graphene, making it a semiconductor with an energy gap of ~ 5 eV. Continuing the growth, the next layer appears under the buffer layer, and the previous buffer layer detaches from the substrate, becoming epitaxial monolayer graphene (EMLG). EMLG exhibits the characteristic linear electronic dispersion, responsible for the excellent electronic properties of graphene.

The epitaxial graphene samples used in our experiments (reported in Chapter 6) were grown in an AIXTRON black magic cold walled CVD reactor, starting from com-
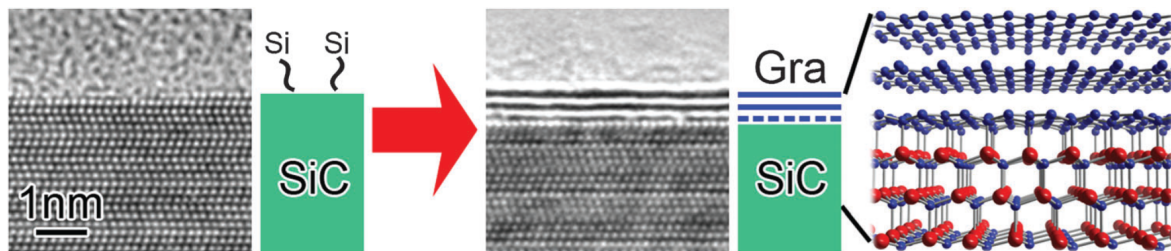
Figure 2.4: Basics of graphene growth by thermal decomposition of SiC, together with the structural model of bilayer graphene on SiC, showing the buffer and the two graphene layers. The dashed blue line and the continuous blue lines indicate, respectively, the buffer and the graphene layers. Figure and caption adapted from Ref. 110.

mercially produced and polished 6H silicon carbide wafers (purchased from SiCrystal, Germany), by Dr. Neeraj Mishra of the Dr. Camilla Coletti group at NEST Laboratory. After the initial hydrogen etching (heating for 4 minutes at 1200 °C in an argon–hydrogen atmosphere at 450 mbar) in order to remove the scratches on the SiC(0001) surface, the samples were grown by heating up to 1250 – 1300 °C for several minutes (in the range of 12 – 15 minutes) in argon atmosphere of 750 – 790 mbar. The resulting samples are characterized by Raman spectroscopy and AFM measurements, in order to obtain information on the number of layers (from the Raman spectra) and the graphene surface coverage (from the AF images). In our experiments the surface of the samples is mainly EMLG (between 60 and 80 %) with some areas of buffer layer or bi–layer graphene.

2.2 Graphene Nanosheets and rGO dispersion

Liquid–phase exfoliation (LPE), being simple and direct, is a very powerful technique for preparing graphene nanosheets (GNS).[111] Here, we already started from exfoliated graphene and rGO nanoflakes (in the form of commercial graphene and rGO powders). However, in order to perform the functionalization, they need to be re–dispersed in a suitable solvent. Therefore, we explored and compared two widely used methods: sonication and homogenization. In addition, a fundamental parameter is that the interactions between solvent and graphene must at least be comparable with those between the aggregated graphene sheets, in order to allow for the most efficient dispersion. Hence, we compared the dispersant efficiency of two common dispersant solvents, which are also suitable solvents for the cycloaddition to occur: 1-methyl-2-pyrrolidinone (NMP) and N,N-dimethylformamide (DMF).

2.2.1 Sonication

Sonication has been widely utilized to induce exfoliation of bulk materials through growth and collapse of micro–bubbles due to pressure fluctuations in liquids (see Figure 2.5).[112,113] Typically, sonication of graphite (or graphene powder) is considered a non–destructive process,[114] because the defects introduced by the sonication process are mainly of a topological (boundary-like) nature.[115]

Here, graphene powder (35 mg) was dispersed in NMP or DMF (140 mL). Sonication (using a SONOPULS Ultrasonic HD 2070 from Bandelin) was performed for

different time periods, from 15 minutes to 2 hours, at 60 W and 20 kHz. The samples were maintained in an ice bath, during the sonication, in order to prevent excess heating and avoid degradation of the solvent (along with possible oxidation of the graphene flakes).[116]
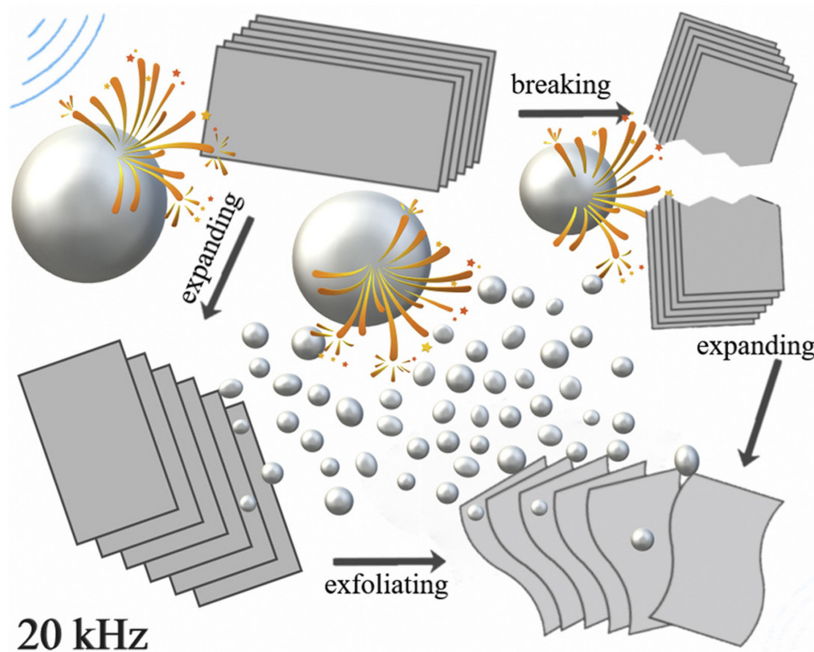
Figure 2.5: The driving force of LPE is the implosion of micrometer–sized, vigorously oscillating bubbles. When they collapse, the energy is instantaneously released, resulting in the exfoliation of the graphite layers. Figure and caption adapted from Ref. 113.

2.2.2 Homogenization

Recently, also homogenization has been demonstrated to achieve excellent exfoliation of graphite, even in a more scalable way, and, similarly to sonication, it introduces mainly topological (boundary-like) defects.[104] A high–speed rotating mixer generates high shear stress in the narrow gap ($\sim 100~\mu$m) between the rotor and stator (see Figure 2.6).

Here, graphene powder (35 mg) was dispersed in NMP or DMF (140 mL). For the dynamic light scattering measurements, homogenization (using an OV5 Homogenizer from VELP Scientifica) was performed in time steps of 10 minutes, up to 1 hour, at 30000 rpm. For the functionalization procedure, homogenization was performed for 30 minutes at 30000 rpm. Similarly, rGO powder (10 mg) was dispersed in DMF (40 mL), and homogenization was performed for 30 minutes at 30000 rpm.

2.3 Chemical Reaction

The reaction mechanism of the *1,3–dipolar cycloaddition* (1,3–DC) is well known.[118] The name of this type of reactions derives from the presence of a 1,3–dipolar compound as one of the reagents.
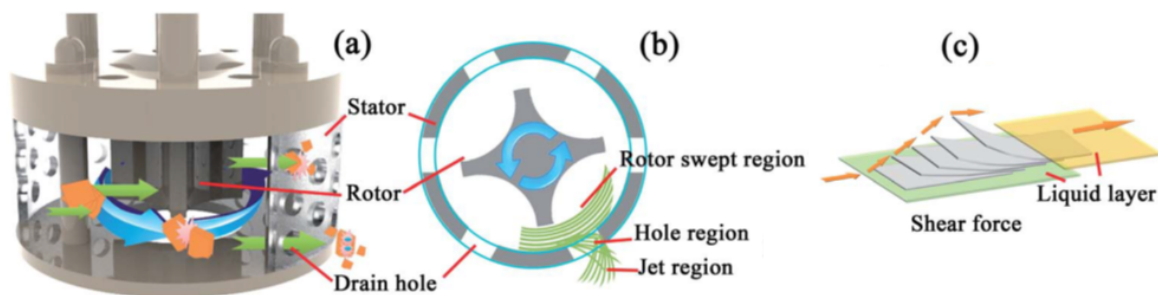
Figure 2.6: (a) 3D sectional drawing of the shear stress generator. (b) Main energy dissipation regions of the high shear mixer (sectional view). (c) The schematic model of preparing GNSs by shear force. Figure and caption adapted from Ref. 117.

Here, in collaboration with Dr. Giovanni Signore and Aldo Moscardini at NEST Laboratory, we selected N-methylglycine (sarcosine) and 3,4-dihydroxybenzaldehyde as reagents (see Figure 2.7), to form azomethine ylide as 1,3–dipolar compound, which is one of the most reactive among them. The dipolar compound, in our case, must be produced *in–situ*, i.e. in proximity of the graphene sheet, in order to allow the reaction to happen.

Figure 2.7: Scheme of the azomethine ylide (1,3–dipolar compound) formation.

In order to obtain a dipolar compound, the use of the N-methylated α–amino acid is crucial, because the condensation of a secondary amine (the N-methylglycine, having two organic substituents and one hydrogen bound to the nitrogen) with an aldehyde leads to the formation of an imine with a positive charge (one part of the dipolar compound). The presence of an electron–withdrawing group, like the carboxylic group (COOH), on the α carbon easily leads to the deprotonation a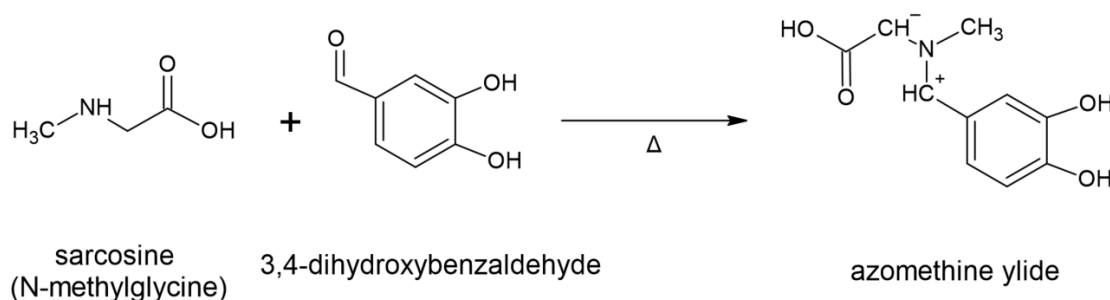nd the formation of the azomethine ylide. Then, the 1,3–dipolar ylide compound grafts onto graphene's structure thanks to the electron charge displacement between the ylide and the graphene, closing a five–member C–ring (see Figure 2.8). Noticeably, the presence of the aromatic ring of the aldehyde can favor the alignment of the ylide with the graphene lattice, thanks to π–π interactions. According to the Sustman's terminology, in the case of a 1,3–DC reaction of an azomethine ylide, the dominant interaction, using the frontier molecular orbitals theory, is that of the HOMO (highest occupied molecular orbital) of azomethine ylide with the LUMO (lowest unoccupied molecular orbital) of graphene.[119] Finally, because of the highest localization of electronic charges in the presence of defects, the preferred reaction sites are the graphene edges (more chemically reactive). Anyways, also the delocalized C=C bonds of the graphene basal planes are expected to participate in the 1,3–DC reaction (via electron charge displacement

with the azomethine ylides), as also confirmed from literature.[69]
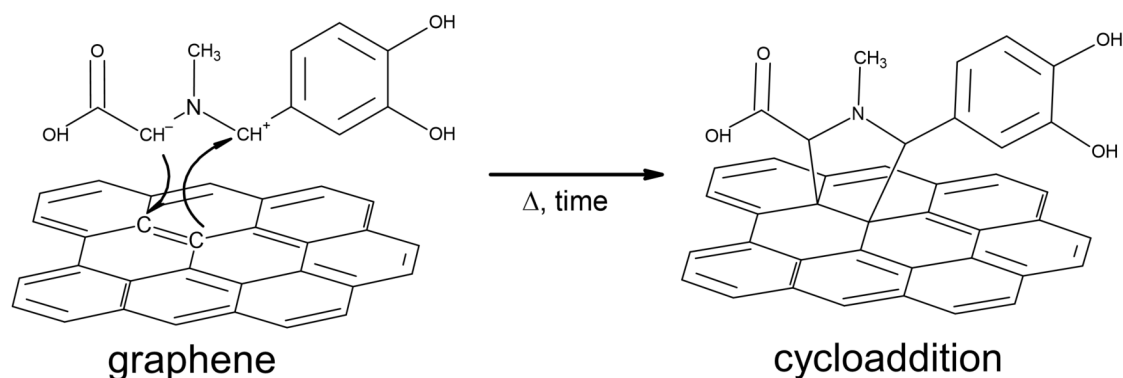
Figure 2.8: Scheme of the cycloaddition of azomethine ylide onto graphene (the dashed arrows indicate the direction of the electron displacements).

2.3.1 1,3–DC of dispersed GNS and rGO

To perform the organic functionalization, 3,4-dihydroxybenzaldehyde (25 mg, corresponding to 0.18 mmol) and an excess of N-methylglycine (25 mg, 0.28 mmol) were added to the GNS dispersion (22 mL, 0.20 mg mL^{-1}) in NMP or DMF. The same process was employed for rGO dispersed in DMF (22 mL, 0.20 mg mL^{-1}). Sodium carbonate (5 mg, 0.05 mmol) was added in order to lower the acidity of the environment. This helps both the formation of the 1,3–dipolar compound and to prevent the loss of the carboxyl group of the azomethine ylide. The reaction mixture was kept at 150 °C for 120 h, under magnetic stirring, with successive additions of the reagents every 24 h (see Figure 2.9 for the setup).
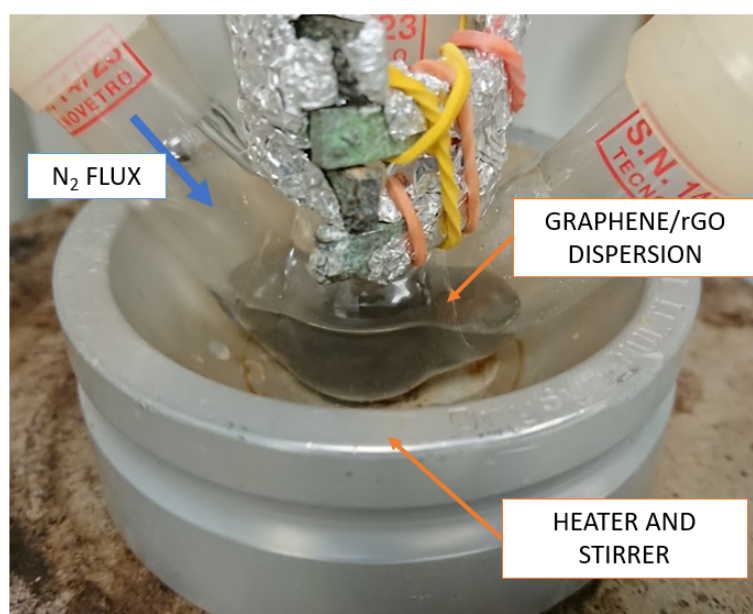
Figure 2.9: Setup for the 1,3–DC of dispersed graphene and rGO.

In order to limit secondary reactions from the oxidation of the solvent at high temperature, an inert atmosphere (N$_2$) was kept during the functionalization reaction.

The resulting mixture was then thoroughly washed with clean solvent (several passages of centrifugation and pipetting off the solvent).

2.3.2   1,3–DC of exfoliated graphene flakes

The organic functionalization has been carried out in a Schlenk–type glass flask, adding 3,4-dihydroxybenzaldehyde (40 mg, 0.29 mmol) and an excess of N-methylglycine (40 mg, 0.45 mmol) to 20 mL of NMP. The chip with the graphene flakes (described in detail in Section 2.1.3) was submersed in the reaction mixture and placed on a custom made Teflon support, which allowed for a safe magnetic stirring underneath with no risk of collision with the chip (see Figure 2.10 for the setup). The reaction environment was kept at 150 °C for 16 h, under magnetic stirring. During the functionalization reaction an inert atmosphere (N_2) was kept, in order to limit secondary reactions from the oxidation of the solvent at high temperature. The chip was then thoroughly washed several times with clean NMP, ethanol, dichloromethane, and finally air dried.
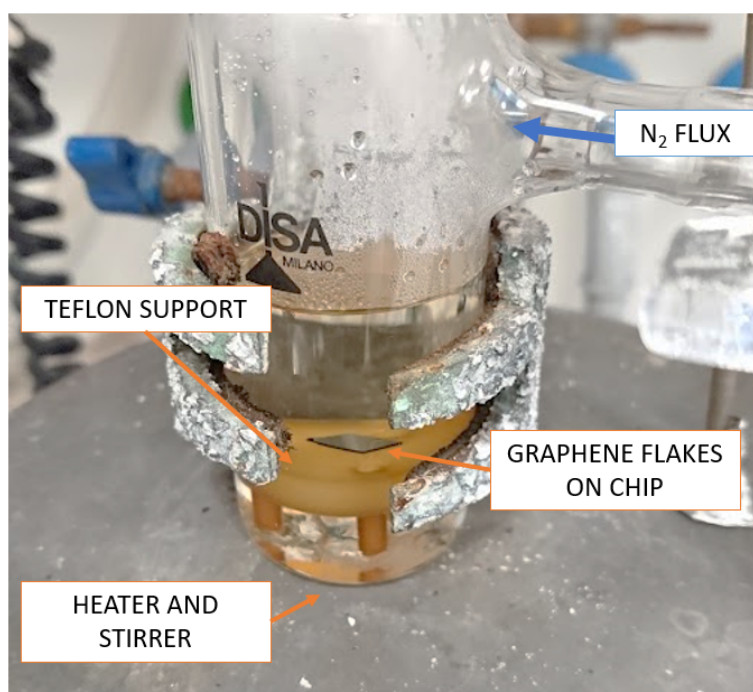
Figure 2.10: Setup for the 1,3–DC of exfoliated monolayer flakes.

As aforementioned, sodium carbonate (Na_2CO_3) can be added in order to facilitate the cycloaddition reaction. Here, the functionalization procedure was initially performed with and without the adding of sodium carbonate, with no evidence of changes in the Raman analysis of the functionalized graphene. After the 1,3–dipolar cycloaddition, without Na_2CO_3, the carboxyl group would be partially lost, due to the temperature of the reaction environment. Anyway, in order to minimize the number of reagents, simplifying the reaction and avoiding undesirable residues (which would appear in further chemical analysis such as the XPS, as shown in Chapter 3), and considering that the Raman analysis of the functionalized graphene shows the vibrational peak arising from the carboxyl group (confirming its presence in the final product), from this point forward we decided to perform the functionalization procedure without the addition of sodium carbonate. Moreover, it is well known[120] that the sarcosine

does not undergo decarboxylation before closing the 1,3–dipolar cycloaddition, hence the effectiveness of the functionalization would not be deeply affected.

2.3.3   1,3–DC of epitaxial graphene

Analogously to previous experiments, epitaxial graphene samples were submersed in a reaction mixture of 3,4-dihydroxybenzaldehyde (40 mg, 0.29 mmol) and N-methyl-glycine (40 mg, 0.45 mmol) in 20 mL of NMP. The experimental setup is the same as in Figure 2.10. An inert N_2 atmosphere was kept and the reaction environment was heated under magnetic stirring at 150 ℃ for 1 to 10 days. Subsequently, the EG samples were thoroughly washed several times with clean NMP, ethanol, dichloromethane, and finally air dried.

2.3.4   Chemicals

1-methyl-2-pyrrolidinone (NMP, ReagentPlus, 99%), N,N-dimethylformamide (DMF, anhydrous, 99.8%), dichloromethane (puriss, $\geq$99.9%), ethanol (puriss, $\geq$96%), N-methylglycine (98%), and 3,4-dihydroxybenzaldehyde (97%) were purchased from Sigma–Aldrich–Merck, Germany, while sodium carbonate (for analysis, $\geq$99.5%) was purchased from Carlo Erba, Italy.

2.4   Dynamic Light Scattering

Dynamic Light Scattering (DLS) is an established and reliable technique for measuring the size distribution of spherical particles dispersed in liquid solvents. When in solution, particles move randomly (Brownian motion) and cause laser light to be scattered at different intensities. These time–dependent intensity fluctuations are related to the rate of diffusion of the particles through the solvent and, therefore, to the particle dimensions, specifically to their hydrodynamic radius (larger particles diffuse slower, causing less rapid fluctuations in the intensity than smaller particles, as shown in Figure 2.11(a)).[121] For non–spherical particles, as in the case of dispersed graphene, the measured hydrodynamic radius corresponds to the radius of a sphere that has the same average translation diffusion coefficient as the particle being measured (see Figure 2.11(b)). Advantages of DLS are a non–invasive nature, simple and fast measurements, and sensitivities in the submicron region.

Here, DLS measurements were performed with a Malvern Zetasizer Nano ZS (provided with a 633 nm HeNe laser), using quartz cuvettes (1 mL). Samples were equilibrated to 25 °C for 30 seconds before measuring, and the data were acquired with a scattering angle of 12.8°. Values for NMP viscosity and refractive index at 25 °C are 1.6660 cP and 1.468, while for DMF they are 0.8020 cP and 1.428, respectively (data from the supplier). Graphene refractive index and absorption at 25 °C are 2.704 and 0.023, respectively.[122]
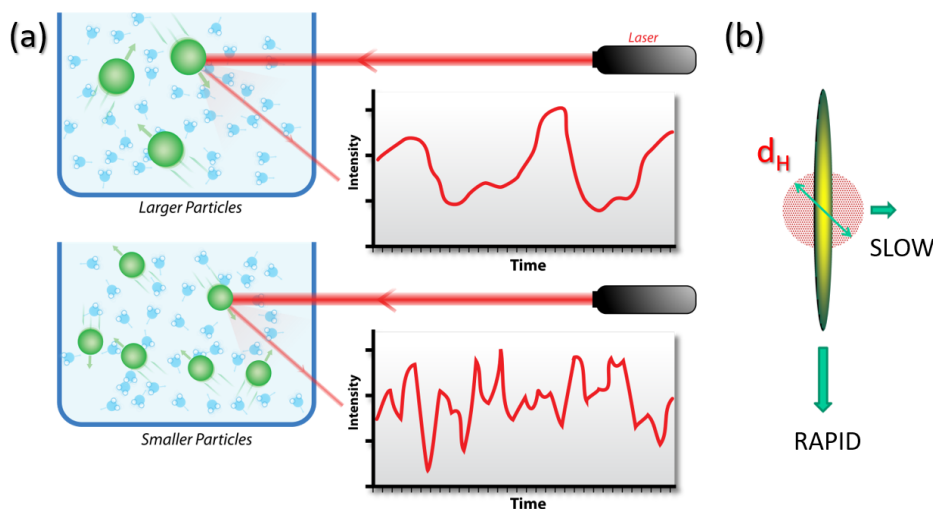
Figure 2.11: (a) Hypothetical dynamic light scattering of two samples: larger particles at the top and smaller particles at the bottom. Figure and caption adapted from Ref. 123. (b) Hydrodynamic diameter for a non–spherical particle.

2.5   Electron Beam Irradiation

Electron–beam irradiation (EBI), i.e. the exposure of a sample to a focused beam of energetic electrons, is a versatile method that satisfies the requirements for a controlled introduction of structural defects in graphene. Depending on the electron energy, a large variety of structural defects can be created, such as topological defects, vacancies, or sp^3–defects.[10] Coupling a pattern generator system to a scanning electron microscope (SEM), as in a standard electron beam lithography system, structural defects can be patterned across the graphene surface in a very flexible way (see Figure 2.12(a)).
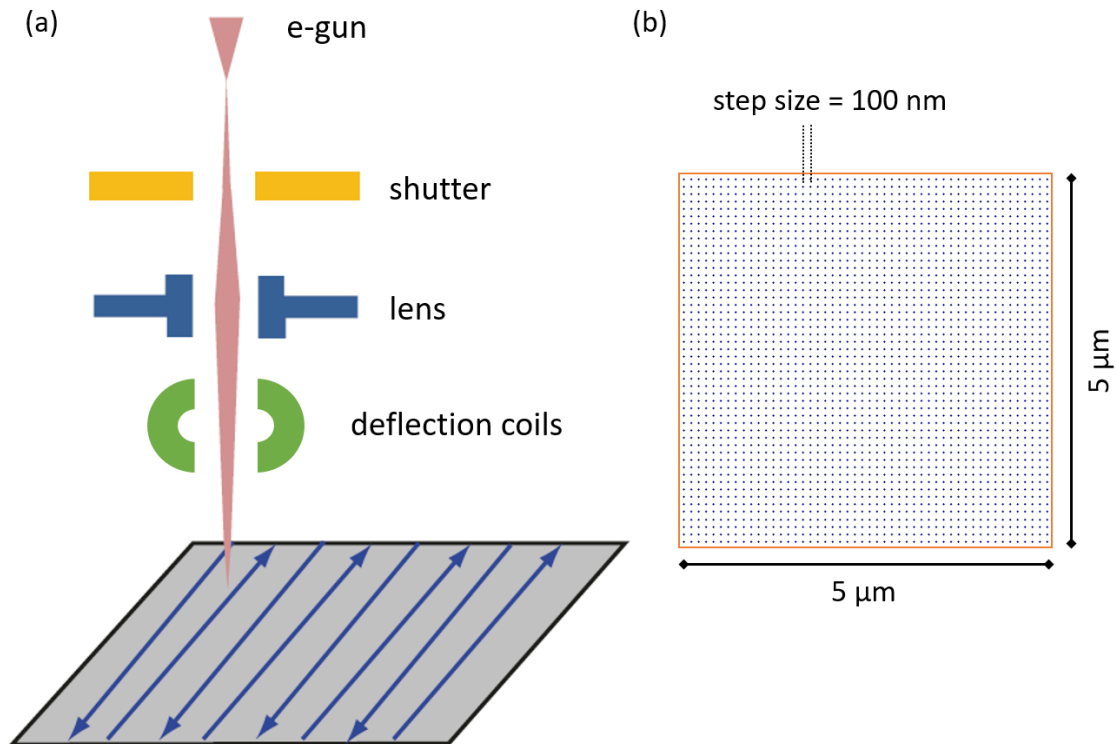
Figure 2.12: (a) Schematic illustration of the setup for EBI: a lens focuses the e–beam on the surface while a beam–blanking shutter mechanism and magnetic deflection coils are used to scan the beam across the sample. Figure and caption adapted from Ref. 124. (b) Exemplary pattern design with a step size of 100 nm, in an area $5 \times 5 \ \mu m^2$ wide.

Here, for the experiments reported in Chapter 4, a defective area was created by irradiating, in a single step, the graphene flakes with electrons accelerated to 20 keV or 30 keV. This area was well–defined by a pattern generator coupled–SEM and is 4 μm long and as wide as the graphene flakes. The dimensions of the defect–rich area were arbitrarily chosen in order to be sufficiently resolved by the used micro–Raman system. The e–beam (current of about 0.15 nA) was scanned with a step–size of 100 nm (see Figure 2.12(b)). The dose was varied from 5 to 200 mC/cm^2, resulting in a dwell–time ranging from 3 to 140 ms. Similarly, for the experiments described in Chapter 5, the defective area was created by irradiating, in a single step, the graphene flakes with electrons accelerated to 20 keV. The e–beam was scanned with a step–size of 100 nm and a current of about 0.15 nA. The dose was 40 mC/cm^2, resulting in a dwell–time of 30 ms. Finally, for the patterning of EG (reported in Chapter 6), the e–beam parameters were: electrons acceleration voltage 20 kV, beam current 90 pA, electron dose between 10 mC/cm^2 and 120 mC/cm^2 (corresponding dwell time from 12 ms up

to 140 ms), and scan step–size between 100 nm and 500 nm. The time needed to complete the designed pattern depends on the chosen settings and the total pattern extension. For example, in order to irradiate an area of $100 \times 100~\mu m^2$ using a step–size of 200 nm, an e–beam current of ~ 100 pA, and a dose of ~ 100 mC/cm^2, about 7 hours are required. The EBI procedures were performed by Dr. Federica Bianco at NEST Laboratory.

2.6 Raman Spectroscopy

Raman spectroscopy is one of the most suitable techniques for the characterization of graphene–based materials, being able to provide both structural and electronic information, and allowing for fast and non–destructive measurements.[125,126] A laser of a known wavelength is focused onto the surface of graphene, and the scattered photons are collected and analyzed in terms of parameters as wavelength, polarization, and scattering angle (see Figure 2.13(a) for the setup). Most of the scattered light has the same wavelength as the laser (elastic light scattering or Rayleigh scattering), but a small amount of the scattered light has a different wavelength than the excitation photon, due to the creation or annihilation of phonons (quantized excitation in the material). This light scattering process is inelastic and known as the Raman effect.[127] Graphene has a characteristic Raman spectrum which has become a standard in identifying the number of layers in the sample, as well as the amount of defects or the chemical modifications in its surface (see Figure 2.13(b)).[128,129]

Here, Raman spectroscopy was carried out with a Renishaw InVia system, equipped with a confocal microscope, a 532 nm excitation laser and a 1800 line/mm grating (spectral resolution 2 cm^{-1}). For the experiments reported in Chapter 3, all spectra were measured with the following parameters: excitation laser power 500 μW, single acquisition time for each spectrum 20 s, two acquisitions per spectrum, with a 100$\times$ objective (NA = 0.85, spot size 1 μm). At least 3 different samples were measured, both for pristine and functionalized graphene, and they all showed the same features as the ones reported here as representative results. The samples were prepared by dropcasting (2 μL) onto a clean silica substrate and dried under vacuum for several days. Similarly, the same parameters were used for the experiments described in Chapter 4. In addition, a proper step–size of 0.5 μm was used to map the Raman modes across the surface of the graphene flakes. The defects induced by electrons were investigated just after the exposure with the same parameters of pre–exposure investigation. For the experiments described in Chapter 5, single spectra were measured with the following parameters: single acquisition time for each spectrum 3 s, 10 acquisitions per spectrum, excitation laser power from 22 μW to 1560 μW, with a 100$\times$ objective (NA = 0.85, spot size 1 μm). Maps were collected with the following parameters: single acquisition time for each spectrum 3 s, 4 acquisitions per spectrum, excitation laser power 120 μW, with a 100$\times$ objective (NA = 0.85, spot size 1 μm). A Newport power meter, model 843-R, with a low–power calibrated photodiode sensor was used to measure the incident Raman laser power for different nominal percentages (between 0.1% and 5%).
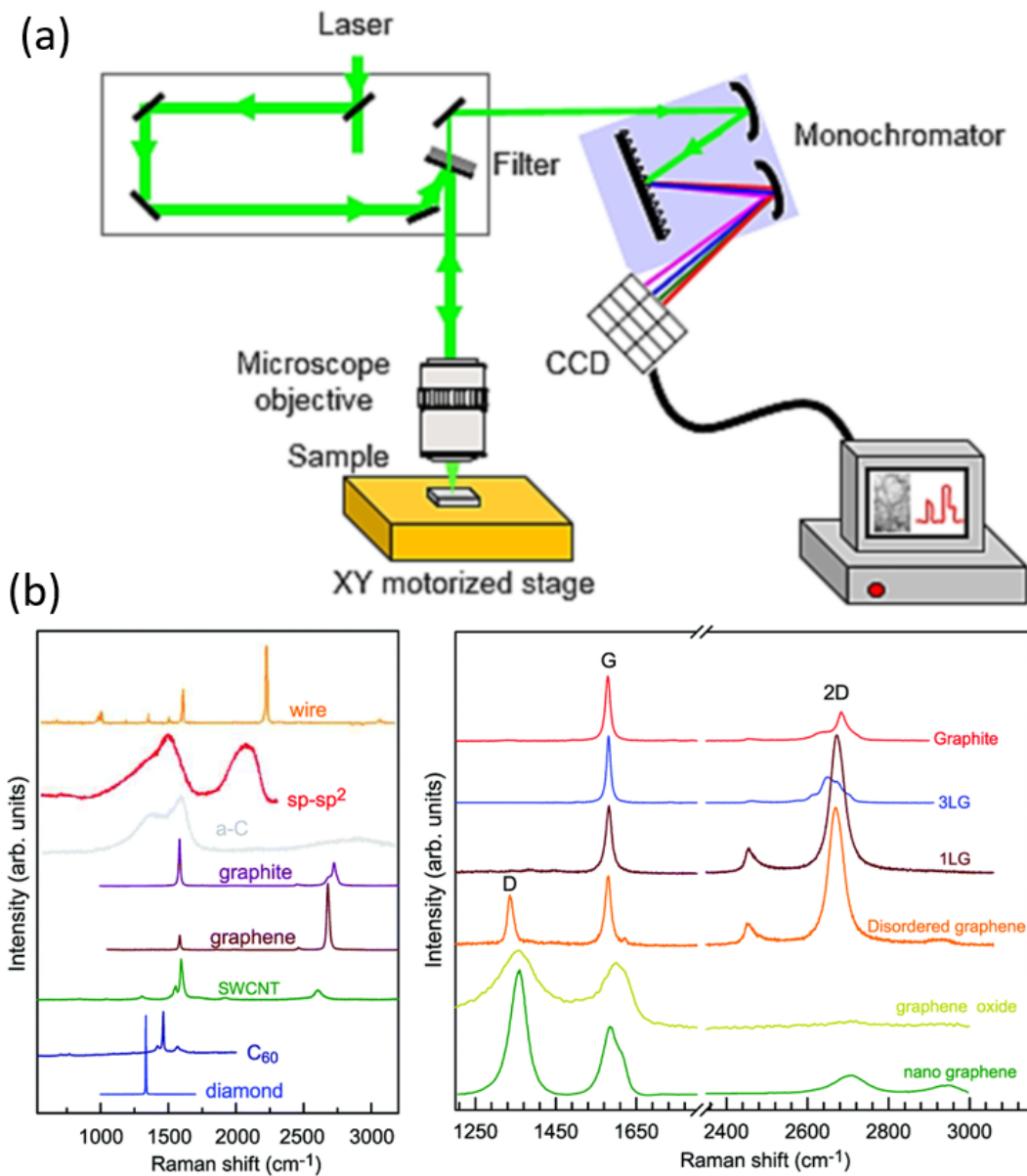
Figure 2.13: (a) Experimental setup for Raman spectroscopy (figure and caption adapted from Ref. 130). (b) Raman spectra of carbon solids, carbon nanostructures, and graphene–based materials, including graphite, 1LG, 3LG, disordered graphene, graphene oxide and nanographene. Figure and caption adapted from Ref. 131.

2.7 Scanning Transmission Electron Microscopy– EDX/EELS

In a *Scanning Transmission Electron Microscope* (STEM) a high–energy e–beam is focused on the sample surface. Using lenses and deflection coils, this focused probe is scanned across the sample and local information can be collected with high resolution (atomically resolved images can be achieved with aberration–corrected STEMs). In particular, *Electron Energy–Loss Spectroscopy* (EELS) and *Energy Dispersive X–ray spectroscopy* (EDX) allow to identify the chemical elements of the surface enabling compositional evaluations, elemental mapping, and electronic property analysis (see Figure 2.14 for the setup). In EELS, the electrons in the e–beam experience an energy loss as they move through the sample due to interactions with the electrons in the sample, they are scattered inelastically, and their energy distribution is measured. Similarly, EDX reveals the emission energy of the X–rays created when high–energy electrons from the e–beam cause the ejection of the sample's atoms inner shell electrons and the subsequential relaxation of outer shell electrons.

Here, STEM–EDX/EELS measurements were carried out with a Zeiss Libra 120 microscope operating at an accelerating voltage of 120 kV, equipped with a thermionic LaB_6 source and an in–column Omega filter for energy–filtered imaging and EELS analysis. EELS spectra were collected by integrating the EELS signal on the TEM CCD (a TRS 2k × 2k CCD camera binned 2 by 2) and by selecting the measured area using the entrance slit aperture of the Omega filter. The samples were prepared by washing the dispersant solvent with ethanol several times and collected on carbon film–supported copper grids. STEM–EDX/EELS measurements were performed by Dr. Andrea Griesi at NEST Laboratory.
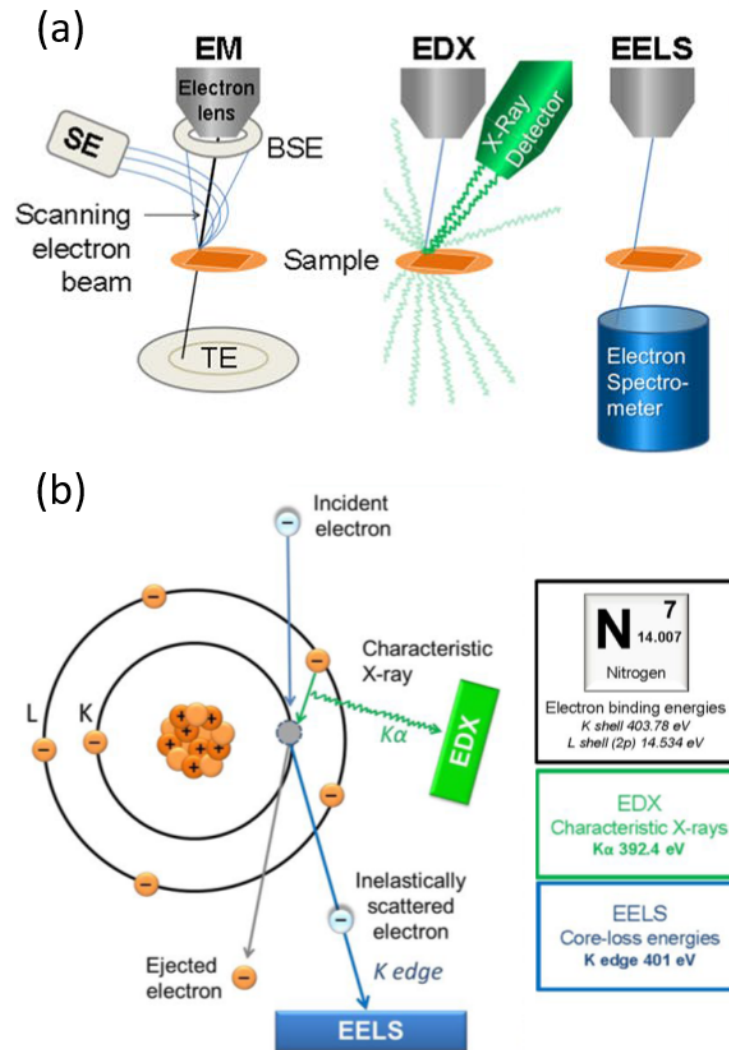
Figure 2.14: (a) Arbitrary microscope configurations of EM, EDX, and EELS. Note that with EELS, the spectrometer must be on the transmission side of the sample. For EDX, this is typically not the case. (b) EDX and EELS physical principles. The atomic origin of EDX and EELS signals is indicated for a nitrogen (N) atom. N has seven electrons arranged in two orbital shells: K and L. Electron binding energies of specified orbitals are shown (right). When an incident electron dislodges an electron from the K shell, inner–shell ionization occurs (left). To fill the vacancy, an electron from the L shell drops, and the difference in binding energies is released as a characteristic X–ray. A K shell vacancy being filled from an L shell electron results in a K_α line. This K_α X–ray is used to fingerprint N in the collected spectra. The incident electron that created the vacancy has lost an amount of energy approximately equal to the binding energy of the ejected electron. Therefore, in the EELS spectrum, transmitted electrons that have lost 401 eV represent N content in the sample. The zero–loss peak represents transmitted electrons that did not lose energy, and may be used to determine the sample thickness. Ionization edges represent the inner–shell ionization of sample atoms. Figure and caption adapted from Ref. 132.

2.8 X–ray Photoelectron Spectroscopy

X–ray Photoelectron Spectroscopy (XPS) is a highly surface–sensitive technique, which allows chemical and quantitative analysis of the top few atomic layers (1 – 10 nm) of the sample. XPS detects the photoelectrons emitted from the surface under irradiation with X–rays (see Figure 2.15 for the setup) and measures their kinetic energy. The surface elements and their chemical state can be derived from the detected energy, being directly connected to the photoelectrons' binding energy (B.E.) inside the parent atom.

Here, XPS core level emission spectra were acquired using a Surface Science Instrument SSX-100-301 spectrometer operating an Al K_α source ($h\nu = 1486.5$ eV), achieving an overall energy resolution of 0.85 eV. The collected spectra were fitted using the XP-SPEAK software, subtracting a Shirley–type background[133] and fitting the peaks using mixed Gaussian and Lorentzian components. The samples were prepared by repeated dropcasting onto clean highly doped silicon substrates (with native oxide), and dried under vacuum between several drops and at the end of the deposition process. XPS measurements were performed by Dr. Silvia Rubini at CNR IOM Laboratory in Trieste, Italy.
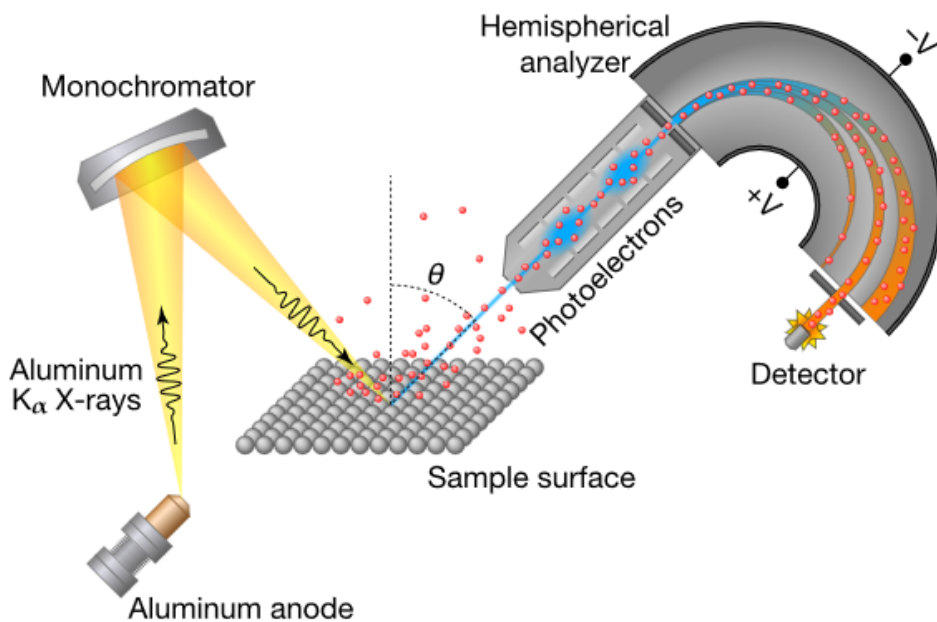
Figure 2.15: Scheme of XPS: X–rays hit the sample surface and interact with core–level electrons. The electrons closer to the surface (the top few nanometers) manage to escape and are collected and measured. Figure and caption adapted from Ref. 134.

2.9   Atomic Force Microscopy

Atomic Force Microscopy (AFM) is a scanning probe technique that allows to image the morphology of a sample's surface, with resolution at the nanometer scale.
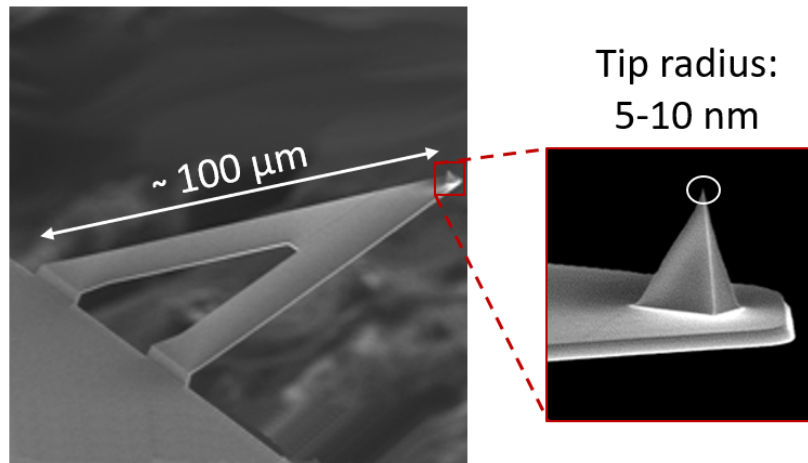
Figure 2.16: TEM images of exemplary silicon nitride triangular cantilever and tip used in AFM measurements. Figures adapted from Ref. 135.

In an AFM measurement in *contact* mode, a sharp tip (typical tip radius 5 – 10 nm) at the end of a flexible cantilever (as shown in Figure 2.16) is brought into contact with the sample and scanned across the sample's surface. A piezoelectric actuator and a feedback system maintain a constant force (or a constant height) between the tip and the sample. The bending of the cantilever during the scan movements is detected by a laser beam focused on the cantilever and reflected into a 4–quadrant photodiode. Although this imaging mode is fast, simple and allows to simultaneously measure other parameters such as the surface friction or resistance, it presents the risk of damaging the tip because of lateral forces and drag across the surface. On the contrary, in *non–contact* mode the tip is kept at a small distance from the surface of the sample and the cantilever is made oscillating at its resonance frequency and with low amplitude. While scanning, the amplitude, the frequency and the phase of the cantilever oscillation change because of the interactions between the tip and the sample's surface, and can be recorded simultaneously, giving information about the sample's topography or composition. Typically, because non–contact mode requires demanding performances from the feedback system in order to avoid an excessive decrease in the lateral resolution, an intermediate technique is preferred. In *tapping* AFM mode, the tip touches the sample surface only for a short time while the cantilever oscillates at its resonance frequency and with higher amplitude normal to the sample surface. Hence, intense lateral forces that can damage both the sample and the tip are minimized (see Figure 2.17 for the setup). Noteworthy, unlike Scanning Tunneling Microscopy, AFM permits to image both conductive and non–conductive surfaces.

Here, AFM was performed for surface analysis utilizing an Anasys Instruments AFM operating in tapping mode, coupled with a microscope system for positioning.
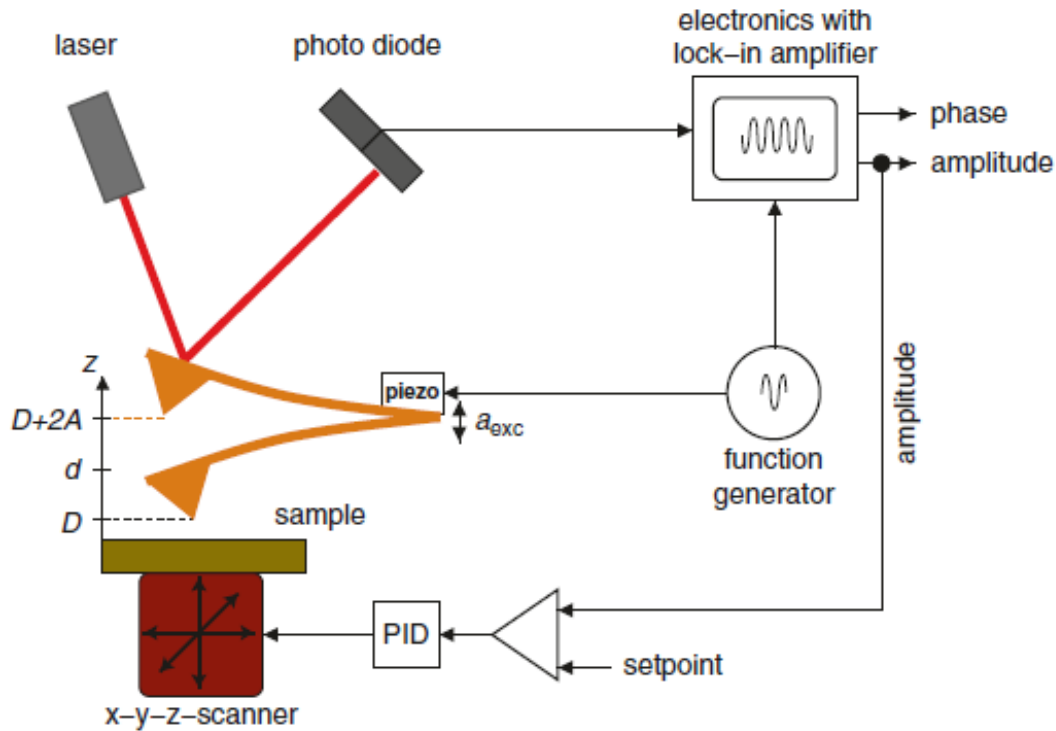
Figure 2.17: Setup of AFM operated in non–contact mode. A laser beam is deflected by the back side of the cantilever, and its deflection is detected by a split photodiode. The cantilever vibration is caused by an external frequency generator driving an excitation piezo. A lock–in amplifier is used to compare the cantilever drive with its oscillation. The amplitude signal is held constant by a feedback loop controlling the cantilever–sample distance. Figure and caption adapted from Ref. 124.

Peak Force – Quantitative NanoMechanical (PF–QNM) mode is an AFM imaging mode based on Bruker's proprietary Peak Force Tapping™ technology. This technique simultaneously provides information about the nanomechanical properties of nanomaterials and the topography of the sample. This is possible if the individual force curves from each tap that occurs during the scan are instant–by–instant acquired and analyzed instead of time–averaged as in standard AFM imaging. Therefore, PF–QNM requires that the bandwidth of the force sensor is significantly higher than the frequency of the periodic interactions. Then, the force curve is converted into a force vs. tip–sample separation plot which, with further analysis, reveals the mechanical properties of the sample, such as adhesion, modulus, deformation, and dissipation (see Figure 2.18).

Here, PF–QNM was performed using a Bruker Dimension ICON–PT operating in tapping mode, coupled with a microscope system for positioning. The Gwyddion software package was used to analyze the AFM and PF–QNM images.[137]
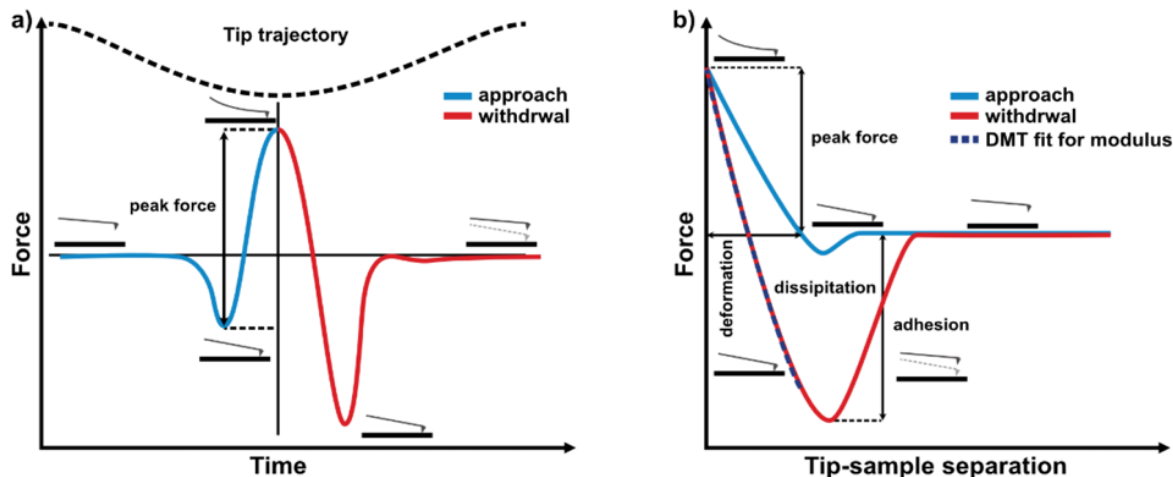
Figure 2.18: (a) Scheme of the force curve for a cantilever operating in Peak Force Tapping and (b) scheme of the single cycle force vs. separation curve with the dark blue dashed line fitted to the retract curve using the Derjaguin–Muller–Toporov (DMT) model. Figures and caption adapted from Ref. 136.

2.10   Scanning Tunneling Microscopy and Scanning Tunneling Spectroscopy

A *Scanning Tunneling Microscope* (STM) is used for investigating surfaces at the atomic level (on the scale of Å), and therefore visualizing the atoms' positions on the sample surface. The STM is based on the quantum–mechanical tunneling effect: when a conductive atomically sharp tip is brought very close to the surface to be examined, electrons can tunnel through the vacuum (or air) between them. If no bias voltage is applied between the tip and the surface the net tunneling current is zero, otherwise the resulting current is a function of several parameters, as tip position, applied bias voltage, and the local density of states (LDOS) of the sample.[138] Once tunneling is established, the tip's bias and position with respect to the sample can be varied, and moving the tip across the sample in the x–y plane allows to obtain surface images. Images can be acquired in two different modes: in the *constant height* mode the tip–sample distance is maintained fixed by a feedback mechanism while the changes in the current are measured, whereas in the *constant current* mode the current is fixed and the tip is moved closer to or further away from the sample (see Figure 2.19(a) for the setup).

Similarly, *Scanning Tunneling Spectroscopy* (STS) relies on the tunneling effect in order to measure the electronic properties of a material. The scanning tip is stopped in a fixed position and distance from the sample's surface (with the feedback mechanism off) and a voltage sweep is performed, while recording the tunneling current. Using a lock–in amplifier and a small AC signal added to the DC bias, the differential conductance dI/dV is calculated, which is proportional to the LDOS of the sample (see Figure 2.19(b)).[139] It is important to underline that, in order to be able to investigate a sample surface with STM or STS, the sample must be able to allow a tunneling current to flow. Hence, these techniques are restricted to conductive (metallic or semiconductor) samples.

Here, STM and STS measurements were performed with an ultra–high vacuum (UHV) STM from RHK Technologies, at room temperature, in an UHV chamber (base pressure $\sim 10^{-11}$ mbar).
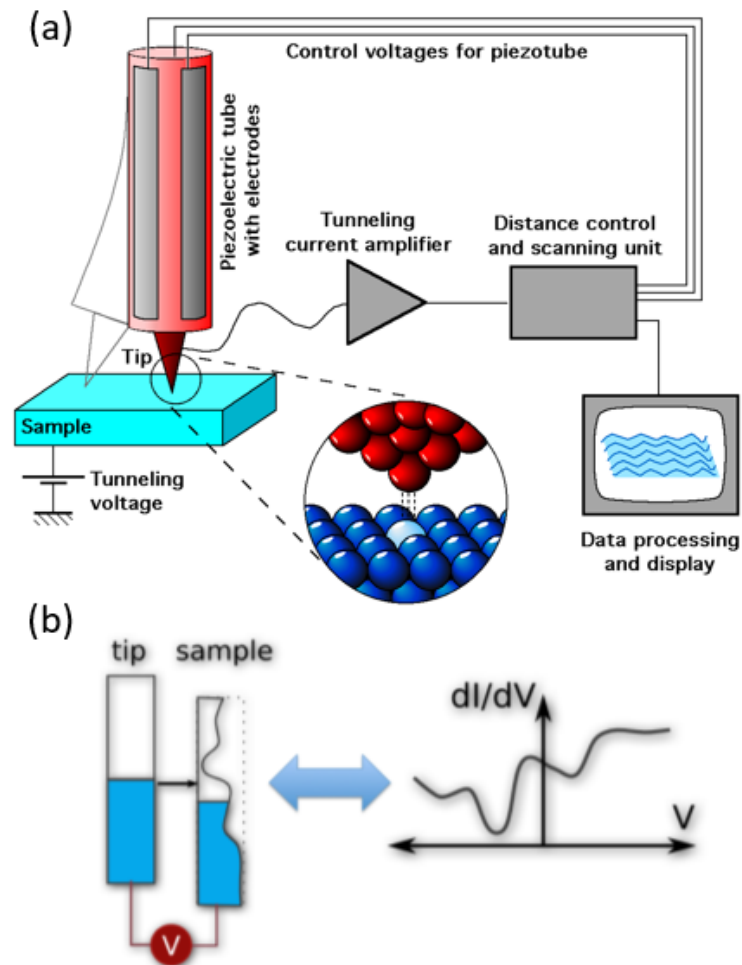
Figure 2.19: (a) Schematic view of an STM: a tube scanner moves the probe tip, via 3D piezoelectric elements, on the sample surface. Moving the tip in the z direction and applying a bias voltage, the tunneling condition can be established. If the tip is moved across the sample in the x–y plane, the changes in surface height and density of states cause changes in current, which are mapped in images. The current is amplified and the data are processed and shown on the computer. (b) Energy band diagram for the tip and the sample when a positive bias is applied to the sample, such that electrons flow from the filled states of the tip to the empty states of the sample (black arrow). During a STS measurement, the voltage applied between the tip and the sample is swept. Since the density of states of a metallic tip is constant, the differential conductance represents the density of states of the sample. Figures adapted from Refs. 139,140.

2.11 Computational Methods

All calculations reported in Chapters 3 and 5 are performed with the CP2K[141,142] program at the density functional theory (DFT) level using the Perdew–Burke–Ernzerhof (PBE) exchange and correlation functional.[143] Second–generation dispersion corrections (D2)[144] were used to take into account a proper description of van der Waals interactions. The Gaussian–and–Plane–Waves (GPW) method as implemented in CP2K[145] was used; the energy cutoff for the auxiliary plane–wave basis was set to 340 Ry. The wavefunction convergence criterion was set to 10^{-6} Hartree. Geometry optimization of the systems was performed by using the Broyden–Fletcher–Goldfarb–Shanno (BFGS) algorithm by setting a root mean square (RMS) value of 10^{-4} Hartree/Bohr for the force and 10^{-4} Bohr for the geometry as convergence criteria. Goedecker–Teter–Hutter (GTH) pseudopotentials,[146] together with double–zeta quality basis sets (DZVP), were used. The systems were treated with periodic boundary conditions.
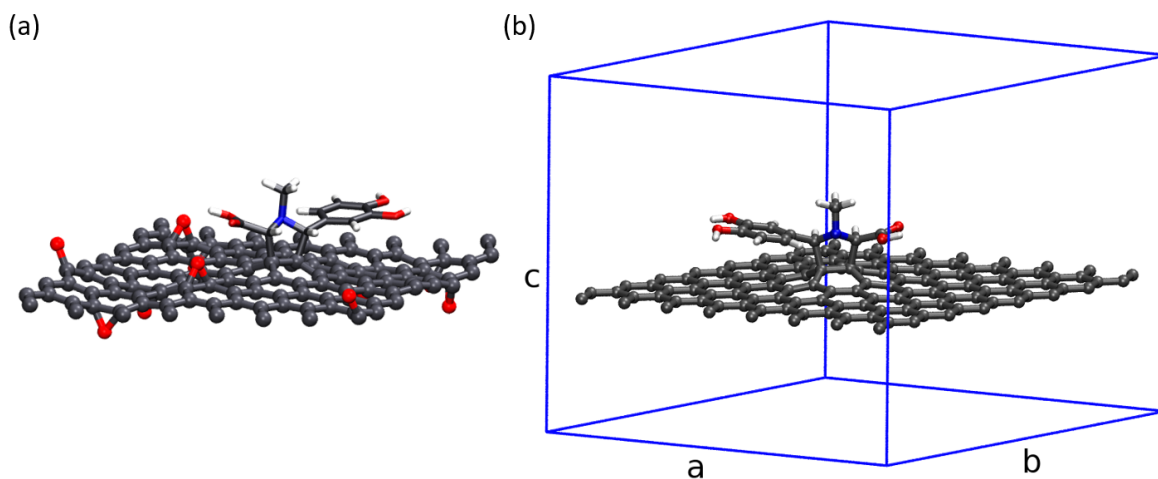
Figure 2.20: Hexagonal (a) rGO and (b) graphene computational cells. The boundaries of the cell (a = b = 1.98 nm, c = 2 nm) are shown only for graphene and are the same for rGO. Dark grey: C atoms, blue: N, red: O, white: H.

Reduced graphene oxide was modeled starting from an hexagonal graphene cell (a = b = 1.98 nm, c = 2 nm) consisting of 154 atoms (128 carbons plus 26 atoms of the ylide molecule) and positioning 10 oxygen atoms on top of randomly chosen carbon atoms (as shown in Figure 2.20(a)). The total amount of oxygen was 8% in weight, in agreement with similar rGO models in literature.[147] The Restrained Electrostatic Potential (RESP) charges[148] for periodic systems were evaluated by using REPEAT methods[149] as implemented in CP2K.[150]

After structural optimization, the functionalized system was subject to free molecular dynamics (MD). MD simulations were performed in the NVT ensemble (canonical ensemble, T = 300 K) employing a canonical–sampling–through–velocity–escalating (CSVR) thermostat[151] with a time constant of 500 fs. A single integration time step of 0.4 fs was used. MD simulations were carried out for 12 ps. Vibrational spectra were obtained by calculating the Fourier transform of the atoms velocity auto–correlation function (VACF) taken from the last 10 ps of the simulated trajectory of the system (see Figure 2.21 for a scheme of the steps of the computational simulations).[152]

Similarly, functionalized graphene was modeled starting from an hexagonal graphene cell (a = b = 1.98 nm, c = 2 nm) including 154 atoms (128 graphene's carbons plus 26
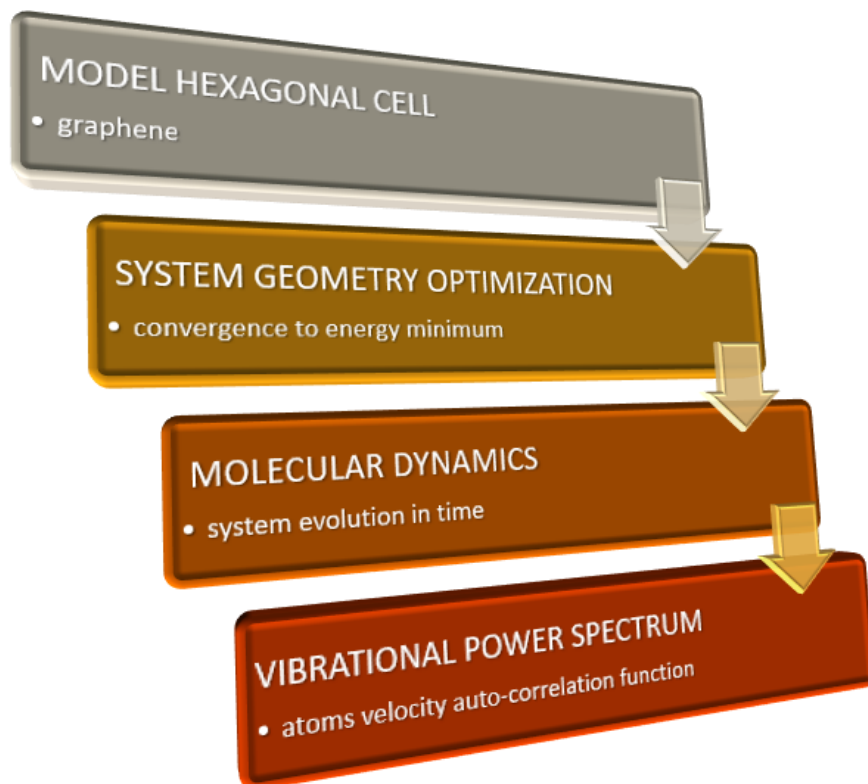
Figure 2.21: Scheme of the simulation steps: it begins with the model of the hexagonal graphene cell, followed by the geometry optimization of the entire system, then MD simulations are performed, and the vibrational power spectrum is eventually obtained.

atoms of the ylide molecule, as shown in Figure 2.20(b)). After structural minimization, the system was subjected to a 38 ps MD run, performed in the NVT ensemble (T = 300 K) using a CSVR thermostat with a time constant of 500 fs. A single integration time step of 0.4 fs was used. Vibrational spectra were obtained through the Fourier transform of the atoms VACF taken over the last 36 ps of the MD simulation. Normal modes and vibrational analysis were performed for graphene and functionalized graphene using the VIBRATIONAL–ANALYSIS module of CP2K. All DFT simulations were performed by Dr. Luca Bellucci, in collaboration with Dr. Valentina Tozzini, at NEST Laboratory.

For the calculations described in Chapter 4, Monte Carlo simulations were carried out with the CASINO software,[153] considering the following experimental conditions: $\sim 8 \times 10^5$ and 4×10^6 incident electrons (corresponding to about 40 mC/cm^2 and 200 mC/cm^2, respectively), and beam radius of 10 nm. These calculations were performed by Dr. Federica Bianco at NEST Laboratory.

Functionalization of dispersed GNS and rGO

3

Here we present a detailed investigation on 1,3–DC of azomethine ylide on both graphene nanosheets (GNS) and reduced graphene oxide (rGO), including solvent effects. We compare sonication and homogenization as dispersion techniques, while 1-methyl-2-pyrrolidinone (NMP) and N,N-dimethylformamide (DMF) are used as dispersant solvents, for their excellent efficiency in dispersing graphene as well as facilitating the in situ production and the grafting of the ylide onto graphene. Energy–dispersive X–ray spectroscopy (EDX) and electron energy loss spectroscopy (EELS) confirm the organic functionalization of graphene and verify its homogeneity on the entire surface. While these techniques have already been applied to analogous systems, a detailed characterization of functionalized graphene with Raman spectroscopy is presented here for the first time. Raman spectroscopy, performed on both the pristine and functionalized samples, allowed the detection of the characteristic Raman signature of graphene together with new distinctive peaks from the ylide. Moreover, X–ray photoelectron spectroscopy (XPS) is used to estimate the coverage and the efficiency of the functionalization process, assessing the elemental composition. An ab initio density–functional theory (DFT) molecular dynamics simulation illustrates how the presence of epoxy groups in the rGO surface induces a local inhomogeneity of the partial charges of the structure of graphene, promoting the 1,3–DC of azomethine ylide and showing how defects (like functional groups, edges, or vacancies) could be exploited to acquire control on the degree of the functionalization. Finally, the simulated power spectrum provides a precise idea of the Raman signature of functionalized graphene, in agreement with the experimental data.

3.1   Dispersion of GNS

Exfoliated GNS produced by wet–jet milling (as described in Section 2.1.1)[105] were dispersed in NMP and DMF in order to obtain a stable dispersion with a concentration of ~ 0.2 mg mL^{-1}, as shown in Figure 3.1. It is well known that these are well–suited organic solvents for the dispersion of graphene,[114] since they minimize the interfacial tension between solvent and graphene. Moreover, both NMP and DMF are commonly used in 1,3–dipolar cycloadditions for their ability to favor the reaction.[68,69,154,155] Both these aspects are fundamental for the functionalization procedure, which will be described in the following.

Sonication has been widely utilized to induce exfoliation of bulk materials through growth and collapse of micro–bubbles due to pressure fluctuations in liquids.[112] Recently, also homogenization, which consists in the shear mixing in suitable stabilizing liquids, has been demonstrated to achieve excellent exfoliation of graphite, even in a more scalable way.[104]
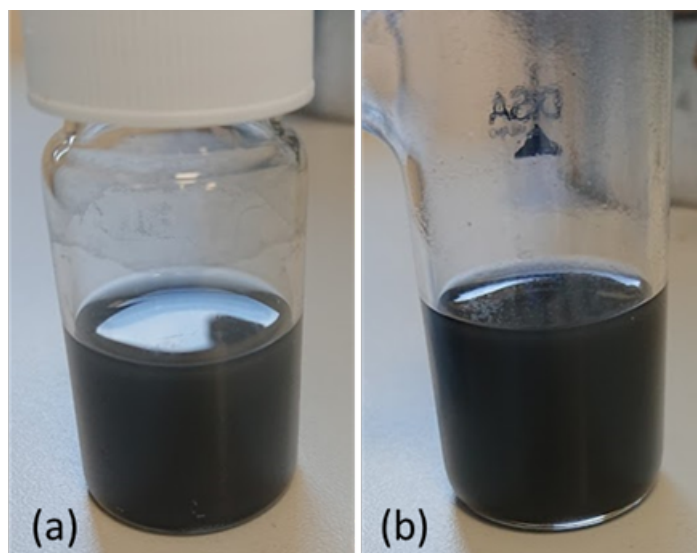
Figure 3.1: Dispersion of GNS in NMP after (a) sonication and (b) homogenization.

In order to compare NMP and DMF as dispersion solvents, as well as sonication and homogenization as dispersion techniques, we performed dynamic light scattering (DLS) measurements on dispersed GNS (0.25 mg mL^{-1}). A commercially available Malvern Zetasizer Nano ZS equipped with a 633 nm HeNe laser was used for this purpose. In the automatic setting, the system optimizes the focal position and the attenuation of the incident beam before the data acquisition. The Zetasizer software uses a set of algorithms to analyze the correlation of scattering events and gives as output the relative intensity of light scattered by particles of a given average lateral dimension. We have to keep in mind that, as explained in detail in Section 2.4, because we are not measuring spherical particles the lateral dimensions resulting from the DLS measurements are not the actual dimensions of the dispersed graphene. However, being related, they still allow a quantitative analysis. The values are collected in Table 3.1.

Comparing the average lateral dimension of the dispersed nanosheets, we noticed a reduction in size from 850 nm to 600 nm (using sonication) or 400 nm (using homogenization) after 60 minutes in NMP, in contrast with a decrease in size from 950 nm

Table 3.1: Average lateral dimension of GNS dispersed in NMP or DMF, via sonication (60 W) or homogenization (30000 rpm), measured at the beginning and after 30, 60, and 120 minutes of re–dispersion. (—) : not measured.

Solvent	Dispersion technique	Start [nm]	After 30 minutes [nm]	After 60 minutes [nm]	After 120 minutes [nm]
NMP	sonication	850 ± 100	—	600 ± 100	500 ± 100
NMP	homogenization	850 ± 50	600 ± 40	400 ± 20	—
DMF	sonication	950 ± 150	—	850 ± 150	800 ± 150
DMF	homogenization	950 ± 150	800 ± 50	600 ± 50	—

to 850 nm (using sonication) or 600 nm (using homogenization) in DMF. A better dispersion was achieved in NMP with respect to DMF (smaller dimensions indicate thinner GNS, with fewer layers). This can be explained as a result of the optimal surface tension of NMP ($\gamma = 40$ mJ m^{-2}), compared to DMF ($\gamma = 37.1$ mJ m^{-2}), which falls in the ideal range for graphene liquid phase exfoliation (40 – 50 mJ m^{-2}).[111,156] We also observed that in both NMP and DMF, homogenization allows a faster dispersion of GNS. For example, sonication in NMP for 60 minutes allows a decrease of the average lateral dimension from 850 nm to 600 nm, while the same result was obtained after only 30 minutes of homogenization. Therefore, homogenization results to be the advisable dispersion procedure, and the subsequent experiments were performed after dispersion via homogenization.

3.2 1,3–DC of GNS and rGO

Functionalized GNS were prepared by adding N-methylglycine and 3,4-dihydroxybenzaldehyde to the GNS dispersion, as schematically represented in Figure 3.2. The 1,3–DC of GNS was performed both in NMP and in DMF, in order to allow a comparison between the two solvents. As will be shown below, a higher degree of functionalization was achieved for GNS dispersed in DMF. Moreover, together with their dispersant efficiency, an important parameter to take into account is the boiling point of the solvents, 202 ℃ for NMP and 153 ℃ for DMF. A higher boiling point results in a more time–consuming procedure for removing the solvent under vacuum, after dropcasting the functionalized graphene onto the substrates for characterization. Taking all this into consideration, rGO was dispersed only in DMF (~ 0.2 mg mL^{-1}) and only via homogenization, while the subsequent functionalization procedure remained the same.
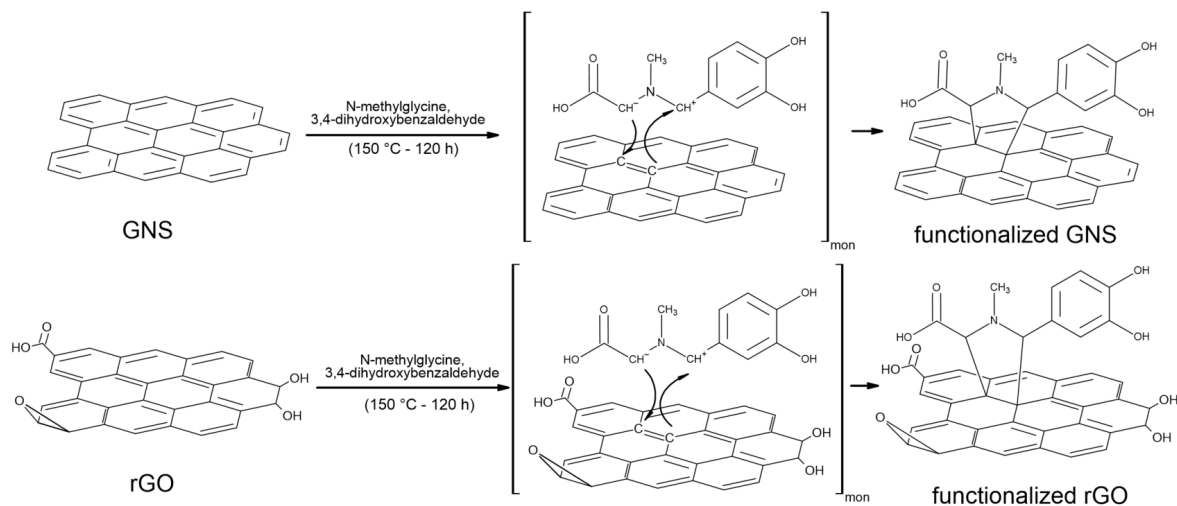
Figure 3.2: Schematic representation of the 1,3–DC of azomethine ylide on GNS and rGO.

3.3 EDX/EELS analysis

After the functionalization procedure, the dispersant solvent was removed by several washings with ethanol, and graphene was deposited on carbon film–supported copper TEM grids. Several scanning transmission electron microscopy (STEM) images were acquired in order to identify the GNS (a representative STEM image is shown in Figure 3.3), while the successful functionalization of graphene was confirmed with energy–dispersive X–ray spectroscopy (EDX) and electron energy loss spectroscopy (EELS), which are very useful techniques for the elemental analysis or the chemical characterization of a sample.
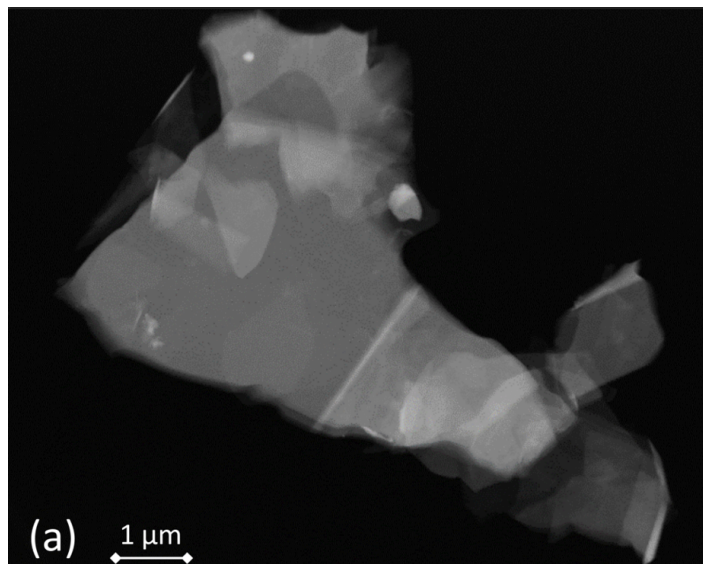
Figure 3.3: Representative STEM image of an exfoliated few–layers GNS.

The detection of N and O peaks from functionalized graphene in the EDX spectra (shown in Figure 3.4) confirms the presence of azomethine ylides on graphene's surface, which present functional groups containing nitrogen and oxygen. EDX spectra were acquired using carbon film–supported copper grids, therefore, signal from C and Cu of

the grid is expected, in addition of the C signal from the graphene lattice, and thus a quantitative analysis is not possible.
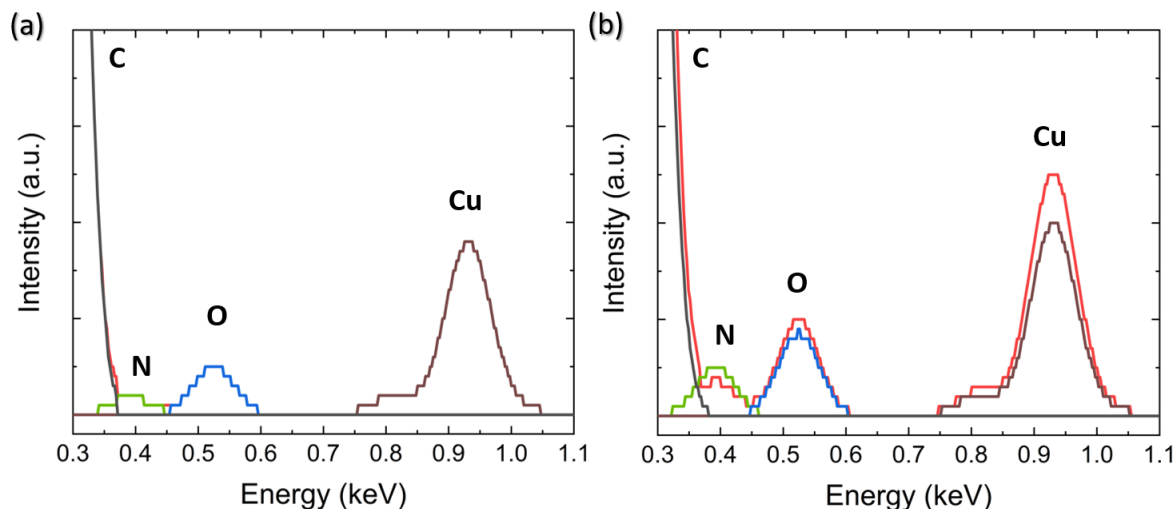
Figure 3.4: EDX spectra (red line) of functionalized (a) GNS in NMP and (b) GNS in DMF (colored lines: deconvolution). Only a zoom of the region of interest is shown.

As shown in Figure 3.5, EELS spectra of the N K–edge of functionalized GNS and rGO exhibit two bands, centered at 402 eV and at 410 eV, assigned respectively to π^* and σ^* contributions. Like in the EDX measurements, signal from nitrogen is expected only from the azomethine ylides, and its presence confirms the success of the functionalization.
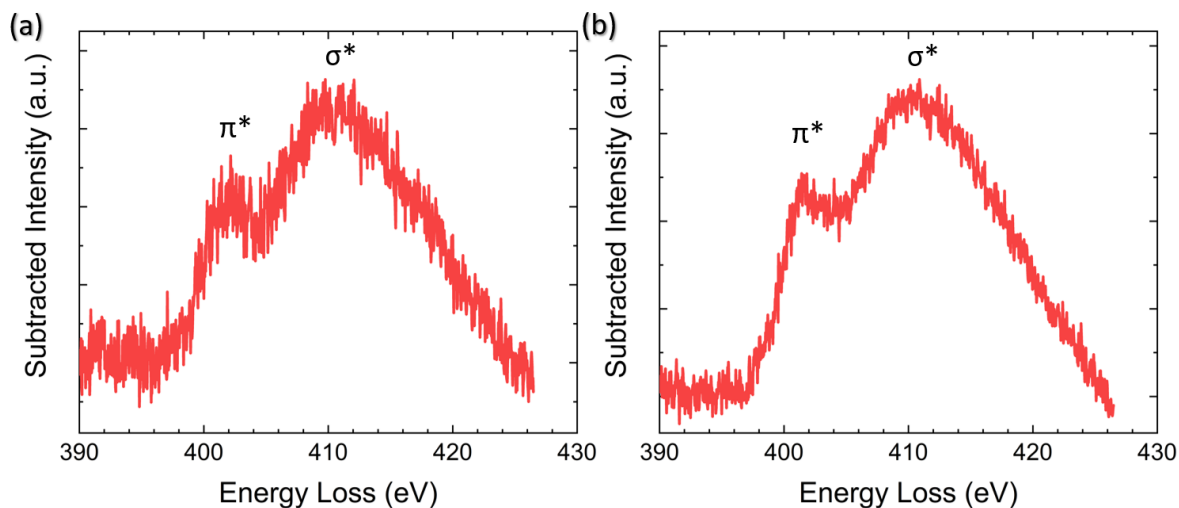
Figure 3.5: EELS spectra of functionalized (a) GNS in DMF and (b) rGO in DMF. The background was subtracted from the spectra in order to highlight the K–edges of N.

The elemental signature of nitrogen was detected mapping the functionalized GNS, and is shown as superimposed map (green signal) on the STEM image of the graphene flake in Figure 3.6. It is interesting to notice that the molecules bond with graphene not only along the edges of the GNS, but also at the central C=C, as indicated by the uniform distribution of the N signal in the EDX map.
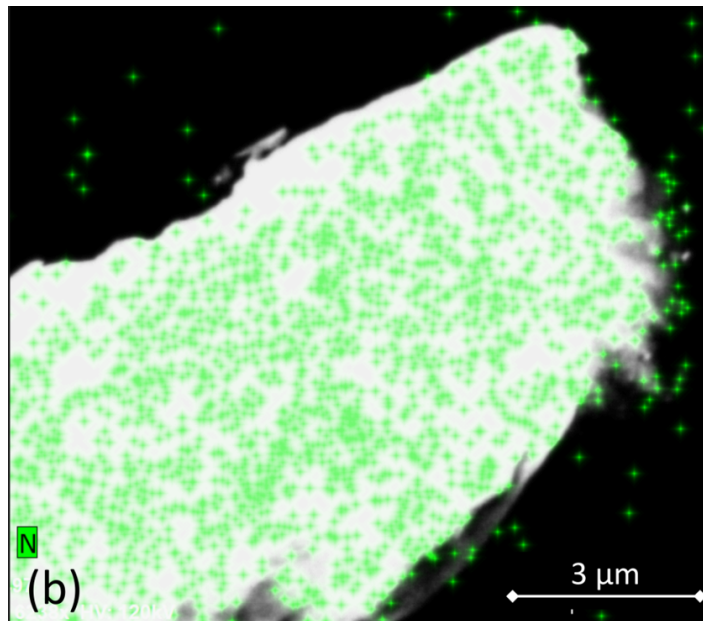
Figure 3.6: EDX map of a functionalized GNS (superimposed on the STEM image) showing the uniform distribution of the signal (green pixels) arising from N atoms.

3.4 Raman spectra of pristine and functionalized GNS

Both pristine and functionalized GNS were dropcasted onto clean silica substrates, and the solvent was removed under vacuum (see Figure 3.7(a,b)), in order to investigate them with Raman spectroscopy.

Since a Raman spectrum of graphene was first recorded in 2006,[125] this technique has become one of the most suitable methods for the characterization of carbon–based nanomaterials, allowing to obtain both structural and electronic information, and being fast and non–destructive.[126] Figure 3.8 shows the Raman spectra of pristine GNS dispersed in NMP and in DMF, along with the fit and the assignment of the 5 characteristic peaks of graphene. The most recognizable features in the Raman spectrum of graphene are the G band, here centered at 1581 cm^{-1}, and the 2D band, here centered at 2695 cm^{-1} (for both GNS in NMP and GNS in DMF). The G band comes from the in–plane bond–stretching motion of pairs of C atoms of the graphene ring, while the 2D peak is the second order of the D peak and originates from a double–phonon process, where momentum conservation is satisfied.[125] Because no defects are required for their activation, both G and 2D peaks are always present. It is well–established that the width (FWHM) of the 2D band is related to the number of layers of graphene sheets.[125] In particular, a single curve with a FWHM of about 24 cm^{-1} [128] can be used for the fitting of the spectrum of monolayer graphene, while several curves (or a broader single
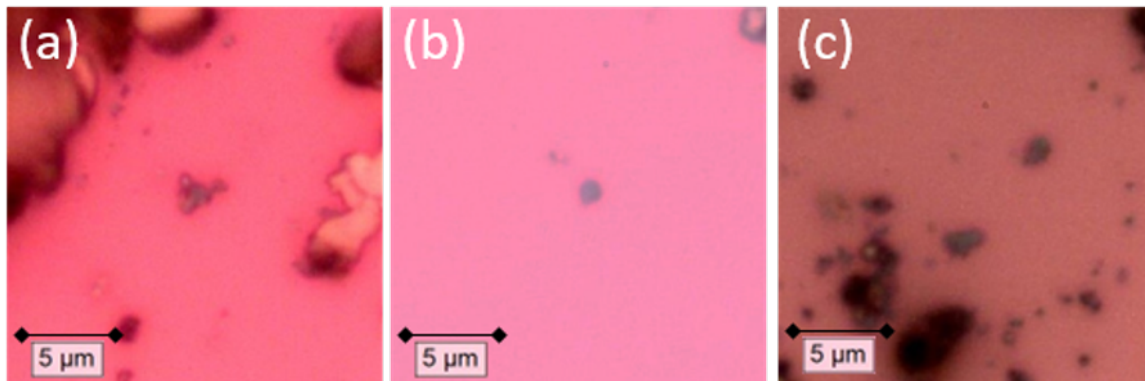
Figure 3.7: Optical microscopy images of functionalized GNS in (a) NMP and (b) in DMF, and (c) functionalized rGO in DMF dropcasted onto silica substrates for Raman measurements.

one) are needed for the fitting of the spectrum of multilayer graphene. Here we can fit the 2D band with a single symmetrical Gaussian–Lorentzian curve, with a FWHM of about 75 cm^{-1} for GNS in NMP ($\sim$ 70 cm^{-1} for GNS in DMF), which allows us to identify the GNS as few layer graphene (less than five layers thick, following the criterion described in Ref. 105).
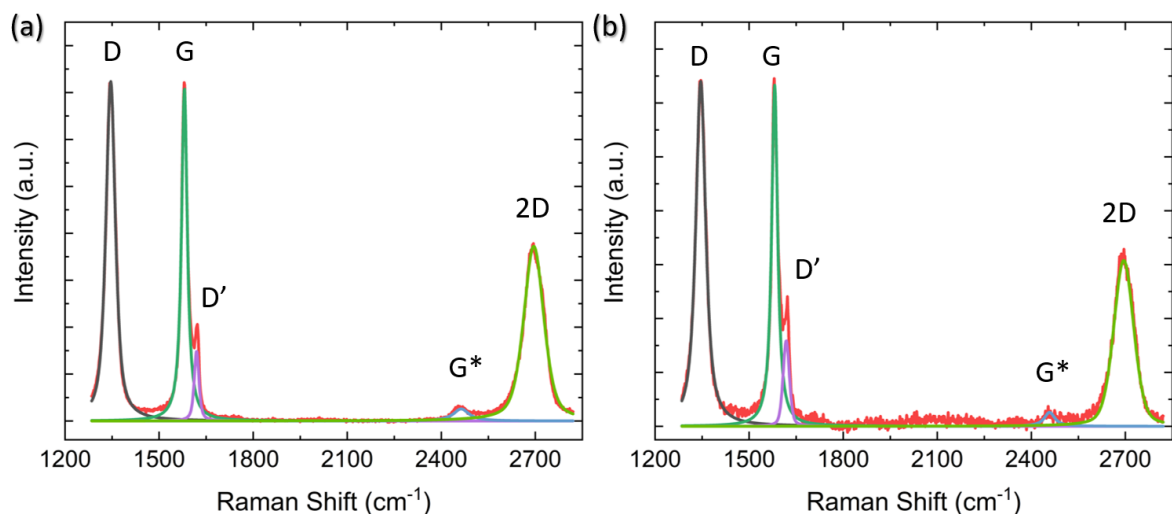
Figure 3.8: Raman spectra of pristine GNS in (a) NMP and in (b) DMF. The fit of each spectrum is shown and all peaks are labeled.

In the presence of small size graphene and/or defects, which we can relate to the breaking of the symmetry of the infinite carbon honeycomb lattice,[157] additional bands appear. The D peak, here centered at 1346 cm^{-1}, and the D' peak, here centered at 1620 cm^{-1} (for both GNS in NMP and GNS in DMF), involve respectively intervalley and intravalley double resonance processes, and for low defect concentrations their intensities are proportional to the amount of defects.[131] The intensity ratio of the D and D' peaks has been shown to indicate the nature of the defects in the graphene lattice. In particular, $I(\text{D})/I(\text{D'})$ reaches a maximum value of $\sim$ 13 for sp^3–defects, decreases to $\sim$ 7 for vacancy–like defects, and has a minimum of $\sim$ 3.5 for boundary–like defects.[157] Here, $I(\text{D})/I(\text{D'})$ is 4.89 in case of pristine GNS in NMP, and 4.02 in case of pristine GNS in DMF, confirming the boundary–like nature of the defects in

pristine GNS. Finally, a weak G* band is visible, here centered at 2460 cm^{-1} for GNS in NMP (2463 cm^{-1} for GNS in DMF), which arises from an intervalley process involving an in–plane transverse optical phonon and one longitudinal acoustical phonon (also called G + A$_{2U}$).[158] Here, as in the following chapters, the identification of the G* peak is reported only for completeness and no further analysis are performed due to its low intensity.
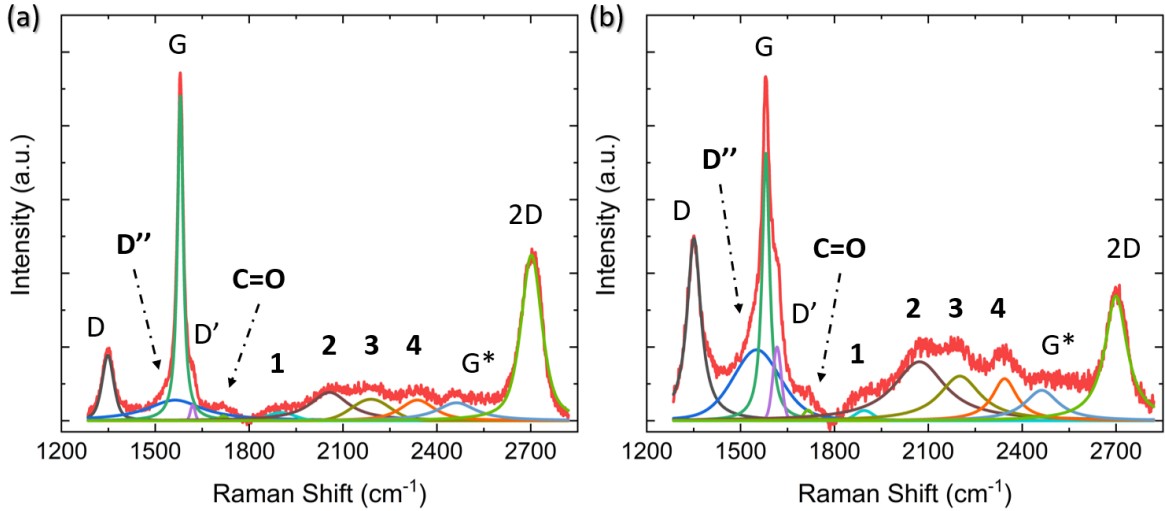
Figure 3.9: Raman spectra of functionalized GNS in (a) NMP and in (b) DMF. The fit of each spectrum is shown and all peaks are labeled (the peaks that appear only after the functionalization of GNS by 1,3–DC of azomethine ylide are in bold).

The Raman spectra of functionalized GNS exhibit new features and modifications, as shown in Figure 3.9. The intensity of the D peak substantially decreases. The ratio between D and G intensities is a benchmark for the grain size and the defect concentration.[159,160] The ratio $I(D)/I(G)$ passes from an initial value of 1.02 for pristine GNS in NMP to a final value of 0.20 for functionalized GNS in NMP. Similarly $I(D)/I(G)$ decreases from 1.01 to 0.68 for GNS in DMF. The decrease of $I(D)/I(G)$ can be explained considering that the azomethine ylides are grafting onto graphene's most favorable bonding sites, which are in the defected areas of the lattice, possibly leading to a local structural relaxation and a decrease in the Raman intensity of the defects. Considering that the GNS lateral size is comparable with the Raman laser spot ($\sim 1\ \mu$m), the initial high intensity of the D peak before the functionalization also derives from the high density of edge defects, which are passivated by the presence of the azomethine ylides after the functionalization, leading to a decrease of the intensity of the D peak. Observing the 2D peak, its intensity remains almost constant, with $I(2D)/I(G)$ slightly changing from 0.53 to 0.51 for GNS in NMP and from 0.49 to 0.47 for GNS in DMF. This behavior of the 2D peak confirms that the long–range order of the graphene lattice is maintained, and that we are not introducing some strong disorder towards amorphous graphene. A further sign of the successful functionalization of GNS is the rise of a new broad peak centered at 1548 cm^{-1} for GNS in NMP and at 1545 cm^{-1} for GNS in DMF. This band, called D" and usually seen in the range 1500 – 1550 cm^{-1}, is thought to be related to either the amorphous phase (increasing with the decrease of crystallinity)[161] or to interstitial defects associated with the functionalization with small molecules.[162–164] As aforementioned, the constant intensity of the 2D peak suggests that we are not inducing an amorphous phase, while the functionaliza-

tion with azomethine ylide would explain the creation of interstitial defects. Moreover, the peak centered at 1717 cm^{-1} for GNS in NMP and at 1716 cm^{-1} for GNS in DMF is usually assigned to the presence of the C=O functional group,[165] and would reasonably arise from the carboxyl group of the azomethine ylide. Finally, a set of four new peaks appears, which are labeled here as 1, 2, 3, and 4, centered respectively at around 1902 cm^{-1}, 2057 cm^{-1}, 2190 cm^{-1}, and 2338 cm^{-1} for GNS in NMP and at 1895 cm^{-1}, 2072 cm^{-1}, 2201 cm^{-1}, and 2343 cm^{-1} for GNS in DMF. These peaks are located in a region which is usually silent in Raman spectroscopy, and remarkably their positions do not significantly change with the change of the solvent. Hence, we tentatively attribute these peaks to Raman–active features of the azomethine ylide. This will be discussed in more detail in Section 3.6. Lastly, the G* peak is slightly visible also in the spectra of functionalized GNS, centered at 2463 cm^{-1} for GNS in NMP and at 2459 cm^{-1} for GNS in DMF. Table 3.2 summarizes the position and the appearance of all peaks, both for pristine and functionalized GNS in NMP and in DMF.
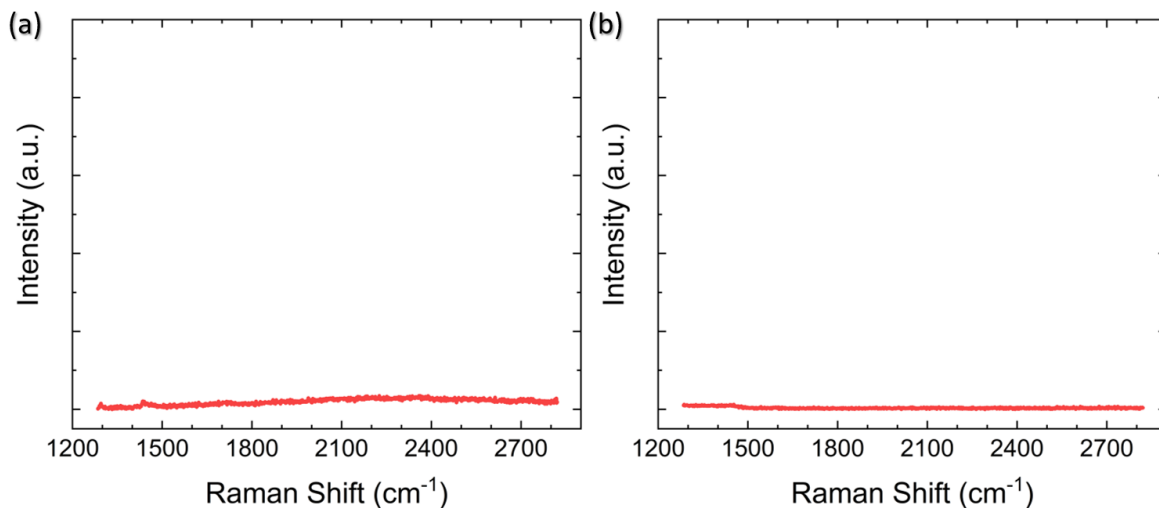
Figure 3.10: Raman spectra of residuals of (a) NMP and (b) DMF after drying under vacuum (same intensity scale of Figure 3.9).

Finally, in order to properly assign the Raman features that arise from the functionalization by 1,3–DC of azomethine ylide, Raman spectroscopy was performed also on residuals of NMP and DMF (see Figure 3.10). Both solvents were dropcasted on clean substrates, which were then dried under vacuum, and analyzed. Noticeably, the intensities of the spectra are evidently small, with respect to the intensities of the spectra of pristine and functionalized graphene. No characteristic peaks are present in the intermediate zone of the spectrum, where peaks 1 – 4 were detected on functionalized GNS and rGO. This result confirms that this set of new peaks originates from the azomethine ylide and not from the solvents.

Table 3.2: Presence (•) and position of the peaks from the fitting of the Raman spectra of pristine and functionalized GNS in NMP and in DMF.

GNS in NMP	D	D''	G	D'	C=O	1	2	3	4	G*	2D
pristine	•		•	•						•	•
position [cm^{-1}]	1346		1581	1620						2460	2695
error [cm^{-1}]	±1		±1	±1						±2	±1
functionalized	•	•	•	•	•	•	•	•	•	•	•
position [cm^{-1}]	1349	1563	1580	1620	1717	1902	2057	2190	2338	2463	2702
error [cm^{-1}]	±1	±3	±1	±2	±2	±6	±10	±10	±5	±3	±1

GNS in DMF	D	D''	G	D'	C=O	1	2	3	4	G*	2D
pristine	•		•	•						•	•
position [cm^{-1}]	1346		1581	1620						2463	2695
error [cm^{-1}]	±1		±1	±1						±2	±1
functionalized	•	•	•	•	•	•	•	•	•	•	•
position [cm^{-1}]	1351	1552	1581	1617	1716	1895	2072	2201	2344	2459	2700
error [cm^{-1}]	±1	±3	±1	±1	±3	±5	±6	±3	±3	±3	±1

3.5 Raman spectra of pristine and functionalized rGO

Raman investigation was also performed on pristine and functionalized rGO, after drop-casting onto a silica substrate (see Figure 3.7(c)) and drying under vacuum. Figure 3.11 shows the Raman spectra, which were collected in three overlapping regions (lower, intermediate, and higher) in order to allow a more detailed comparison. Because of the initial presence of oxygen functional groups in graphene oxide (GO) and the subsequent chemical reduction process, rGO presents several defects in its structure.[147,166] This leads to the broadening of the characteristic D and G bands of graphene, here centered at 1345 cm^{-1} and 1595 cm^{-1}, as shown in Figure 3.11(a). Of fundamental interest is the broad valley between the two peaks, which has been reported for carbon–based materials and rGO.[162,164,167] By deconvolution we can identify three additional peaks, centered at 1240 cm^{-1}, 1515 cm^{-1}, and 1621 cm^{-1}.
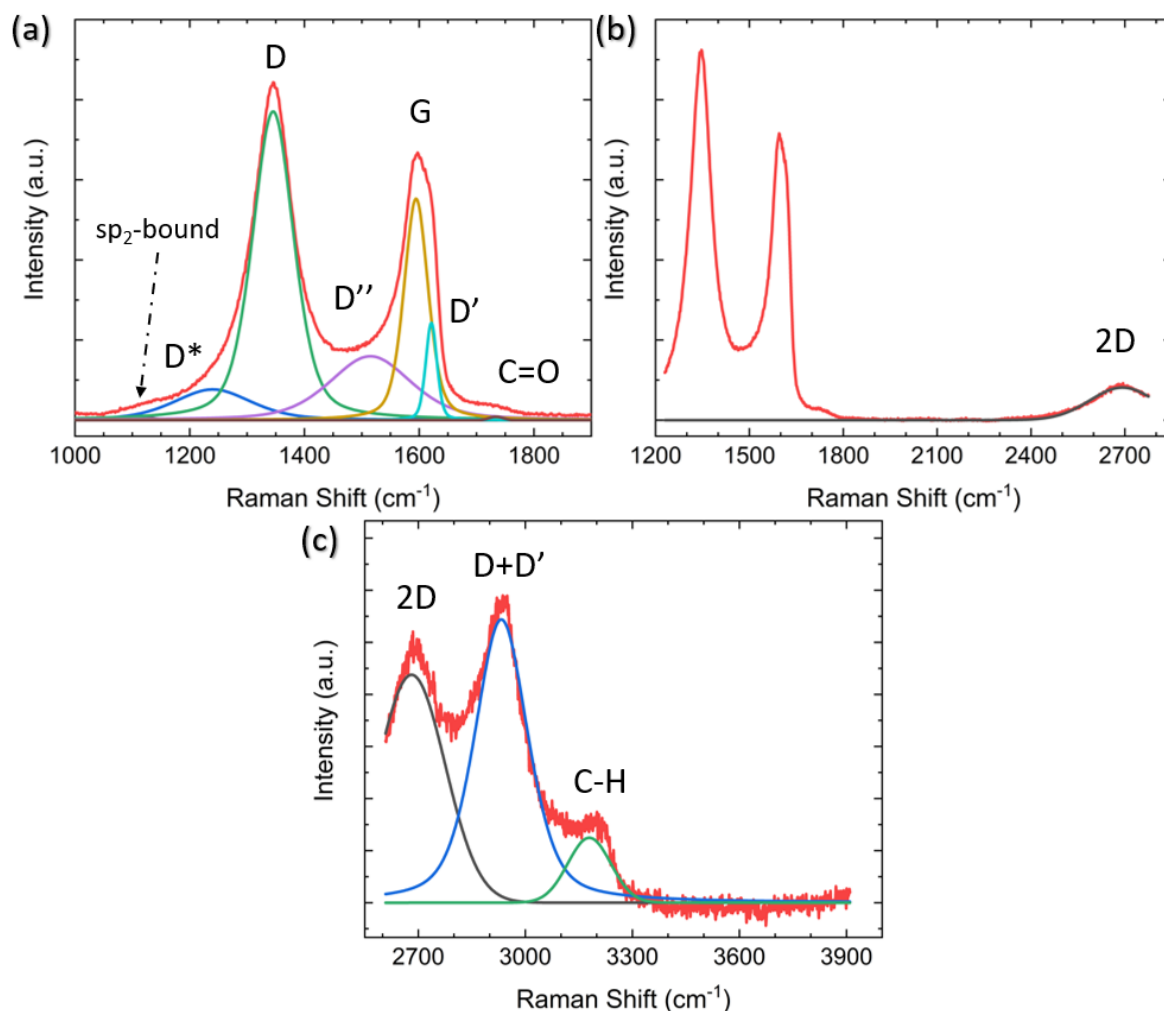
Figure 3.11: Raman spectra of pristine rGO taken in the (a) lower, (b) intermediate, and (c) higher region of Raman shift.

The first peak, usually called D*, can be related to disordered graphitic lattices provided by sp^2–sp^3 bonds at the edges of networks,[162] whereas the second peak can be identified as the D" band and the last one as the D' band. While in pristine GNS

the D" peak is not present, here its appearance can be explained by the presence of a number of C sp^3 bonds from residual functional groups already present in the rGO structure before the functionalization. Correspondingly, the band centered at 1734 cm^{-1} can be attributed to the presence of C=O functional groups. Moreover, a weak band centered at 1108 cm^{-1} is visible. A similar peak around 1150 cm^{-1} has been reported in nanocrystalline diamond to be due to the sum and difference modes of sp^2 C=C and C–H vibrations of trans–polyacetylene–type segments occurring at grain boundaries.[168] Likewise, a peak around 1130 cm^{-1} has been observed arising from the edges and holes of GO flakes which present similar H–ending C=C chains.[169] We use here the same nomenclature, labeling it as sp^2–bound. As expected, in higher disorder graphene[170] the intensity of the 2D band decreases and broadens, as observed in Figure 3.11(b). At higher Raman shift values (see Figure 3.11(c)), besides the 2D band centered at 2681 cm^{-1}, the D+D' combination band is visible, centered at 2933 cm^{-1}. Finally, we can assign the peak centered at 3179 cm^{-1} to the C–H stretching mode.[169]
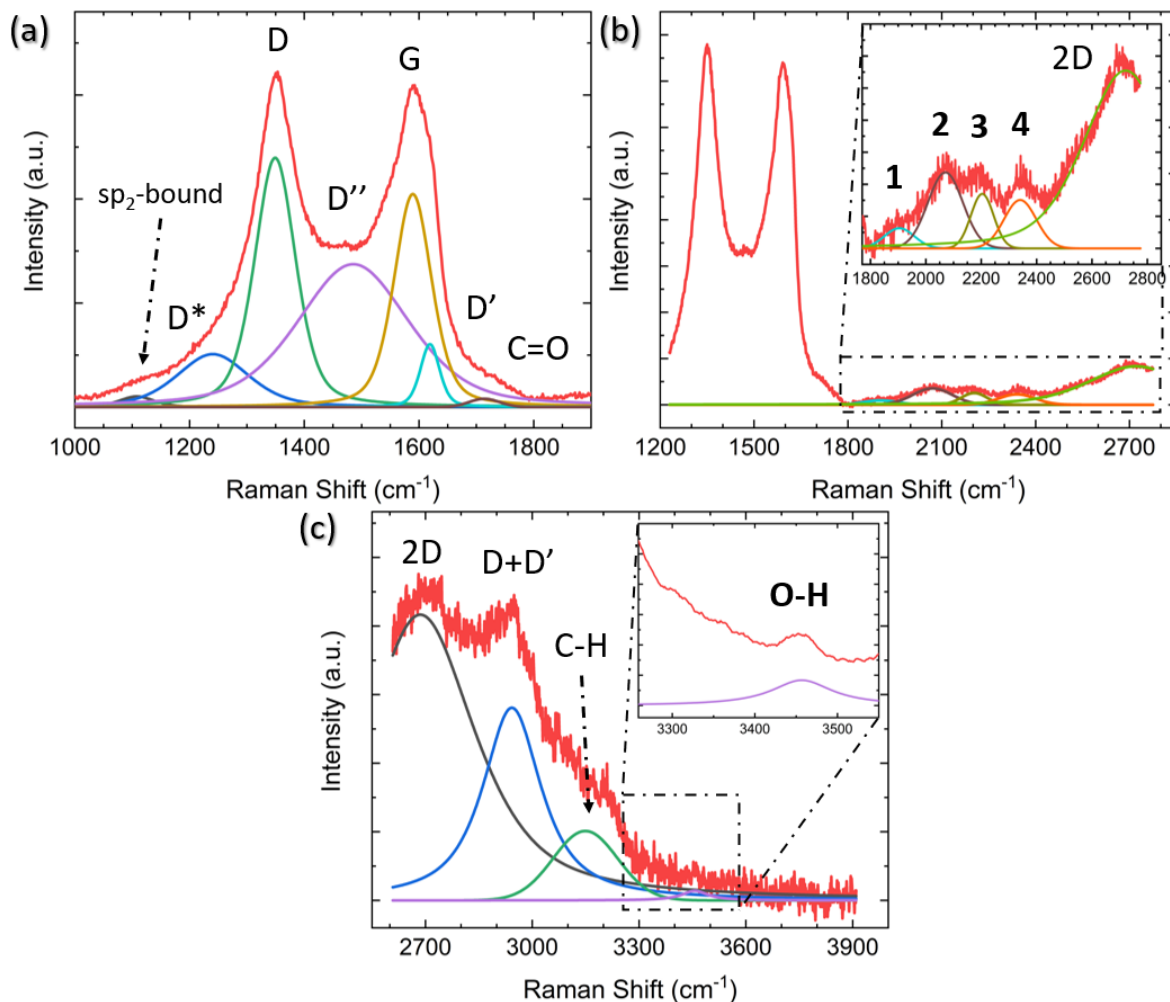
Figure 3.12: Raman spectra of functionalized rGO taken in the (a) lower, (b) intermediate (zoom is shown in the inset), and (c) higher region (zoom, where a smoothing of the signal was performed, is shown in the inset) of Raman shifts. The fit of each spectrum is shown and all peaks are labeled (the peaks that appear only after the functionalization of rGO by 1,3–DC of azomethine ylide are in bold).

The Raman spectrum of functionalized rGO shows new and interesting features

(see Figure 3.12). As already seen for functionalized GNS, the intensity of the D peak decreases (as shown in Figure 3.12(a)), and the $I(D)/I(G)$ ratio passes from 1.39 to 1.17 after the 1,3–DC of azomethine ylide. Likewise, $I(D')/I(G)$ decreases from 0.44 to 0.29. Furthermore, the intensity of the D" peak increases, with $I(D")/I(G)$ moving from 0.29 before to 0.67 after the 1,3–DC, indicating the functionalization due to the presence of azomethine ylides. It is interesting to notice that also the intensity of the Raman signal from the C=O group increases. As shown in Figure 3.12(b), the same set of four peaks (1 – 4) arises in the Raman spectrum after the functionalization. Similarly to what we see in functionalized GNS, peak 1 is centered at 1904 cm^{-1}, peak 2 at 2071 cm^{-1}, peak 3 at 2204 cm^{-1}, and peak 4 at 2341 cm^{-1}. In the region of higher Raman shift, shown in Figure 3.12(c), the decrease of the intensity of the D+D' peak is clearly visible, explicable with the corresponding decrease of the D and D' intensities. Finally, a new weak band centered at 3457 cm^{-1} appears. This peak can be attributed to the O–H stretching[171] of the carboxyl or the catechol groups in the azomethine ylide, and to our knowledge this is the first time it is seen in functionalized graphene. Table 3.3 summarizes the position and the appearance of all peaks, for both pristine and functionalized rGO.

Significantly, the appearance of the peaks 1 – 4 is in complete agreement between functionalized GNS in NMP and in DMF and functionalized rGO in DMF. Moreover, the exact correspondence of the positions of the peaks 1 – 4 within error intervals is noteworthy. This result corroborates the conclusion that these peaks do not originate from the solvents (same position in NMP and in DMF) or the substrate (same position for GNS and rGO), but arise from the functionalization with the azomethine ylide.

Finally, acquiring Raman spectra in a lower Raman shift region, the broad shoulder [950 – 1050] cm^{-1} coming from the Si signal of the substrate is clearly detected in the Raman spectra of both functionalized GNS and rGO (see Figure 3.13).
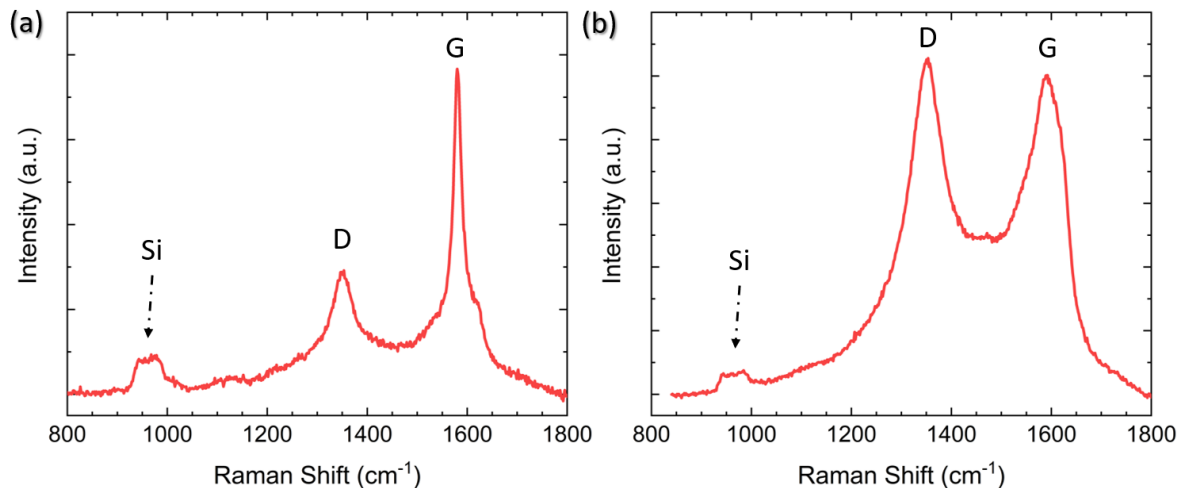
Figure 3.13: Raman spectra of functionalized (a) GNS in DMF and (b) rGO in DMF. The shoulder arising from the Si signal of the substrate is indicated by an arrow.

Table 3.3: Presence (•) and position of the peaks from the fitting of the Raman spectra of pristine and functionalized rGO in DMF.

rGO in DMF	sp^2–bound	D*	D	D"	G	D'	C=O
pristine	•	•	•	•	•	•	•
position [cm^{-1}]	1108	1240	1345	1515	1595	1621	1722
error [cm^{-1}]	± 10	± 2	± 1	± 3	± 1	± 2	± 5
functionalized	•	•	•	•	•	•	•
position [cm^{-1}]	1108	1241	1349	1486	1589	1619	1714
error [cm^{-1}]	± 4	± 2	± 1	± 2	± 1	± 2	± 4

rGO in DMF (cont'd)	1	2	3	4	2D	D+D'	C–H	O–H
pristine					•	•	•	
position [cm^{-1}]					2681	2933	3179	
error [cm^{-1}]					± 2	± 1	± 2	
functionalized	•	•	•	•	•	•	•	•
position [cm^{-1}]	1904	2071	2204	2341	2686	2943	3149	3457
error [cm^{-1}]	± 5	± 6	± 4	± 3	± 1	± 1	± 3	± 5

3.6 Computational simulations

In order to deepen our understanding of the functionalized graphene after 1,3–DC of azomethine ylide, models for pristine and functionalized rGO were built. Pristine rGO was modeled by positioning 10 oxygen atoms on top of randomly chosen carbon atoms, followed by structural minimization (as described in detail in Section 2.11). Functionalized rGO was modeled by adding the azomethine ylide in the central area of the rGO structure, followed by structural minimization. Functionalized rGO appears mildly corrugate, with a final morphology depending on the position of the epoxy groups and the azomethine ylide.
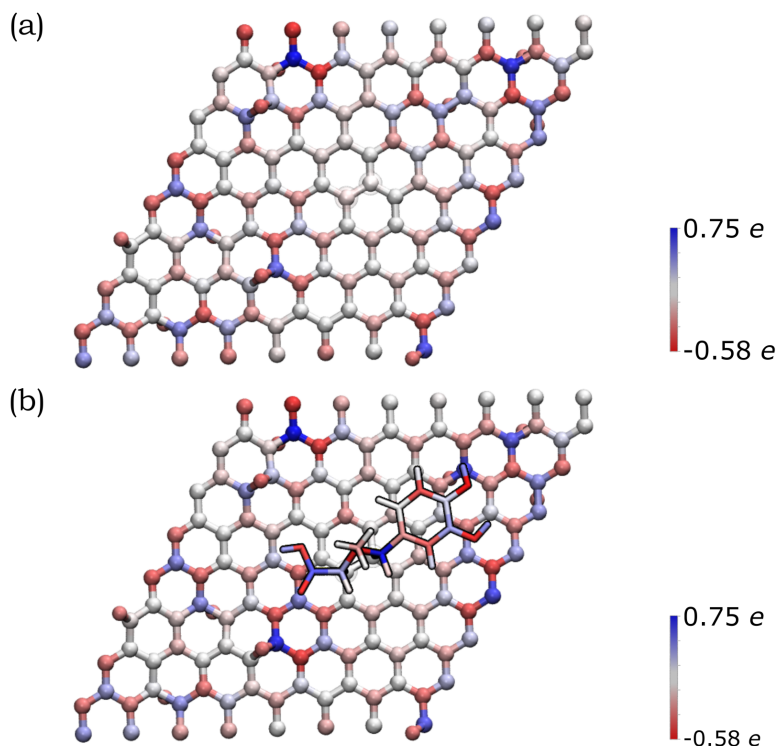
Figure 3.14: Distribution of the RESP–derived partial atomic charges reported as a color gradient for the atoms in (a) pristine rGO and (b) functionalized rGO (blue = positive, red = negative). The highest positive/negative charge values are close to the epoxy groups (that present O atoms outside the graphene plane). The amplification of the charge gradient due to the presence of the azomethine ylide is visible.

Both models were characterized by evaluating the restrained electrostatic potential (RESP) derived partial atomic charges.[148] The RESP-derived partial charges, mapping the electrostatic features of the system, highlight the localization of the charges in the pristine rGO induced by the presence of the epoxy groups. The highest positive/negative charge values are, in fact, localized in the sp^3 carbon atoms linked to the epoxy groups (blue/red in Figure 3.14(a)). The partial charge in the sp^3 atoms affects theirs neighbors, an effect that gradually decreases at longer distances. Remarkably, the presence of the azomethine ylide amplifies the localization ot the charges (see Figure 3.14(b)), demonstrating that the functionalization can modulate the distribution of

charges on the lattice, eventually favoring the further binding of additional molecules.
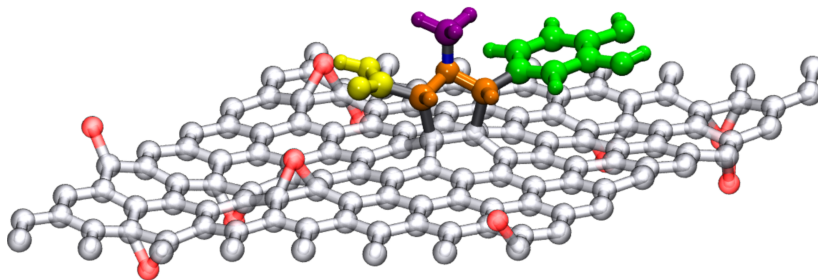
Figure 3.15: Model of the azomethine ylide attached to rGO, where the red atoms are the oxygens of the epoxy groups. The functional groups of interest are highlighted: carboxyl group = yellow, nitrogen and the connected atoms = orange, methyl group = violet, cathecol group = green.

The functionalized system was then subjected to 12 ps of molecular dynamics (MD) simulation at 300 K. During the MD simulation, the lattice did not undergo a large conformational rearrangement. The vibrational density of states has been obtained as the Fourier transform of the velocity autocorrelation function. The power spectrum was then decomposed and analyzed by computing the power spectra of the autocorrelation function of appropriate groups of atomic coordinates (highlighted in different colors in Figure 3.15), and is shown in Figure 3.16. In the intermediate region, the characteristic vibrational peak from the C=O in the carboxyl group of the azomethine ylide is visible, centered at 1730 cm^{-1}. Moreover, there is a set of four vibrational regions (labeled as 1', 2', 3', and 4' in the inset of Figure 3.16) corresponding to the C–N stretching from the nitrogen of the azomethine ylide, centered around 920 cm^{-1}, 980 cm^{-1}, 1050 cm^{-1}, and 1200 cm^{-1} respectively. If we consider the second order of these bands, we obtain four vibrational bands around (1900 ± 100) cm^{-1}, (2000 ± 100) cm^{-1}, (2100 ± 100) cm^{-1}, and (2400 ± 100) cm^{-1} (the errors are related both to the simulation and to the extension of the regions 1' – 4'). These values are consistent with the Raman features which appear in the intermediate region of both functionalized GNS and rGO. The corresponding first–order Raman bands are not visible in the experimental Raman spectra, being covered by the broad shoulder from the silicon substrate around 950 – 1050 cm^{-1} (shown in Figures 3.13). The simulated power spectrum also exhibits a vibrational band from the C–H groups of the aromatic catechol of the azomethine ylide around 2980 – 3200 cm^{-1}, in agreement with the experimental peak seen in functionalized rGO. Finally, the O–H groups of the ylide possess stretching bands around 3460 cm^{-1} and over 3650 cm^{-1}, in agreement with the result from the experimental Raman spectrum of functionalized rGO.
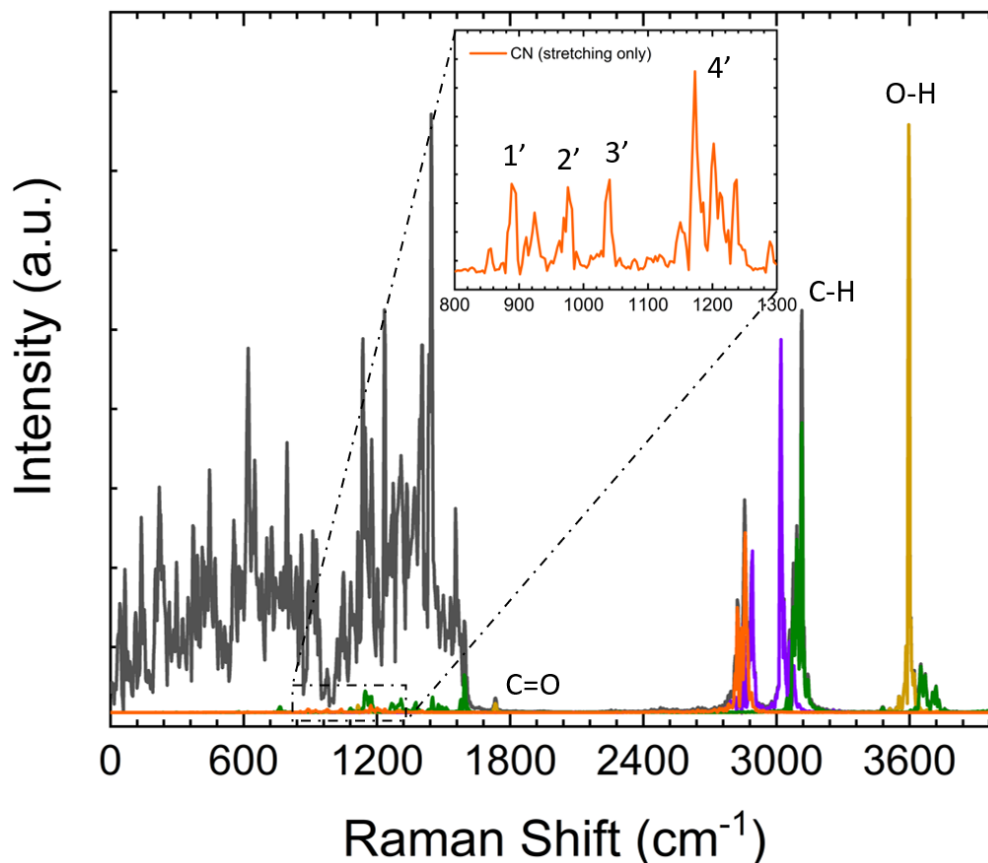
Figure 3.16: Power spectrum (PS) of the velocity autocorrelation function (black). Projections on the PS for the functional groups of interest are highlighted in the same colors of Figure 3.15. The regions of interest are labeled. The inset shows the zoom of the region where the stretching of the CN bonds are visible. It is worth to recall that the intensities of the peaks in the simulated PS do not directly correspond to the ones from the experimental Raman spectra, where additional selection rules are involved.

3.7 XPS analysis

X-ray photoelectron spectroscopy (XPS) provides a powerful and direct method for the determination of the surface elemental composition of a material. This information is crucial in order to quantify the efficiency of the functionalization, as well as the atomic abundance. Figure 3.17(a) shows the wide–range survey collected on each sample, showing the core levels of interest for the study of functionalized graphene. Here, the investigation was focused on the C 1s, N 1s, and O 1s core levels, which are related to the graphene substrate and the functionalizing material.

Pristine and functionalized GNS and rGO were dropcasted onto silica substrates, and the solvent was removed under vacuum. This procedure was repeated several times in order to achieve a homogeneous coverage of the entire surface of the substrate, allowing measurements without any signal arising from the substrate. Performing the deconvolution of the C 1s core level photoemission spectra of functionalized graphene (both GNS and rGO), we can identify five different components. Figure 3.17(b–d) shows the spectra of functionalized GNS in DMF, GNS in NMP, and rGO in DMF. The main peak centered at a binding energy (B.E.) of 284.4 eV can be assigned to the sp^2 C–C bonds of the graphene sheet, while a second weaker peak due to sp^3 C–C bonds is
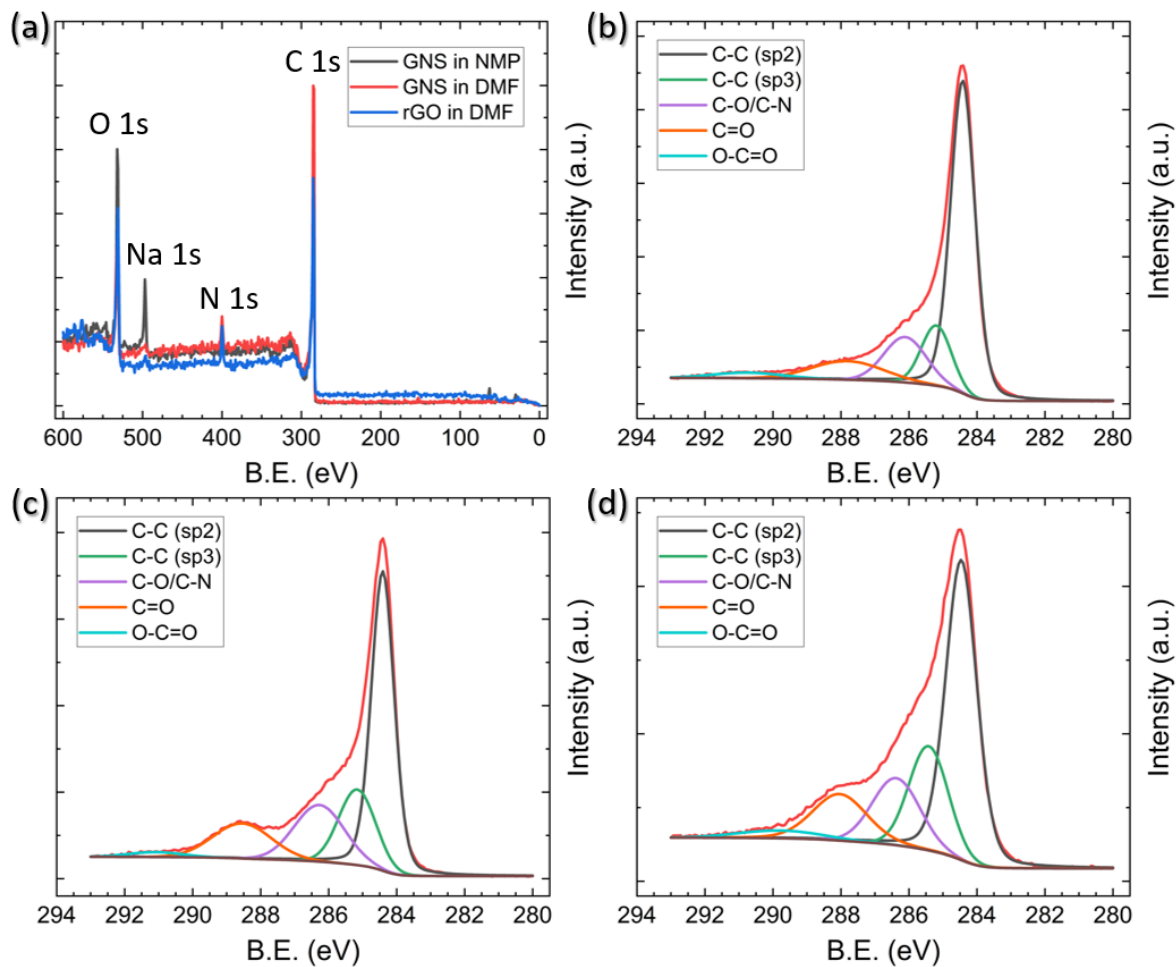
Figure 3.17: (a) XPS survey spectra (B.E. = binding energy) collected on functionalized samples. XPS spectra of the C 1s core level from functionalized (b) GNS in DMF, (c) GNS in NMP, and (d) rGO in DMF (Shirley–type background in brown).

distinguishable at 285.2 eV.[172] The additional peak arising from carbon atoms bound to oxygen (C–O) and to nitrogen (C–N) is found at 286.1 eV.[173] Finally, the contributions from C=O and O–C=O are seen at 287.8 eV and 290.8 eV, respectively.[174]

The XPS C 1s core level spectrum taken on functionalized rGO shows a higher intensity of the component of C–C sp^3, consistent with a higher degree of functionalization and a higher presence of defects in the initial structure of rGO. This is also noticeable from the comparison of the spectra (see Figure 3.18): the spectrum collected on functionalized rGO shows a broader shape with respect to the ones collected on functionalized GNS.
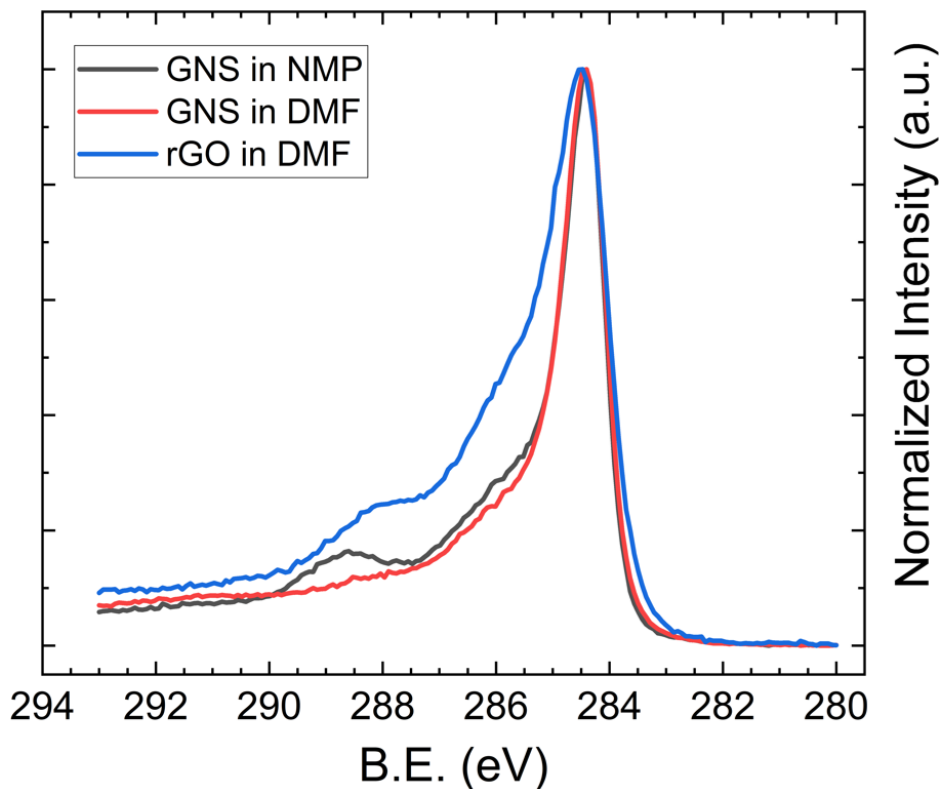
Figure 3.18: XPS spectra of the C 1s core level from functionalized GNS in NMP, GNS in DMF, and rGO in DMF. The data was normalized for better comparison of the spectra.

Further information can be derived from the N 1s core level photoemission spectra. First of all, in order to measure the B.E. of the N atoms from the solvents, pristine GNS dispersed in NMP and pristine rGO dispersed in DMF were deposited via dropcasting onto silicon substrates, following the same procedure used for functionalized samples, and then analyzed with XPS. From the fitting of the N 1s core level spectra (see Figure 3.19), the B.E. of both NMP and DMF were calculated, resulting in 400.9 eV for NMP and 400.0 eV for DMF. These components arise from the residual solvent that remains adsorbed or trapped after the dropcasting process and was not removed during the drying under vacuum. The values obtained from these preliminary experiments were then used as references in the fitting of functionalized samples.
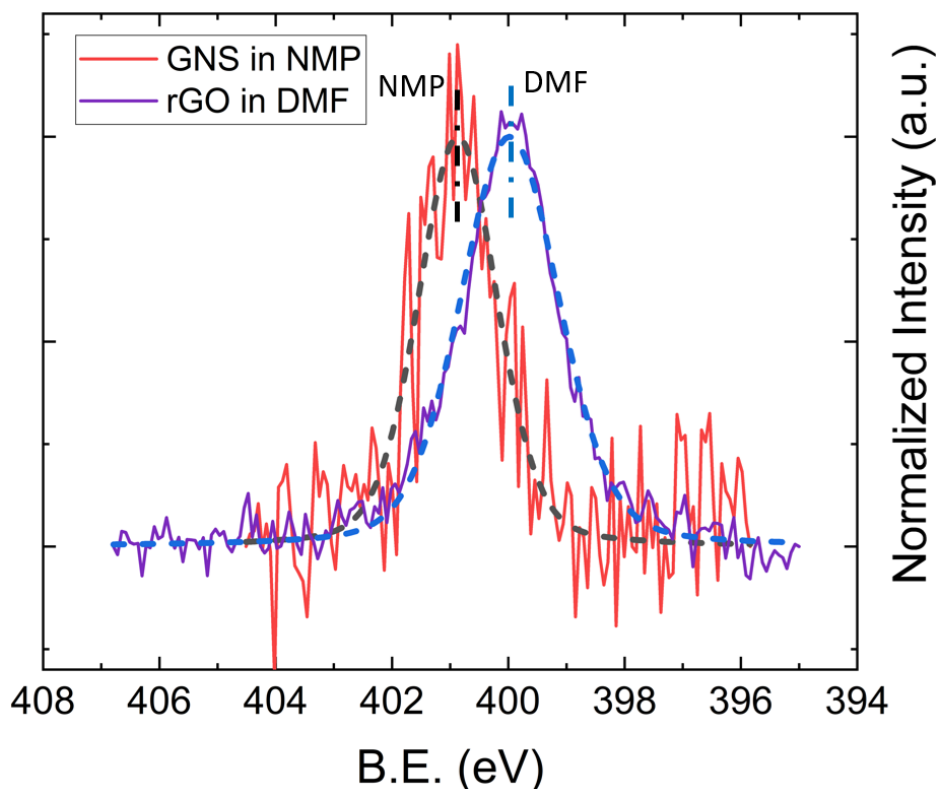
Figure 3.19: XPS spectra of the N 1s core level from pristine GNS in NMP and pristine rGO in DMF. The fit of each spectrum is shown, as well.

From the N 1s core level spectra of functionalized graphene (see Figure 3.20) we can see that all spectra display a shoulder for lower values of the B.E. which can be assigned to the peak coming from the N atom of the azomethine ylide. This peak is always centered at around 398.8 eV. The principal peaks seen in the N 1s spectra are identified as coming from the N atoms of the solvents and their presence is related to the specific sample preparation procedure for XPS. Indeed, Raman analysis has never shown peaks related to the solvent.

Comparing the N 1s core level spectra acquired after annealing of functionalized GNS in DMF at 90 °C, 130 °C, and 180 °C, the decrease of the intensity of the peak centered around 400.1 eV (black dash line in Figure 3.21) indicates the desorption of the solvent. Remarkably, the intensity of the peak arising from the azomethine ylide (green dash line in Figure 3.21) remains almost constant, validating the stability of the functionalization. The isolated peak centered at 403.7 eV, visible only in functionalized
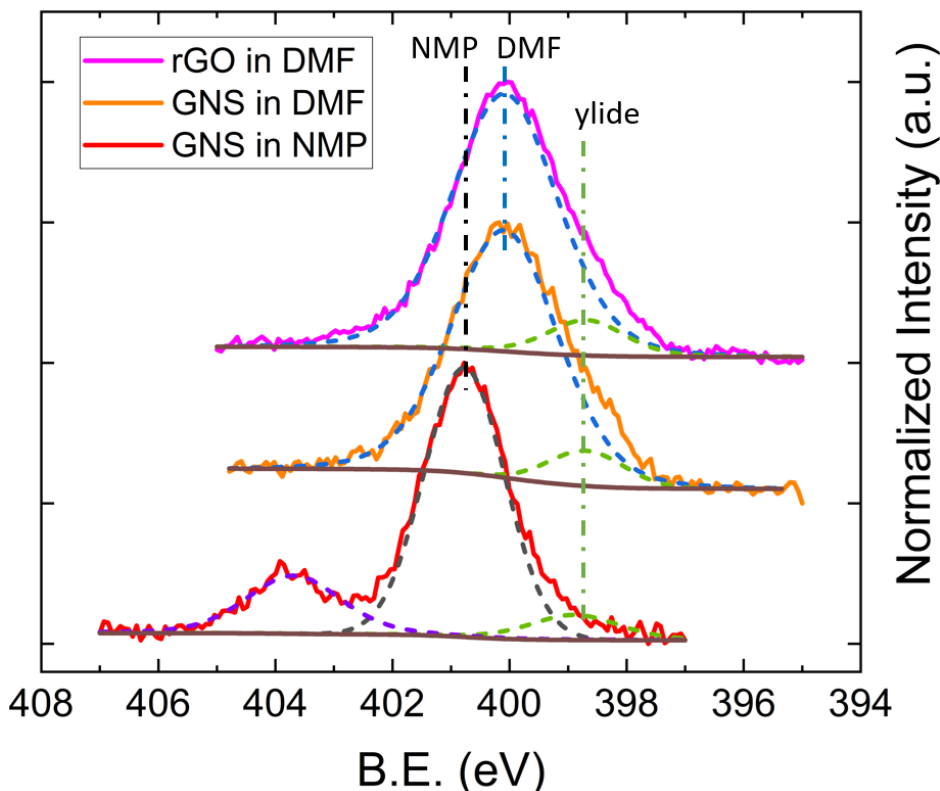
Figure 3.20: Normalized XPS spectra of N 1s core levels of functionalized GNS in NMP, GNS in DMF, and rGO in DMF (shifted in height). The different positions of the peak related to the solvent are labeled (dashed black line for NMP, dashed blue line for DMF), together with the constant position of the peak from the ylide (dashed green line). Each fit is shown by a dashed line, with a Shirley–type background in brown (the spectrum of functionalized GNS in NMP shows an additional signal arising from $NaNO_2$, and its fit is shown as dashed violet line).

GNS in NMP (see Figure 3.20), derives from the NO_2 (from partial degradation of the NMP solvent) bonded to Na (added to lower the acidity of the environment, as explained in details in Section 2.3.1), and disappears after annealing at 180 °C.[175] After the annealing at 90 °C the B.E. of both the solvent and the ylide shift towards higher value (by the same amount of 0.3 eV), and then remain the same after the successive annealing experiments. Similarly, also the other core level peaks shift to higher B.E. after the first annealing. This shift of the entire spectrum possibly indicates a shift in the Fermi level of the system after the annealing at 90 °C, which probably arises from the desorption of a little quantity of water which was adsorbed from the environment. In fact, it is know that water can induce doping in graphene samples on silica substrates.[176] Moreover, in vacuum water desorbs below 100 °C and, therefore, is reasonable to expect the residual humidity to desorb after the first annealing at 90 °C. In order to properly assess the cause of this shift, however, further measurements would be required.

Finally, the O 1s core level photoemission spectra of functionalized graphene are shown in Figure 3.22. From the spectrum taken on functionalized GNS in NMP, the overlapping of the KLL Na Auger can be distinguished (as aforementioned, Na is used as base in the reaction procedure of the 1,3–DC). From the spectrum collected on functionalized rGO, the peak originating from O–H bonding is noticeable, as a result
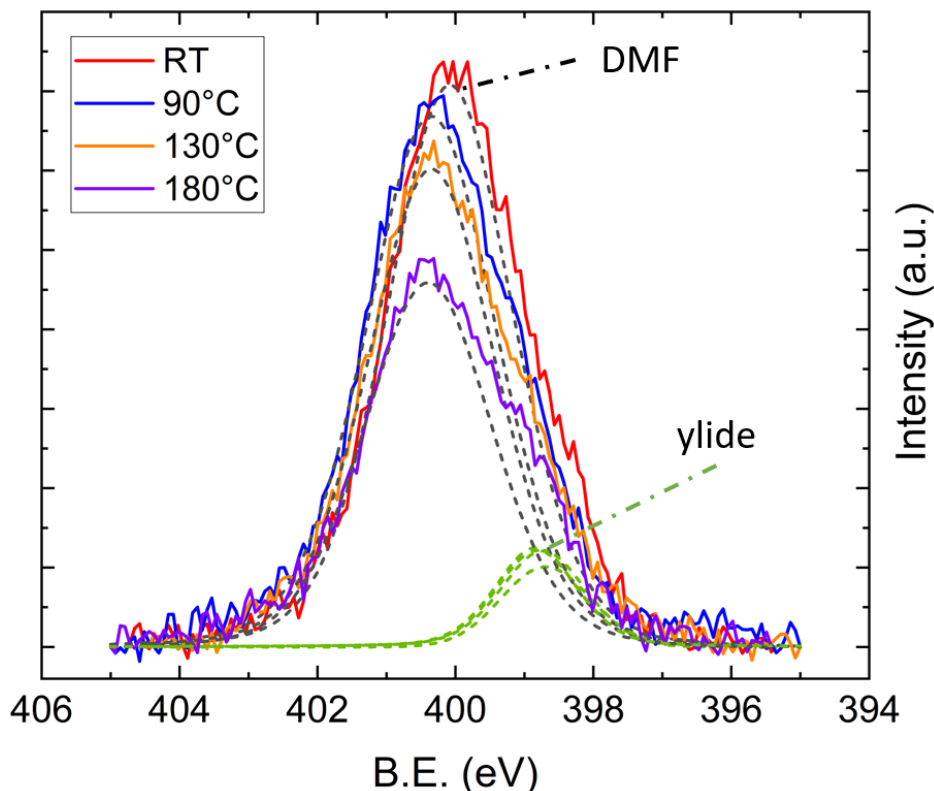
Figure 3.21: XPS spectra of the N 1s core level from functionalized GNS in DMF at room temperature, and after annealing at 90 °C, 130 °C, and 180 °C. The fit of each spectrum is shown, as well (peak from DMF in black dashed line, peak from the ylide in green dashed line).

of the higher abundance of this functional group already in the initial structure of rGO.

From the intensities of the C 1s, N 1s, and O 1s spectra, we can calculate the elemental abundances after the 1,3–DC of azomethine ylide, which are presented in Table 3.4. As expected, the oxygen abundance in functionalized rGO is higher than in functionalized GNS, deriving from the fact that pristine rGO already contains around 13% of O (data from the supplier). The data in Table 3.4 also provide an estimation of the efficiency of the functionalization, resulting in the presence of 1 azomethine ylide every ~ 225 carbons in case of GNS in NMP, 1 ylide every ~ 170 carbons for GNS in DMF, and 1 ylide every ~ 110 carbons for rGO in DMF. A higher degree of functionalization for GNS in DMF is consistent with the fact that DMF is a better organic solvent for the reaction process, having a superior capability to stabilize the reaction intermediate, with respect to NMP. The higher coverage of ylides in rGO is attributed to the higher presence of defects in its graphene–like surface, which increases the number of favorable binding positions for the azomethine ylide. As shown in the RESP–derived charge map, the epoxy groups in the pristine structure affect the electronic distribution, providing localized partial charges in the pristine rGO which favor the 1,3–DC.
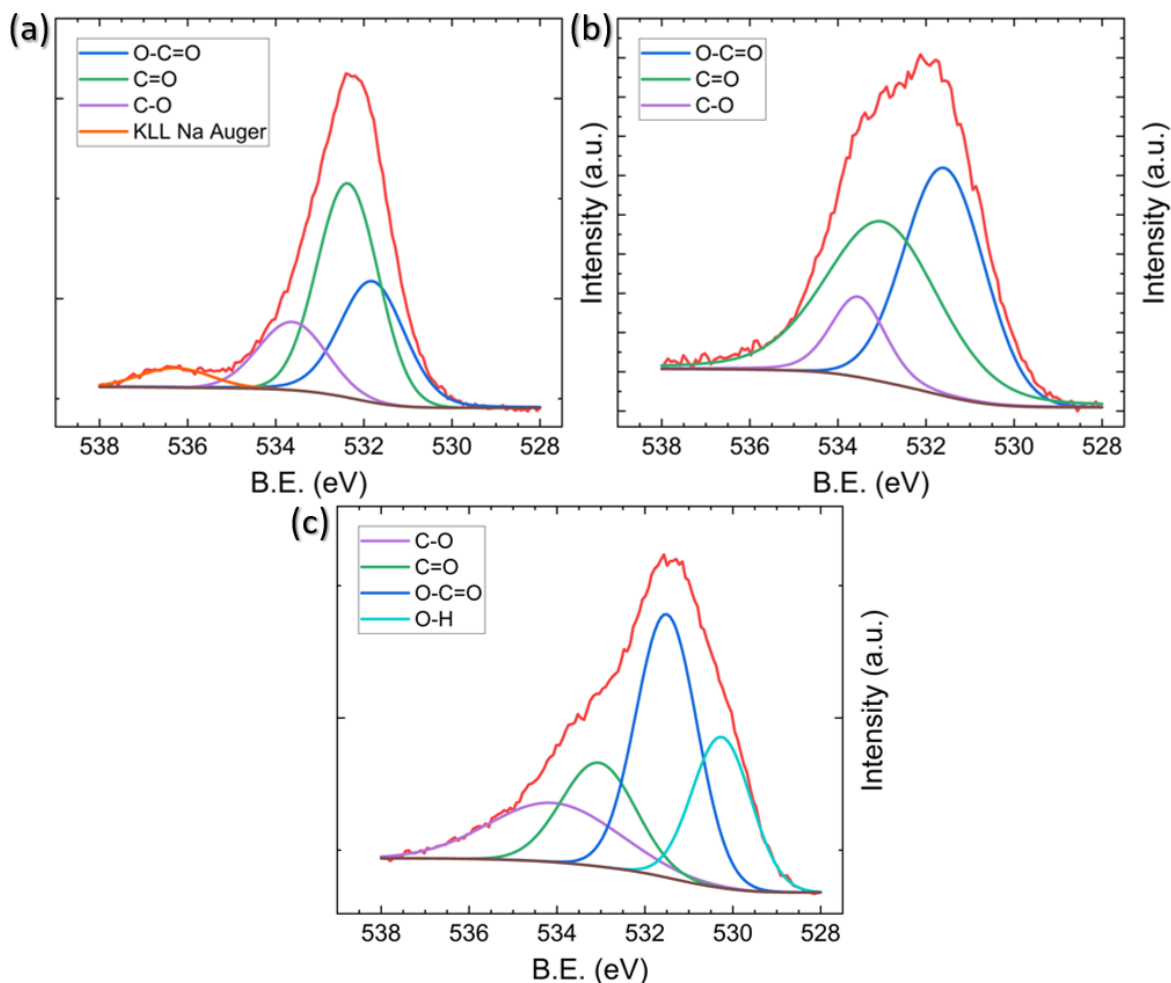
Figure 3.22: XPS spectra of the O 1s core level from functionalized (a) GNS in NMP, (b) GNS in DMF, and (c) rGO in DMF. The fit of each spectrum is shown, as well (Shirley–type background in brown).

3.8 Conclusions

In this initial experiment we have successfully functionalized graphene via 1,3–dipolar cycloaddition of azomethine ylide. For the first time, a comparison of the efficiency of this reaction in different dispersant solvents is provided. Even if the dispersion capability of NMP for graphene is slightly higher, the reaction proceeds more efficiently in DMF, allowing a greater organic functionalization of graphene in the liquid phase. To begin with, the functionalization was confirmed by detecting the presence of nitrogen in functionalized graphene with XPS, EDX, and EELS measurements. New Raman features arising from the functionalization with azomethine ylide were detected both in functionalized GNS and in functionalized rGO, and were assigned with the help of DFT simulations of the vibrational power spectrum of functionalized graphene. Thanks to the local inhomogeneity of the partial charges, due to the presence of oxygen functional groups in the pristine structure, a higher functionalization was achieved on rGO. This validates the interest in further exploring the possibility to control the position and the nature of defects, towards a precise building up of specific nanostructures, by exploring the design of the organic functionalization. Further chemical modifications of the functionalized graphene could be implemented by activating the carboxyl group of the

Table 3.4: Elemental composition of functionalized GNS and rGO, calculated from the XPS intensities.

	C [%]	N(ylide) [%]	N(solvent) [%]	O [%]
GNS in NMP	80.2	0.34	3.7	15.7
GNS in DMF	82.1	0.45	4.6	12.8
rGO in DMF	72.6	0.60	5.4	21.4

azomethine ylide, with N-hydroxysuccinimmide for example, which would allow the binding of linker molecules and additional functional groups. Moreover, the efficiency of 1,3–DC of azomethine ylide suggests its use in future organic functionalization of higher quality graphene systems, like exfoliated flakes or epitaxial monolayer samples, where the controlled use of defect engineering would allow the realization of tailored devices starting from a performing substrate, in terms of transport properties. These results have been published in *Nanoscale Advances – RSC* (see Ref. 177) and open the route for a wider range of applications, such as electrochemical devices for gas sensing or storage, enzymatic essays, catalysis, or protein interaction. Some of these aspects will be explored in the following Chapters.

Defect Engineering of Monolayer Graphene Flakes via Electron Beam Irradiation

<div style="text-align: right; color: #aa3322; font-size: 3em;">4</div>

Chemical, mechanical, thermal and/or electronic properties of bulk or low–dimensional materials can be engineered by introducing structural defects to form novel functionalities. When using particle irradiation, these defects can be spatially arranged to create complex structures, like sensing circuits, where the lateral resolution of the defective areas plays a fundamental role.

Here, we show that structural defects can be patterned by low–energy electrons in monolayer graphene sheets with lateral resolution strongly defined by the surface of the supporting substrate. In particular, we present that surface treatments of the substrate supporting graphene sheet play a key role in improving the lateral resolution of defective regions induced by low–energy electron beam irradiation (EBI). Two–dimensional micro–Raman mapping reveals that unintentional defects are created in the surroundings of the exposed areas, whose extension and density strongly depend on the used surface cleaning method. Monte Carlo simulations point out that these defects are produced by the back–scattered electrons (BSEs) and by the interaction of the secondary electrons (SEs) generated near the substrate surface by BSEs with organic impurities (for instance hydrocarbons) that are adsorbed on silicon/silicon dioxide (Si/SiO$_2$) substrate, as shown by the full agreement between simulation and experimental data.

4.1 Defect introduction and analysis

Before electron irradiation, the initial conditions of as–exfoliated graphene resulted in negligible intrinsic defects density (absence of Raman mode D, see black line in Figure 4.1(a)). When irradiating a part of the graphene sheet with electrons of 30 keV (violet area in the inset of Figure 4.1(a), 4 μm long and wider than the graphene flake), D and D' peaks clearly appear in the Raman spectrum (violet line in Figure 4.1(a)), unambiguously indicating the lattice symmetry breaking.[131] In particular, the ratio between the intensity of D and G peaks ($I(D)/I(G)$) quantifies the defect density in the sampled area.[159,160,178,179]
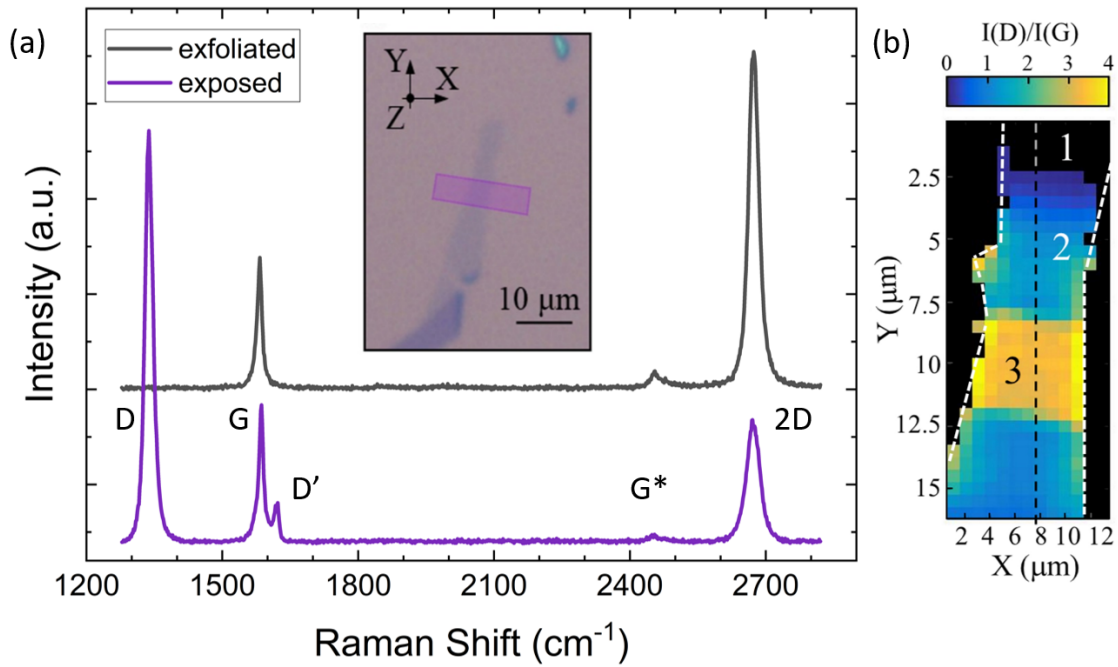
Figure 4.1: (a) Representative Raman spectra of as–exfoliated (black curve) and e–beam exposed graphene (violet curve) on a no–plasma–treated substrate, shifted in height for clarity. The inset is the optical image of the graphene flake, where the violet area indicates the exposed area. In both spectra also the G* peak is visible. The electron kinetic energy is 30 keV and the dose is 40 mC/cm². (b) Two–dimensional spatial distribution of $I(D)/I(G)$. The white dashed lines indicate the flake edges. Zone 1 is the unexposed area; zone 2 is the transition area; zone 3 is the irradiated region.

Figure 4.1(b) shows the spatial distribution of $I(D)/I(G)$ estimated across the graphene flake on a no–plasma–treated substrate after irradiation with electrons of 30 keV and a dose $\sim$ 40 mC/cm² (as presented in detail in Section 2.5, the surface of no–plasma–treated substrates was cleaned only by e–beam resist residue removal solution). As expected, $I(D)/I(G)$ reaches the maximum value ($\sim$ 3.5) in the region exposed to the electron beam (zone 3), while it drops to zero in the unexposed area (zone 1). Assuming the model proposed in Ref. 178, the measured $I(D)/I(G)$ value in zone 3 corresponds to a density of defects of about 7×10^{11} cm^{-2}. Interestingly, the transition between zone 1 and zone 3 is not abrupt, but a region containing non–zero $I(D)/I(G)$ values exists in between (zone 2). As shown in the averaged profile along the Y–axis (Figure 4.2), $I(D)/I(G)$ assumes a constant value ($\sim$ 1.5) in the first 2 μm from the edge of the irradiated area, and then monotonically decreases to zero. This

transition area has an overall extension of about 5 μm and is homogeneously distributed along the X–axis (see inset in Figure 4.2).
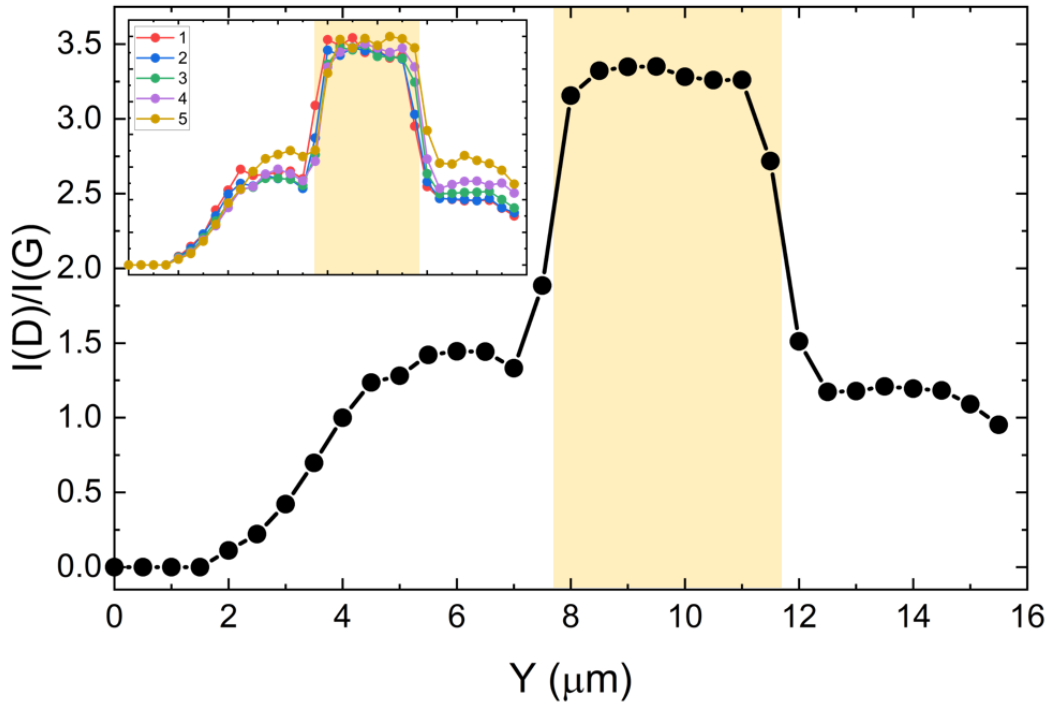
Figure 4.2: Averaged $I(\mathrm{D})/I(\mathrm{G})$ profile along the Y–axis calculated from the 5 profiles extracted along the reference line (black dashed line in Figure 4.1(b)) shown in the inset. The yellow area indicates the irradiated area. The solid line is a guide to the eye.

Graphene irradiated at 20 keV with the same dose shows similar behavior: the presence of an area with monotonic decrease of $I(\mathrm{D})/I(\mathrm{G})$ to zero that is followed by an almost constant $I(\mathrm{D})/I(\mathrm{G})$ zone (Figure 4.3(a)). Unlike 30 keV, irradiation with 20 keV–electrons generates a transition area having much smaller extension (about 2.5 μm), while the irradiated zones have comparable $I(\mathrm{D})/I(\mathrm{G})$ values. A different evolution was observed when exposing graphene to a 200 mC/cm^2 dose at 30 keV, as shown in Figure 4.3(b). As expected, a much higher $I(\mathrm{D})/I(\mathrm{G})$ value was quantified in the irradiated area due to the larger e–beam dwell time (140 ms compared to 30 ms for 40 mC/cm^2), while the transition zone expands for a longer distance (about 6 – 7 μm) compared to the smaller dose. It is worth to notice that the data for the 40 mC/cm^2 exposure in Figure 4.3(b) were acquired in a different flake compared to the one of Figure 4.2 and Figure 4.3(a). This confirms the systematic creation of similar unintentional defects in the adjacency of irradiated areas.
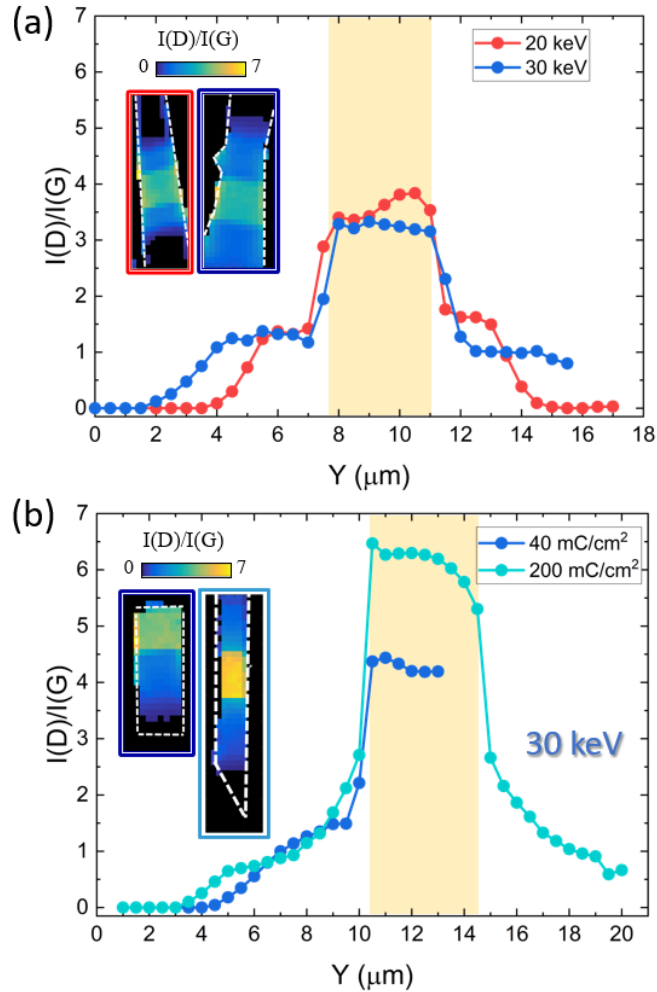
Figure 4.3: Defect dependency on irradiation conditions for graphene on a no–plasma–treated substrate: (a) averaged $I(D)/I(G)$ profile along the Y–axis after 20 keV (orange curve) and 30 keV (blue curve) EBI. (b) Averaged $I(D)/I(G)$ profile along the Y–axis as a function of the irradiation dose for electrons of 30 keV. The blue curve is for 40 mC/cm^2 and the cyan curve for 200 mC/cm^2. The yellow area in the main panel indicates the irradiated area. In both panels, insets show the spatial distribution of $I(D)/I(G)$ across the graphene flakes. The white dashed lines indicate the flake edges.

4.2 Monte Carlo simulations

Although electrons–irradiated graphene has been largely studied,[96–99] the analysis of the crystalline structure of the overexposed graphene edges has been only poorly investigated by two–dimensional mapping.[180] In order to understand the origin of the observed defects, we simulated the scattering events of primary electrons within our structure for the two used kinetic energies, as shown by the trajectories reported in Figure 4.4(a).

When multiple scattering events occur, some electrons can generate secondary electrons (SEs energy < 50 eV) and some others can be scattered back towards the surface and escape at a distance that depends on the energy of the primary electrons (with energy ~ 60 – 80% of primary energy). As a result, BSEs are laterally spread with a radial distance, i.e. the distance of the escaping position from the landing point of
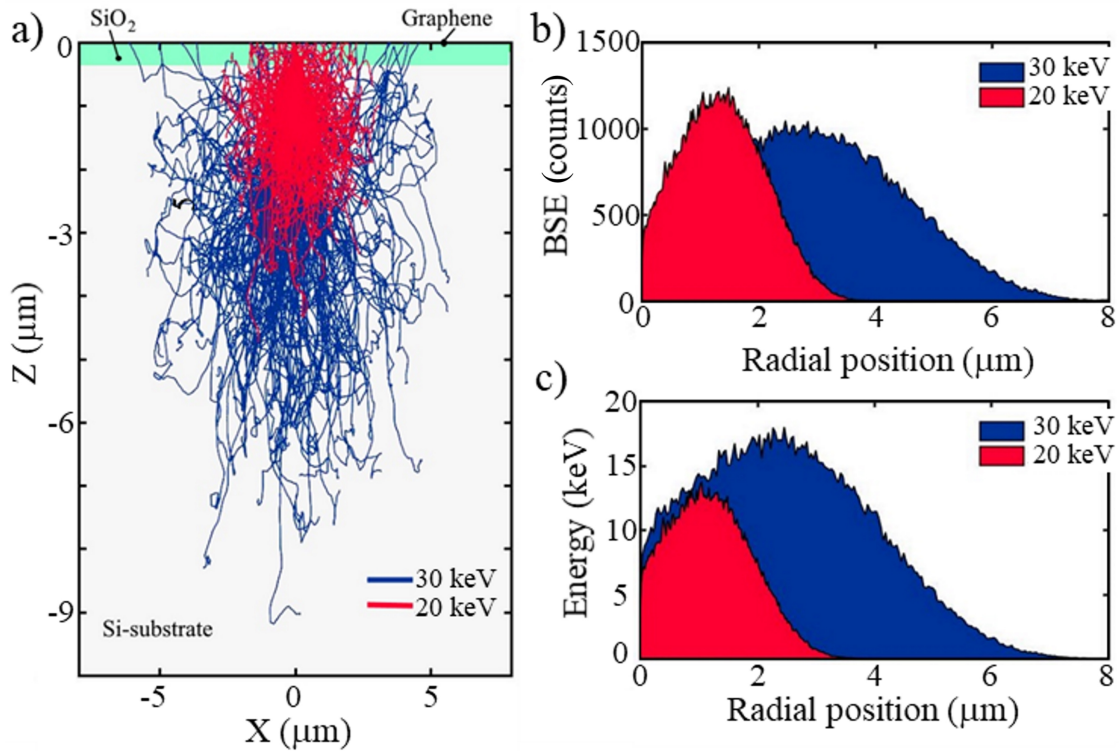
Figure 4.4: Monte Carlo simulations: (a) representative 500 trajectories of primary electrons simulated considering 8×10^5 electrons having kinetic energy of 20 keV (red curves) and 30 keV (blue curves). (b) The number of escaping BSEs and (c) the energy of BSEs as a function of the radial distance from the primary beam landing position simulated for kinetic energy of 20 keV (filled red curve) and 30 keV (filled blue curve).

the primary electrons, that can be of the order of few microns. When irradiating with kinetic energy of 20 keV, Monte Carlo simulations show that BSEs can escape at distance of the order of ~ 3 μm, while at 30 keV this distance increases up to ~ 6 μm (see Figure 4.4(b)), due to the larger penetration depth of the primary electrons (see Figure 4.4(a)). Moreover, kinetic energy of BSEs has a functional dependency on the radial distance. As shown in Figure 4.4(c), BSEs from 20 keV primary electrons have maximum kinetic energy of about 10 keV at a radial distance of about 1 μm. Instead, at 30 keV beam energy, BSEs having a maximum energy of 15 keV can escape at about 2.5 μm from the primary electrons landing point.

By comparing the radial distribution of the number and kinetic energy of BSEs with the spatial dependence of $I(D)/I(G)$ values within the transition area (zone 2), we found a very good agreement between the two distributions. As shown in Figure 4.5, for both primary electron kinetic energies, the area where $I(D)/I(G)$ has constant value corresponds to the region with the largest number of high energetic BSEs that escape from the surface. Indeed, irradiation in scanning mode implies a superposition of several BSE radial distributions, thus an almost homogeneous dose of BSEs is expected within a radial distance of ~ 1 μm and ~ 3 μm at 20 keV and 30 keV, respectively.
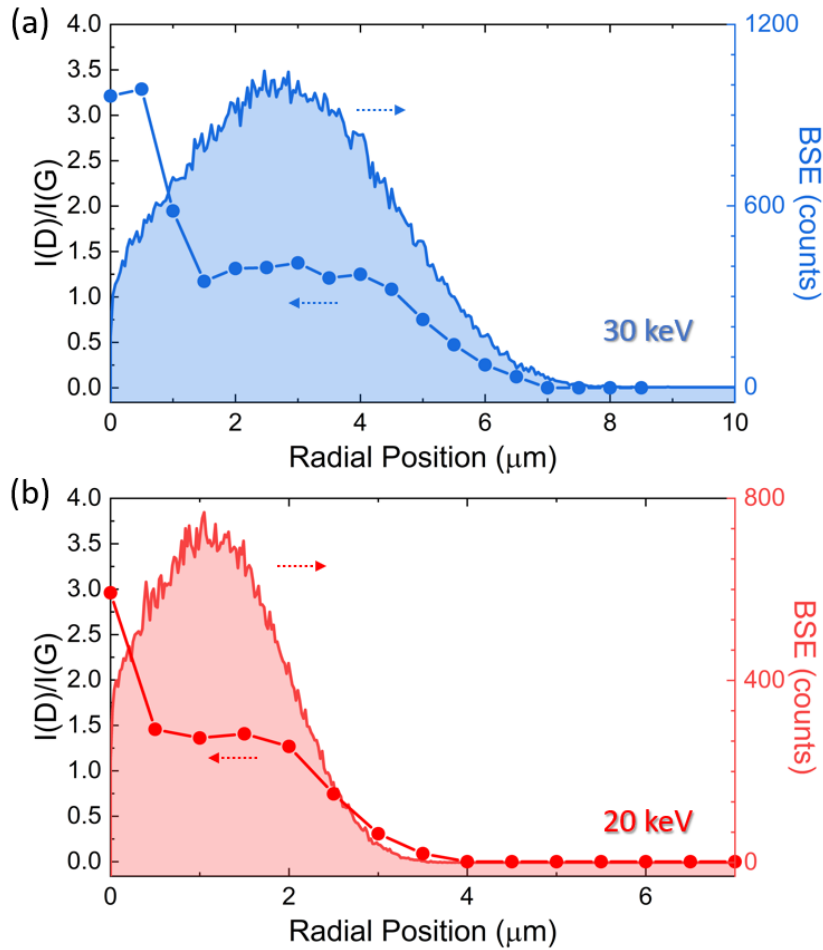
Figure 4.5: Comparison of Monte Carlo simulations with experimental data: spatial dependence of $I(D)/I(G)$ values quantified starting from the edges of the irradiated area [(a): dotted blue curve for 30 keV; (b): dotted orange curve for 20 keV] and radial distance of escaping BSEs [(a): filled blue curve for 30 keV; (b): filled red curve for 20 keV].

4.3 Comparison of substrate surface treatments

Interestingly, similar experiments carried out on graphene exfoliated onto plasma–treated substrates revealed very different results (as detailed in Section 2.1.3, the surface of plasma–treated substrates was cleaned by e–beam resist residue removal solution and by oxygen plasma at 100 W for 5 minutes). As shown in Figure 4.6, by increasing the exposure dose from 5 mC/cm² to 200 mC/cm² no strongly defective areas emerge outside the irradiated zones, except for the largest dose. This strong reduction of unintentional defective regions can be more clearly seen when comparing the normalized $I(D)/I(G)$ trends for graphene on no–plasma– and plasma–treated substrates when exposing to EBI. Figure 4.7 shows EBI at 20 keV and 40 mC/cm², and at 30 keV and 200 mC/cm², respectively. The difference is highlighted by plotting the two dimensional map of the normalized $I(D)/I(G)$ ratio across the graphene flake. An example is given in the inset of Figure 4.7(a) when irradiating at 20 keV with 40 mC/cm². Table 4.1 summarizes the data, which were normalized by the values of $I(D)/I(G)$ in irradiated zones.

The maximum extension of unintentional defects at 20 keV is about 1.5 μm in plasma–treated substrates and the maximum $I(D)/I(G)$ of the transition zone is ~ 0.1

Table 4.1: Maximum extension of unintentional defect zones (indicated by the dash–dotted arrows in Figure 4.7) for different primaries kinetic energies, electron doses and surface treatments.

Defect extension	Kinetic energy	Dose	Surface treatment
3.5 μm	20 keV	40 mC/cm^2	no–plasma
1.5 μm	20 keV	40 mC/cm^2	plasma
7 μm	30 keV	200 mC/cm^2	no–plasma
3.5 μm	30 keV	200 mC/cm^2	plasma

times the one in the irradiated area, while it is about 3.5 μm and a factor ~ 0.4 in no–plasma–treated substrates, respectively. At 30 keV the maximum radial distance reachable in plasma–treated substrates is about 3.5 μm, while it is 6 – 7 μm in no–plasma–treated substrates. In plasma–treated areas the $I(D)/I(G)$ value is a factor ~ 0.15 of the irradiated zone, instead of ~ 0.4 in no–plasma–treated substrates. On no–plasma–treated substrates, the non–zero $I(D)/I(G)$ zones precisely reproduce the spatial distribution of arrival BSEs (as shown in Figure 4.7). In fact, the $I(D)/I(G)$ ratio reaches a plateau in the transition zone and the black dashed line, which indicates the distance at which the largest number of BSEs escape from the surface according to Monte Carlo simulations, is right in the middle of the transition zone. Instead, on plasma–treated substrates the $I(D)/I(G)$ ratio reaches zero within the distances where the largest number of BSEs escapes from the surface. Consequently, the BSEs appear having only a minor effect on the adjacent areas of the irradiation in plasma–treated substrates, suggesting the contribution from additional defects sources in no–plasma–treated substrates. The reduction of the defect extension after plasma cleaning reported here was observed and measured on several samples, with similar results (at least 10 samples after EBI at 20 keV and 40 mC/cm^2 and 5 samples after EBI at 30 keV and 200 mC/cm^2).

A possible explanation to the obtained data can involve secondary electrons. As already mentioned, secondary electrons can be generated during the scattering events of primary electrons passing through solids. However, the penetration depth of primary electrons in silicon is much larger than the escape depth of SEs, thus their contribution in forming SEs is expected to be low. Instead, the BSEs can dissipate their energy in the SEs escape region. Thus, they can extensively contribute to SEs creation even when the backscattering coefficient is relatively small.[181] Conventionally, SEs are defined as particles having energy lower than 50 eV. It is worth mentioning that this energy range matches with the energy of maximum dissociation cross section of molecules like hydrocarbons or other organic molecules.[182,183] For example, a complete or partial hydrogenation process mediated by SE–induced fragmentation of adsorbed H_2O molecules has been reported in electron–irradiated graphene.[184,185] Hence, under EBI, adsorbant dissociation can occur on the solids surface, creating reactive radicals far from the landing point of primary electrons and within a spatial length determined by the radial escaping distance of BSEs. Consequently, when irradiating graphene placed
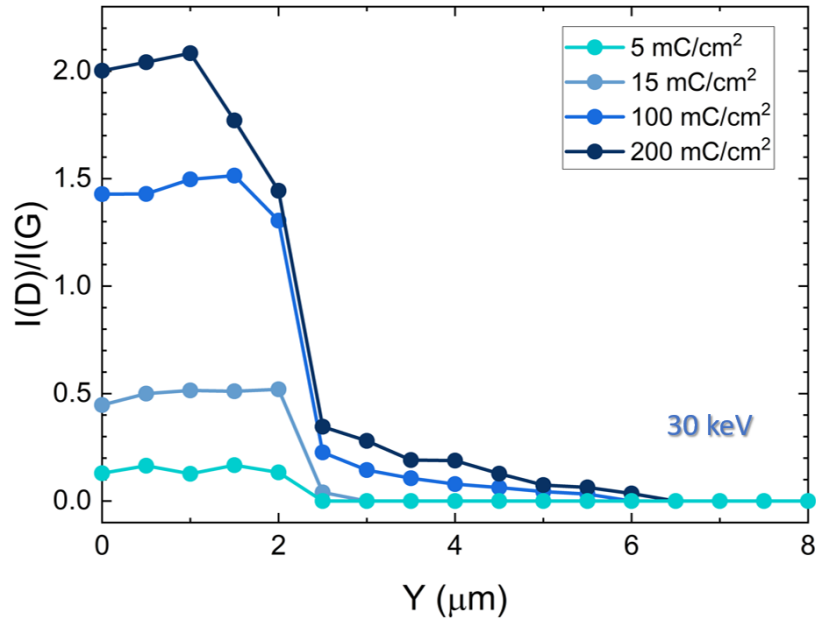
Figure 4.6: $I(\mathrm{D})/I(\mathrm{G})$ profile along the Y–axis for different doses (from 5 mC/cm^2 to 200 mC/cm^2) when irradiating graphene on a plasma–treated substrate at 30 keV.

onto surfaces (here SiO$_2$) with residual organic compounds, the SE–formed radicals are trapped at the interface between graphene and SiO$_2$ and are expected to interact with the graphene lattice and/or its defects, promoting the formation of Raman–active bond deformations, and thus the appearance of D peak in the Raman spectrum, and charge transfer to graphene.[182,186] Based on these considerations, the large D peak in the transition zones observed in no–plasma–treated substrates may be explained by the presence of SE–dissociated organic contaminants that are trapped at the interface between graphene and SiO$_2$.[187] Indeed, the solvent stripper, like specific resist remover, is less effective in removing most organic contaminants, while oxygen plasma cleaning results in SiO$_2$ surfaces clean of adsorbents due to the strong action of plasma activated species.[188]

4.4 Transition zone doping analysis

To further corroborate our hypothesis, we also analyzed the doping condition of the transition zones, because, as mentioned, radicals can induce a charge doping in the graphene sheet. An unambiguous Raman fingerprint of the doping status in graphene is represented by the width of the G peak ($\Gamma(\mathrm{G})$).[189] In pristine graphene, the $\Gamma(\mathrm{G})$ value is mainly determined by the chemical potential, as the possible electron–hole pair formation is controlled by Pauli blocking. In intrinsic graphene, $\Gamma(\mathrm{G}) \sim 16$ cm^{-1}, whereas $\Gamma(\mathrm{G})$ symmetrically decreases as electron or hole concentration increases, due to the limited phonon decay paths.[179] Instead, in electron–irradiated graphene, the $\Gamma(\mathrm{G})$ value arises from the competitive action of carrier concentration (G peak narrowing) and defect density (G peak broadening), where the latter mainly dominates for $I(\mathrm{D})/I(\mathrm{G}) > 3$.[98]

Figure 4.8 shows the Y–axis profile of the difference of Γ_G with respect to its value in as–exfoliated graphene in plasma– and no–plasma–treated substrates when irradiating
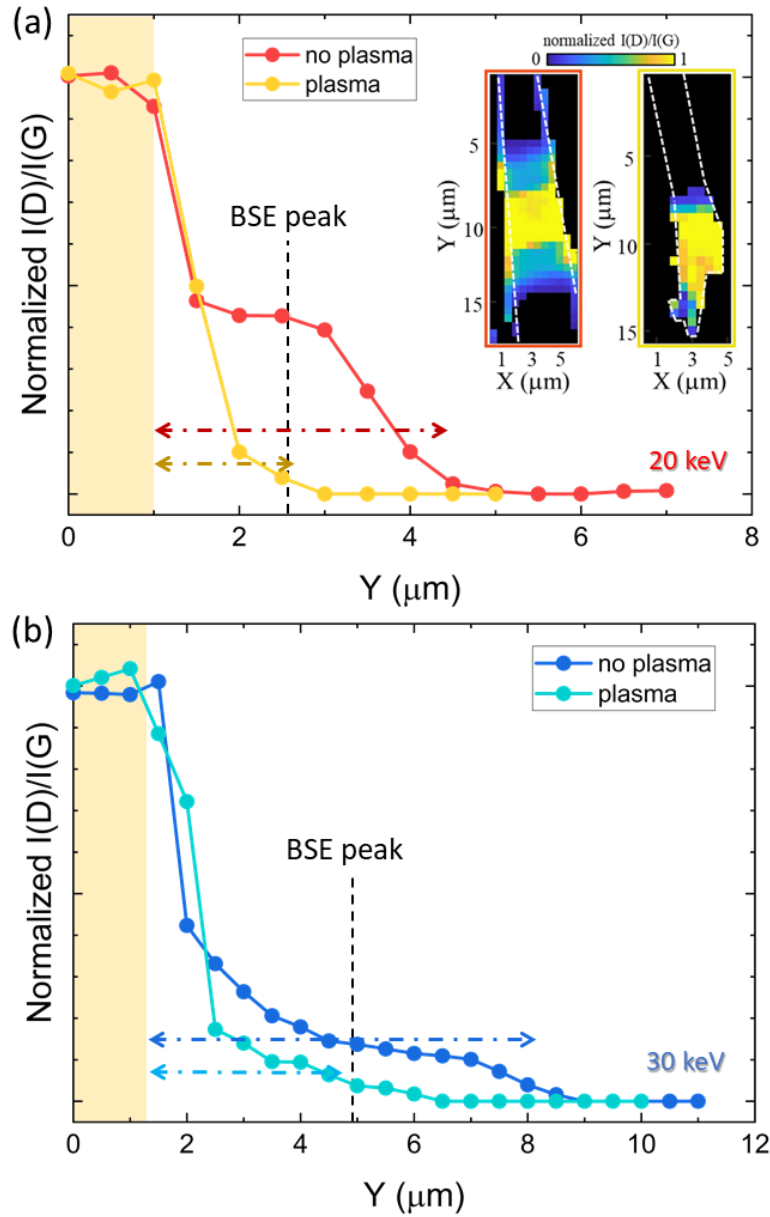
Figure 4.7: (a) Comparison between normalized $I(D)/I(G)$ profiles of irradiated graphene on no–plasma–treated (orange dotted curve) and plasma–treated substrate (yellow dotted curve) for 20 keV and 40 mC/cm^2. The inset shows the two–dimensional spatial distribution of normalized $I(D)/I(G)$ across the graphene flake on no–plasma– (left orange–framed panel) and plasma–treated (right yellow–framed panel) substrate. The white dashed lines indicate the flake edges. (b) Comparison between normalized $I(D)/I(G)$ profiles of irradiated graphene on no–plasma–treated (blue dotted curve) and plasma–treated substrates (cyan dotted curve) for 30 keV and 200 mC/cm^2. In both panels, the yellow area indicates the irradiated area, the dash–dotted arrows show the maximum extension of the unintentional defects zones, and the dashed–line indicates the distance at which the largest number of BSEs escape from the surface according to Monte Carlo simulations.
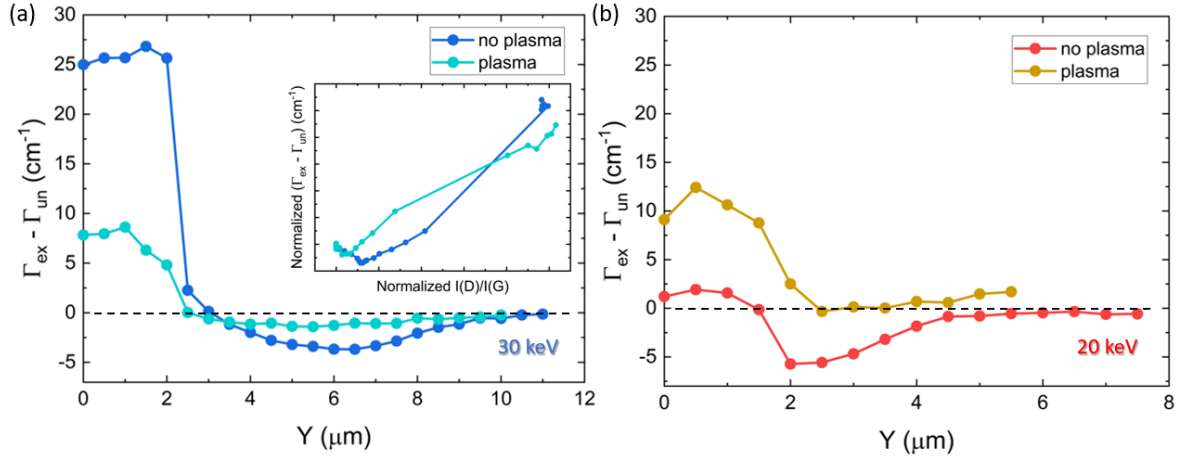
Figure 4.8: Irradiation effects on G peak width: (a) profile of the difference between G–peak width in 30 keV–exposed (Γ_{ex}) and as–exfoliated (Γ_{un}) graphene along the Y–axis in no–plasma– (blue dotted–line) and plasma–treated (cyan dotted–line) substrates. The electron dose was 200 mC/cm^2. Inset: $\Gamma_{ex} - \Gamma_{un}$ as a function of $I(D)/I(G)$ (both normalized by their maximum values in the irradiated zone). (b) Profile of the difference between G–peak width in 20 keV–exposed (Γ_{ex}) and as–exfoliated (Γ_{un}) graphene along the Y–axis in no–plasma– (orange dotted–line) and plasma–treated (yellow dotted–line) substrates. The electron dose was 40 mC/cm^2.

with 30 keV (Figure 4.8(a)) and 20 keV (Figure 4.8(b)). For both electron kinetic energies, the irradiated areas have G peak width (Γ_{ex}) larger than in as–exfoliated (Γ_{un}) graphene, both in plasma– and no–plasma–treated substrates, as expected due to the larger defect–dominated scattering contribution.[98] In the transition areas of graphene on plasma–treated substrates, $\Gamma_{ex} - \Gamma_{un}$ goes to zero. Instead, a narrowing of the G peak is observed in the transition zones of graphene on no–plasma–treated substrates, confirming the doping of graphene in these areas. This result is also supported by the analysis of the G peak width as a function of $I(D)/I(G)$. As shown in the inset of Figure 4.8(a), the G peak width firstly decreases for low defect density (corresponding to the transition area) and then increases reaching its maximum value in the irradiated area. Similar data are obtained also at 20 keV. Additionally, these narrower Γ_G values have Y–axis profiles that follow the spatial distribution of BSEs, like for $I(D)/I(G)$, reaching the minimum value at the same radial distance at which the maximum number of BSEs escapes from the surface. Instead, in plasma–treated–substrates Γ_G is almost equal to the value of as–exfoliated graphene, suggesting a negligible doping related to the electrons irradiation. In both substrates, the G peak has almost unaltered width when considering zones very far from the patterned areas, indicating a conservation of the graphene conditions during the entire experiment. Hence, the combination of $I(D)/I(G)$ and Γ_G data pointed out the relevant role of BSEs and SEs in affecting the lateral resolution of defects–patterning in graphene sheets: BSEs possess sufficient kinetic energy to introduce defects in the graphene lattice, as revealed in plasma–treated substrates; BSEs–generated SEs, instead, induce molecular dissociation of surface organic residues, which results in both structural defects and charge doping, as clearly observed in no–plasma–treated substrates.

4.5   Conclusions

Here, we created patterned structural defects on graphene sheets by low–energy EBI and analyzed their distribution by spatially–resolved micro–Raman spectroscopy. Surface treatments of the graphene–supporting substrate have strong impact on the lateral resolution that can be achieved on the final defective pattern. Micrometer–large unintentional defect–rich zones were revealed in the adjacent parts of the irradiated areas and have $I(D)/I(G)$ spatial distribution that strongly depends on primary electron dose and kinetic energy, but also on SiO_2 surface cleaning methods. Indeed, in no–plasma– treated substrates, the irradiation–surrounding areas have large $I(D)/I(G)$ values with a few–μm–long lateral extension, whereas plasma–treated substrate areas show smaller $I(D)/I(G)$ values in a shorter distance from the primaries impact point. Simulation of primary electrons scattering events via Monte Carlo method demonstrated that these transition zones originate within the area where BSEs and BSE–created SEs escape from the SiO_2 surface. In no–plasma–treated substrates, the radial distribution of unintentional defective areas is in very good agreement with the simulated one of BSEs. In these substrates, the $I(D)/I(G)$ values is larger and has longer extension due to the combined action of BSEs and SEs. BSEs have sufficient energy to induce defects on the graphene lattice. Instead, SEs dissociate organic residues trapped between graphene and SiO_2 surface. These SE–created radicals, interacting with the graphene sheet, cause additional structural defects and charge doping. The latter was confirmed by analyzing the G peak width. Instead, in plasma–treated substrates, only BSEs affect the lateral resolution of defects–patterning, as the plasma treatment removes the impurities adsorbed on the substrate. In general, the BSE contribution can be mitigated by using very low Z–number materials or, alternatively, by reducing the thickness of the substrate.

These results have been published in *Surfaces and Interfaces – Elsevier* (see Ref. 190) and have been exploited in order to engineer a more controlled defect pattern and design monolayer graphene flakes with improved chemical reactivity towards organic functionalization, as discussed in the next Chapter.

Functionalization of Patterned Monolayer Graphene Flakes

5

Here, we present the selective covalent functionalization of defect–engineered monolayer graphene with 1,3–dipolar cycloaddition (1,3–DC) of azomethine ylide. Atomic force microscopy (AFM) and Raman spectroscopy allow the analysis of the samples as–exfoliated, after the patterning, and after the functionalization. Raman spectroscopy maps show the appearance of the characteristic D peak only in the patterned area, while AFM images confirm the spatial distribution of the pattern designed via low–energy EBI. The 1,3–DC of azomethine ylide involves dipolarophile species (e.g. the localization of a C=C bond of the graphene structure),[60,191] which is favorable in presence of defects hence introducing a selective control of the chemical reactivity of graphene. In fact, as shown in literature[88] and confirmed in the experiments reported in Chapter 3, the presence of defects in the graphene lattice induces electron charge localization, which remarkably favors the organic functionalization via 1,3–DC reaction.

Indeed, the Raman analysis of the functionalized graphene flakes exhibits new features in the region $1050 - 1750$ cm^{-1}, only in the patterned areas, whereas the unexposed areas still present the spectrum of pristine graphene, confirming the selectivity of functionalization introduced via defect patterning. To deepen our understanding of the system, a model for functionalized graphene is built, and ab initio molecular dynamics, at density functional theory (DFT) level, is exploited to evaluate the power spectrum (PS).[152] Evaluating the PS for specific groups allows to identify the contribution of the functional groups of the azomethine ylide grafted on the graphene surface (methyl, carboxyl, and catechol groups) and of the modified vibrational modes of the graphene sheet. Furthermore, the functionalization is shown to be reversible under irradiation with a focused laser beam (100× objective, up to 1.6 mW). The desorption of the ylide is indicated by the recovery of the Raman spectrum towards the spectrum of non–functionalized patterned graphene, a result which opens the possibility for a controlled removing of the molecules and an even finer tailoring of the surface, toward a functional integrated circuit (IC) architecture. Indeed, laser ablation of azomethine ylide paves the way for a sequence of functionalization/ablation steps in order to build a functional super–array of molecules expressing different capabilities. This device processing mimics the IC design.

5.1 Pattern design on graphene flakes via EBI

Monolayer graphene flakes (labeled here as Flake 1, 2, and 3) are mechanically exfoliated on silicon dioxide substrates. Even if this was the first method used by Novoselov et al.[4] to produce graphene monolayers, mechanical exfoliation still plays a fundamental role in the production of high quality single crystal graphene samples for research scale experiments.[192] The pristine high quality monolayer graphene flakes are initially characterized by Raman spectroscopy and AFM. Then, a part of each flake is exposed to EBI with electrons accelerated to 20 keV and a dose of 40 mC/cm². The irradiated area is designed in order to expose half of the length and the entire width of each flake (as shown in Figure 5.1, where the exposed area on Flake 2 is 8 μm $\times$ 14 μm), with a homogeneous irradiation pattern (as shown in Figure 2.12(b)) and an electron beam step–size of 100 nm.
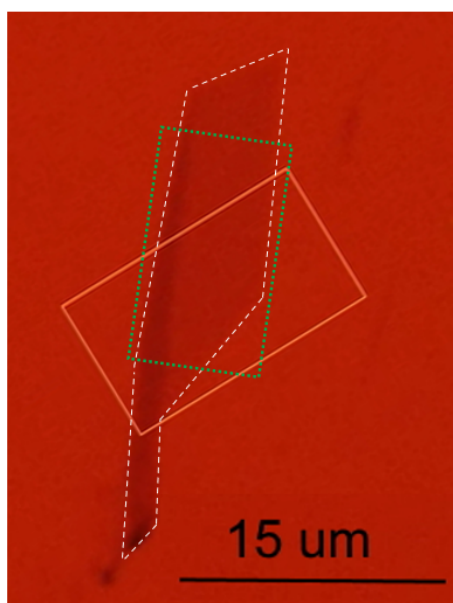
Figure 5.1: Optical microscopy image of Flake 2. The white dashed line follows the edges of the flake, the orange rectangle indicates the patterned area (8 μm $\times$ 14 μm), and the green dotted rectangle is the area mapped by Raman spectroscopy (8 μm $\times$ 12 μm, the maps are shown in Figure 5.2).

Figure 5.2 shows a representative Raman spectrum collected on the unexposed area of the graphene monolayer (in black) along with a Raman spectrum recorded on the irradiated area (in red). The spectrum of the pristine graphene shows the characteristic G band, here centered at 1583 cm⁻¹, and 2D band, here centered at 2675 cm⁻¹, and the absence of the defect–activated D peak. Both G and 2D peaks are always present in the Raman spectra of graphene–based nanomaterials, since no defects are required for their activation. In particular, a single Lorentzian peak is the benchmark for the spectrum of single layer graphene.[128] Here, we can fit the 2D peak with a single symmetrical Lorentzian curve, with a FWHM of 24.3 cm⁻¹. Besides the absence of the D peak, further evidence for the high quality of the pristine monolayer graphene is the intensity ratio of the 2D and the G peaks.[193] Here $I(2D)/I(G) \sim 3$ for the unexposed graphene flake, confirming its single–layer structure. Finally, the weak G* band is visible, here centered at 2460 cm⁻¹.[158]
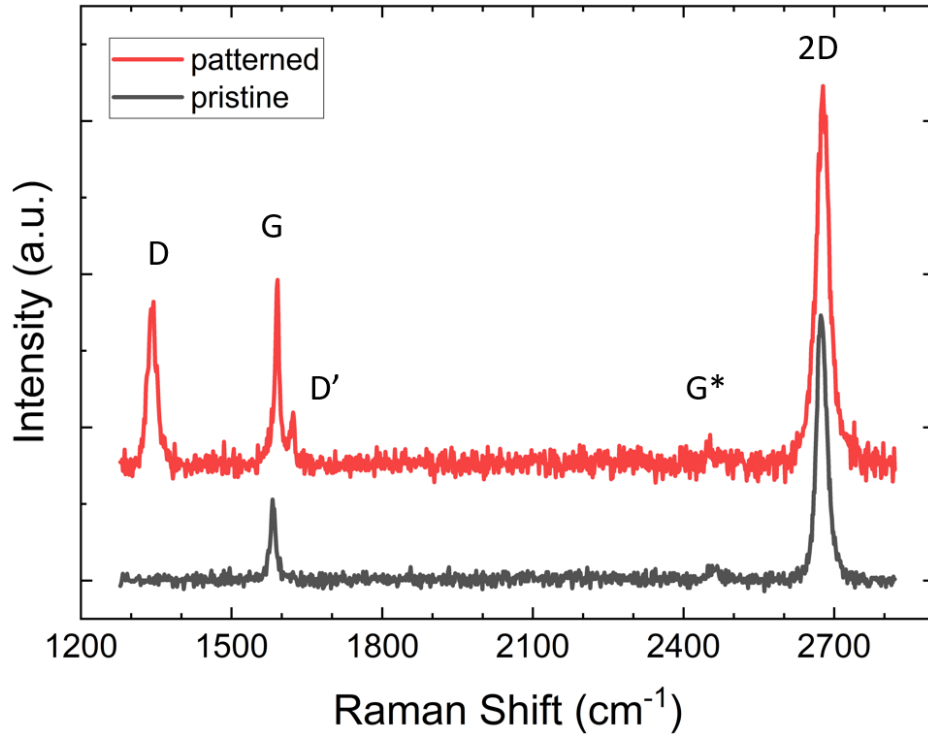
Figure 5.2: Exemplary Raman spectra collected in the pristine (black) and patterned (red) areas of the flake (shifted in height), with the characteristic peaks labeled.

The Raman spectrum of patterned graphene (the red line in Figure 5.2) exhibits additional bands, which are known to appear in the presence of structural defects. The D peak, here centered at 1342 cm^{-1}, and the D' peak, here centered at 1621 cm^{-1}, involve respectively intervalley and intravalley double resonance processes, and for low defect concentrations their intensities are proportional to the number of defects.[131] It has been shown that the intensity ratio of the D and D' peaks indicates the nature of the defects in the graphene lattice. In particular, $I(\text{D})/I(\text{D}')$ reaches a maximum value of ~ 13 for sp^3–defects, decreases to ~ 7 for vacancy–like defects, and has a minimum of ~ 3.5 for boundary–like defects.[157] Here, we obtain $I(\text{D})/I(\text{D}') \sim 4$ for Flake 2 ($I(\text{D})/I(\text{D}') \sim 5.5$ for Flake 3), indicating a dominant presence of boundary–like and vacancy–like defects. We expects these types of defects to be the most beneficial towards the subsequent cycloaddition because they induce modifications in the electronic structure of graphene (in particular electron localization)[88] without saturating it through sp^3 hybridization.

Acquiring Raman maps of the patterned flake, it is possible to verify the spatial distribution of the defects. In the patterned area, the intensity of the 2D band (Figure 5.3(a)) decreases to an average value of $I(2\text{D})/I(\text{G}) \sim 2$, while the 2D band width (Figure 5.3(b)) increases to an average value of FWHM ~ 31 cm^{-1}. As defects are introduced in the graphene lattice, defect–dominated scattering processes become more likely, which results in a decrease of the intensity of the 2D peak and an increase in its width.[157,194,195] From the intensity ratio of the D and G peaks, here $I(\text{D})/I(\text{G}) \sim 0.9$, it is possible to estimate the amount of disorder in the graphene sheet, both in case of boundary–like and point–like defects. For the former, we can estimate the nanocrystalline size L_α using the Tuinstra–Koenig relation: $I(\text{D})/I(\text{G}) = C(\lambda)/L_\alpha$.[196,197] $I(\text{D})$ and $I(\text{G})$ are the D and G peak intensities, L_α is the graphene nanocrystalline size, and the factor $C(\lambda)$ is empirically derived and depends on the
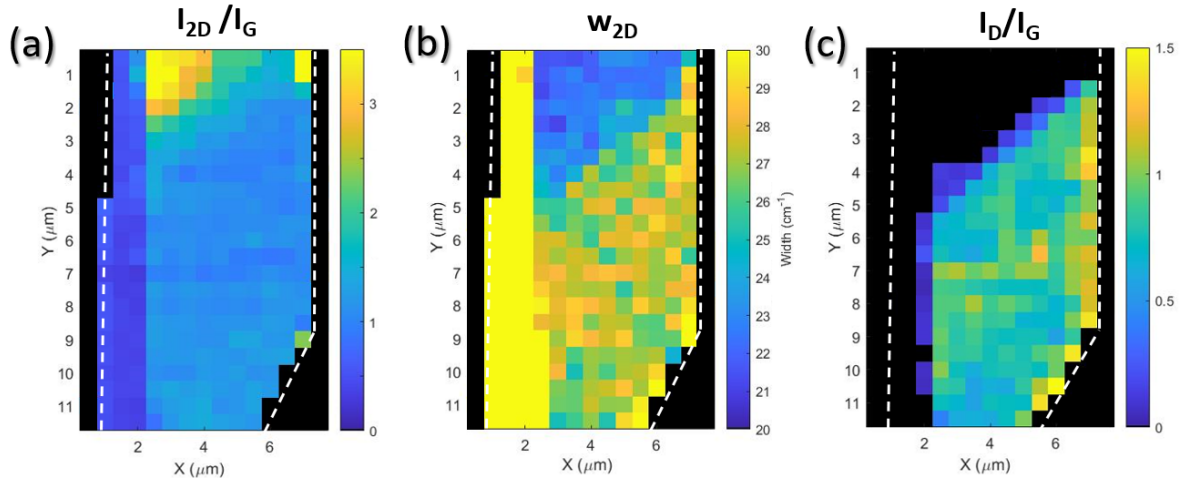
Figure 5.3: Raman maps of (a) $I(2D)/I(G)$ intensity ratio, (b) 2D peak width (w_{2D}), and (c) $I(D)/I(G)$ intensity ratio collected on the flake after exposure to EBI (in the area identified by the green dotted rectangle in Figure 5.1). The white dashed lines follow the edges of the flake, and the X and Y axis refer to the position of the laser spot during the Raman mapping of the area (8 μm $\times$ 12 μm in size).

excitation laser wavelength λ. From the work of Cançado et al. (reported in Ref. [198]), we can calculate $C(\lambda)$ for our experiment: $C(\lambda) = (2.4 \times 10^{-10})\, \lambda^4(\text{nm}) = 19.2$ nm, at $\lambda = 532$ nm. Therefore, in case of patterned graphene, we obtain $L_\alpha \sim 21$ nm, confirming that we remain in the low–defect regime ($L_\alpha > 20$ nm).[199] In case of point–like defects in graphene, an useful measure for the amount of disorder is the distance between defects, L_D.[199] In case of low–disordered graphene, $I(D)/I(G)$ was found to be inversely proportional to $L_D{}^2$, and from the analysis presented in the work of Cançado et al. (see Refs. [179,200]) it is possible to obtain the following empirical relation: $L_D{}^2(\text{nm}^2) = [(1.8 \times 10^{-9})\, \lambda^4(\text{nm})] \,/\, [I(D)/I(G)]$. Therefore, in our case, we can estimate $L_D \sim 11$ nm at $\lambda = 532$ nm, which means a defect density $n_D(\text{cm}^{-2}) = 10^{14}/(\pi L_D{}^2) \sim 2.5 \times 10^{11}$ defects/cm^2. Moreover, the presence of defects influences also the G peak, which blue shifts to 1591 cm^{-1}, while its width remains almost constant (FWHM ~ 12 cm^{-1}). While the position of the G peak is particularly sensitive to doping, its width follows two competing mechanisms: due to doping it tends to decrease, while due to disorder it tends to increase. In the regime of a low concentration of defects ($I(D)/I(G) \leq 1$) these two effects compensate each other.[201] Finally, mapping the intensity ratio of the D and G peaks (Figure 5.3(c)) allows to confirm that no defects are introduced in the unexposed area of the flake.

AFM is a powerful technique for the investigation of surfaces and interfaces at the micro– and nano–scale, allowing to detect features with high spatial resolution (down to few nanometers). Here, the acquisition of AFM images of the patterned flake allows to clearly reveal the defect pattern, both in the height and in the phase channels (see Figure 5.4). The AFM phase channel reveals the defect spots with higher contrast, showing a step size of ~ 100 nm (see Figure 5.5), which exactly reproduces the input parameter of the EBI. From the AFM height image, the RMS roughness measured in the pristine area is 0.79 nm, while the RMS roughness of the patterned area is 0.80 nm. These similar values confirm that, via low–energy EBI, no significant structural defects are introduced in the graphene lattice, which maintains a similar roughness. Again, no defect pattern is visible in the unexposed area of the flake.
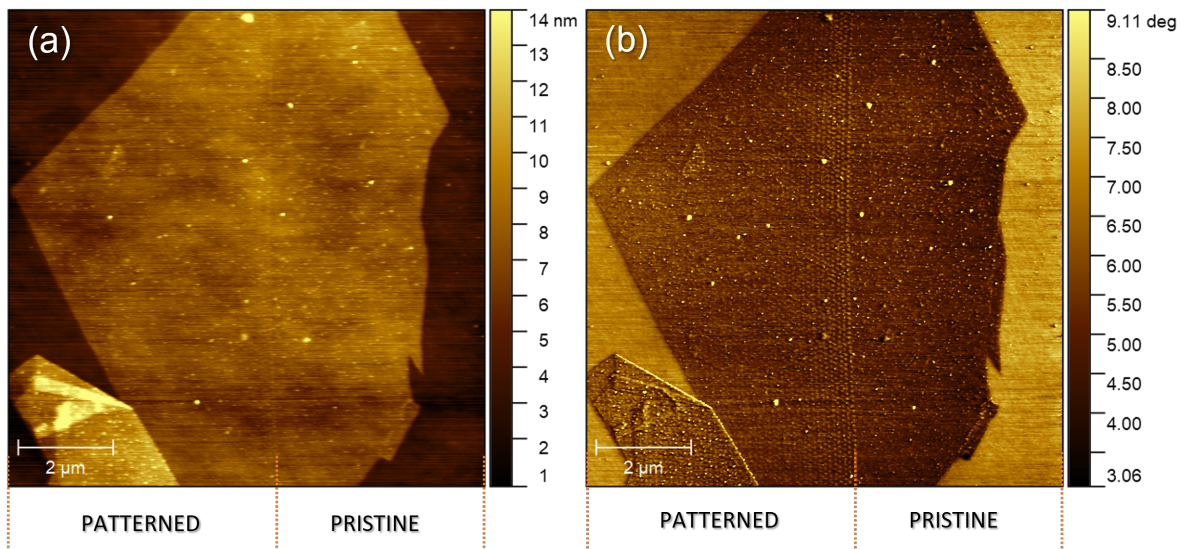
Figure 5.4: AFM (a) height and (b) phase images ($10 \times 10 \ \mu m^2$) of Flake 1. As indicated below the figure, the left side of the flake is patterned, the right side is pristine.
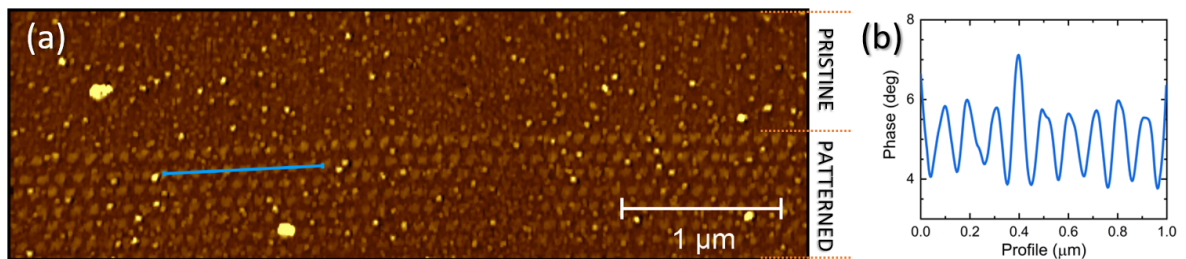
Figure 5.5: (a) AFM phase image of patterned graphene (Flake 1) showing the defect pattern in the lower part of the image. (b) Profile taken along the blue line in panel (a), showing a pitch of $\sim$ 100 nm.

5.2 Functionalization of patterned graphene via 1,3–DC

Patterned graphene is functionalized via a wet chemistry process, by adding N-methyl-glycine and 3,4-dihydroxybenzaldehyde in NMP. The 1,3–DC of azomethine ylide occurs involving the localization of a C=C bond of the graphene lattice, as schematically represented in Figure 5.6. After the functionalization, the solvent is removed by several rinses (as described in detail in Section 2.3.2), and finally AFM and Raman spectroscopy are performed.
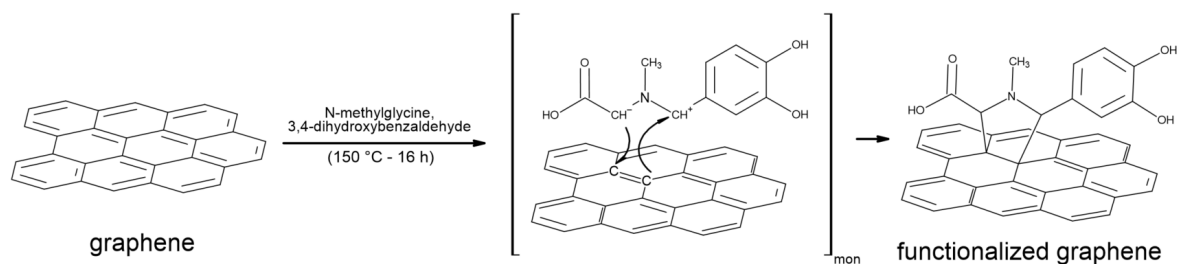
Figure 5.6: Schematic representation of the in–situ 1,3–DC of azomethine ylide on graphene.

5.2.1 AFM images of functionalized patterned graphene

Figures 5.7 shows AFM images of patterned graphene (Flake 2 and Flake 3) before and after the functionalization. After the functionalization procedure, the part of the graphene flake that was exposed to EBI remains adhered to the silicon dioxide substrate, while most of the non–irradiated part of the flake detached from the substrate and folded.
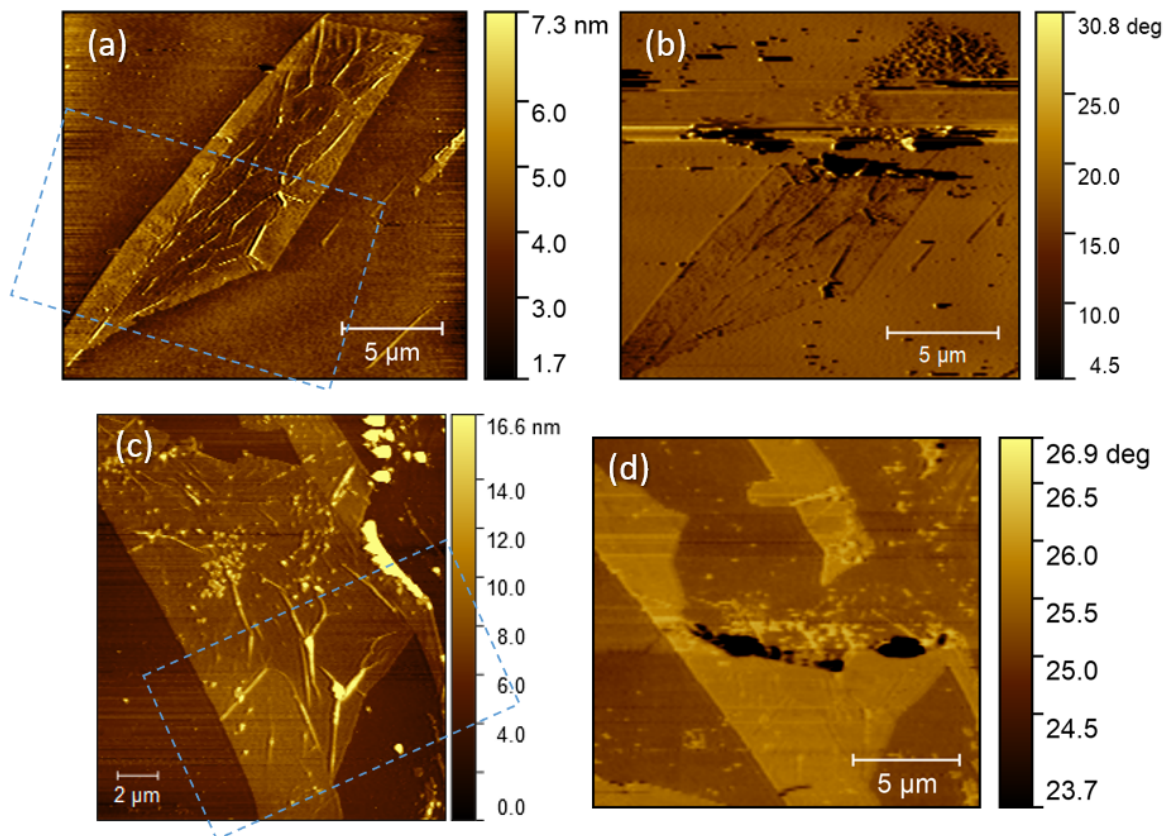
Figure 5.7: AFM height image of Flake 2 (a) after low–energy EBI (the blue rectangle shows the area which was exposed) and (b) after functionalization. The most part of the non–patterned zone of the flake detached from the silicon dioxide substrate and folded, while the patterned zone remains adhered to the substrate. AFM height image of Flake 3 (c) after low–energy EBI (the blue rectangle shows the area which was exposed) and (d) after functionalization. The most part of the non–patterned zone of the flake detached from the silicon dioxide substrate and folded. Here, also part of the patterned area has folded.

It is well known that NMP is an optimal organic solvent commonly used in 1,3–DC for its ability to favor the reaction by both dissolving the reagents and stabilizing the intermediates of reaction. On the other hand, it is among the best solvents for the dispersion of graphene, since its surface tension falls in the ideal range of 40 – 50 mJ/m^2.[111] This means that NMP, while promoting the 1,3–DC of azomethine ylide on graphene, introduces an adhesion issue for the graphene flake. Remarkably, patterned graphene exhibits an improved adhesion towards the silicon dioxide substrate (as can be seen in Figure 5.7), overcoming the risk of dispersing the flake in the reaction solvent during the functionalizing procedure and allowing for further analysis and use of the graphene flake after the functionalization in NMP.

Notably, this result could help when fabricating devices based on graphene flakes

functionalized with organic molecules. Indeed, designing defect patterns ad hoc would yield to both spatially resolved–functionalization and adhesion promotion of the functionalized graphene sheet. Moreover, the original pattern with a step size of ~ 100 nm is still present after the organic functionalization, as shown in Figure 5.8. Hence, as expected, the functionalization process preserves the designed pattern. Finally, the RMS roughness measured on the non–patterned area of the graphene flake (shown in Figure 5.8(a)) is 0.96 nm, while the one measured on the patterned area is 1.38 nm. Even if, unfortunately, no molecular resolution was achieved from AFM images, to a first approximation the increase in the roughness of the patterned graphene area (+ 0.57 nm) is compatible with the size of the azomethine ylides (the height of the molecule is ~ 0.55 nm).
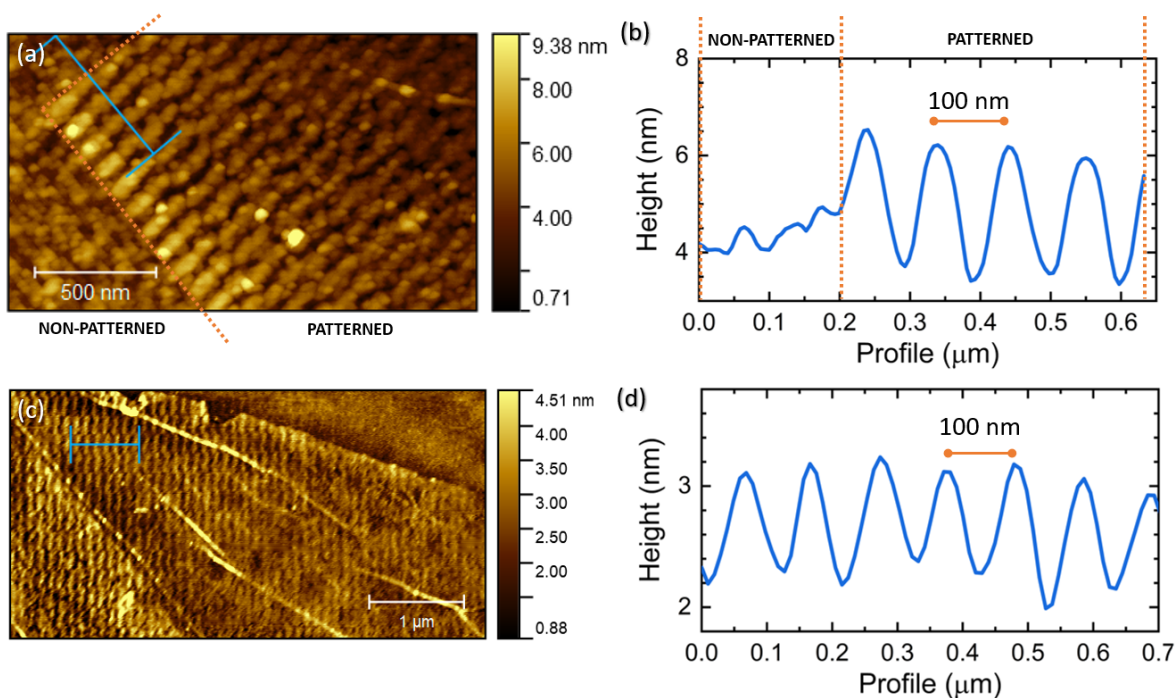
Figure 5.8: (a) AFM height image of Flake 2 after the functionalization showing both a patterned area (on the right) and a non–patterned area (on the left) as indicated. (b) Profile taken along the blue line in panel (a) showing a step size of 100 nm, as originally designed via EBI, in the patterned area. (c) AFM height image of the patterned area of Flake 2, in a different zone, after the functionalization. (d) Profile taken along the blue line in panel (c), showing a step size of 100 nm, as originally designed via EBI.

5.2.2 Raman analysis of functionalized patterned graphene

The selectivity of the chemical functionalization is confirmed by the Raman maps collected on graphene after the functionalization procedure. Although most of the non–patterned area is folded, a narrow stripe of defect–free graphene is still present, and its Raman spectrum can be investigated. The Raman spectra of functionalized graphene collected in the non–patterned area and in the patterned area of the flake show very different behavior (see Figure 5.9).

The spectrum of functionalized patterned graphene exhibits new features and several modifications, as presented in detail below. In particular, there is a complete
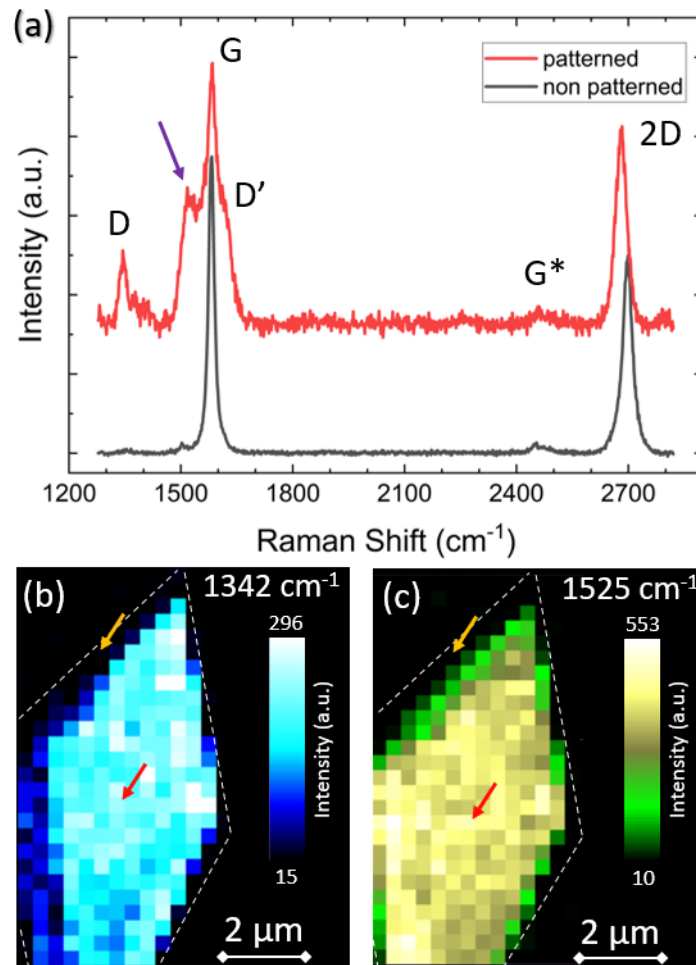
Figure 5.9: (a) Raman spectra of the functionalized Flake 2 collected in the non–patterned (black line) and patterned (red line) areas of the flake (shifted in height). New Raman features are visible only in the spectrum of patterned functionalized graphene (the violet arrow indicates the most intense peak arising from the functionalization, at 1525 cm⁻¹). Raman maps of (b) D peak intensity and (c) intensity at 1525 cm⁻¹ collected on Flake 2 after the functionalization procedure (the white dashed line follows the edges of the flake). The yellow and red arrows indicate respectively the positions where the spectra of patterned and non–patterned graphene after functionalization (shown in panel (a)) were collected.

correspondence between the spatial distribution of the Raman intensity of the defect–activated D peak at 1342 cm⁻¹ (shown in Figure 5.9(b)), and the Raman intensity at 1525 cm⁻¹ (shown in Figure 5.9(c)), which arises from the organic functionalization (as described in detail below). This correlation confirms the selectivity of the organic functionalization introduced by the spatially–resolved defect engineering of graphene via EBI. On the other hand, non–patterned graphene after the functionalization presents a decrease in the intensity of the 2D peak in comparison to the non-patterned graphene spectrum acquired before the functionalization ($I(2D)/I(G)$ decreases from 2 to 0.65), and a shift of the positions of the G peak (from 1591 cm⁻¹ to 1582 cm⁻¹) and the 2D peak (from 2677 cm⁻¹ to 2696 cm⁻¹). It is worth to mention that the 2D peak intensity decrease possibly indicates electron doping[202–204] while a frequency shift of the G and 2D peaks is known to occur in presence of strain.[205–207]

5.2.3 Computational simulations

In order to deepen our understanding of the functionalized graphene after 1,3–DC of azomethine ylide and assign the new Raman bands that arise, a model for functionalized graphene is developed (see Figure 5.10).
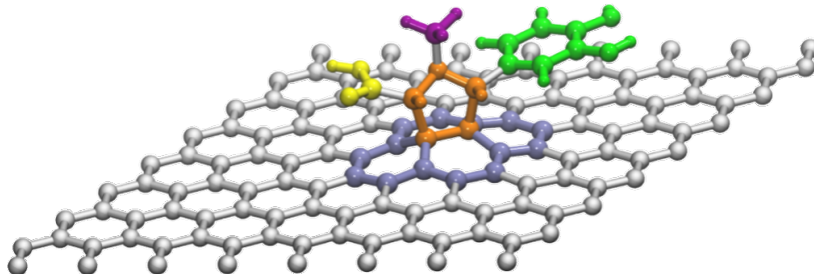
Figure 5.10: Model of the azomethine ylide attached to graphene. Highlighted with different colors are the functional groups of interest: carboxyl group = yellow, pyrroline ring = orange, methyl group = violet, cathecol group = green. The carbon atoms of graphene at the base of the molecule are highlighted in blue.

The system is subjected to an ab initio molecular dynamics (MD) simulation at 300 K for 38 ps. During the MD simulation, the graphene lattice does not undergo a large conformational rearrangement.
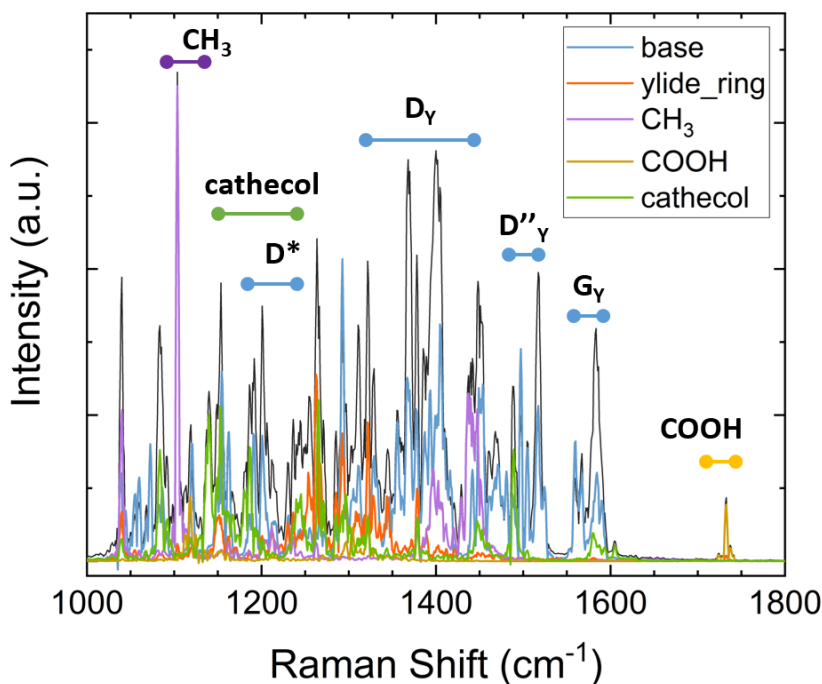
Figure 5.11: Power spectrum (PS) of the velocity autocorrelation function (black). The projection of the functional groups of interest on the PS are highlighted by the same colors as in Figure 5.10. The regions that correspond to the peaks detected in the Raman spectra are indicated by colored lines and labeled. It is worth to recall that the intensities of the peaks in the simulated PS do not directly correspond to those from the experimental Raman spectra, where additional selection rules are involved.

The vibrational density of states is obtained performing the Fourier transform of the velocity autocorrelation function.[152] Then, by computing the power spectra of

the autocorrelation function of appropriate groups of atomic coordinates, the power spectrum (PS) is decomposed and analyzed. The functional groups of interest are highlighted in different colors in Figure 5.10, and their corresponding projections are shown in Figure 5.11.

Figures 5.12 and 5.13 present in detail the experimental Raman spectra of functionalized patterned graphene collected on Flake 2 and Flake 3, respectively, with a fit to the data. For both Flake 2 and Flake 3, looking at the 2D peak, here centered at 2682 cm^{-1}, the intensity ratio $I(2D)/I(G)$ decreases from 2 to ~ 1.5, and the 2D width increases to a FWHM ~ 37 cm^{-1}. These modifications of the 2D peak are consistent with the presence of small doped domains due to the introduction of the organic molecules.[208] Also the intensity ratio between the D peak, here centered at 1343 cm^{-1}, and the G peak, here centered at 1586 cm^{-1}, decreases from an initial value of $I(D)/I(G) \sim 1$, for patterned graphene, to a value of $I(D)/I(G) \sim 0.3$, for patterned functionalized graphene. The decrease of $I(D)/I(G)$ is due to the introduction of new covalent bonds between the carbons of the graphene lattice and the molecules of azomethine ylide around the defects, as already seen in Chapter 4 and in literature.[195,177] A further sign of the functionalization is the rise of new bands in the Raman shift region 1050 – 1750 cm^{-1}, which can be assigned with the aid of the computed PS (see Figure 5.11).
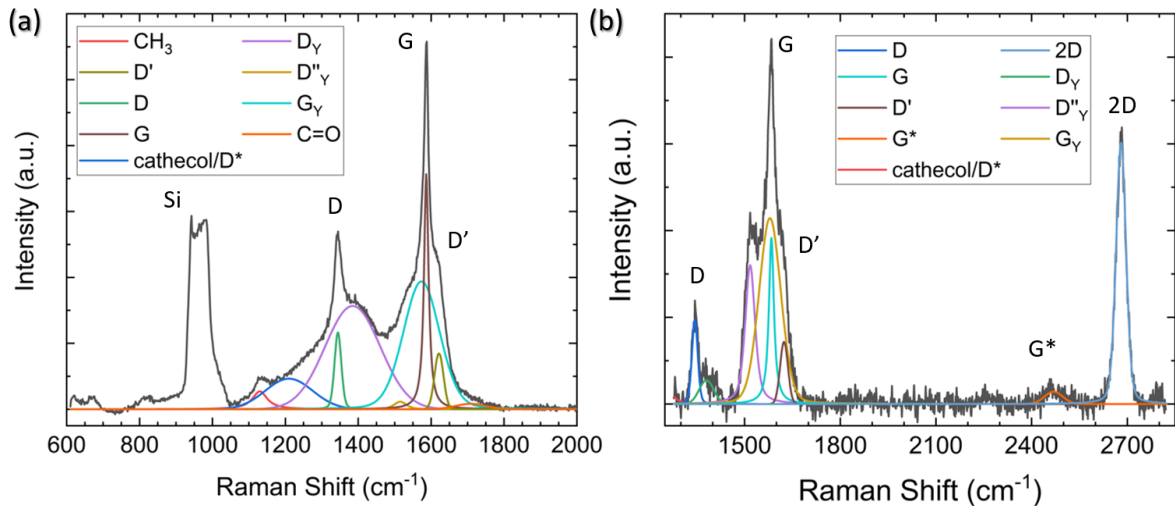
Figure 5.12: Raman spectra of functionalized patterned graphene (Flake 2) collected at 1560 μW laser power in the (a) lower and (b) higher Raman shift regions. A fit to the data is also shown, and the main peaks of graphene are labeled. The broad band [920 — 1050] cm^{-1} originating from the Si signal of the silica substrate is visible in panel (a).

The characteristic vibrational peak from C=O is centered at 1730 cm^{-1} (as shown in the PS) arises from the carboxyl group (COOH) of the azomethine ylide. This corresponds to the peak centered at 1705 cm^{-1} in the experimental Raman spectrum, as also seen in literature.[177,165] Another functional group of the azomethine ylide is the methyl group (CH$_3$), which possesses characteristic vibrational modes around 1110 cm^{-1} (as shown in the PS). This could correspond to the new band revealed in the Raman spectrum of functionalized graphene, centered at 1130 cm^{-1}, which is, therefore, labeled CH$_3$.

The cathecol group of the azomethine ylide, being a more complex part of the molecule, possesses a broader set of vibrational stretching modes, which fall around
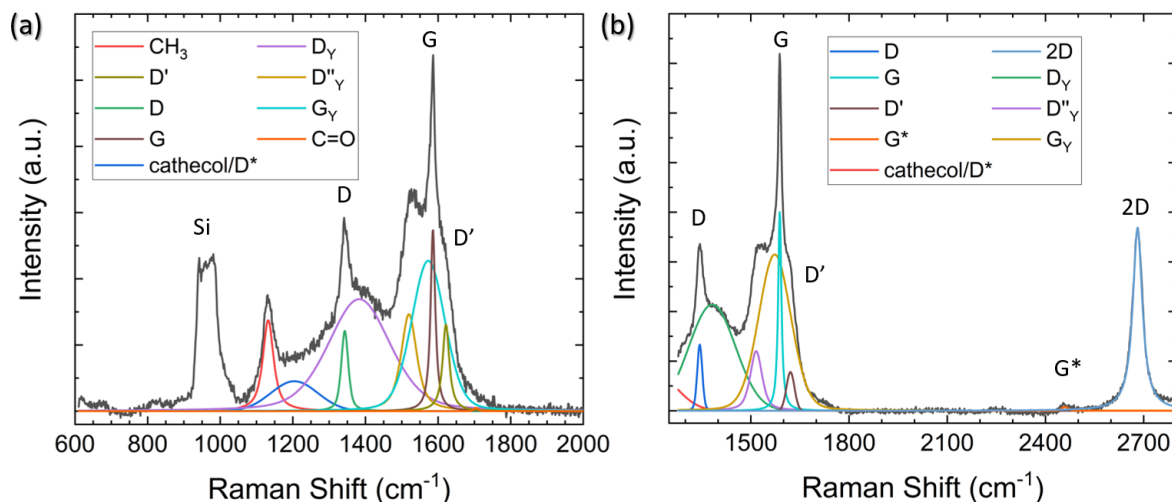
Figure 5.13: Raman spectra of functionalized patterned graphene (Flake 3) collected at 120 μW laser power in the (a) lower and (b) higher Raman shift regions. A fit to the data is also shown, and the main peaks of graphene are labeled. The broad band [920 — 1050] cm^{-1} originating from the Si signal of the silica substrate is visible in panel (a).

1150 – 1250 cm^{-1} (as shown in the Figure 5.11). Moreover, in the same region also contributes also the D* band, usually found around 1180 – 1200 cm^{-1}, which can be related to disordered graphitic lattices provided by sp^2–sp^3 bonds at the edges of networks.[162] These bands correspond to the wider band in the Raman spectrum that is centered at 1204 cm^{-1}, and is labeled as catechol/D*. Finally, three sets of vibrational modes can be identified in the region between the D and the G bands. From the projections on the PS of the carbon atoms of graphene at the base of the azomethine ylide, it can be inferred that these bands originate from vibrational normal modes of the modified graphene lattice. In particular, these bands are very close in frequency to the well–known D, D", and G bands of graphene. The D" band, usually seen in the range 1500 – 1550 cm^{-1}, is thought to be related to either interstitial defects associated with the functionalization with small molecules[162–164] or to the evolution to an amorphous phase, i.e., decreasing crystallinity.[161] In the case of functionalized graphene, the presence of a molecule of azomethine ylide grafted on the graphene sheet breaks its homogeneity and slightly modifies the symmetry and the frequency of the vibrational normal modes of the graphene lattice. For example, computing the normal modes of the functionalized graphene, in the region around the G and D peaks, vibrational symmetries very similar to the ones of the canonical G and D peaks appear (see Figure 5.14). Hence, the bands in the Raman spectrum centered at 1383 cm^{-1}, at 1520 cm^{-1}, and at 1574 cm^{-1} are labeled here as D$_Y$, D"$_Y$, and G$_Y$ respectively, since they originate from modified graphene lattice vibrations due to the grafting of azomethine ylide.

In comparison with the results shown in Chapter 3, here is possible, thanks to the high quality of the graphene substrate, to identify the Raman peaks arising from the azomethine ylide in the region 1000 – 1300 cm^{-1}, which is a region where several bands related to structural defects appear, especially in highly defected graphene samples. On the other hand, the second order of the stretching vibrational bands of the ylide (which should arise in the region 1900 – 2400 cm^{-1}) are here not detected, possibly due to a lower degree of functionalization (because of a lower density of defects in the

graphene substrate).
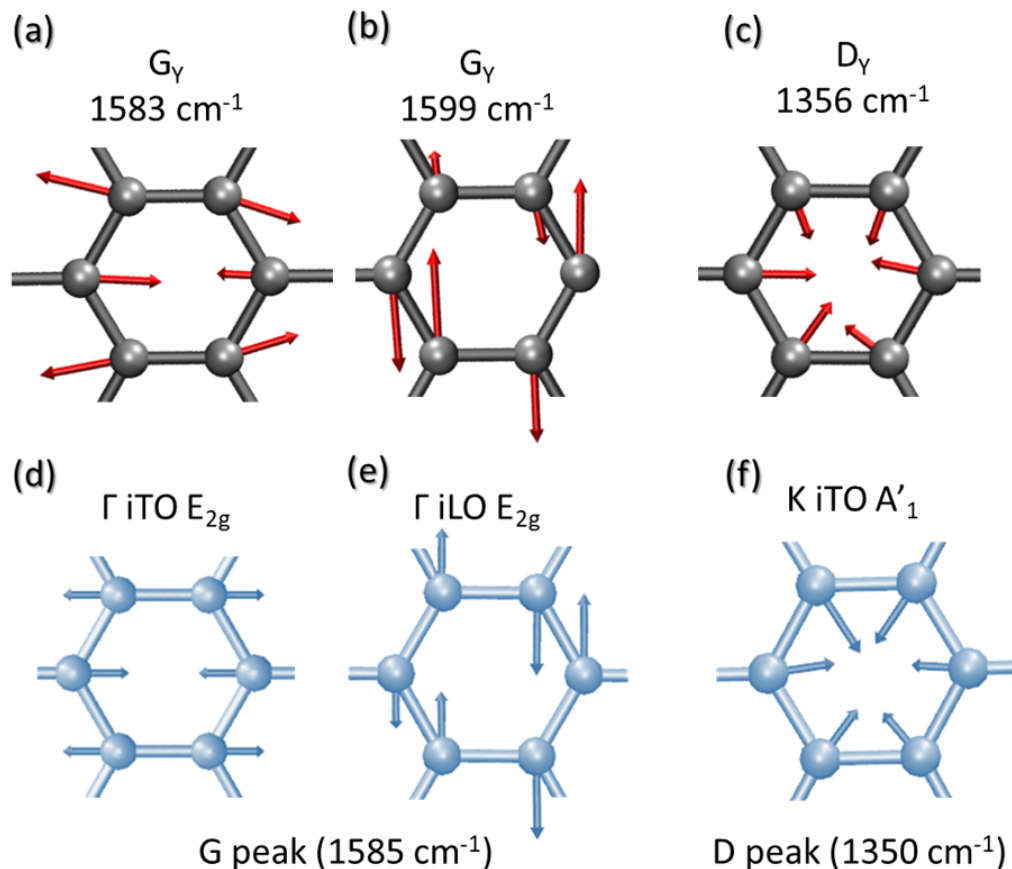
Figure 5.14: Computed vibrational normal modes (calculated using the VIBRATIONAL–ANALYSIS module of CP2K) in the region of (a–b) the G_Y and (c) the D_Y bands, slightly different from the well–known classic normal modes of (d–e) the G peak in pristine graphene and (f) the D peak in defective graphene.[209]

5.3 Reversibility of the functionalization

Finally, the evolution of the surface functionalization for increasing laser power irradiation is investigated. In order to explore it, subsequential Raman spectra are collected from the same position in the functionalized patterned area of the graphene flake (Flake 3). The power of the excitation laser can be varied with different internal optical filters allowing measurements at various incident powers, which were accurately measured with a power meter. The actual incident laser powers used in this investigation are 22 μW, 120 μW, 210 μW, and 1560 μW. As shown in Figure 5.15, for increasing laser power irradiation, the intensity of the Raman modes previously assigned to the functionalization of the graphene lattice with azomethine ylide gradually decreases.

In order to quantify the modifications in the Raman spectra, fits with the same bands that were identified from the previous analysis (see Figure 5.13 for reference) were performed. For each Raman spectrum, it is useful to normalize all peak intensities to the intensity of the G peak (see Table 5.1). Looking at the bands that originate from the functional groups of the azomethine ylide, we notice that $I(\text{CH}_3)/I(\text{G})$ passes
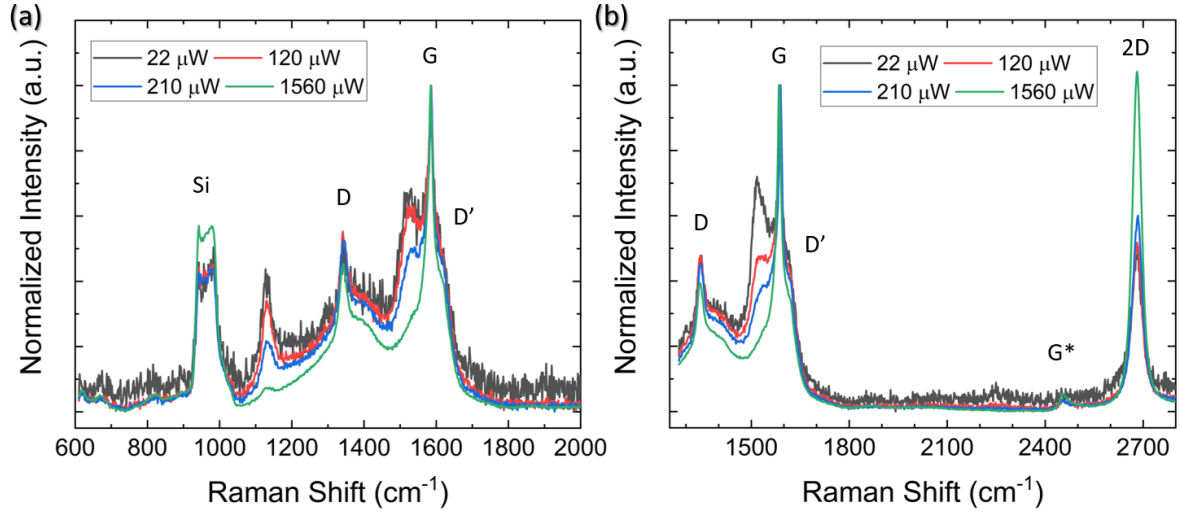
Figure 5.15: Raman spectra of de–functionalization. Raman spectra (normalized to the intensity of the G peak) of functionalized graphene (Flake 3) collected at increasing laser power (a) in the region 600 – 2200 cm^{-1} and in (b) the region 1350 – 2800 cm^{-1}.

from 0.83 (for the spectrum collected at 22 μW) to 0.07 (for the spectrum collected at 1560 μW). Similarly, I(catechol/D*)/I(G) passes from 0.18 to 0.10. Also the modified graphene vibrational bands gradually decrease in intensity when increasing the incident power. In fact, I(D$_Y$)/I(G) passes from 0.83, for the spectrum collected at 22 μW, to 0.39 for the spectrum collected at 1560 μW. Likewise, I(D"$_Y$)/I(G) decreases from 0.64 to 0.05, and I(G$_Y$)/I(G) from 1.28 to 0.42. Finally, I(2D)/I(G) notably increases from 0.88 to 1.54, while the 2D peak FWHM decreases from 40 cm^{-1} to 30 cm^{-1}.

Table 5.1: Intensity of the Raman peaks arising from functionalized graphene normalized to the G peak intensity, for spectra collected at different incident laser power.

Laser power	22 μW	120 μW	210 μW	1560 μW
I(CH$_3$)/I(G)	0.83	0.50	0.28	0.07
I(cathecol/D*)/I(G)	0.18	0.17	0.15	0.10
I(D)/I(G)	0.37	0.44	0.44	0.30
I(D$_Y$)/I(G)	0.83	0.62	0.56	0.39
I(D"$_Y$)/I(G)	0.64	0.54	0.30	0.05
I(G$_Y$)/I(G)	1.28	0.83	0.77	0.42
I(2D)/I(G)	0.88	0.92	0.98	1.54

The partial recovery towards the spectrum of non–functionalized patterned graphene suggests the desorption of the azomethine ylide from the surface. The broad band [920 – 1050] cm^{-1} coming from the Si signal of the silica substrate is visible in Figure 5.15(a). The intensity of the Si peak increases with increasing laser power, which is consistent with the desorption of the ylides. Often, surface reactions promoted by laser irradiation are thermally activated processes, but in this case the substrate heating is estimated to be less than a few degrees, due to the very low laser power used in the

Raman measurements. Therefore, other photoinduced chemical processes are involved in the desorption of the azomethine ylide. Possibly, the energy of the incident photons (2.3 eV) would activate a resonant vibrational excitation[210] that can overcome the two C–C bonds of the molecule with the graphene surface (the C–C bond energy is estimated to be ~ 1 eV).[211] Consequently, a photoinduced dissociation process could activate the retro–cycloaddition (as seen in case of functionalized fullerenes),[212] resulting in the desorption of the azomethine ylide. The complete understanding of the desorption process will require further investigations. However, our results undoubtedly indicate the reversibility of the functionalization. Indeed, this is a valuable result in view of designing more complex surface functionalization, by implanting different molecules in sequential steps for example, or simply to recover a clean graphene sheet.

5.4 Conclusions

In this Chapter we have presented a technique that successfully allowed a spatially–resolved functionalization of monolayer graphene by combining low–energy EBI with 1,3–dipolar cycloaddition of azomethine ylide. Low–energy EBI is shown to be a versatile method for defect engineering in graphene, allowing for the introduction of mild modifications of the graphene lattice. Due to the defect pattern, which can be designed with the high spatial resolution of the EBI (few nm), it was possible to selectively enhance both the chemical activity of the graphene sheet towards the organic functionalization and the adhesion of the graphene monolayer to the silicon dioxide substrate. AFM and Raman spectroscopy analysis demonstrated a homogeneous distribution of the defects in the patterned area after low–energy EBI. After the functionalization procedure, only the patterned area of graphene, which maintained the original pattern periodicity, exhibited new Raman features, which were assigned with the aid of DFT simulations of the vibrational power spectrum of functionalized graphene. These new features originated from the presence of the azomethine ylide, both from the functional groups of the molecule itself and from the modifications that the molecule induced in the vibrational normal modes of the graphene sheet. Their identification in the Raman spectra of chemically modified graphene is now available as a new method for the assessment of the covalent functionalization of graphene systems, even in case of low–density coverage, when the Raman signature of the ylide cannot be directly detected. Finally, the organic functionalization was shown to be thermally stable (up to 180 ℃ for analogous systems, as shown in Chapter 3) but reversible through laser irradiation.

While cycloaddition reactions were already used in previous works for the covalent functionalization of graphene in the liquid phase, the achievement of a selective organic functionalization of a higher quality graphene system like exfoliated monolayer flakes opens the route for a wider range of applications. In fact, by exploring the controlled use of defect engineering, the precise building of specific nanostructures is possible, such as electrochemical devices for sensing or gas storage. Moreover, specifically designed surface patterns will support the assembly of graphene multilayer systems, where the molecules that act as spacers or linkers can be precisely positioned over the tailored graphene surface. These results, available in the preprint version online (see Ref. 213) and currently in the submission process, also validate the interest in further exploring the nature, the shape, and the quantity of the defects in different high quality graphene systems, like multilayer exfoliated flake, monolayer or multilayer epitaxial graphene, and CVD grown graphene. Remarkably, the stability of the functionaliza-

tion is an advantage for applications at room temperature. Finally, the possibility of local de–functionalization via high resolution laser irradiation opens the route for a further tailoring of the surface with different organic species towards multi–functional graphene–based devices, such as printed 2D integrated circuits.

Functionalization of Epitaxial Graphene

6

In this last chapter, we present some preliminary results on the organic functionalization of epitaxial graphene (EG) on silicon carbide (SiC). EG unlocks the invaluable potential of Scanning Tunneling Microscopy/Spectroscopy (STM/STS) measurements directly on the graphene sample, without further procedures. On the contrary, because silica (SiO_2), which is the common substrate for dispersed nanosheets and exfoliated flakes due to the favorable optical contrast for graphene on it, is not conductive, STM/STS measurements on these graphene systems would require the complex transfer on a conductive substrate or the metallic patterning around the graphene on silica. Indeed, EG allows STM/STS investigation and avoids the risk of introducing contaminants during further procedures. Being capable of molecular and atomic resolution, STM and STS are extremely beneficial for fundamental studies and detailed investigations at the nanoscale and below. For this reason, even if due to time limitations these experiments were not completed, useful data were obtained.

EG on SiC is investigated with STM and Raman spectroscopy before and after the 1,3–dipolar cycloaddition (1,3–DC) with azomethine ylide. STM images of functionalized EG reveal the appearance of new structures, randomly arranged over the flat terraces (with lower density) and along the edges (with higher density), with an average height in the range (2 – 15) Å, and a graphene surface coverage of $\sim 14\%$. The graphene structure is preserved after the functionalization procedure, as confirmed by atomically resolved STM images of its hexagonal lattice. STS spectra acquired on functionalized EG indicate the opening of a bandgap (of $0.13 - 0.20$ eV) in the local density of states (LDOS) of these new structures, in contrast with the zero–gap linear behavior measured on non–functionalized graphene. The Raman analysis of functionalized EG exhibit new features in the region $1300 - 1550$ cm^{-1}, together with a downshift of the G and 2D peaks. Even though the complex Raman peak structure of the SiC substrate lies in the same region of these new peaks, these results are analogous to the ones revealed in previous experiments on functionalized exfoliated graphene flakes (reported in Chapter 5) and are consistent with the grafting of azomethine ylides on graphene.

After patterning with low–energy Electron Beam Irradiation (EBI), Peak Force – Quantitative NanoMechanical (PF–QNM) measurements allow to identify the designed defect pattern, confirming the spatial resolution of the technique (with different electron doses and e–beam scan step sizes). Moreover, the analysis of the adhesion forces mapped over patterned and non–patterned EG (both monolayer and buffer layer) presents a qualitative comparison of the different interactions between the EG and the substrate. The patterning results in an enhancement of the adhesion of the graphene

with the substrate, as already seen in previous experiments (see Chapter 5).

Although incomplete, these are valuable results in the outlook of a deterministic and controlled chemical functionalization of EG on SiC. Firstly, the detection and analysis of new features arising from the 1,3–DC of azomethine ylides endorse this functionalization procedure also for EG. Secondly, low–energy EBI is demonstrated to be a viable method for the introduction of defect patterns in EG. The correspondence between the designed pattern parameters and the measured morphology of patterned EG (such as electron dose or scan step size) confirms the reliability of this technique. Finally, our investigation suggests the optimal EBI parameters for a patterning towards a future chemical functionalization.

6.1 Pristine Epitaxial Graphene

6.1.1 STM images of pristine EG

STM is a powerful scanning probe microscopy technique, which exploits the exponential decay of the tunnel current between the sample surface and the metal tip to achieve atomic spatial resolution (as explained in detail in Section 2.10). In our setup (constant current mode), a voltage bias of ~ 1 V is applied between the sample and the tungsten tip, and a current setpoint of ~ 1 nA is set, which means that the distance between the sample surface and the tip is less than 10 Å. Being so close to the surface, the scanning tip is extremely sensitive to every feature in the sample surface. Therefore, in order to remove any adsorbates (such as water or gases molecules) coming from the environment, prior to the STM measurements our EG samples were initially degassed in UHV (base pressure $\sim 10^{-10}$ mbar) at ~ 600 °C overnight, followed by a short 10 minutes degassing at ~ 800 °C.
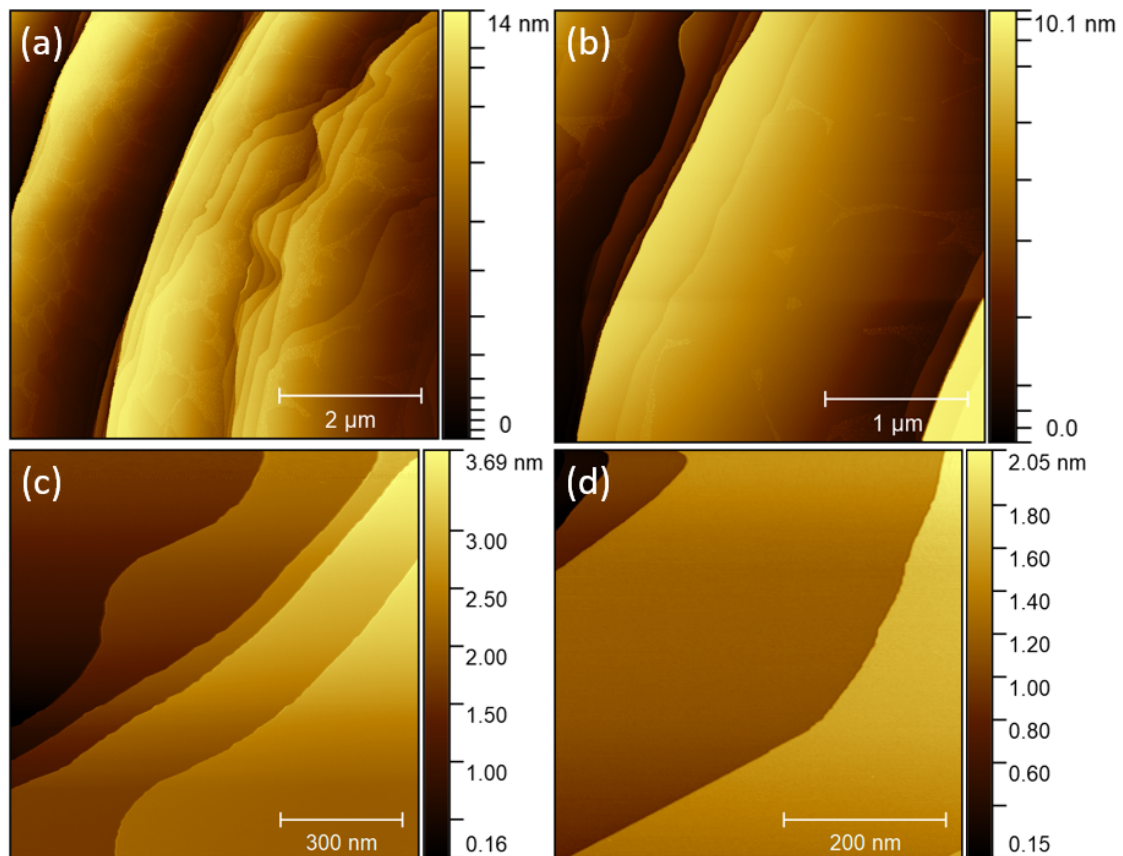
Figure 6.1: STM images of pristine EG in different zones: (a) $6 \times 6~\mu m^2$ (image parameters: 0.7 V, 1.0 nA), (b) $3 \times 3~\mu m^2$ (1.0 V, 1.0 nA), (c) $1 \times 1~\mu m^2$ (1.0 V, 1.0 nA), and (d) $0.5 \times 0.5~\mu m^2$ (1.2 V, 1.0 nA) wide areas.

Pristine epitaxial graphene on SiC exhibits an atomically flat surface with steps. These steps belong to the SiC substrate and result from the small angle off the crystallographic axis at which the silicon carbide substrate was cut. The average width of the terraces depends on the miscut angle. As can be seen from the STM images of pristine EG (see Figure 6.1), our samples present μm–large terraces with principally

monolayer graphene and a very low percentage of buffer layer graphene, which can be clearly identified even at larger scale by its higher corrugation.[214]

Because these samples are mostly monolayer EG, the STM images at lower scale were acquired principally in zones with no buffer layer. Smaller scale STM images collected in the monolayer parts exhibit atomic resolution (see Figure 6.2), confirming the high quality of the graphene samples. In fact, a defect–free graphene honeycomb lattice is revealed, with a lattice parameter of (2.4 ± 0.2) Å, in perfect agreement with the theoretical value of 2.46 Å.[10] Also the measured corrugation, with a RMS average of (0.31 ± 0.08) Å, corresponds to the literature value for monolayer graphene (~ 0.4 Å).[214]
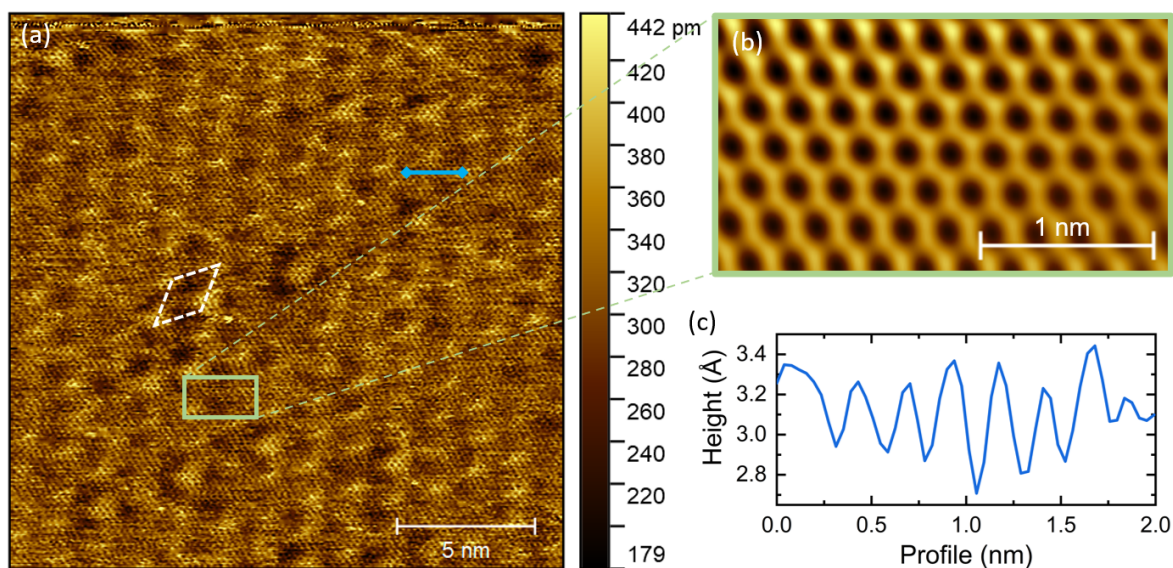
Figure 6.2: STM image of pristine monolayer EG at small scale: (a) a 20×20 nm^2 wide area (image parameters: 0.73 V, 0.40 nA), showing the quasi–(6×6) unit cell (white dashed diamond), (b) a FFT–filtered zoom of the area indicated by the green rectangle, showing the atomic graphene lattice, (c) height profile taken along the blue line shown in panel (a) (showing the graphene lattice periodicity of ~ 2.4 Å).

Moreover, Figure 6.2(a) shows the characteristic quasi–(6×6) periodicity,[215] associated with the Moiré pattern. In the case of EG on SiC, the hexagonal buffer layer (with a lattice parameter of 2.46 Å)[10] differs from the hexagonal faces of SiC (with a lattice parameter of ~ 3.08 Å).[216] The resulting super structure is called Moiré pattern,[217] and is transferred to the monolayer graphene on top, resulting in a periodicity of ~ 1.8 nm (indicated by the white dashed diamond in Figure 6.2(a)).[218]

6.1.2 Raman spectrum of pristine EG

Epitaxial graphene lies on the silicon carbide substrate underneath, with the buffer layer chemically bound to the substrate and the monolayer just on top of it. Therefore, Raman analysis of EG on SiC has to take into account the complex peak structure arising from the silicon carbide crystal. The Raman signature of SiC was recorded by collecting several spectra on a substrate before the graphene growth, performing the average. The SiC contribution is particularly important under 2000 cm^{-1} of Raman shift, as shown in Figure 6.3 (red line).
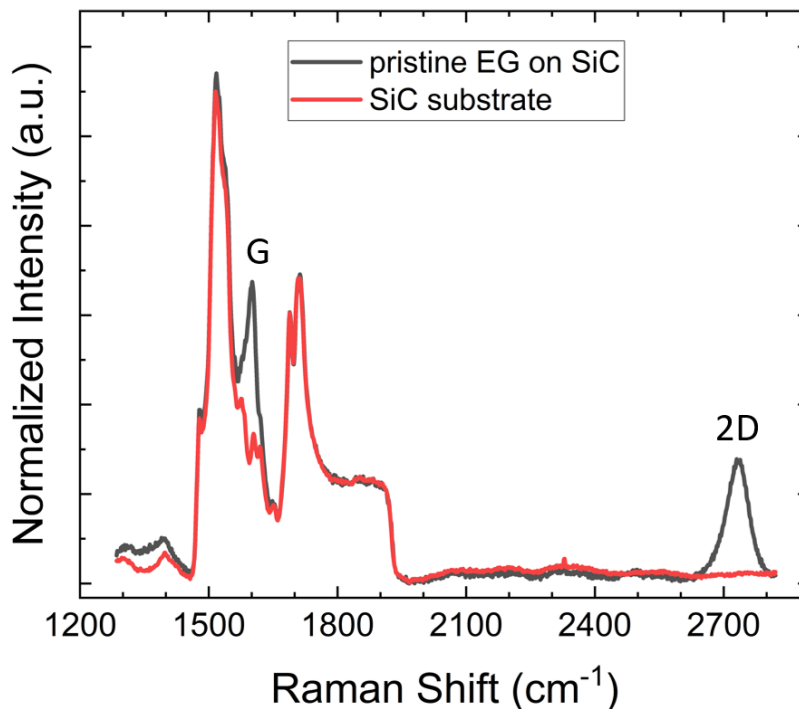
Figure 6.3: Raman spectra collected on the SiC substrate (red line) and on pristine EG on SiC (black line). For an easier comparison, the spectrum of EG was normalized to the spectrum of SiC, which is the average of several spectra collected in different positions, using the intensity of the broad shoulder at ~ 1900 cm^{-1} as reference. The characteristic graphene G and 2D peaks are labeled.

The spectrum of pristine EG on SiC (shown as black line in Figure 6.3) exhibits the characteristic G peak, arising from the in–plane stretching of the bond of C–atom pairs in the graphene hexagonal ring, and 2D peak, originating from a process which involves two phonons and in which momentum is conserved. The G peak, here centered at 1598 cm^{-1}, is often difficult to extract since it is in the middle of the complex peak structure of the silicon carbide spectrum. Moreover, due to the interaction between the substrate and the graphene that forms on top of the silicon carbide, a perfectly flat background cannot be recovered by simply subtracting the SiC spectrum (see Figure 6.4). On the other hand, the 2D peak, here centered at 2732 cm^{-1}, lies in a Raman shift region where the SiC contribution is negligible, allowing for a more reliable analysis. The shape of the 2D peak provides a reliable method to assess the number of layers of epitaxial graphene on SiC. First of all, an asymmetrical shape indicates multilayer (> 2) graphene, towards the well-known spectrum of graphite.[219] In case of a single symmetrical 2D band, from its fitting, it is possible to distinguish the monolayer EG (single peak) from the bilayer graphene (four peak contributions). More in general, even in the case when a single peak cannot be distinguished from multiple contributions, a 2D width (FWHM) below 65 cm^{-1} indicates monolayer EG, 65 cm^{-1} < FMHW < 75 cm^{-1} indicates bi-layer EG, and FMHW > 80 cm^{-1} indicates multilayer EG.[220] Here, the 2D peak can be fitted with a single symmetrical Lorentzian curve, with a FWHM of 52 cm^{-1}, confirming that the sample is principally monolayer graphene. In addition, a small D peak is detected, here centered at 1358 cm^{-1}, which involves intervalley double resonance processes in presence of defects. Considering

that, like the G peak, also the D peak lies in the zone where the SiC contribution is relevant, its intensity cannot be measured with precision. However, we can estimate an indicative value for the ratio $I(D)/I(G) \sim 0.1$, very low, which means that our samples present a near defect–free graphene surface.

Finally, as seen in previous graphene samples, the weak G* band is visible, here centered at 2484 cm^{-1}, arising from an intervalley process involving an in–plane transverse optical phonon and one longitudinal acoustic phonon.
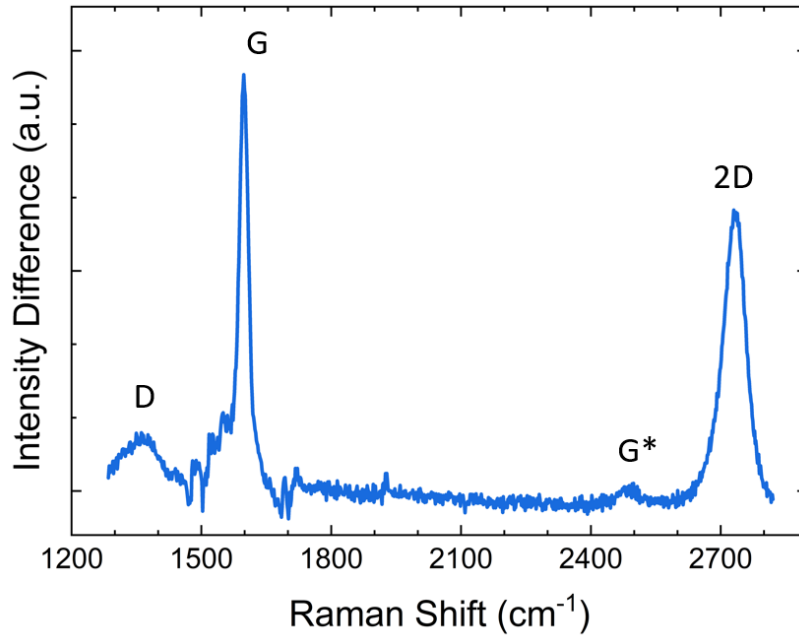
Figure 6.4: Intensity difference between the Raman spectra shown in Figure 6.3. The characteristic graphene D, G, G*, and 2D peaks are labeled.

6.2 Functionalization of near defect–free Epitaxial Graphene via 1,3–DC

Pristine, near defect–free, monolayer EG is functionalized via a wet chemistry process, by adding N-methylglycine and 3,4-dihydroxybenzaldehyde in NMP, as explained in Section 2.3.3. Several time intervals were explored for the functionalization procedure, increasing the time, step by step, from 1 up to 10 days, in order to explore the possibility of a higher functionalization with the azomethine ylide molecules. Finally, the solvent is removed by multiple rinses, and subsequently Raman spectroscopy and STM/STS measurements are performed. Both the Raman and the STM analyses show similar results for each of the different functionalized samples, independent of the duration of the functionalization process. Therefore, here the results obtained after the 10 days are presented.

After the functionalization procedure, in order to avoid any possible degradation or desorption of the ylide, no high temperature degassing is performed. Instead, EG samples are stored in UHV for several days, at a pressure in the range of $\sim 5 \times 10^{-10}$ mbar, allowing for a slower degassing of surface adsorbates. The pressure of the UHV chamber is monitored, and after a couple of days it recovers its base value of $\sim 1 \times 10^{-10}$ mbar. This means that no excessive dirt or environmental gases are still adsorbed on the graphene surface, and, therefore, STM measurements can be performed without severe risks for the scanning tip. However, this procedure does not completely avoid the presence of residual adsorbates from the chemical functionalization, which could affect the resolution of the STM images.

6.2.1 STM analysis

From the STM images acquired at intermediate range (see Figure 6.5) new structures can be detected, which were not present on the surface of pristine EG.

Cluster–like structures are randomly distributed on the flat part of the graphene sample, whereas filament–like structures are mostly aligned along the step edges. The higher chemical reactivity of the graphene at the edges is well know[221] and, therefore, a higher density of edge–aligned filaments with respect to clusters is expected, as can be seen it Figures 6.5(a) and 6.5(d). Interestingly, the position of the clusters does not change in successive images, and, therefore, the scanning tip does not carry them around. This is a first indication that these structures are chemisorbed (and not only physisorbed) on graphene. Collecting several height profiles on these structures, it is possible to obtain their average dimensions, with a height in the range of $2 - 10$ Å for clusters (see Figures 6.5(b), 6.5(e) and 6.6(b)) and in the range of $5 - 15$ Å for filaments (see Figures 6.5(c) and 6.5(f)). Moreover, mapping the area of clusters and filaments grafted on the graphene, it is possible to calculate the surface coverage, as an indication of the functionalization efficiency. Here, considering only the area of the flat terraces, we obtain an average graphene surface coverage of $\sim 5\%$. Otherwise, taking into account also the larger coverage along the edges, an average graphene surface coverage of $\sim 14\%$ is calculated. These values show that, in case of near defect–free EG, only a low percentage of functionalization is achieved.

While acquiring smaller scale STM images of EG after the functionalization, it is very difficult to resolve the atomic graphene lattice. This issue comes from the presence of the clusters and their unstable interaction with the scanning tip. Therefore, as shown
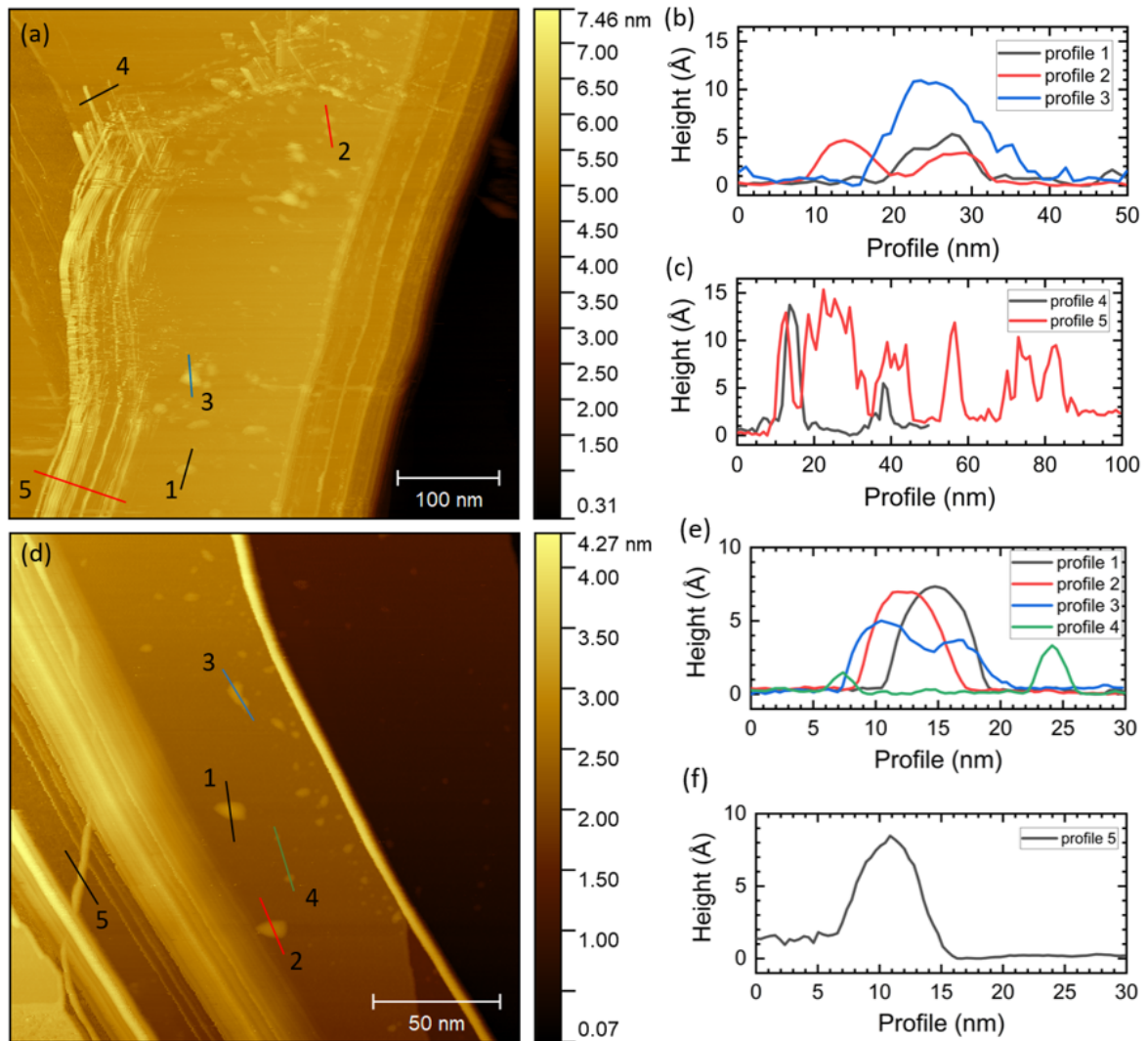
Figure 6.5: STM images of functionalized EG. (a) 500 × 500 nm^2 wide area (image parameters: 1.0 V, 0.70 nA) showing both cluster–like and filament–like new structures and height profiles collected on (b) clusters and (c) filaments taken along the lines indicated in panel (a). (d) 200 × 200 nm^2 wide area (0.8 V, 0.30 nA) showing both cluster–like and filament–like structures. Height profiles collected on (e) clusters and (f) filaments taken along the lines indicated in panel (d).

in Figure 6.6(a), after passing on top of a cluster, the resolution of the background graphene surface is worsen and scanning–line artifacts appear.
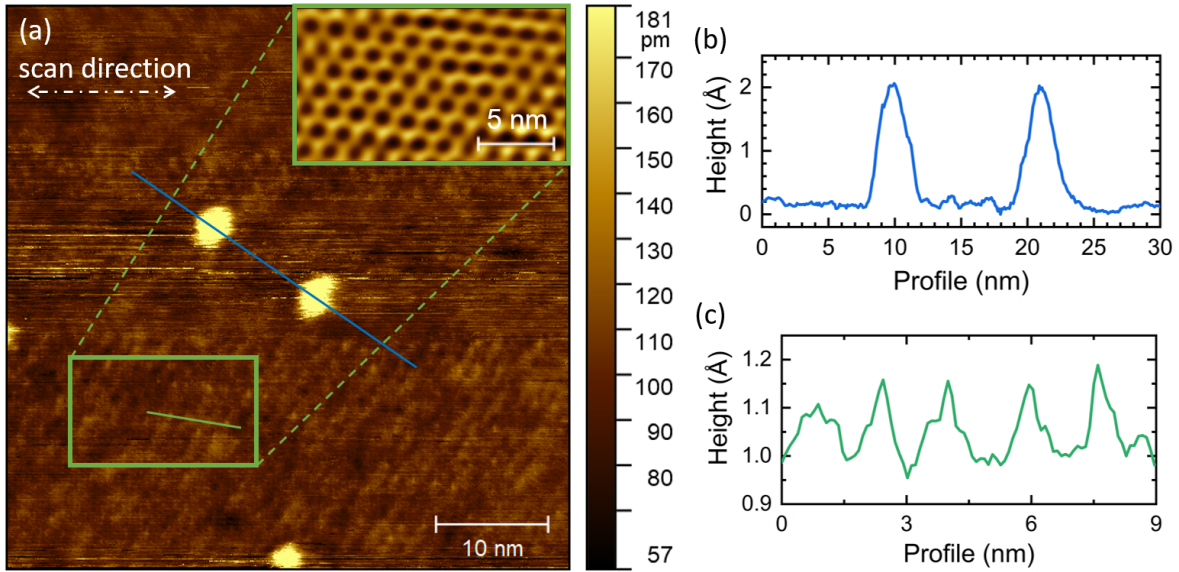
Figure 6.6: STM image of monolayer EG after functionalization: (a) a 50×50 nm^2 wide area (image parameters: 0.70 V, 0.30 nA) showing cluster–like structures and the Moirè pattern of monolayer EG in the background (the inset shows a FFT filtering on the area indicated by the green rectangle, so that the Moirè pattern is highlighted). The scan line direction is indicated by the withe arrow. Height profiles collected on (b) clusters and (c) clean EG taken along the blue and the green lines, respectively, indicated in panel (a). The height profile taken on clean EG shows the Moirè periodicity of ~ 1.7 nm.

A possible way to mitigate this problem is to slow the scanning tip, increasing the time of a scan line. On the other hand, in order to avoid thermal drift (not negligible at room temperature), the tip cannot be too slow. Here, we increase the scan line time from 0.16 s to 1.08 s. Over a scan area of 50×50 nm^2, for example, this means to decrease the tip scanning velocity from ~ 300 nm/s down to ~ 50 nm/s. Still, the resolution does not improve. This can be due to the residual presence of unstable adsorbates on the sample surface (keep in mind that no high temperature degassing was performed). These small adsorbates may interact with the scanning tip and be carried around over the surface during the scan, generating noise and artifacts in the images. Notwithstanding these problems, the Moiré pattern can be resolved in the flat area around the clusters (see the inset of Figure 6.6(a), with a periodicity of (1.7 ± 0.2) nm (see the height profile in Figure 6.6(c)), confirming that the monolayer EG is preserved after the functionalization procedure.

Eventually, after numerous scans, atomic resolution of the graphene hexagonal lattice is achieved in an area with no clusters or filaments (see Figure 6.7(a)). The FFT–filtering allows for a clear visualization of the honeycomb lattice (see Figure 6.7(b)), while from the height profile a periodicity of (2.3 ± 0.2) Å is measured (see Figure 6.7(c)). These measurements, again, confirm that the functionalization procedure preserves the graphene lattice around the new structures, without breaking its hexagonal symmetry.

Unfortunately, no atomic resolution is achieved neither on cluster–like nor filament–like structures. Therefore, a more detailed identification of these new structures is not possible only with STM experiments, and STS measurements are performed.
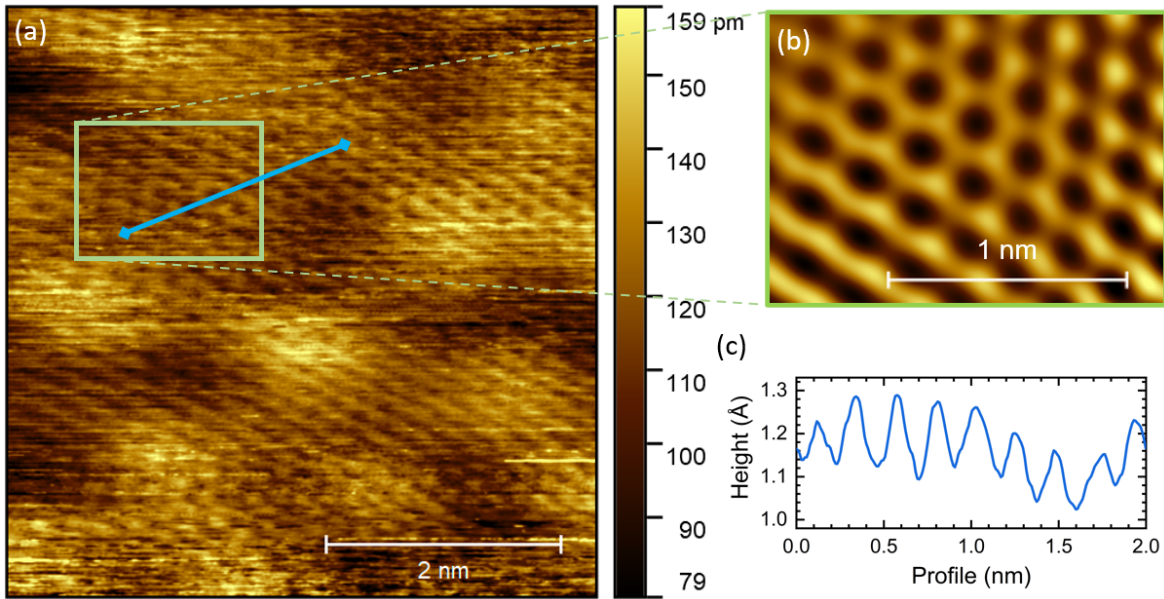
Figure 6.7: STM image of monolayer EG after functionalization: (a) a 5×5 nm^2 wide area (image parameters: 0.70 V, 0.40 nA) with no clusters or filaments, (b) FFT–filtered zoom of the area indicated by the green rectangle in panel (a), highlighting the atomic graphene lattice, (c) height profile taken along the blue line shown in panel (a) (showing the graphene lattice periodicity of ~ 2.3 Å).

6.2.2 STS analysis

Spatially–resolved spectroscopy is permitted by the precise control of the scanning tip. Therefore, the local electronic properties and the variations in the LDOS can be investigated, point by point, on the surface of functionalized EG.

Figure 6.8 shows a STM image of an area where, over the clean graphene background (as confirmed by the Moiré pattern), both clusters and filaments are imaged. After the acquisition of the image, the scan is stopped, and the tip is moved on top of the three locations marked with the blue, green, and red crosses. In order to perform STS measurements, the tip is fixed at the chosen position and a current setpoint is selected. Then, the feedback system is disconnected, so the tip stays at a fixed distance from the surface while the bias voltage is swept. 20 consecutive spectra are acquired, in the range $(-0.80$ to $0.60)$ V.

The average spectra for the three measurements are shown in Figure 6.9. The spectrum collected on the clean graphene surface (blue line) shows its characteristic metallic behavior with no band–gap: from a minimum at zero bias (which indicates the Fermi energy of the system, E_F, i.e. the energy boundary between filled and empty electron states), the dI/dV curve increases sharply for both empty and filled states. The local minimum at ~ -0.4 V, corresponds to the Dirac point of graphene. As shown by the schematic band structure in the inset of Figure 6.9, the Dirac point indicates the crossing of the linear π and π^* bands, which occurs at the K point of the Brillouin zone of graphene. The position of E_F, ~ 0.4 eV above the Dirac point, is indicative of n–type doping. This doping of the graphene layer arises from the growth process, in which electrons from the n–type SiC migrate and accumulate into graphene, and its value is in agreement with literature.[222,223]

On the contrary, the spectra acquired on the cluster–like (green line) and filament–
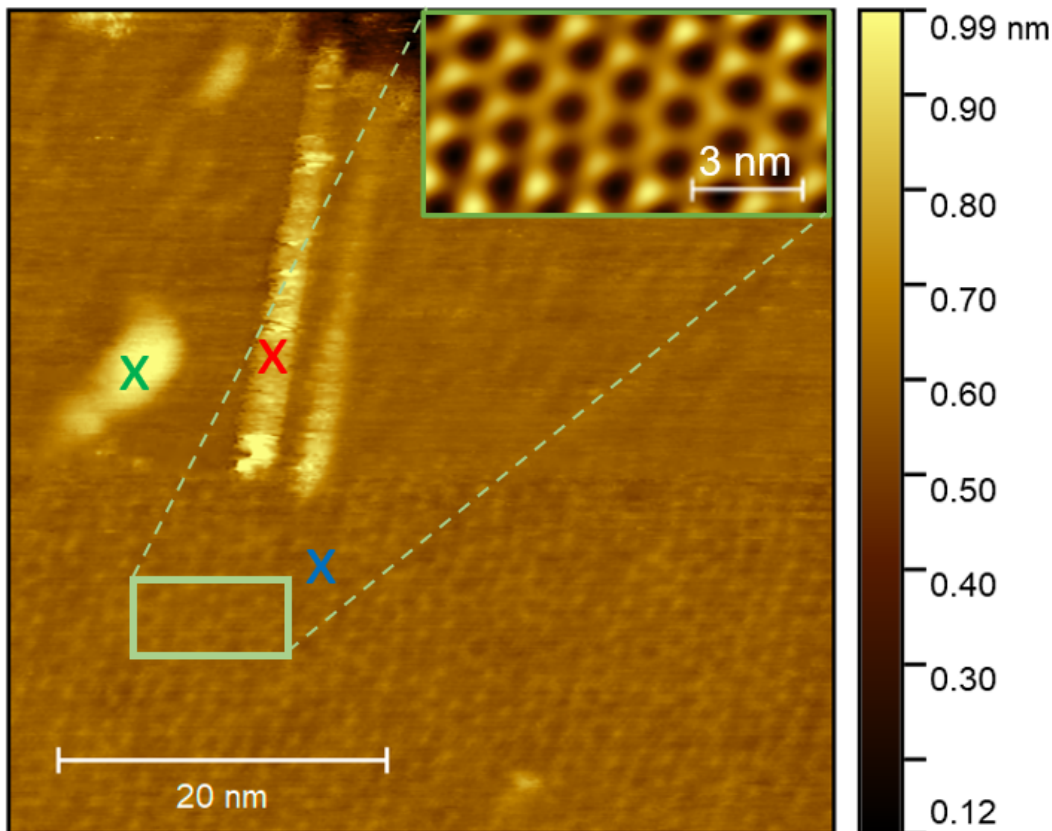
Figure 6.8: STM image of monolayer EG after functionalization: a 50×50 nm^2 wide area (image parameters: 0.30 V, 0.30 nA) where both clusters and filaments are imaged, and the Moiré pattern from the graphene background surface is resolved (with a measured periodicity of ~ 1.7 nm). The inset shows a FFT–filtered zoom of the area indicated by the green rectangle, highlighting the Moiré pattern. The colored crosses indicate the locations where the STS spectra shown in Figure 6.9 where acquired.

like (red line) features exhibit a different nature. Their dI/dV curves present a range of zero values, indicative of the opening of a band gap in the electronic structure, of (0.20 ± 0.04) eV for clusters and (0.13 ± 0.02) eV for filaments. This trend is consistent with the functionalization of EG with azomethine ylide. In fact, as the ylides covalently attach onto the graphene surface, the original sp^2 hybridization is disrupted, and the zero–gap linear characteristic dispersion is broken. Indeed, covalent modifications of graphene with cycloadditions and diazonium salts have shown an analogous gap opening in the range $0.15 - 0.5$ eV.[56,224,225]
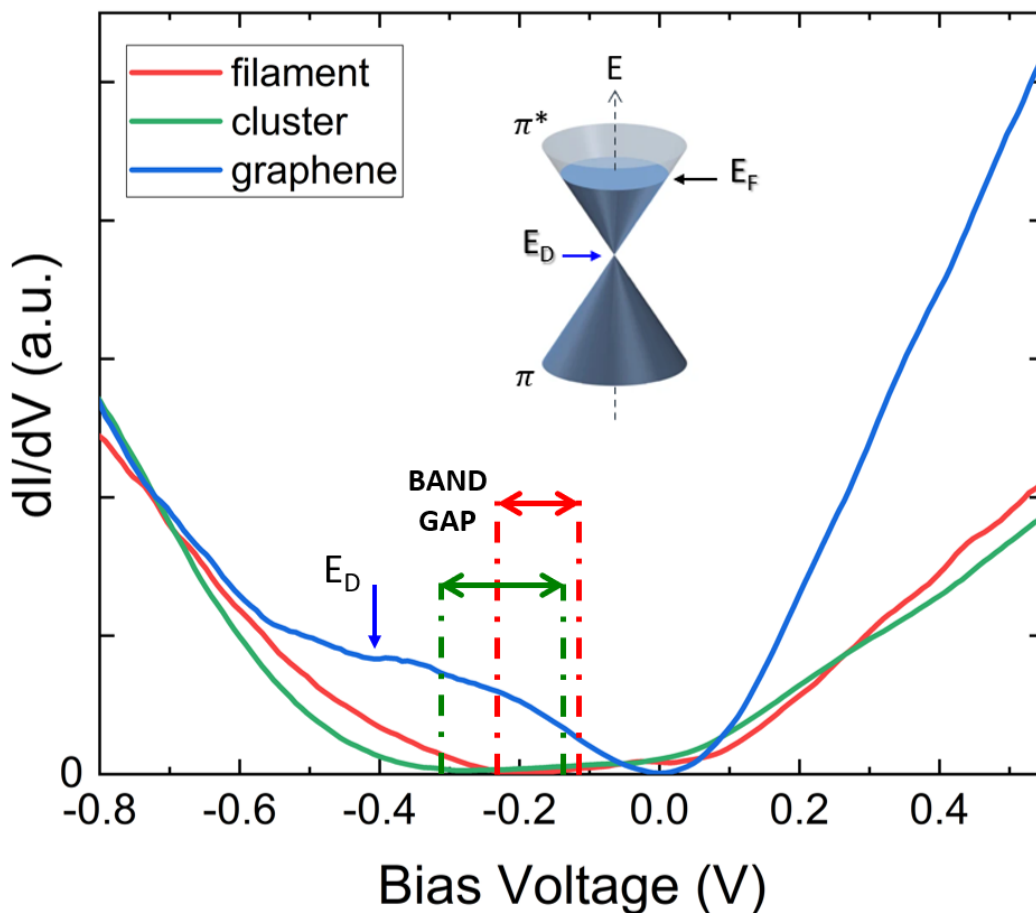
Figure 6.9: Average STS spectra acquired on different positions of EG after functionalization (spectra parameters: sweep range (−0.80 to 0.60) V, setpoint 0.30 nA): graphene background surface (blue line), cluster–like (green line) and filament–like (red line) structures. The colors of the spectra correspond to the colored crosses in Figure 6.8. The blue arrow indicates the Dirac point in the graphene spectrum, the red and green arrows indicate the gap in the filament and cluster spectra. The inset shows a schematic of a n–doped graphene Dirac cone (the energy levels of the Fermi energy and the Dirac point are indicated).

6.2.3   Raman analysis

After the functionalization procedure, the samples are investigate with Raman spectroscopy, in order to visualize new features arising from the chemical modification. Figure 6.10 shows the spectrum of functionalized EG (blue line) in comparison with the spectra of pristine EG (red line) and the SiC substrate (black line). Functionalized EG exhibits a large downshift of the 2D peak and a moderate similar downshift of the G peak. In addition, new features arise between the G and the D peaks.
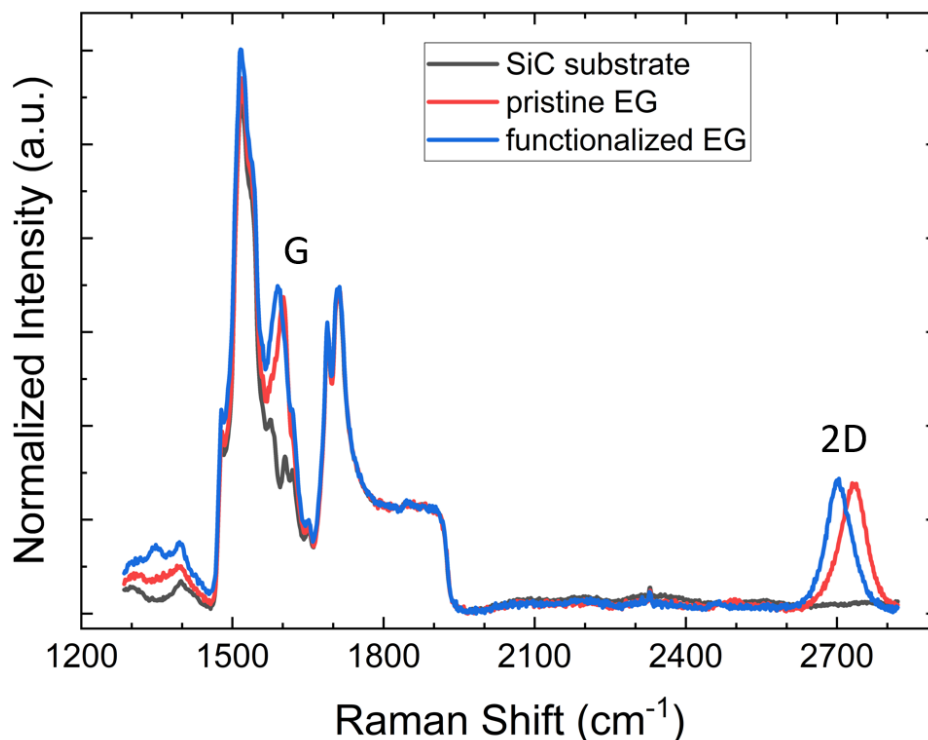
Figure 6.10: Raman spectrum collected on functionalized EG (blue line) compared with the spectra acquired on the SiC substrate (black line) and on pristine EG on SiC (red line). For an easier comparison, the spectra are normalized to the spectrum of SiC (using the intensity of the broad shoulder at $\sim$ 1900 cm^{-1} as reference). The characteristic graphene G and 2D peaks are labeled.

In order to better analyze the new Raman features of functionalized EG, the SiC spectrum is subtracted from the spectrum of functionalized EG (see Figure 6.11, blue line). Again, we have to keep in mind that, due to the interaction between the SiC substrate and the graphene on top, this simple procedure does not produce a completely reliable graphene spectrum. However, it helps to visualize the new features and allows to estimate the peaks modifications.

A downshift of both the G and the 2D peaks is noticeable: the G peak after functionalization is centered at 1593 cm^{-1}, while before it was at 1598 cm^{-1}. The 2D peak is centered at 2703 cm^{-1}, while before it was at 2732 cm^{-1}. The moderate redshift of the G peak (-5 cm^{-1}) together with a greater redshift of the 2D peak (-29 cm^{-1}) can be interpreted with the appearance of strain in the functionalized graphene structure.[205,226,227] This strain is consistent with the grafting of the azomethine ylides, which locally modify the flat graphene lattice. A frequency shift of the G and 2D peaks could also originate from electron doping.[202–204] As shown by the STS results, the electronic
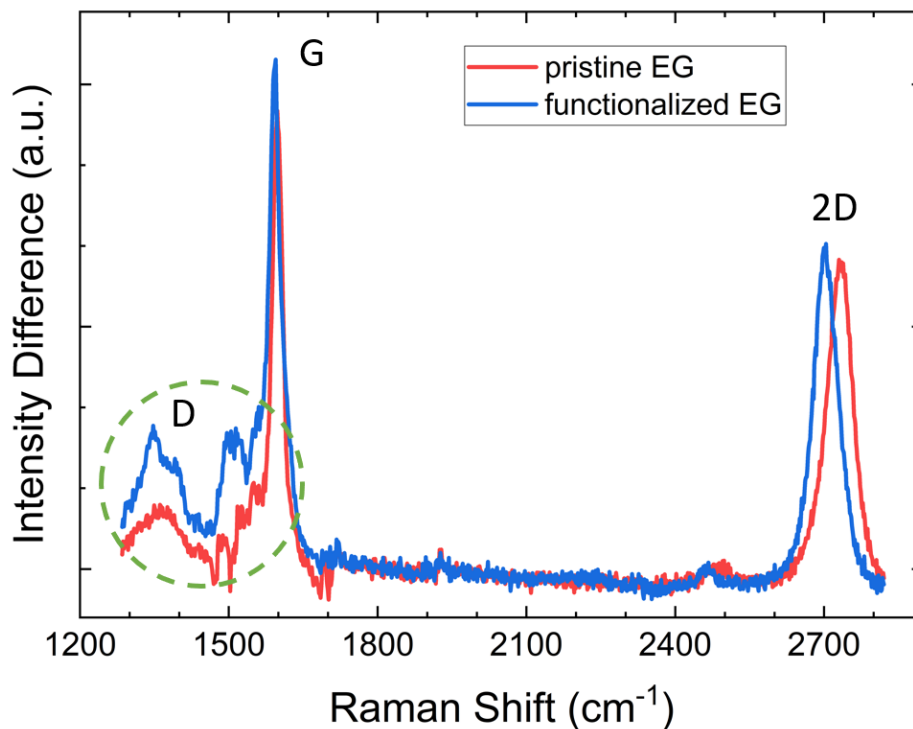
Figure 6.11: Comparison of the intensity difference between the Raman spectra of pristine EG (red line) and functionalized EG (blue line), with the silicon carbide substrate contribution subtracted. The characteristic graphene D, G, and 2D peaks are labeled, and the region where new features arise from the functionalization is indicated by the green circle. Also, the shift of the G and 2D peaks is visible.

properties of functionalized EG are modified by the ylides, which can act as an electron dopant.[228] Moreover, new Raman features arise in the region $1300 - 1550$ cm^{-1}, which are clearly shown in Figure 6.12 (intensity difference between the two curves of Figure 6.11). A new peak, centered at 1347 cm^{-1} is visible near the D peak, together with a new peak, centered at 1515 cm^{-1}, near the G peak. As discussed in Chapter 5, the presence of the azomethine ylide molecules grafted on the graphene sheet breaks its homogeneity and slightly modifies the symmetry and the frequency of the vibrational normal modes of the graphene lattice. Using the same nomenclature, here we can identify these new peaks as the D_Y and the D''_Y, respectively. The D_Y consists in the variation of the D peak, arising from the presence of new defects in the graphene structure, while the D''_Y corresponds to the modification of the D'' band, which can be associated with chemical functionalization with small molecules.[162–164]

In comparison with the results shown in previous chapters, due to the broad and complex peak structure of the SiC substrate and its interaction with the graphene layer, here it is not possible to clearly identify the Raman peaks arising directly from the functional groups of the azomethine ylide, which are found on functionalized patterned graphene flakes in the region $1000 - 1300$ cm^{-1}. On the other hand, in the region $1900 - 2400$ cm^{-1} the SiC substrate does not contribute much to the Raman spectrum and, therefore, we would expect to see the second order bands of the stretching vibrational bands of the ylide, which were found on functionalized GNS and rGO. However, possibly due to a lower coverage of the functionalization, these bands are not visible here.
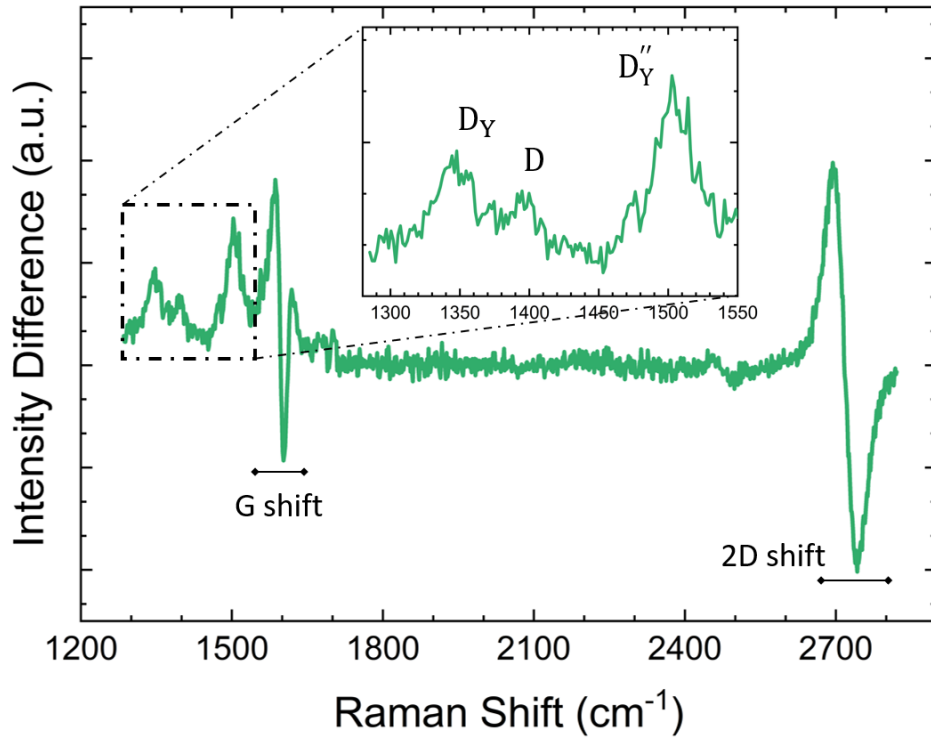
Figure 6.12: Difference between the two curves shown in Figure 6.11, highlighting the modifications arising from the functionalization. The shift of the G and 2D peaks is visible. The inset shows the zoom of the region 1300 – 1550 cm^{-1}, in which the new D$_Y$ and D"$_Y$ peaks arise.

6.3 Peak Force–QNM of Patterned Epitaxial Graphene via EBI

In order to increase the efficiency of the covalent functionalization of EG and, in particular, to be able to spatially design the functionalization of EG, defect patterning via EBI is explored. First of all, to find the optimal parameters for EBI, such as electron dose and scan step size, different EG samples are irradiated and their topography is imaged using PF–QNM. In fact, PF–QNM measurements are less time–consuming than STM measurements, allowing a faster optimization process.

Initially, gold markers are lithographed by e–beam for defining recognizable positions on the surface of the sample. Then, using different electron doses, from 10 mC/cm^2 to 120 mC/cm^2 (which corresponds to a dwell time from 12 ms to 140 ms), different patterns are designed in different positions. The other exposure parameters are kept the same for each pattern: electrons acceleration voltage 20 kV, beam current 90 pA.

Figure 6.13 shows the PF–QNM height images taken on an area irradiated with a dose of 10 mC/cm^2 (panel (a)) and on an area irradiated with a dose of 120 mC/cm^2 (panel (b)). The EG sample used for this experiments shows both a less homogeneous monolayer graphene, due to an imperfect epitaxial growth, and residual particles on the surface, probably polymer residuals from the lithography process. However, we can infer that the patterned dots cannot be detected at low dose, while they are clearly visible at higher dose. Therefore, in the following experiments, the electron dose is set to 120 mC/cm^2.
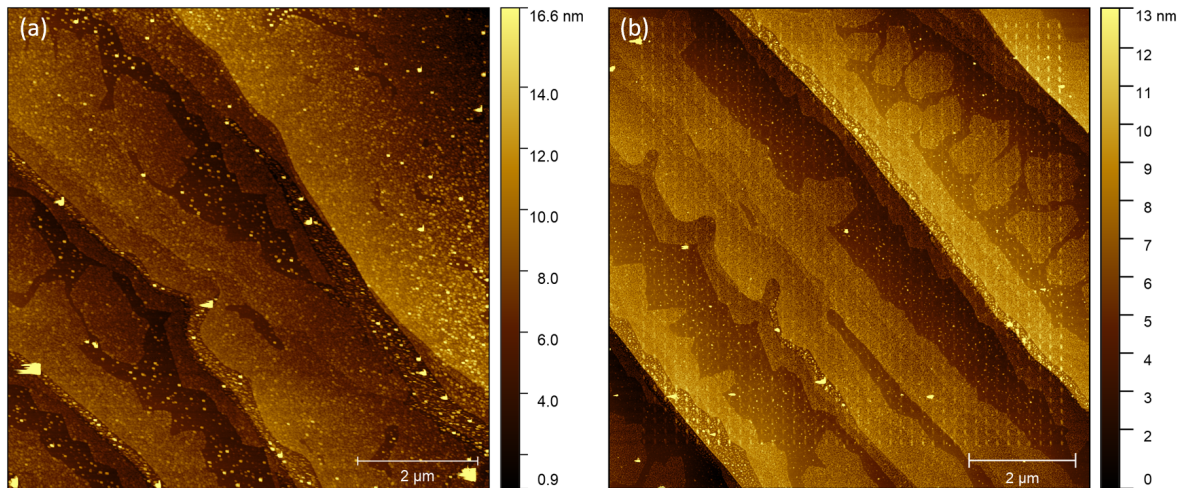
Figure 6.13: PF–QNM height images of patterned EG: (a) $8 \times 8 \ \mu m^2$ wide area irradiated with a dose of 10 mC/cm^2 and (b) $9 \times 9 \ \mu m^2$ wide area irradiated with a dose of 120 mC/cm^2.

Then, different scan step sizes are used during the EBI of a second sample: six 350 μm $\times$ 350 μm wide areas are patterned exactly in the middle of an EG sample, so, no markers are needed here. Figure 6.14 presents the CAD pattern design of a single region, with the repetition of five columns of squares, each square 5 μm $\times$ 5 μm wide, of different step size, from 100 nm to 500 nm.
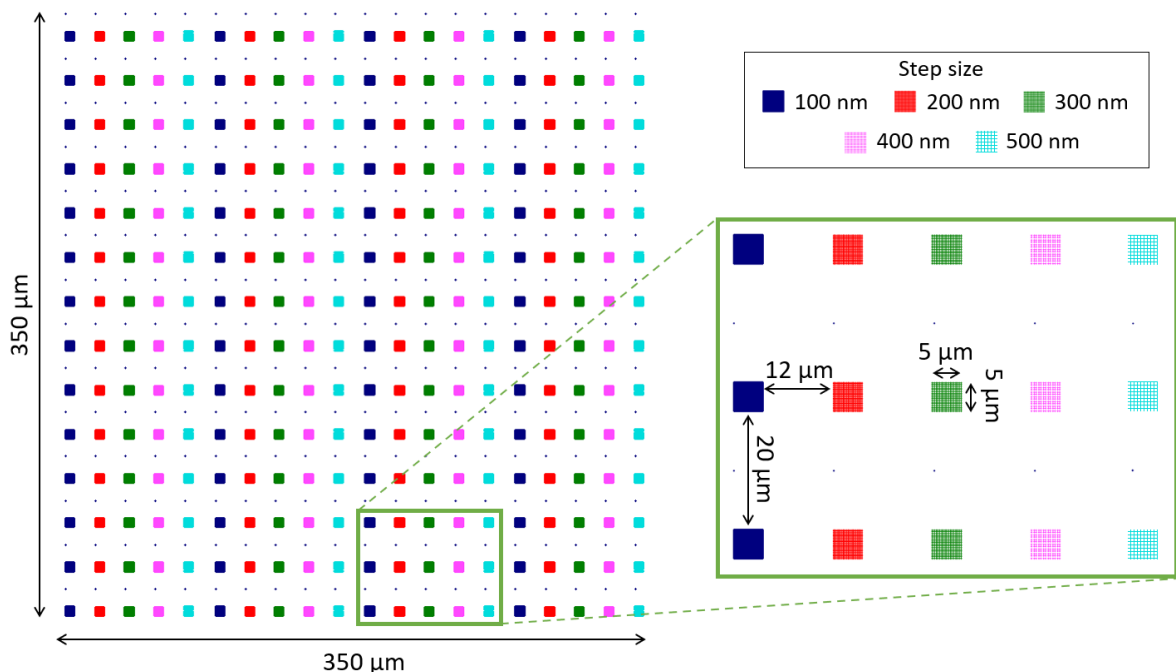
Figure 6.14: CAD project for the EBI pattern with five different step sizes, from 100 nm to 500 nm. Each square is $5 \times 5 \ \mu m^2$ wide.

Figure 6.15 shows a PF–QNM height image at large scale ($40 \times 40 \ \mu m^2$) where six patterned squares are imaged, with different scan step size. Intermediate scale PF–QNM height images ($8 \times 8 \ \mu m^2$) of 100 nm and 200 nm patterned areas are shown in Figure 6.16. Each irradiated dot is distinguishable, with no overlap or merging, even at the higher density, confirming that these EBI parameters allow to obtain a high

spatial resolution for the patterning on EG.
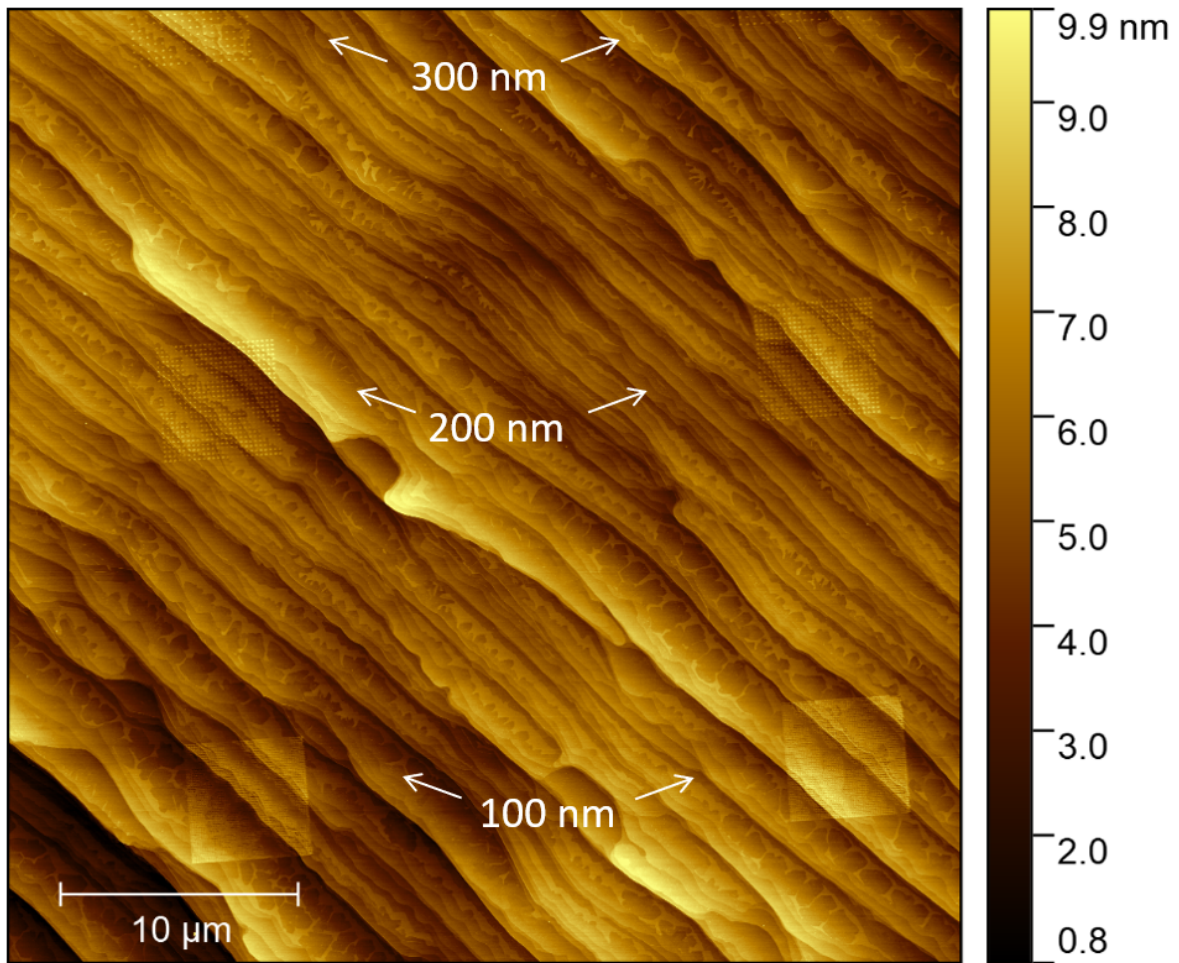
Figure 6.15: PF-QNM height image of patterned EG: a 40×40 μm^2 wide area. Six patterned regions are imaged, with step sizes of 100 nm, 200 nm, and 300 nm.

Finally, useful data can be obtain analyzing the adhesion channel of the PF–QNM images of patterned EG. Figure 6.17(a) shows a large scale adhesion force image (40×40 μm^2) where six patterned squares, with different scan step size, are visible (it is the adhesion channel of the same image shown in Figure 6.15). As seen also in the height channel images, at large scale the contrast of the patterned region decreases with increasing pitch. A smaller scale adhesion image (500×500 nm^2) collected in a patterned region, showing individual dots with 100 nm step size, is shown in Figure 6.17(b).

At both scales, a lower adhesion force is measured over the irradiated regions, especially over monolayer graphene. Typically, a lower adhesion force between the scanning tip and the topmost layer of the sample suggests a higher adhesion between the topmost layer and the ones underneath. In literature, a decrease in the adhesion between the scanning tip and the sample surface was reported in case of laser–induced graphene nanobubbles.[229] In that case it was attributed to a decrease in the contact surface between the measuring tip apex and the nanobubble, due to the temporarily modified morphology as the nanobubble acts like an elastic membrane under the tip. Here, however, the lateral resolution of our measuring PF–QNM technique ($\sim$ 5 nm) is smaller than the dimension of the irradiated dots on patterned EG ($\sim$ 50 nm), which,
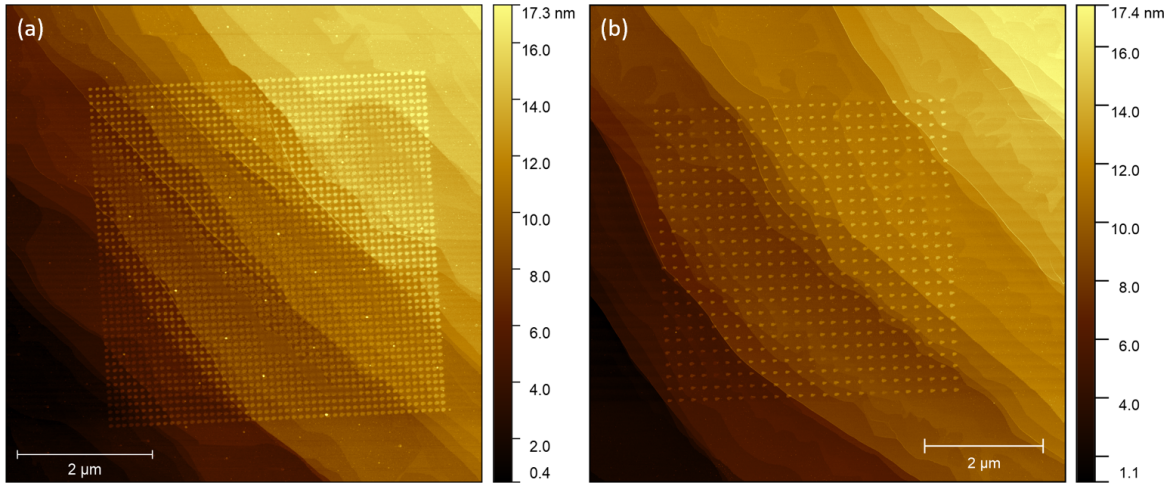
Figure 6.16: PF-QNM height images of patterned EG: $8 \times 8~\mu m^2$ wide areas showing (a) 100 nm and (b) 200 nm step size patterns.

therefore, are homogeneously mapped. For a uniform contact surface between tip and sample, the adhesion force is determined by the respective interactions, i.e. attractive or repulsive forces. Even though for a complete analysis a variety of intermolecular interactions and phenomena that affect adhesion should be taken into account, such as van der Waals forces, electrostatics, or capillarity forces,[230,231] the present study is limited to a qualitative picture. Under EBI, various defects can be introduced in the graphene structure, such as point–like or boundary–like topological defects, or even vacancies. These structural defects locally enhance the chemical reactivity of the graphene lattice, increasing its interaction with the substrate. Indeed, an enhanced adhesion between patterned monolayer graphene and the substrate was previously seen in case of patterned exfoliated flakes (see Chapter 5), where the patterned areas of the flakes remain attached to the silica substrate while the non–patterned areas detach during the functionalization procedure.

From the adhesion image shown in Figure 6.17(b), it is possible to measure and compare the adhesion force between graphene and the PF–QNM tip. On non–patterned graphene the adhesion between the buffer layer and the tip is $A_{BL—tip} \sim 0.77$ nN and the adhesion between the monolayer EG and the tip is $A_{MLEG—tip} \sim 1.18$ nN. On the patterned areas, we measure $A_{p-BL—tip} \sim 0.74$ nN and $A_{p-MLEG—tip} \sim 0.79$ nN. Because, in our setup, it is not possible to precisely calibrate the mechanical characteristics of the scanning tip, it is to be kept in mind that these are not absolute values. However, they permit a reliable qualitative comparison. Noteworthy, for the buffer layer, the adhesion measured on non–patterned and patterned areas is nearly the same ($A_{BL—tip} \sim 0.77$ nN vs. $A_{p-BL—tip} \sim 0.74$ nN). On the contrary, a bigger decrease is measured over monolayer EG ($A_{MLEG—tip} \sim 1.18$ nN vs. $A_{p-MLEG—tip} \sim 0.79$ nN), which, after EBI, reaches a value very similar to the one measured over the buffer layer. This result supports the idea that topological defects break the perfect sp^2–hybridization of monolayer graphene, introducing sp^3 bonds, similarly to the buffer layer structure. In addition, a lower adhesion between the tip and the buffer layer with respect to the one between the tip and the monolayer was expected, due to the residual interactions of the carbon atoms of the buffer layer with the SiC substrate underneath. Finally, a similar adhesion decrease, of ~ -0.40 nN, was measured on patterned graphene with respect to non–
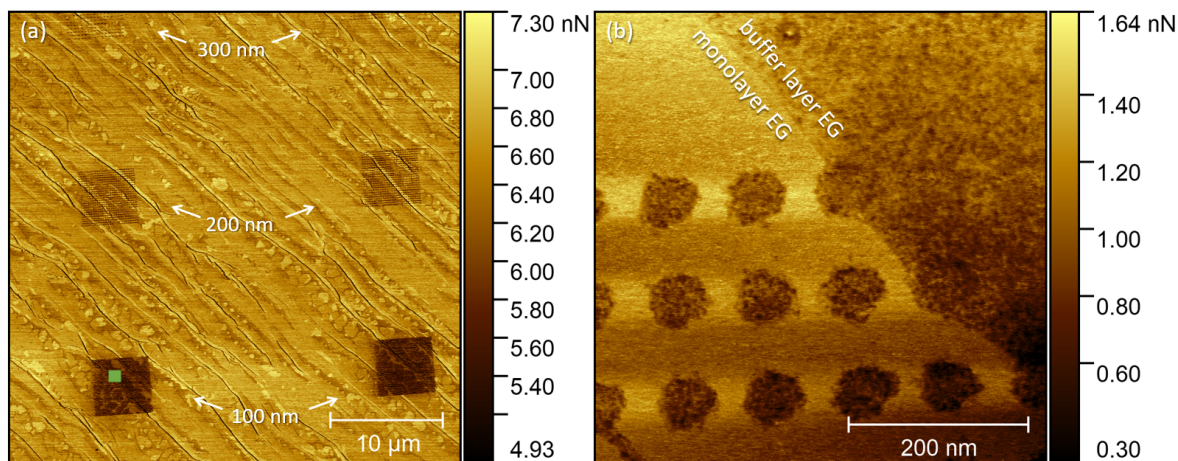
Figure 6.17: PF–QNM adhesion image of patterned EG: (a) a large scale $40 \times 40 \ \mu\text{m}^2$ wide area showing six patterned regions, with step size of 100 nm, 200 nm, and 300 nm, and (b) a small scale $500 \times 500 \ \text{nm}^2$ wide area with step sizes of 100 nm collected in the region indicated by the green square in panel (a) (the edge between monolayer and buffer layer EG is labeled). Noteworthy, lower adhesion force is mapped over the irradiated spots.

patterned areas in a preliminary QNM investigation on exfoliated graphene flakes on silica substrates.

6.4 Conclusions

In these preliminary experiments on EG on SiC, we have presented surface modifications of EG obtained via 1,3–DC of azomethine ylide. The chemical functionalization modified both the surface morphology and the Raman signature of EG. In particular, new cluster–like and filament–like structures appeared on the graphene surface after functionalization. The first ones were randomly placed over the monolayer flat terraces, with low density, while the latter tended to aggregate with higher density along the terrace edges, which are known to present higher chemical reactivity. Although no atomic resolution was achieved, spatially resolved STS measurements indicated a gap–like behavior for these new features, completely different from the standard linear LDOS of clean graphene. Moreover, Raman spectroscopy of functionalized EG revealed structural modifications of the graphene lattice, with the appearance of new peaks and redshifts of the G and 2D peaks. These results are consistent with the grafting of azomethine ylides onto EG.

Finally, a patterning of EG on SiC via EBI was performed. Preliminary investigations on the electron dose and the e–beam scan step size were explored, and PF–QNM height and adhesion images were collected on patterned EG. The successful introduction of the designed defect pattern was confirmed, and the analysis of the mechanical properties of the system revealed an enhanced adhesion between patterned graphene and the substrate. This effect was already seen in previous experiments (as shown in Chapter 5) and, here, PF–QNM allowed a deeper qualitative measurement and a comparison of the adhesion forces.

While in the previous chapters we demonstrated the functionalization of different graphene systems, a successful and deterministic covalent functionalization of EG would be extremely beneficial for the fabrication of high quality devices at the nanoscale. In

fact, EG on SiC eliminates the need for transfer procedures and presents favorable characteristics for large–scale graphene electronics, such as a near–defect free intrinsic lattice. Moreover, the SiC substrate is a semiconductor with a large bandgap, widely used in electrochemical and sensing devices. The promising results shown here open the route for a controlled functionalization of EG with designed molecules, which could act both as active functional groups or passive spacers towards multilayered graphene systems optimized for hydrogen storage or gas sensing. Moreover, the control electronics for readout of the functional groups would be integrated on the same SiC wafer.

Summary and Outlook 7

Summary

The research project realized in this PhD thesis led to novel and valuable advances in the field of chemically functionalized graphene–based systems.

Different graphene structures were explored, and 1,3–dipolar cycloaddition of azomethine ylides was achieved on dispersed rGO and GNS, on monolayer flakes on silica, and on epitaxial graphene on silicon carbide, moving towards higher quality graphene systems. The successful functionalization was confirmed with several characterization techniques, adapting to the different properties of the individual systems.

At large scale (with $\sim 0.1 - 1$ μm lateral resolution), EDX/EELS, XPS, and Raman spectroscopy revealed the presence of the functional groups of the ylide on graphene. EDX/EELS and XPS measurements detected the presence of nitrogen from the functionalized groups, allowing to distinguish the ylide from the residuals of the organic solvents and quantitatively estimate the efficiency of the functionalization. Significantly, the Raman signature of this molecule was detected here for the first time, initially in functionalized rGO and GNS. Moreover, in higher quality graphene systems, such as monolayer exfoliated flakes and epitaxial graphene, Raman spectroscopy on the functionalized samples identified new vibrational features of modified graphene, arising from the grafting of the ylide onto the graphene lattice. This result was achieved in collaboration with the computational group at NEST Laboratory, with the help of DFT simulations of the vibrational power spectrum of functionalized graphene. The identification of these novel features in the Raman spectra of chemically modified graphene is now available as a new method for the assessment of its covalent functionalization, even in case of low–density coverage, when the Raman signature of the ylide cannot be directly detected.

An enhancement of the chemical reactivity of graphene towards the cycloaddition of azomethine ylide was distinctively correlated with the presence of structural defects in its atomic lattice. In fact, the presence of oxygen functional groups (sp^3–defects) in rGO generates a local inhomogeneity of the partial charges which led to a higher functionalization of rGO with respect to GNS. This motivated the interest in exploring low–energy electron beam irradiation as a spatially controlled technique for introducing defect patterns in high–quality graphene, in collaboration with Dr. Federica Bianco at NEST Laboratory. The Raman investigation on patterned monolayer graphene flakes on silica revealed the importance of substrate surface treatments in order to avoid unintentional defected zones and charge doping in the proximity of the designed pattern.

Therefore, the removal of the substrate impurities with oxygen plasma cleaning before the transfer of graphene is now understood to be a fundamental step in order to achieve the best lateral resolution in the patterning with SEM–based low–energy electron beam irradiation.

This technique was promptly applied to the engineering of spatially–resolved patterned graphene flakes to selectively enhance the chemical functionalization with azomethine ylide. Raman spectroscopy allowed to map the presence of the ylide on the surface of functionalized patterned graphene, confirming the deterministic grafting of the ylide only in the patterned areas. Moreover, through laser irradiation, the reversibility of the functionalization was achieved, towards the recovering of a clean patterned graphene sample. The combination of defect patterning and 1,3–dipolar cycloaddition is now demonstrated to be a valuable method in order to selectively functionalize graphene with high spatial resolution.

At smaller scale (under 100 nm of lateral resolution), AFM and STM measurements revealed new features in the morphology of functionalized graphene. AFM investigation on patterned graphene flakes suggested an increased adhesion of the patterned areas with the silica substrate. The adhesion enhancement was also confirmed with PF–QNM measurements collected on patterned epitaxial graphene on silicon carbide. This result suggests defect patterning as a novel technique for preserving the graphene flakes during wet chemistry functionalization procedures, exploiting the adhesion enhancement. Moreover, the exact correspondence of the irradiated patterns with the designed ones is confirmed with AFM images of both monolayer flakes and epitaxial graphene. STM measurements revealed new structures of few Å size on the surface of functionalized near defect–free graphene and confirmed the preservation of the graphene atomic lattice in the background (via atomically resolved images). In addition, spatially resolved STS measurements revealed the gap–like nature in the LDOS of these novel structures, different from the zero–gap linear behavior of the graphene background.

Outlook

The research reported here opens several routes for advancements. Firstly, high resolution STM images on patterned epitaxial graphene would allow to further investigate the nature, the physical properties, and the evolution in time of the introduced defects. Moreover, by individually identifying the defects in STM images, the estimations for L_α and L_D made in Section 5.1 could be directly compared with experimental values (in a similar graphene system). Then, the 1,3–DC of azomethine ylides on patterned epitaxial graphene would be the natural following step. Such a system would introduce both enhancement and selectivity in the functionalization process, still offering the possibility of atomically resolved STM and STS measurements. The morphology and the electronic properties could be investigated individually on defects and organic molecules, offering novel information on the mechanism of the functionalization and on the new properties introduced by the functional groups. These measurements have already been initiated under the supervision of Dr. Stefano Veronesi and Dr. Stefan Heun at NEST Laboratory.

Moreover, the versatility that 1,3–DC offers as functionalization process could be further explored. The synthesis of a different ylide is currently being tested under the supervision of Aldo Moscardini and Dr. Ylea Vlamidis at NEST Laboratory. The new ylide presents the same dipolar nature that would enable the grafting on the graphene surface and offers an easier possibility of further functionalization with other molecules (as shown in Figure 7.1). Fluorophores and gold nanoparticles (with the adequate linkers) are two examples of the following steps, which would add optical or sensing properties to the system. In addition, the possibility of local de–functionalization via laser irradiation opens the route for multi–step tailoring of the graphene surface with different organic species, towards multi–functional graphene–based devices. Then, a more detailed Raman investigation on functionalized graphene, in order to distinguish the contributions from strain and doping, also comparing the old with the new ylide molecules, would provide a deeper insight in the electro-chemical modification of the graphene sheet after functionalization.
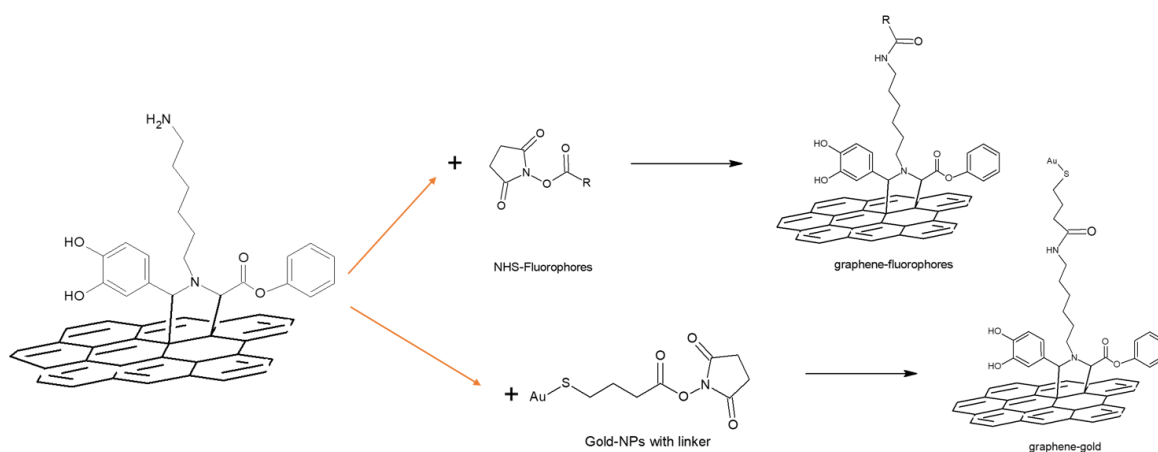
Figure 7.1: New ylide for further functionalization steps towards multi–functional graphene–based devices.

Finally, patterning of graphene paves the way for a designed positioning of organic molecules on its surface, which could act as either passive or active pillars towards spaced multilayer graphene systems (see Figure 7.2). Similar structures would present enhanced gas storage capabilities (hydrogen, for example) or add sensing and catalysis properties. The design and practical development of such structures would benefit from the input deriving from the DFT computational simulations performed by Dr. Luca Bellucci and Dr. Valentina Tozzini at NEST Laboratory in an ongoing collaboration.
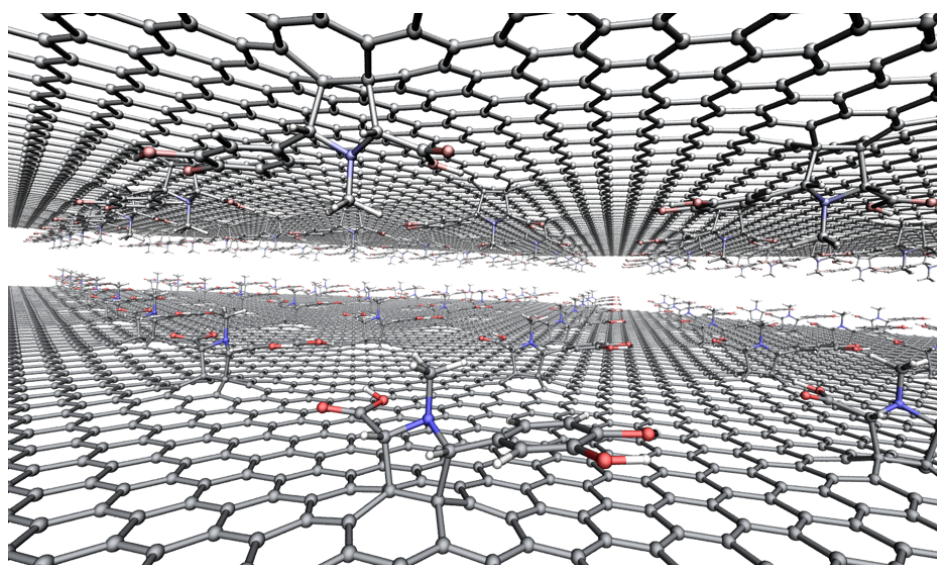
Figure 7.2: DFT model for a pillared graphene multilayer system, with azomethine ylides as spacers. Figure courtesy of Dr. Luca Bellucci.

Bibliography

[1] R. P. Feynman. There's plenty of room at the bottom. *Journal of Microelectromechanical Systems [transcript]*, 1(1):60–66, 1992.

[2] R. Peierls. Quelques propriétés typiques des corps solides. *Annales de l'institut Henri Poincaré*, 3:177–222, 1935.

[3] D. N. Mermin. Crystalline order in two dimensions. *Physical Review*, 176(1):250, 1968.

[4] K. S. Novoselov, A. K. Geim, S. V. Morozov, D. Jiang, Y. Zhang, S. V. Dubonos, I. V. Grigorieva, and A. A. Firsov. Electric field effect in atomically thin carbon films. *Science*, 306:666–669, 2004.

[5] A. A. Balandin, S. Ghosh, W. Bao, I. Calizo, D. Teweldebrhan, F. Miao, and C. N. Lau. Superior thermal conductivity of single-layer graphene. *Nano Letters*, 8:902–907, 2008.

[6] C. Lee, X. Wei, J. W. Kysar, and J. Hone. Measurement of the elastic properties and intrinsic strength of monolayer graphene. *Science*, 321:385–388, 2008.

[7] J. H. Seol, I. Jo, A. L. Moore, L. Lindsay, Z. H. Aitken, M. T. Pettes, X. Li, Z. Yao, R. Huang, D. Broido, et al. Two-dimensional phonon transport in supported graphene. *Science*, 328:213–216, 2010.

[8] S. P. Koenig, N. G. Boddeti, M. L. Dunn, and J. S. Bunch. Ultrastrong adhesion of graphene membranes. *Nature Nanotechnology*, 6:543, 2011.

[9] X. Liang. *Transition from tubes to sheets—a comparison of the properties and applications of carbon nanotubes and graphene*. Elsevier, 2014.

[10] G. Yang, L. Li, W. B. Lee, and M. C. Ng. Structure of graphene and its disorders: a review. *Science and Technology of Advanced Materials*, 19(1):613–648, 2018.

[11] R. Kundu. Tight-binding parameters for graphene. *Modern Physics Letters B*, 25(03):163–173, 2011.

[12] P. R. Wallace. The band theory of graphite. *Physical Review*, 71(9):622, 1947.

[13] K. S. Novoselov, A. K. Geim, S. V. Morozov, D. Jiang, M. I. Katsnelson, I. V. Grigorieva, S. V. Dubonos, and A. A. Firsov. Two-dimensional gas of massless Dirac fermions in graphene. *Nature*, 438:197–200, 2005.

[14] A. K. Geim and K. S. Novoselov. The rise of graphene. *Nature Materials*, 6:183–191, 2007.

[15] M. Yankowitz, Q. Ma, P. Jarillo-Herrero, and B. J. LeRoy. van der Waals heterostructures combining graphene and hexagonal boron nitride. *Nature Reviews Physics*, 1(2):112–125, 2019.

[16] F. Schedin, A. K. Geim, S. V. Morozov, E. W. Hill, P. Blake, M. I. Katsnelson, and K. S. Novoselov. Detection of individual gas molecules adsorbed on graphene. *Nature Materials*, 6(9):652–655, 2007.

[17] K. F. Mak, L. Ju, F. Wang, and T. F. Heinz. Optical spectroscopy of graphene: From the far infrared to the ultraviolet. *Solid State Communications*, 152(15):1341–1349, 2012.

[18] R. R. Nair, P. Blake, A. N. Grigorenko, K. S. Novoselov, T. J. Booth, T. Stauber, N. M. R. Peres, and A. K. Geim. Fine structure constant defines visual transparency of graphene. *Science*, 320:1308–1308, 2008.

[19] S. Tanabe, Y. Sekine, H. Kageshima, M. Nagase, and H. Hibino. Carrier transport mechanism in graphene on SiC (0001). *Physical Review B*, 84(11):115458, 2011.

[20] J.-H. Ahn and B. H. Hong. Graphene for displays that bend. *Nature Nanotechnology*, 9(10):737–738, 2014.

[21] X. Yu, H. Cheng, M. Zhang, Y. Zhao, L. Qu, and G. Shi. Graphene-based smart materials. *Nature Reviews Materials*, 2:17046, 2017.

[22] F. Schwierz. Graphene transistors. *Nature Nanotechnology*, 5:487, 2010.

[23] A. Ambrosi, C. K. Chua, A. Bonanni, and M. Pumera. Electrochemistry of Graphene and Related Materials. *Chemical Reviews*, 114:7150–7188, 2014.

[24] V. B. Mohan, K.-T. Lau, D. Hui, and D. Bhattacharyya. Graphene-based materials and their composites: A review on production, applications and product limitations. *Composites Part B: Engineering*, 142:200–220, 2018.

[25] H. Y. Mao, Y. H. Lu, J. D. Lin, S. Zhong, A. T. S. Wee, and W. Chen. Manipulating the electronic and chemical properties of graphene via molecular functionalization. *Progress in Surface Science*, 88(2):132–159, 2013.

[26] J. Liu, J. Tang, and J. J. Gooding. Strategies for chemical modification of graphene and applications of chemically modified graphene. *Journal of Materials Chemistry*, 22:12435–12452, 2012.

[27] A. Hirsch, J. M. Englert, and F. Hauke. Wet chemical functionalization of graphene. *Accounts of Chemical Research*, 46:87–96, 2013.

[28] M. Woszczyna, A. Winter, M. Grothe, A. Willunat, S. Wundrack, R. Stosch, T. Weimann, F. Ahlers, and A. Turchanin. All-carbon vertical van der Waals heterostructures: Non-destructive functionalization of graphene for electronic applications. *Advanced Materials*, 26:4831–4837, 2014.

[29] P. Laaksonen, M. Kainlauri, T. Laaksonen, A. Shchepetov, H. Jiang, J. Ahopelto, and M. B. Linder. Interfacial engineering by proteins: exfoliation and functionalization of graphene by hydrophobins. *Angewandte Chemie*, 122:5066–5069, 2010.

[30] H. Bai, Y. Xu, L. Zhao, C. Li, and G. Shi. Non-covalent functionalization of graphene sheets by sulfonated polyaniline. *Chemical Communications*, 13:1667–1669, 2009.

[31] V. Georgakilas, J. N. Tiwari, K. C. Kemp, J. A. Perman, A. B. Bourlinos, K. S. Kim, and R. Zboril. Noncovalent functionalization of graphene and graphene oxide for energy materials, biosensing, catalytic, and biomedical applications. *Chemical Reviews*, 116:5464–5519, 2016.

[32] P. Arranz-Mascarós, M. L. Godino-Salido, R. López-Garzón, C. García-Gallarín, I. Chamorro-Mena, F. J. López-Garzón, E. Fernández-García, and M. D. Gutiérrez-Valero. Non-covalent functionalization of graphene to tune its band gap and stabilize metal nanoparticles on its surface. *ACS Omega*, 5:18849–18861, 2020.

[33] X. Dong, Y. Shi, Y. Zhao, D. Chen, J. Ye, Y. Yao, F. Gao, Z. Ni, T. Yu, Z. Shen, et al. Symmetry breaking of graphene monolayers by molecular decoration. *Physical Review Letters*, 102(13):135501, 2009.

[34] W. Chen, D. Qi, X. Gao, and A. T. S. Wee. Surface transfer doping of semiconductors. *Progress in Surface Science*, 84(9-10):279–321, 2009.

[35] Q. Su, S. Pang, V. Alijani, C. Li, X. Feng, and K. Müllen. Composites of graphene with large aromatic molecules. *Advanced Materials*, 21(31):3191–3195, 2009.

[36] D. W. Boukhvalov and Y.-W. Son. Covalent functionalization of strained graphene. *ChemPhysChem*, 13:1463–1469, 2012.

[37] C. Hu, D. Liu, Y. Xiao, and L. Dai. Functionalization of graphene materials by heteroatom-doping for energy conversion and storage. *Progress in Natural Science: Materials International*, 28:121–132, 2018.

[38] M. Melucci, E. Treossi, L. Ortolani, G. Giambastiani, V. Morandi, P. Klar, C. Casiraghi, P. Samorì, and V. Palermo. Facile covalent functionalization of graphene oxide using microwaves: bottom-up development of functional graphitic materials. *Journal of Materials Chemistry*, 20:9052–9060, 2010.

[39] A. Criado, M. Melchionna, S. Marchesan, and M. Prato. The covalent functionalization of graphene on substrates. *Angewandte Chemie International Edition*, 54:10734–10750, 2015.

[40] R. A. Bueno, J. I. Martínez, R. F. Luccas, N. R. Del Árbol, C. Munuera, I. Palacio, F. J. Palomares, K. Lauwaet, S. Thakur, J. M. Baranowski, et al. Highly

selective covalent organic functionalization of epitaxial graphene. *Nature Communications*, 8:15306, 2017.

[41] A. Stergiou, R. Cantón-Vitoria, M. N. Psarrou, S. P. Economopoulos, and N. Tagmatarchis. Functionalized graphene and targeted applications-highlighting the road from chemistry to applications. *Progress in Materials Science*, 114:100683, 2020.

[42] M. Dieng, M. Bensifia, J. Borme, I. Florea, C. M. Abreu, C. Jama, C. Léonard, P. Alpuim, D. Pribat, A. Yassar, et al. Wet-chemical noncovalent functionalization of CVD graphene: Molecular doping and its effect on electrolyte-gated graphene field-effect transistor characteristics. *The Journal of Physical Chemistry C*, 126(9):4522–4533, 2022.

[43] L. Najafi, B. Taheri, B. Martin-Garcia, S. Bellani, D. Di Girolamo, A. Agresti, R. Oropesa-Nunez, S. Pescetelli, L. Vesce, E. Calabro, et al. MoS_2 quantum dot/graphene hybrids for advanced interface engineering of a $CH_3NH_3PbI_3$ perovskite solar cell with an efficiency of over 20%. *ACS Nano*, 12(11):10736–10754, 2018.

[44] W. Liu, N. Liu, Y. Yue, J. Rao, F. Cheng, J. Su, Z. Liu, and Y. Gao. Piezoresistive pressure sensor based on synergistical innerconnect polyvinyl alcohol nanowires/wrinkled graphene film. *Small*, 14(15):1704149, 2018.

[45] A. G. Klechikov, G. Mercier, P. Merino, S. Blanco, C. Merino, and A. V. Talyzin. Hydrogen storage in bulk graphene-related materials. *Microporous and Mesoporous Materials*, 210:46–51, 2015.

[46] E. Quesnel, F. Roux, F. Emieux, P. Faucherand, E. Kymakis, G. Volonakis, F. Giustino, B. Martín-García, I. Moreels, S. A. Gürsel, et al. Graphene-based technologies for energy applications, challenges and perspectives. *2D Materials*, 2(3):030204, 2015.

[47] V. Tozzini and V. Pellegrini. Prospects for hydrogen storage in graphene. *Physical Chemistry Chemical Physics*, 15:80–89, 2013.

[48] J. Zhu, D. Yang, Z. Yin, Q. Yan, and H. Zhang. Graphene and graphene-based materials for energy storage applications. *Small*, 10:3480–3498, 2014.

[49] F. Bonaccorso, L. Colombo, G. Yu, M. Stoller, V. Tozzini, A. C. Ferrari, R. S. Ruoff, and V. Pellegrini. Graphene, related two-dimensional crystals, and hybrid systems for energy conversion and storage. *Science*, 347:1246501, 2015.

[50] L. Bellucci, F. Delfino, and V. Tozzini. In silico design, building and gas adsorption of nano-porous graphene scaffolds. *Nanotechnology*, 32:045704, 2020.

[51] J. W. Burress, S. Gadipelli, J. Ford, J. M. Simmons, W. Zhou, and T. Yildirim. Graphene oxide framework materials: theoretical predictions and experimental results. *Angewandte Chemie International Edition*, 49:8902–8904, 2010.

[52] W.-S. Hung, C.-H. Tsou, M. De Guzman, Q.-F. An, Y.-L. Liu, Y.-M. Zhang, C.-C. Hu, K.-R. Lee, and J.-Y. Lai. Cross-linking with diamine monomers to

prepare composite graphene oxide-framework membranes with varying d-spacing. *Chemistry of Materials*, 26(9):2983–2990, 2014.

[53] P. Huang, L. Jing, H. Zhu, and X. Gao. Diazonium functionalized graphene: microstructure, electric, and magnetic properties. *Accounts of Chemical Research*, 46:43–52, 2013.

[54] Y. Li, W. Li, M. Wojcik, B. Wang, L.-C. Lin, M. B. Raschke, and K. Xu. Light-assisted diazonium functionalization of graphene and spatial heterogeneities in reactivity. *The Journal of Physical Chemistry Letters*, 10:4788–4793, 2019.

[55] G. Ambrosio, A. Brown, L. Daukiya, G. Drera, G. Di Santo, L. Petaccia, S. De Feyter, L. Sangaletti, and S. Pagliara. Impact of covalent functionalization by diazonium chemistry on the electronic properties of graphene on SiC. *Nanoscale*, 12(16):9032–9037, 2020.

[56] M. Z. Hossain, M. A. Walsh, and M. C. Hersam. Scanning tunneling microscopy, spectroscopy, and nanolithography of epitaxial graphene chemically modified with aryl moieties. *Journal of the American Chemical Society*, 132(43):15399–15403, 2010.

[57] M. A. Bissett, S. Konabe, S. Okada, M. Tsuji, and H. Ago. Enhanced chemical reactivity of graphene induced by mechanical strain. *ACS Nano*, 7(11):10335–10343, 2013.

[58] S. Sarkar, E. Bekyarova, and R. C. Haddon. Chemistry at the Dirac point: Diels–Alder reactivity of graphene. *Accounts of Chemical Research*, 45(4):673–682, 2012.

[59] M. Maggini, G. Scorrano, and M. Prato. Addition of azomethine ylides to C60: synthesis, characterization, and functionalization of fullerene pyrrolidines. *Journal of the American Chemical Society*, 115:9798–9799, 1993.

[60] V. Georgakilas, K. Kordatos, M. Prato, D. M. Guldi, M. Holzinger, and A. Hirsch. Organic functionalization of carbon nanotubes. *Journal of the American Chemical Society*, 124:760–761, 2002.

[61] N. Tagmatarchis and M. Prato. The addition of azomethine ylides to [60] fullerene leading to fulleropyrrolidines. *Synlett*, 2003:0768–0779, 2003.

[62] C. Cioffi, S. Campidelli, F. G. Brunetti, M. Meneghetti, and M. Prato. Functionalisation of carbon nanohorns. *Chemical Communications*, 20:2129–2131, 2006.

[63] D. Tasis, N. Tagmatarchis, A. Bianco, and M. Prato. Chemistry of carbon nanotubes. *Chemical Reviews*, 106:1105–1136, 2006.

[64] K. Kostarelos, L. Lacerda, G. Pastorin, W. Wu, S. Wieckowski, J. Luangsivilay, S. Godefroy, D. Pantarotto, J.-P. Briand, S. Muller, et al. Cellular uptake of functionalized carbon nanotubes is independent of functional group and cell type. *Nature Nanotechnology*, 2:108–113, 2007.

[65] M. Prato. [60] fullerene chemistry for materials science applications. *Journal of Materials Chemistry*, 7:1097–1109, 1997.

[66] N. Tagmatarchis and M. Prato. Functionalization of carbon nanotubes via 1,3-dipolar cycloadditions. *Journal of Materials Chemistry*, 14:437–439, 2004.

[67] S. V. Giofrè, M. Tiecco, C. Celesti, S. Patanè, C. Triolo, A. Gulino, L. Spitaleri, S. Scalese, M. Scuderi, and D. Iannazzo. Eco-friendly 1, 3-dipolar cycloaddition reactions on graphene quantum dots in natural deep eutectic solvent. *Nanomaterials*, 10(12):2549, 2020.

[68] V. Georgakilas, A. B. Bourlinos, R. Zboril, T. A. Steriotis, P. Dallas, A. K. Stubos, and C. Trapalis. Organic functionalisation of graphenes. *Chemical Communications*, 46:1766–1768, 2010.

[69] M. Quintana, K. Spyrou, M. Grzelczak, W. R. Browne, P. Rudolf, and M. Prato. Functionalization of graphene via 1,3-dipolar cycloaddition. *ACS Nano*, 4:3527–3533, 2010.

[70] A. Jangizehi, F. Schmid, P. Besenius, K. Kremer, and S. Seiffert. Defects and defect engineering in soft matter. *Soft Matter*, 16(48):10809–10859, 2020.

[71] O. V. Yazyev and S. G. Louie. Topological defects in graphene: Dislocations and grain boundaries. *Physical Review B*, 81(19):195420, 2010.

[72] O. V. Yazyev and Y. P. Chen. Polycrystalline graphene and other two-dimensional materials. *Nature Nanotechnology*, 9(10):755–767, 2014.

[73] J. Lahiri, Y. Lin, P. Bozkurt, I. I. Oleynik, and M. Batzill. An extended defect in graphene as a metallic wire. *Nature Nanotechnology*, 5(5):326–329, 2010.

[74] L. Tsetseris, B. Wang, and S. T. Pantelides. Substitutional doping of graphene: The role of carbon divacancies. *Physical Review B*, 89(3):035411, 2014.

[75] G. J. Kubas. Hydrogen activation on organometallic complexes and H_2 production, utilization, and storage for future energy. *Journal of Organometallic Chemistry*, 694:2648–2653, 2009.

[76] V. B. Parambhath, R. Nagar, K. Sethupathi, and S. Ramaprabhu. Investigation of spillover mechanism in palladium decorated hydrogen exfoliated functionalized graphene. *The Journal of Physical Chemistry C*, 115:15679–15685, 2011.

[77] C. Weeks, J. Hu, J. Alicea, M. Franz, and R. Wu. Engineering a robust quantum spin Hall state in graphene via adatom deposition. *Physical Review X*, 1(2):021001, 2011.

[78] J. C. Meyer, C. Kisielowski, R. Erni, M. D. Rossell, M. F. Crommie, and A. Zettl. Direct imaging of lattice atoms and topological defects in graphene membranes. *Nano Letters*, 8(11):3582–3586, 2008.

[79] A. V. Krasheninnikov, P. O. Lehtinen, A. S. Foster, P. Pyykkö, and R. M. Nieminen. Embedding transition-metal atoms in graphene: structure, bonding, and magnetism. *Physical Review Letters*, 102(12):126807, 2009.

[80] X. Sun, B. Li, and M. Lu. A covalent modification for graphene by adamantane groups through two-step chlorination-Grignard reactions. *Journal of Solid State Chemistry*, 251:194–197, 2017.

[81] L. Liu, M. Qing, Y. Wang, and S. Chen. Defects in graphene: generation, healing, and their effects on the properties of graphene: a review. *Journal of Materials Science & Technology*, 31(6):599–606, 2015.

[82] H. Malekpour, P. Ramnani, S. Srinivasan, G. Balasubramanian, D. L. Nika, A. Mulchandani, R. K. Lake, and A. A. Balandin. Thermal conductivity of graphene with defects induced by electron beam irradiation. *Nanoscale*, 8(30):14608–14616, 2016.

[83] Y. Anno, Y. Imakita, K. Takei, S. Akita, and T. Arie. Enhancement of graphene thermoelectric performance through defect engineering. *2D Materials*, 4(2):025019, 2017.

[84] D. W. Boukhvalov and M. I. Katsnelson. Chemical functionalization of graphene with defects. *Nano Letters*, 8(12):4373–4379, 2008.

[85] S. C. Hernandez, F. J. Bezares, J. T. Robinson, J. D. Caldwell, and S. G. Walton. Controlling the local chemical reactivity of graphene through spatial functionalization. *Carbon*, 60:84–93, 2013.

[86] X.-L. Ye, J. Cai, X.-D. Yang, X.-Y. Tang, Z.-Y. Zhou, Y.-Z. Tan, S.-Y. Xie, and L.-S. Zheng. Quantifying defect-enhanced chemical functionalization of single-layer graphene and its application in supramolecular assembly. *Journal of Materials Chemistry A*, 5(46):24257–24262, 2017.

[87] A. Lherbier, S. M.-M. Dubois, X. Declerck, Y.-M. Niquet, S. Roche, and J.-C. Charlier. Transport properties of graphene containing structural defects. *Physical Review B*, 86(7):075402, 2012.

[88] W. Zhang, W.-C. Lu, H.-X. Zhang, K. M. Ho, and C. Z. Wang. Lattice distortion and electron charge redistribution induced by defects in graphene. *Carbon*, 110:330–335, 2016.

[89] H. Wang, Y. Wang, B. Bai, X. Guo, and J. Xue. Electronic transport properties of graphene with Stone-Wales defects and multiple vacancy chains: a theoretical study. *Applied Surface Science*, 531:147347, 2020.

[90] Y. Zhou and K. P. Loh. Making patterns on graphene. *Advanced Materials*, 22(32):3615–3620, 2010.

[91] A. Nourbakhsh, M. Cantoro, T. Vosch, G. Pourtois, F. Clemente, M. H. van der Veen, J. Hofkens, M. M. Heyns, S. De Gendt, and B. F. Sels. Bandgap opening in oxygen plasma-treated graphene. *Nanotechnology*, 21(43):435203, 2010.

[92] M. Baraket, R. Stine, W. K. Lee, J. T. Robinson, C. R. Tamanaha, P. E. Sheehan, and S. G. Walton. Aminated graphene for DNA attachment produced via plasma functionalization. *Applied Physics Letters*, 100(23):233123, 2012.

[93] W. Yuan and G. Shi. Graphene-based gas sensors. *Journal of Materials Chemistry A*, 1(35):10078–10091, 2013.

[94] G. Lee, G. Yang, A. Cho, J. W. Han, and J. Kim. Defect-engineered graphene chemical sensors with ultrahigh sensitivity. *Physical Chemistry Chemical Physics*, 18(21):14198–14204, 2016.

[95] Y.-W. Lan, W.-H. Chang, B.-T. Xiao, B.-W. Liang, J.-H. Chen, P.-h. Jiang, L.-J. Li, Y.-W. Su, Y.-L. Zhong, and C.-D. Chen. Polymer-free patterning of graphene at sub-10-nm scale by low-energy repetitive electron beam. *Small*, 10(22):4778–4784, 2014.

[96] I. Childres, L. A. Jauregui, M. Foxe, J. Tian, R. Jalilian, I. Jovanovic, and Y. P. Chen. Effect of electron-beam irradiation on graphene field effect devices. *Applied Physics Letters*, 97(17):173109, 2010.

[97] G. Liu, D. Teweldebrhan, and A. A. Balandin. Tuning of graphene properties via controlled exposure to electron beams. *IEEE Transactions on Nanotechnology*, 10(4):865–870, 2011.

[98] I. Childres, L. A. Jauregui, and Y. P. Chen. Raman spectra and electron-phonon coupling in disordered graphene with gate-tunable doping. *Journal of Applied Physics*, 116(23):233101, 2014.

[99] L. Tao, C. Qiu, F. Yu, H. Yang, M. Chen, G. Wang, and L. Sun. Modification on single-layer graphene induced by low-energy electron-beam irradiation. *The Journal of Physical Chemistry C*, 117(19):10079–10085, 2013.

[100] B. W. Smith and D. E. Luzzi. Electron irradiation effects in single wall carbon nanotubes. *Journal of Applied Physics*, 90(7):3509–3515, 2001.

[101] L. Sun, F. Banhart, and J. Warner. Two-dimensional materials under electron irradiation. *MRS Bulletin*, 40(1):29–37, 2015.

[102] C. Backes, A. M. Abdelkader, C. Alonso, A. Andrieux-Ledier, R. Arenal, J. Azpeitia, N. Balakrishnan, L. Banszerus, J. Barjon, R. Bartali, et al. Production and processing of graphene and related materials. *2D Materials*, 7(2):022001, 2020.

[103] W. Zhao, M. Fang, F. Wu, H. Wu, L. Wang, and G. Chen. Preparation of graphene by exfoliation of graphite using wet ball milling. *Journal of Materials Chemistry*, 20(28):5817–5819, 2010.

[104] K. R. Paton, E. Varrla, C. Backes, R. J. Smith, U. Khan, A. O'Neill, C. Boland, M. Lotya, O. M. Istrate, P. King, et al. Scalable production of large quantities of defect-free few-layer graphene by shear exfoliation in liquids. *Nature Materials*, 13:624–630, 2014.

[105] A. E. D. R. Castillo, V. Pellegrini, A. Ansaldo, F. Ricciardella, H. Sun, L. Marasco, J. Buha, Z. Dang, L. Gagliani, E. Lago, et al. High-yield production of 2D crystals by wet-jet milling. *Materials Horizons*, 5:890–904, 2018.

[106] C. K. Chua and M. Pumera. Chemical reduction of graphene oxide: a synthetic chemistry viewpoint. *Chemical Society Reviews*, 43(1):291–312, 2014.

[107] M. Yi and Z. Shen. A review on mechanical exfoliation for the scalable production of graphene. *Journal of Materials Chemistry A*, 3(22):11700–11715, 2015.

[108] P. N. First, W. A. de Heer, T. Seyller, C. Berger, J. A. Stroscio, and J.-S. Moon. Epitaxial graphenes on silicon carbide. *MRS Bulletin*, 35(4):296–305, 2010.

[109] G. R. Yazdi, T. Iakimov, and R. Yakimova. Epitaxial graphene on SiC: a review of growth and characterization. *Crystals*, 6(5):53, 2016.

[110] W. Norimatsu and M. Kusunoki. Epitaxial graphene on SiC {0001}: advances and perspectives. *Physical Chemistry Chemical Physics*, 16(8):3501–3511, 2014.

[111] Y. Hernandez, V. Nicolosi, M. Lotya, F. M. Blighe, Z. Sun, S. De, I. T. McGovern, B. Holland, M. Byrne, Y. K. Gun'Ko, et al. High-yield production of graphene by liquid-phase exfoliation of graphite. *Nature Nanotechnology*, 3:563–568, 2008.

[112] Z. Y. Xia, S. Pezzini, E. Treossi, G. Giambastiani, F. Corticelli, V. Morandi, A. Zanelli, V. Bellani, and V. Palermo. The exfoliation of graphene in liquids by electrochemical, chemical, and sonication-assisted techniques: A nanoscale study. *Advanced Functional Materials*, 23:4684–4693, 2013.

[113] A. V. Tyurnina, I. Tzanakis, J. Morton, J. Mi, K. Porfyrakis, B. M. Maciejewska, N. Grobert, and D. G. Eskin. Ultrasonic exfoliation of graphene in water: a key parameter study. *Carbon*, 168:737–747, 2020.

[114] A. Ciesielski and P. Samori. Graphene via sonication assisted liquid-phase exfoliation. *Chemical Society Reviews*, 43:381–398, 2014.

[115] M. V. Bracamonte, G. I. Lacconi, S. E. Urreta, and L. E. F. Foa Torres. On the nature of defects in liquid-phase exfoliated graphene. *The Journal of Physical Chemistry C*, 118(28):15455–15459, 2014.

[116] M. Lotya, Y. Hernandez, P. J. King, R. J. Smith, V. Nicolosi, L. S. Karlsson, F. M. Blighe, S. De, Z. Wang, I. T. McGovern, et al. Liquid phase production of graphene by exfoliation of graphite in surfactant/water solutions. *Journal of the American Chemical Society*, 131(10):3611–3620, 2009.

[117] L. Liu, Z. Shen, M. Yi, X. Zhang, and S. Ma. A green, rapid and size-controlled production of high-quality graphene sheets by hydrodynamic forces. *RSC Advances*, 4(69):36464–36470, 2014.

[118] J. H. Ryan. 1,3-dipolar cycloaddition reactions of azomethine ylides with aromatic dipolarophiles. *ARKIVOC: Online Journal of Organic Chemistry*, 2015, 2015.

[119] K. V. Gothelf and K. A. Jørgensen. Asymmetric 1,3-dipolar cycloaddition reactions. *Chemical Reviews*, 98(2):863–910, 1998.

[120] E. M. Martinis, A. Montellano, A. Sartorel, M. Carraro, M. Prato, and M. Bonchio. Microwave-assisted 1, 3-dipolar cycloaddition of azomethine ylides to [60] fullerene: Thermodynamic control of bis-addition with ionic liquids additives. *European Journal of Organic Chemistry*, 2021(25):3545–3551, 2021.

[121] W. I. Goldburg. Dynamic light scattering. *American Journal of Physics*, 67(12):1152–1160, 1999.

[122] J. W. Weber, V. E. Calado, and M. C. M. Van De Sanden. Optical constants of graphene measured by spectroscopic ellipsometry. *Applied Physics Letters*, 97:091904, 2010.

[123] Wikipedia. Dynamic light scattering. https://en.wikipedia.org/wiki/Dynamic_light_scattering. Accessed on 10.08.2022.

[124] B. Bhushan, editor. *Encyclopedia of Nanotechnology*. Springer Dordrecht, 2 edition, 2016.

[125] A. C. Ferrari, J. C. Meyer, V. Scardaci, C. Casiraghi, M. Lazzeri, F. Mauri, S. Piscanec, D. Jiang, K. S. Novoselov, S. Roth, et al. Raman spectrum of graphene and graphene layers. *Physical Review Letters*, 97:187401, 2006.

[126] A. C. Ferrari and D. M. Basko. Raman spectroscopy as a versatile tool for studying the properties of graphene. *Nature Nanotechnology*, 8:235–246, 2013.

[127] R. Loudon. *The Raman effect in crystals*. Number 52 in 13. Taylor & Francis, 1964.

[128] L. M. Malard, M. A. Pimenta, G. Dresselhaus, and M. S. Dresselhaus. Raman spectroscopy in graphene. *Physics Reports*, 473:51–87, 2009.

[129] D. López-Díaz, M. López Holgado, J. L. García-Fierro, and M. M. Velásquez. Evolution of the Raman spectrum with the chemical composition of graphene oxide. *The Journal of Physical Chemistry C*, 121:20489–20497, 2017.

[130] A. Merlen, J. G. Buijnsters, and C. Pardanaud. A guide to and review of the use of multiwavelength Raman spectroscopy for characterizing defective aromatic carbon solids: From graphene to amorphous carbons. *Coatings*, 7(10):153, 2017.

[131] J.-B. Wu, M.-L. Lin, X. Cong, H.-N. Liu, and P.-H. Tan. Raman spectroscopy of graphene-based materials and its applications in related devices. *Chemical Society Reviews*, 47:1822–1873, 2018.

[132] N. M. Pirozzi, J. P. Hoogenboom, and B. N. G. Giepmans. ColorEM: analytical electron microscopy for element-guided identification and imaging of the building blocks of life. *Histochemistry and Cell Biology*, 150(5):509–520, 2018.

[133] D. A. Shirley. High-resolution X-ray photoemission spectrum of the valence bands of gold. *Physical Review B*, 5:4709, 1972.

[134] A. D. Carl, R. E. Kalan, J. D. Obayemi, M. G. Zebaze Kana, W. O. Soboyejo, and R. L. Grimm. Synthesis and characterization of alkylamine-functionalized Si (111) for perovskite adhesion with minimal interfacial oxidation or electronic defects. *ACS Applied Materials & Interfaces*, 9(39):34377–34388, 2017.

[135] Bruker. Bruker AFM probes. https://www.brukerafmprobes.com/p-3726-scanasyst-air.aspx. Accessed on 22.09.2022.

[136] A. Kwaśniewska, M. Świetlicki, A. Prószyński, and G. Gładyszewski. The quantitative nanomechanical mapping of starch/kaolin film surfaces by Peak Force AFM. *Polymers*, 13(2):244, 2021.

[137] D. Nečas and P. Klapetek. Gwyddion: an open-source software for SPM data analysis. *Open Physics*, 10(1):181–188, 2012.

[138] J. Bardeen. Tunnelling from a Many–Particle Point of View. *Physical Review Letters*, 6:57–59, 1961.

[139] J. C. Chen. *Introduction to Scanning Tunneling Microscopy*. Monographs on the Physics and Chemistry of Materials. Oxford University Press, 3 edition, 2021.

[140] A. Kumar. *Black Phosphorus: Pristine and doped surface investigations using Scanning Tunneling Microscopy*. PhD thesis, Scuola Normale Superiore, 2019.

[141] J. Hutter, M. Iannuzzi, F. Schiffmann, and J. VandeVondele. CP2K: atomistic simulations of condensed matter systems. *Wiley Interdisciplinary Reviews: Computational Molecular Science*, 4:15–25, 2014.

[142] T. D. Kühne, M. Iannuzzi, M. Del Ben, V. V. Rybkin, P. Seewald, F. Stein, T. Laino, R. Z. Khaliullin, O. Schütt, F. Schiffmann, et al. CP2K: An electronic structure and molecular dynamics software package-Quickstep: Efficient and accurate electronic structure calculations. *The Journal of Chemical Physics*, 152:194103, 2020.

[143] J. P. Perdew, K. Burke, and M. Ernzerhof. Generalized gradient approximation made simple. *Physical Review Letters*, 77:3865, 1996.

[144] S. Grimme. Semiempirical GGA-type density functional constructed with a long-range dispersion correction. *Journal of Computational Chemistry*, 27:1787–1799, 2006.

[145] J. VandeVondele, M. Krack, F. Mohamed, M. Parrinello, T. Chassaing, and J. Hutter. Quickstep: Fast and accurate density functional calculations using a mixed Gaussian and plane waves approach. *Computer Physics Communications*, 167:103–128, 2005.

[146] S. Goedecker, M. Teter, and J. Hutter. Separable dual-space Gaussian pseudopotentials. *Physical Review B*, 54:1703, 1996.

[147] A. Bagri, C. Mattevi, M. Acik, Y. J. Chabal, M. Chhowalla, and V. B. Shenoy. Structural evolution during the reduction of chemically derived graphene oxide. *Nature Chemistry*, 2:581–587, 2010.

[148] C. I. Bayly, P. Cieplak, W. Cornell, and P. A. Kollman. A well-behaved electrostatic potential based method using charge restraints for deriving atomic charges: the RESP model. *The Journal of Physical Chemistry*, 97:10269–10280, 1993.

[149] C. Campaná, B. Mussard, and T. K. Woo. Electrostatic potential derived atomic charges for periodic systems using a modified error functional. *Journal of Chemical Theory and Computation*, 5:2866–2878, 2009.

[150] D. Golze, J. Hutter, and M. Iannuzzi. Wetting of water on hexagonal boron nitride@Rh(111): a QM/MM model based on atomic charges derived for nanostructured substrates. *Physical Chemistry Chemical Physics*, 17:14307–14316, 2015.

[151] G. Bussi, D. Donadio, and M. Parrinello. Canonical sampling through velocity rescaling. *The Journal of Chemical Physics*, 126:014101, 2007.

[152] M. Thomas, M. Brehm, R. Fligg, P. Vöhringer, and B. Kirchner. Computing vibrational spectra from ab initio molecular dynamics. *Physical Chemistry Chemical Physics*, 15(18):6608–6622, 2013.

[153] P. Hovington, D. Drouin, and R. Gauvin. CASINO: A new Monte Carlo code in C language for electron beam interaction — part I: Description of the program. *Scanning*, 19(1):1–14, 1997.

[154] P. R. Mali, P. K. Shirsat, N. Khomane, L. Nayak, J. B. Nanubolu, and H. M. Meshram. 1,3-dipolar cycloaddition reactions for the synthesis of novel oxindole derivatives and their cytotoxic properties. *ACS Combinatorial Science*, 19(10):633–639, 2017.

[155] C.-L. Chen, T.-W. Chiu, Y.-W. Chen, and J.-M. Fang. Substituent and solvent effects in the 1, 3-dipolar cycloadditions for synthesis of anti-influenza agent peramivir and its analog. *Tetrahedron*, 75(33):4458–4470, 2019.

[156] Y. Xu, H. Cao, Y. Xue, B. Li, and W. Cai. Liquid-phase exfoliation of graphene: an overview on exfoliation media, techniques, and challenges. *Nanomaterials*, 8(11):942, 2018.

[157] A. Eckmann, A. Felten, A. Mishchenko, L. Britnell, R. Krupke, K. S. Novoselov, and C. Casiraghi. Probing the nature of defects in graphene by Raman spectroscopy. *Nano Letters*, 12(8):3925–3930, 2012.

[158] B. Krauss, T. Lohmann, D.-H. Chae, M. Haluska, K. von Klitzing, and J. H. Smet. Laser-induced disassembly of a graphene single crystal into a nanocrystalline network. *Physical Review B*, 79:165428, 2009.

[159] A. C. Ferrari. Raman spectroscopy of graphene and graphite: Disorder, electron-phonon coupling, doping and nonadiabatic effects. *Solid State Communications*, 143(1-2):47–57, 2007.

[160] I. Childres, L. A. Jauregui, W. Park, H. Cao, Y. P. Chen, et al. Raman spectroscopy of graphene and related materials. *New Developments in Photon and Materials Research*, 1:1–20, 2013.

[161] S. Vollebregt, R. Ishihara, F. D. Tichelaar, Y. Hou, and C. I. M. Beenakker. Influence of the growth temperature on the first and second-order Raman band ratios and widths of carbon nanotubes and fibers. *Carbon*, 50:3542–3554, 2012.

[162] A. Sadezky, H. Muckenhuber, H. Grothe, R. Niessner, and U. Pöschl. Raman microspectroscopy of soot and related carbonaceous materials: spectral analysis and structural information. *Carbon*, 43:1731–1742, 2005.

[163] P. A. Goodman, H. Li, Y. Gao, Y. F. Lu, J. D. Stenger-Smith, and J. Redepenning. Preparation and characterization of high surface area, high porosity carbon monoliths from pyrolyzed bovine bone and their performance as supercapacitor electrodes. *Carbon*, 55:291–298, 2013.

[164] S. Claramunt, A. Varea, D. Díaz, M. M. Velazquez, A. Cornet, and A. Cirera. The importance of interbands on the interpretation of the Raman spectrum of graphene oxide. *The Journal of Physical Chemistry C*, 119:10123–10129, 2015.

[165] A. D. Meade, C. Clarke, F. Draux, G. D. Sockalingum, M. Manfait, F. M. Lyng, and H. J. Byrne. Studies of chemical fixation effects in human cell lines using Raman microspectroscopy. *Analytical and Bioanalytical Chemistry*, 396:1781–1791, 2010.

[166] S. Stankovich, D. A. Dikin, R. D. Piner, K. A. Kohlhaas, A. Kleinhammes, Y. Jia, Y. Wu, S. T. Nguyen, and R. S. Ruoff. Synthesis of graphene-based nanosheets via chemical reduction of exfoliated graphite oxide. *Carbon*, 45:1558–1565, 2007.

[167] A. Cuesta, P. Dhamelincourt, J. Laureyns, A. Martinez-Alonso, and J. M. D. Tascón. Raman microprobe studies on carbon materials. *Carbon*, 32:1523–1532, 1994.

[168] A. C. Ferrari and J. Robertson. Origin of the 1150-cm^{-1} Raman mode in nanocrystalline diamond. *Physical Review B*, 63:121405, 2001.

[169] X. Díez-Betriu, S. Álvarez-García, C. Botas, P. Álvarez, J. Sánchez-Marcos, C. Prieto, R. Menéndez, and A. De Andrés. Raman spectroscopy for the study of reduction mechanisms and optimization of conductivity in graphene oxide thin films. *Journal of Materials Chemistry C*, 1:6905–6912, 2013.

[170] E. H. M. Ferreira, M. V. O. Moutinho, F. Stavale, M. M. Lucchese, R. B. Capaz, C. A. Achete, and A. Jorio. Evolution of the Raman spectra from single-, few-, and many-layer graphene with increasing disorder. *Physical Review B*, 82:125429, 2010.

[171] T. Kawamoto, S. Ochiai, and H. Kagi. Changes in the structure of water deduced from the pressure dependence of the Raman OH frequency. *The Journal of Chemical Physics*, 120:5867–5870, 2004.

[172] W. Konicki, M. Aleksandrzak, D. Moszyński, and E. Mijowska. Adsorption of anionic azo-dyes from aqueous solutions onto graphene oxide: equilibrium, kinetic and thermodynamic studies. *Journal of Colloid and Interface Science*, 496:188–200, 2017.

[173] D. Benne, E. Maccallini, P. Rudolf, C. Sooambar, and M. Prato. X-ray photoemission spectroscopy study on the effects of functionalization in fulleropyrrolidine and pyrrolidine derivatives. *Carbon*, 44:2896–2903, 2006.

[174] Z. Xing, Z. Ju, Y. Zhao, J. Wan, Y. Zhu, Y. Qiang, and Y. Qian. One-pot hydrothermal synthesis of nitrogen-doped graphene as high-performance anode materials for lithium ion batteries. *Scientific Reports*, 6:1–10, 2016.

[175] M. Datta, H. J. Mathieu, and D. Landolt. Characterization of transpassive films on nickel by sputter profiling and angle resolved AES/XPS. *Applications of Surface Science*, 18:299–314, 1984.

[176] T. Koyama, T. Inaba, K. Komatsu, S. Moriyama, M. Shimizu, and Y. Homma. Effect of interfacial water formed between graphene and SiO_2/Si substrate. *Applied Physics Express*, 10(7):075102, 2017.

[177] L. Basta, A. Moscardini, F. Fabbri, L. Bellucci, V. Tozzini, S. Rubini, A. Griesi, M. Gemmi, S. Heun, and S. Veronesi. Covalent organic functionalization of graphene nanosheets and reduced graphene oxide via 1,3-dipolar cycloaddition of azomethine ylide. *Nanoscale Advances*, 3:5841–5852, 2021.

[178] M. Bruna, A. K. Ott, M. Ijäs, D. Yoon, U. Sassi, and A. C. Ferrari. Doping dependence of the Raman spectrum of defected graphene. *ACS Nano*, 8(7):7432–7441, 2014.

[179] R. Beams, L. Gustavo Cançado, and L. Novotny. Raman characterization of defects and dopants in graphene. *Journal of Physics: Condensed Matter*, 27:083002, 2015.

[180] J. A. Gardener and J. A. Golovchenko. Ice-assisted electron beam lithography of graphene. *Nanotechnology*, 23(18):185302, 2012.

[181] H. Kanter. Contribution of backscattered electrons to secondary electron formation. *Physical Review*, 121:681–684, 1961.

[182] S. Kim, D. D. Kulkarni, R. Davis, S. S. Kim, R. R. Naik, A. A. Voevodin, M. Russell, S. S. Jang, V. V. Tsukruk, and A. G. Fedorov. Controlling the physicochemical state of carbon on graphene using focused electron-beam-induced deposition. *ACS Nano*, 8(7):6805–6813, 2014.

[183] S. Kim, M. Russell, D. D. Kulkarni, M. Henry, S. Kim, R. R. Naik, A. A. Voevodin, S. S. Jang, V. V. Tsukruk, and A. G. Fedorov. Activating "invisible" glue: using electron beam for enhancement of interfacial properties of graphene–metal contact. *ACS Nano*, 10(1):1042–1049, 2016.

[184] J. D. Jones, P. A. Ecton, Y. Mo, and J. M. Perez. Comment on "modification of graphene properties due to electron-beam irradiation" [appl. phys. lett. 94, 013101 (2009)]. *Applied Physics Letters*, 95(24):246101, 2009.

[185] J. Jones, K. Mahajan, W. Williams, P. Ecton, Y. Mo, and J. Perez. Formation of graphane and partially hydrogenated graphene by electron irradiation of adsorbates on graphene. *Carbon*, 48(8):2335–2340, 2010.

[186] Z. Wang, K. Yi, Q. Lin, L. Yang, X. Chen, H. Chen, Y. Liu, and D. Wei. Free radical sensors based on inner-cutting graphene field-effect transistors. *Nature Communications*, 10(1544):041–1723, 2019.

[187] K. Saga and T. Hattori. Influence of surface organic contamination on the incubation time in low-pressure chemical vapor deposition. *Journal of The Electrochemical Society*, 144(9):L253–L255, 1997.

[188] E. V. Shun'ko and V. S. Belkin. Cleaning properties of atomic oxygen excited to metastable state $2s^2 2p^4(^1s_0)$. *Journal of Applied Physics*, 102(8):083304, 2007.

[189] C. Casiraghi, S. Pisana, K. S. Novoselov, A. K. Geim, and A. C. Ferrari. Raman fingerprint of charged impurities in graphene. *Applied Physics Letters*, 91(23):233108, 2007.

[190] L. Basta, A. Moscardini, S. Veronesi, and F. Bianco. Substrate surface effects on electron-irradiated graphene. *Surfaces and Interfaces*, 28:101694, 2021.

[191] M. Breugst and H.-U. Reissig. The Huisgen Reaction: Milestones of the 1,3-Dipolar Cycloaddition. *Angewandte Chemie International Edition*, 59(30):12293–12307, 2020.

[192] Y. Huang, Y.-H. Pan, R. Yang, L.-H. Bao, L. Meng, H.-L. Luo, Y.-Q. Cai, G.-D. Liu, W.-J. Zhao, Z. Zhou, et al. Universal mechanical exfoliation of large-area 2D crystals. *Nature Communications*, 11(1):1–9, 2020.

[193] H. D. Le, T. T. T. Ngo, D. Q. Le, X. N. Nguyen, N. M. Phan, et al. Synthesis of multi-layer graphene films on copper tape by atmospheric pressure chemical vapor deposition method. *Advances in Natural Sciences: Nanoscience and Nanotechnology*, 4(3):035012, 2013.

[194] D. M. Basko. Theory of resonant multiphonon Raman scattering in graphene. *Physical Review B*, 78(12):125418, 2008.

[195] A. Eckmann, A. Felten, I. Verzhbitskiy, R. Davey, and C. Casiraghi. Raman study on defective graphene: Effect of the excitation energy, type, and amount of defects. *Physical Review B*, 88(3):035426, 2013.

[196] F. Tuinstra and J. L. Koenig. Raman spectrum of graphite. *The Journal of Chemical Physics*, 53(3):1126–1130, 1970.

[197] M. J. Matthews, M. A. Pimenta, G. Dresselhaus, M. S. Dresselhaus, and M. Endo. Origin of dispersive effects of the Raman D band in carbon materials. *Physical Review B*, 59(10):R6585, 1999.

[198] L. G. Cançado, K. Takai, T. Enoki, M. Endo, Y. A. Kim, H. Mizusaki, A. Jorio, L. N. Coelho, R. Magalhães-Paniago, and M. A. Pimenta. General equation for the determination of the crystallite size La of nanographite by raman spectroscopy. *Applied Physics Letters*, 88(16):163106, 2006.

[199] M. M. Lucchese, F. Stavale, E. H. M. Ferreira, C. Vilani, M. V. d. O. Moutinho, R. B. Capaz, C. A. Achete, and A. Jorio. Quantifying ion-induced defects and Raman relaxation length in graphene. *Carbon*, 48(5):1592–1597, 2010.

[200] L. G. Cançado, A. Jorio, E. H. M. Ferreira, F. Stavale, C. A. Achete, R. B. Capaz, M. V. d. O. Moutinho, A. Lombardo, T. S. Kulmala, and A. C. Ferrari. Quantifying defects in graphene via Raman spectroscopy at different excitation energies. *Nano Letters*, 11(8):3190–3196, 2011.

[201] L. Tao, C. Qiu, F. Yu, H. Yang, M. Chen, G. Wang, and L. Sun. Modification on single-layer graphene induced by low-energy electron-beam irradiation. *The Journal of Physical Chemistry C*, 117(19):10079–10085, 2013.

[202] P. Poncharal, A. Ayari, T. Michel, and J.-L. Sauvajol. Raman spectra of misoriented bilayer graphene. *Physical Review B*, 78(11):113407, 2008.

[203] Z. H. Ni, T. Yu, Z. Q. Luo, Y. Y. Wang, L. Liu, C. P. Wong, J. Miao, W. Huang, and Z. X. Shen. Probing charged impurities in suspended graphene using Raman spectroscopy. *ACS Nano*, 3(3):569–574, 2009.

[204] I. Calizo, W. Bao, F. Miao, C. N. Lau, and A. A. Balandin. The effect of substrates on the Raman spectrum of graphene: Graphene-on-sapphire and graphene-on-glass. *Applied Physics Letters*, 91(20):201904, 2007.

[205] T. M. G. Mohiuddin, A. Lombardo, R. R. Nair, A. Bonetti, G. Savini, R. Jalil, N. Bonini, D. M. Basko, C. Galiotis, N. Marzari, et al. Uniaxial strain in graphene by Raman spectroscopy: G peak splitting, Grüneisen parameters, and sample orientation. *Physical Review B*, 79(20):205433, 2009.

[206] Z. H. Ni, T. Yu, Y. H. Lu, Y. Y. Wang, Y. P. Feng, and Z. X. Shen. Uniaxial strain on graphene: Raman spectroscopy study and band-gap opening. *ACS Nano*, 2(11):2301–2305, 2008.

[207] Z. H. Ni, H. M. Wang, Y. Ma, J. Kasim, Y. H. Wu, and Z. X. Shen. Tunable stress and controlled thickness modification in graphene by annealing. *ACS Nano*, 2(5):1033–1039, 2008.

[208] J. M. Englert, C. Dotzer, G. Yang, M. Schmid, C. Papp, J. M. Gottfried, H.-P. Steinrück, E. Spiecker, F. Hauke, and A. Hirsch. Covalent bulk functionalization of graphene. *Nature Chemistry*, 3(4):279–286, 2011.

[209] A. Jorio, L. G. Cançado, and L. M. Malard. Vibrations in graphene. *2D Materials*, pages 71–89, 2017.

[210] T. J. Chuang. Photodesorption and adsorbate–surface interactions stimulated by laser radiation. *Journal of Vacuum Science & Technology B: Microelectronics Processing and Phenomena*, 3(5):1408–1420, 1985.

[211] P. A. Denis and F. Iribarne. The 1,3 dipolar cycloaddition of azomethine ylides to graphene, single wall carbon nanotubes, and C60. *International Journal of Quantum Chemistry*, 110:1764–1771, 2010.

[212] J. L. Delgado, S. Filippone, A. Martín-Domenech, M. Altable, E. Maroto, F. Langa, N. Martín, and R. Martínez-Alvarez. Mass spectrometry studies of the retro-cycloaddition reaction of pyrrolidino and 2-pyrazolinofullerene derivatives under negative ESI conditions. *Journal of The American Society for Mass Spectrometry*, 22(3):557–567, 2011.

[213] L. Basta, F. Bianco, A. Moscardini, F. Fabbri, L. Bellucci, V. Tozzini, S. Heun, and S. Veronesi. Deterministic covalent organic functionalization of monolayer graphene with 1,3-dipolar cycloaddition via high resolution surface engineering. *arXiv preprint arXiv:2202.06609*, 2022.

[214] S. Goler. *Graphene for Hydrogen Storage*. PhD thesis, Scuola Normale Superiore, 2014.

[215] J. B. Hannon, M. Copel, and R. M. Tromp. Direct measurement of the growth mode of graphene on SiC(0001) and SiC(0001). *Physical Review Letters*, 107(16):166101, 2011.

[216] M. Stockmeier, R. Müller, S. A. Sakwe, P. J. Wellmann, and A. Magerl. On the lattice parameters of silicon carbide. *Journal of Applied Physics*, 105(3):033511, 2009.

[217] F. He, Y. Zhou, Z. Ye, S.-H. Cho, J. Jeong, X. Meng, and Y. Wang. Moiré patterns in 2D materials: A review. *ACS Nano*, 15(4):5944–5958, 2021.

[218] S. Fiori. Li-functionalized graphene on silicon carbide. Master's thesis, Università di Pisa, 2017.

[219] J. Röhrl, M. Hundhausen, K. V. Emtsev, T. Seyller, R. Graupner, and L. Ley. Raman spectra of epitaxial graphene on SiC (0001). *Applied Physics Letters*, 92(20):201918, 2008.

[220] D. S. Lee, C. Riedl, B. Krauss, K. von Klitzing, U. Starke, and J. H. Smet. Raman spectra of epitaxial graphene on SiC and of epitaxial graphene transferred to SiO_2. *Nano Letters*, 8(12):4320–4325, 2008.

[221] I. Shtepliuk, F. Giannazzo, and R. Yakimova. Epitaxial graphene on 4H-SiC(0001) as a versatile platform for materials growth: Mini-review. *Applied Sciences*, 11(13):5784, 2021.

[222] A. Bostwick, T. Ohta, T. Seyller, K. Horn, and E. Rotenberg. Quasiparticle dynamics in graphene. *Nature Physics*, 3(1):36–40, 2007.

[223] S. Rajput, Y. Y. Li, and L. Li. Direct experimental evidence for the reversal of carrier type upon hydrogen intercalation in epitaxial graphene/SiC (0001). *Applied Physics Letters*, 104(4):041908, 2014.

[224] S. Niyogi, E. Bekyarova, M. E. Itkis, H. Zhang, K. Shepperd, J. Hicks, M. Sprinkle, C. Berger, C. N. Lau, W. A. Deheer, et al. Spectroscopy of covalently functionalized graphene. *Nano Letters*, 10(10):4061–4066, 2010.

[225] L. Daukiya, C. Mattioli, D. Aubel, S. Hajjar-Garreau, F. Vonau, E. Denys, G. Reiter, J. Fransson, E. Perrin, M.-L. Bocquet, et al. Covalent functionalization by cycloaddition reactions of pristine defect-free graphene. *ACS Nano*, 11(1):627–634, 2017.

[226] H. Mi, S. Mikael, C.-C. Liu, J.-H. Seo, G. Gui, A. L. Ma, P. F. Nealey, and Z. Ma. Creating periodic local strain in monolayer graphene with nanopillars patterned by self-assembled block copolymer. *Applied Physics Letters*, 107(14):143107, 2015.

[227] G. Mao, Q. Wang, Z. Chai, H. Liu, K. Liu, and X. Ren. Realization of uniaxially strained, rolled-up monolayer CVD graphene on a Si platform via heteroepitaxial InGaAs/GaAs bilayers. *RSC Advances*, 7(24):14481–14486, 2017.

[228] S. Zhang, D. Huang, L. Gu, Y. Wang, and S. Wu. Substrate dopant induced electronic inhomogeneity in epitaxial bilayer graphene. *2D Materials*, 8(3):035001, 2021.

[229] M. Tripathi, A. King, G. Fratta, M. Meloni, M. Large, J. P. Salvage, N. M. Pugno, and A. B. Dalton. Laser-based texturing of graphene to locally tune electrical potential and surface chemistry. *ACS Omega*, 3(12):17000–17009, 2018.

[230] A. Dupré. *Théorie mécanique de la chaleur.* Gauthier-Villars, 1869.

[231] B. Pittenger, N. Erina, and C. Su. Quantitative mechanical property mapping at the nanoscale with PeakForce QNM. *Application Note Veeco Instruments Inc*, 1:1–11, 2010.